PROCEEDINGS OF THE 2004 ANTENNA APPLICATIONS SYMPOSIUM

Volume II of II
Pages 245 - 473

Daniel Schaubert et al.

Final Report: September 2004

APPROVED FOR PUBLIC RELEASE

DTIC ONLY

20050411 080

TECHNICAL REPORT

Proceedings of the 2004 Antenna Applications Symposium, Vol II

Unlimited, Statement A

NOTICE

THIS TECHNICAL REPORT HAS BEEN REVIEWED AND IS APPROVED FOR PUBLICATION.

__//signature//_____

Livio D. Poles
Chief, Antenna Technology Branch

__//signature//_____

Michael N. Alexander
Technical Advisor
Electromagnetics Technology Division

REPORT DOCUMENTATION PAGE

Form Approved
OMB No. 0704-0188

1. REPORT DATE *(DD-MM-YYYY)*	2. REPORT TYPE		3. DATES COVERED *(From - To)*
30 November 2004	Final		15-17 Sept 2004

4. TITLE AND SUBTITLE
Proceedings of the 2004 Antenna Applications Symposium Vol II

5a. CONTRACT NUMBER
ATESRD F33615-02-D-1283

5b. GRANT NUMBER

5c. PROGRAM ELEMENT NUMBER

6. AUTHOR(S)
Daniel Schaubert et, al

5d. PROJECT NUMBER

5e. TASK NUMBER

5f. WORK UNIT NUMBER

7. PERFORMING ORGANIZATION NAME(S) AND ADDRESS(ES)
University of Massachusetts
149 Aubinwood Road
Amherst, MA 01002

8. PERFORMING ORGANIZATION REPORT NUMBER

9. SPONSORING/MONITORING AGENCY NAME(S) AND ADDRESS(ES)
Air Force Research Laboratory
80 Scott Rd
Electromagnetics Technology Division
Sensors Directorate
Hanssom AFB, MA 01731

10. SPONSOR/MONITOR'S ACRONYM(S)
AFRL-SN-HS-TR-2005-016

11. SPONSOR/MONITOR'S REPORT NUMBER(S)

12. DISTRIBUTION/AVAILABILITY STATEMENT
APPROVED FOR PUBLIC RELEASE; DISTRIBUTION UNLIMITED. ESC 05-0109, 21 JAN 2005

13. SUPPLEMENTARY NOTES
Volume I contains Pages 1-244, Volume II 245-473

14. ABSTRACT
The Proceedings of the 2004 Antenna Applications Symposium is a collection of state-of-the art papers relating to antenna arrays, millimeter wave antennas, simulation and measurment of antennas, integrated antennas, and antenna bandwidth and radiation inmprovements.

15. SUBJECT TERMS
Antennas, phased arrays, digital beamforming, millimeter waves, antenna measurements

16. SECURITY CLASSIFICATION OF:			17. LIMITATION OF ABSTRACT	18. NUMBER OF PAGES	19a. NAME OF RESPONSIBLE PERSON
a. REPORT	b. ABSTRACT	c. THIS PAGE			Livio Poles
UL	UL	UL	UL	228	19b. TELEPHONE NUMBER *(Include area code)* 781-377-4087

i

Standard Form 298 (Rev. 8/98)
Prescribed by ANSI Std. Z39.18

2004 ANTENNA APPLICATIONS SYMPOSIUM
(Volume II)
15 – 17 September 2004
Monticello, Illinois

Identifiers for Proceedings of Symposia

The USAF Antenna Research and Development Program

Year	Symp. No.	Identifier
1951	First	
1952	Second	ADB870006
1953	Third	ADB283180
1954	Fourth	AD63139
1955	Fifth	AD90397
1956	Sixth	AD114702
1957	Seventh	AD138500
1958	Eighth	AD301151
1959	Ninth	AD314721
1960	Tenth	AD244388 (Vol. 1)
		AD319613 (Vol. 2)
1961	Eleventh	AD669109 (Vol. 1)
		AD326549 (Vol. 2)
1962	Twelfth	AD287185 (Vol. 1)
		AD334484 (Vol. 2)
1963	Thirteenth	AD421483
1964	Fourteenth	AD609104
1965	Fifteenth	AD474238L
1966	Sixteenth	AD800524L
1967	Seventeenth	AD822894L
1968	Eighteenth	AD846427L
1969	Nineteenth	AD860812L
1970	Twentieth	AD875973L
1971	Twenty-First	AD888641L
1972	Twenty-Second	AD904360L
1973	Twenty-Third	AD914238L

Antenna Applications Symposium

		TR#	ADA#
1977	First	None	955413
1978	Second	None	955416
1979	Third	_____	077167
1980	Fourth	_____	205907
1981	Fifth	_____	205816
1982	Sixth	_____	129356
1983	Seventh	_____	142003; 142754
1984	Eighth	85-14	153257; 153258
1985	Ninth	85-242	166754; 165535
1986	Tenth	87-10	181537; 181536
1987	Eleventh	88-160	206705; 206704
1988	Twelfth	89-121	213815; 211396
1989	Thirteenth	90-42	226022; 226021
1990	Fourteenth	91-156	237056; 237057
1991	Fifteenth	92-42	253681; 253682
1992	Sixteenth	93-119	268167; 266916
1993	Seventeenth	94-20	277202; 277203
1994	Eighteenth	95-47	293258; 293259
1995	Nineteenth	96-100	309715; 309723
1996	Twentieth	97-189	341737
1997	Twenty First	1998-143	355120
1998	Twenty Second	1999-86	364798
1999	Twenty Third	2000-008 (I) (II)	386476; 386477
2000	Twenty Fourth	2002-001 Vol I & II	
2001	Twenty Fifth	2002-002 Vol I & II	
2002	Twenty Sixth	2005-001 Vol I & II	
2003	Twenty Seventh		

S - BAND ELECTRONICALLY SCANNED PHASED ARRAY ANTENNA (PAA) DEVELOPMENT FOR CONTROL AND COMMUNICATIONS OF AIR FORCE AND NASA SATELLITES

Paul J. Oleski,	AFRL, Information Directorate
Robert Patton, 2Lt, USAF	AFRL, Information Directorate
Dr. Shiang Liu,	Space & Missile Center/Aerospace Corp
Dr. Boris Tomasic,	AFRL, Sensor's Directorate
John Turtle,	AFRL, Sensor's Directorate
Dean Paschen,	Ball Aerospace
Sarjit S. Bharj,	Princeton Microwave Technology
Robert Schmier,	Alpha Omega Electromagnetics
Bruce Wilber,	Custom Manufacturing & Engineering
Bill Asiano,	Real Time (RT) Logic

Abstract: The United States Air Force Research Laboratory (AFRL), Space and Missile Systems Center (SMC), AF Space Battle Lab (AFSB), Aerospace Corp, 3 Small Business Innovative Research (SBIR) contractors, and Ball Aerospace as the Systems Integrator have designed, fabricated and tested a six panel subarray to demonstrate the possibility of providing Telemetry, Tracking, Commanding (TT&C) and Communications to Low Earth Satellites (LEOs) with an electronically scanned antenna . This paper will give a general overview of the components, integration, fabrication, and testing that led to the completion of the six panel subarray which is a Proof of Concept (POC) piece of an envisioned dome shaped antenna for possible replacement of the existing AF Satellite Control Network (AFSCN) mechanically steered dishes, currently providing TT&C and Communications signals to the AF Space Command's and NASA's GEO, MEO and LEO satellites. The first Panel of 78 elements was tested at the AFRL/SN Antenna Measurements Facility in Ipswich Mass. With this successful result Ball Aerospace under contract to AFSB integrated the AFRL/IF/SN components (Transmit and Receive (TR) modules, beam formers, radiating elements and antenna control software) into six combined panels for the demonstration and evaluation of the subarray at a NASA Flight Test Facility located on Wallops Island, Va. in August 2004. This paper was submitted during the Phased Array at Wallops Island (PAWS) demonstration. Also an AFRL Portable Universal Ground Processing Unit (PUGPU) provided remote monitoring and receiving of the TT&C signals demonstrating a 5 times reduction in equipment size. Detailed results and analysis of the antenna evaluation will be available from AF Space Battlelab in Jan 2005.

1. Introduction

The subject S-Band Electronically Scanned Antenna (ESA) is being developed for a proposed Geodome Phased Array Antenna (GDPAA) which could replace the functionality of three, thirty foot mechanically steered dishes which currently support the AF Satellite Control Network (AFSCN). The main components of the GDPAA System are a Transmit & Receive (TR) Module by Princeton Microwave Technology, Princeton, NJ, beam former and radiating elements by Alpha Omega Electromagnetics (AOE), Arnold, MD, and Antenna Control Computer (ACC) by Custom Manufacturing & Engineering (CME), St Petersburg, FL. An additional part of the system which was part of the demonstration at Wallops Island and will be an integral part in the future system is a Portable Universal Ground Processing Unit (PUGPU) by RT Logic which is software driven electronics to provide remotely configurable frequencies and wave forms.

Low cost component design is critical in developing a practical multi-beam phase array antenna. Combined RF, digital and monolithic circuits are important but not the only critical issue. This TR module differs from the previous modules, Ref.3 & 4, in that this module has a wider frequency band associated with the transmit section. In addition, diplexers are utilized between each transmit and receive section. Both left-hand and right-hand polarization is used in a special polarization matrix.

Affordable antenna arrays operating at microwave frequencies are envisioned to consist of active modules that employ microwave integrated circuits located at each radiating element of the aperture. The antenna system consists of combined transmit and receive patch radiators capable of rapid beam motion. Beam agility and high-radiated power levels in association with the close spacing between the radiators drive the antenna design. The need for fast beam switching requires digital control circuits to calculate phase shift settings. A high RF radiated power level developed from closely spaced RF amplifiers generates large heat densities. This forces the transmit antenna to increase in area to where beam pointing accuracy limits the array size. The great number of elements in the array emphasizes the need to develop a practical method of distributing control signals throughout the array. A GDPAA is considered for the AFSCN. Implicit in the systems functionality is the ability to achieve full-duplex operation. In addition, the array is capable of controlling fundamental radiation characteristics such as beam width and size; sidelobe levels, and power, in order to realize the different antenna characteristics required by various satellites. The array aperture consists of a large number of radiating elements that are spaced approximately half a wavelength at the upper end of the operational frequency band. The frequency response and excitation of each element in the aperture can be independently controlled. The aperture can be fully or partially utilized either to direct energy over a large volume or intentionally directed in a certain direction. The capability of the array to provide transmit and receive functions simultaneously and to rapidly alter the set of configurations is possible due to an active element control circuit. The active control circuits allow the phase array antenna to control its radiation characteristics. The aperture can be uniformly illuminated to achieve maximum gain or tapered to achieve low sidelobes or a shaped beam. The combination of the variable attenuator and phase shifter in the TR permits the array illumination to be modified and the antenna beam to be scanned in any direction. The filters specify the portion of the

246

aperture used by a particular system. The phase shifter, the variable attenuator and the amplifier are components that have been developed in Microwave Monolithic Integrated Circuit technology (MMIC), in the last decade.

The high isolation requirement between transmit and receive channels focused the effort to investigate what performance measures are achieved when using low-cost ceramic diplexing filters. MMIC based power amplifiers and low noise amplifiers (LNA) are also used in the transmit channel. Due to the bandwidth of the transmit section a broadband phase shifter using low pass and high pass filter sections was designed. The receive band phase shifter was based on switched line methodology.

## 2. Phased Array at Wallops Island (PAWS)

A 6 Panel Phased Array Antenna was successfully demonstrated at the NASA, Wallops Island Flight Facility (WFF); August 2004. This ESA was used to perform all required modes of operation during its AF SGLS satellite and NASA USB satellite contacts. Test equipment included the SMC Det 12 Transportable Space Test Resource (TSTR) and S-Band Transportable Ground Station (STGS), the NASA Telemetry, tracking, and Command (TT&C) equipment at Wallops and the AFRL/IFG Portable Universal Ground Processing Unit (PUGPU). The PAT antenna commanded the satellites to turn on transponders with S-tones. Carrier lock, demodulator lock on the sidebands, and bit synch lock were all achieved using the test equipment, showing proper telemetry operation. Correct ranging values were computed and the system operated in auto track mode. The operations with TT&C, and ranging, covered all required modes of operation. A total of 14 different satellites from several NASA and AFSCN operational areas provide link to the PAWS operations under direction of the AF Space Battlelab (AFSB)/Ball Aerospace demonstration team. The PAWS system was configured to conduct two simultaneous satellite contacts using a 6-panel phased array antenna. PAWS operations were conducted daily August 9-20, 2004. The demonstration verified PAWS capability for TT&C for satellites in different orbits, using transportable AFSCN ground equipment provided by Det 12/SMC and fixed NASA ground equipment provided by WFF. AF Space Battlelab provided coordination with the 22nd Satellite Operations (SOPS). 22 SOPS provided the 24/7 Network management for the demonstration by providing Two Line Elements (TLEs), PAWS and a 12 foot dish STGS and Transportable Satellite Test Resource (TSTR) status, demonstration scheduling information, and function as operational focal point for PAWS users. 22 SOPS integrated the new PAWS site, into the ESD system and AFSCN. NASA and AFSCN operators provided Satellite Control Authority (SCA) and satellites. Below is a picture of the PAWS mounted on a steerable pedestal.
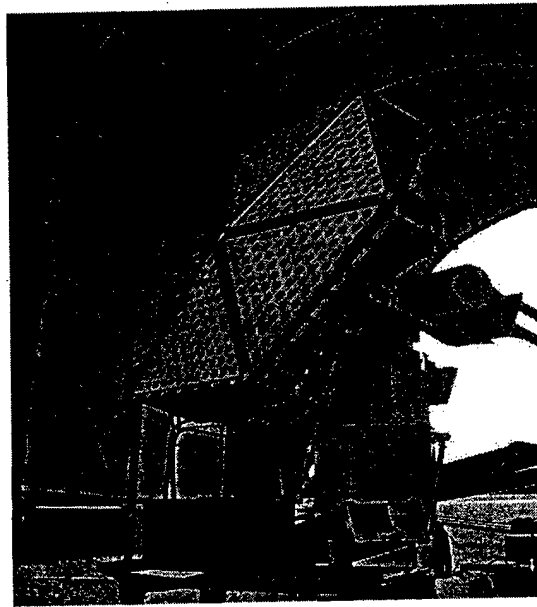
Figure1: Six Panel Phased Array Antenna at Wallops Island (PAWS)

3. TRANSMIT RECEIVE MODULE

The development of the Transmit Receive (TR) modules for the Phase Array Antenna was accomplished under a Phase II Small Business Innovative Research (SBIR) program with Princeton Microwave Technology (PmT®) managed by AFLR/IFGC, Rome, NY. Low design to cost ratio was the overall driving factor conducted from project initiation. In addition, the cost associated with streamlined design components couldn't compromise in the overall Antenna performance requirements. The availability of the active devices from the PCS markets helped greatly reduced the cost of amplifiers and phase shifters. Ceteris paribus, the TR component design and implementation were practical, both effective and economically viable.
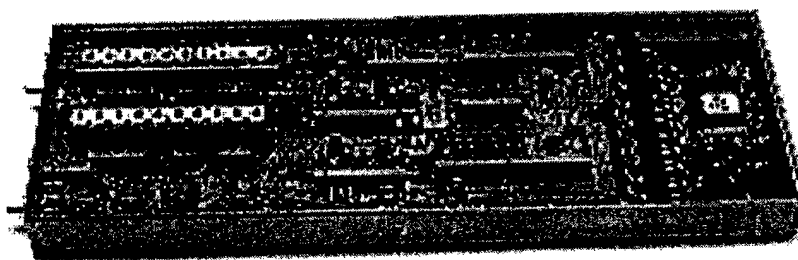
Figure 2: TR module

The T/R module, Figure 2.1, is divided into two sections, a four channel RF section and Digital Controller board. The DC control board produces all necessary controls signals and voltages for the MMIC's on board the RF section. The RF Board is composed of two receive and two transmit channels. The two transmits channels operate at frequencies

from 1.75-2.1 GHz with a measured gain of 20 dB. The receiver frequency of operation is 2.2-2.3 GHz with a channel noise figure of 2 dB measured with an overall gain of in excess of 30 dB. Transmit/receive channel isolation is achieved through a column of 10 low-cost ceramic diplexing filters. In addition, low cost MMIC's based power amplifiers are used for the transmit channels. Effort was also directed towards the design of a low-cost phase shifter. The phase shifter, variable attenuator and amplifier are all TR module sub-components developed in MMIC. A broadband phase shifter using low pass and high pass filter sections was designed to accommodate the bandwidth of the transmit channels. The receive channel phase shifters are based on switched line methodology. The TR module's active element control circuit enables the array to provide simultaneous transmit and receive operation, while seamlessly altering its pattern configurations.

3.1 RF Board

3.1.1 Receiver Layout
The downlink input signal is fed to a high rejection band pass ceramic filter. The input signal passes through a series of amplifiers, phase shifters, attenuators, and SPDT switches before reaching the receiver ports. The total gain across the receiver band is 30 dB. Low noise MMIC amplifiers developed for the satellite and radio market are used. The devices provide a gain of 18 dB with an associated noise figure of 1 dB. The phase shifter design essentially replaces two single pole double throw switches reducing the component count by 50%. The receiver phase shifters are based on the switch line approach and exhibits a 6dB insertion loss. Insertion loss of the phase shifter is measured at 8 dB with a total of 0.4 dB throughout all phase states. Polarization switching is incorporated to enable both LH and RH circular polarization in receive and transmit. Overall receiver +30db gain is attributed to the engineering of its low-loss components.

3.1.2 Transmitter Layout
The transmit path consists of two input and two output ports to transmit and receive from the two antenna ports. The transmit phase shifters are designed with low and high-pass filter sections switched between paths providing 22.5, 45, 90 and 180 ± 10 degrees of phase shift respectfully. Amplitude change for the phase shifter is measured at less than 1 dB for all phase states. The RF path also incorporates a five-bit attenuator (attenuation levels of 1dB, 2dB, 4dB, 8dB, 16dB); a preamplifier; absorptive type SPDT and embedded power combiner. The absorptive SPDT switch is used to induce left hand circular polarization (LHCP) and right hand circular polarization (RHCP) in the signal. A 90-degree hybrid is used to provide quadrature phase in the input signal. The quadrature output of the hybrid is amplified to +30 dBm before transmitting through a high rejection low pass ceramic filter. The overall gain of the transmitter channel is 20 dB.

3.1.3 Transmit/Receive Isolation
Transmit and receive isolation is important during vehicle command and tracking. The isolation prevents the antenna from self jamming. A pair of high Q ceramic resonator diplexers is required to maintain optimum performance. The transmit side of the diplexer filter, inserted after the transmit amplifier, prevents wideband noise from entering the

receiver, and degrading performance. The receive section of the diplexer, prevents the coupled transmit signal from degrading the linearity of the receive Low Noise Amplifier (LNA). The diplexers provide a minimum isolation of 60dB between the high end of the transmit band and low end of the receive band. Typical insertion loss of 0.7dB and 1.0dB is achieved in the transmit and receive pass bands respectively.

3.2 Digital Controller Board

The purpose of the serial to parallel bus arbitrator is to accept serial commands and unit address data and pass these commands to a parallel bus connected to a uniquely addressed unit. The input signals to this circuit are data, clock and latch; the outputs are 16 parallel command lines connected to a single programmable unit. Four addressable units are grouped into a single TR module. In order to avoid hardware redundancy, one unit can be addressed with a base address and the remaining three can be indirectly addressed. In addition, to compensate for data and clock line fan out for a large number of modules; a single module can act as a "Master" module for several modules by buffering the clock, data and latch lines. 32 bits of serial data are clocked into a 32-bit wide shift register. Command data is stored in bits 0 to 15 and the desired unit's address is stored in bits 16 to 31 allowing for 65536 possible units. Once all 32 serial bits are stored in the shift register, a unit with a matching address is determined to exist, and the latch line is subsequently set high for a clock pulse, commands are latched out to the addressed 16 line parallel bus. In each unit, the channel is indirectly addressed 0-3 by subtracting the module's base address from the intended unit's address. The serial to parallel bus arbitrator circuit is now ready to receive the next serial stream of data.

4. BEAM FORMER AND RADIATING ELEMENTS

Under an Air Force Phase II SBIR effort entitled "Affordable Beam Forming Network for TT&C Phased Array Antenna," managed by AFRL/SNHA, Hanscom AFB, MA, Alpha Omega Electromagnetics, LLC (AOE) researched and demonstrated an important and timely technological need, specifically the practical development and demonstration of low-cost, passive dual-frequency, multi-beam phased array subarray technology. This low-cost subarray technology is the fundamental building block required for the practical realization of a large hemispherical phased array useful for horizon-to-horizon simultaneous coverage of multi-satellite tracking. The success of this endeavor rested heavily upon the development of novel radiating element technology in addition to a multi-beam Beamforming Network (BFN), both of which were commensurate with low-cost strategic system objectives. The primary objective of the SBIR effort was to develop and demonstrate the technical feasibility of a low-cost feed network (beamforming network or BFN) with integrated radiating elements. These components were developed for utilization in a phased array antenna in support of satellite tracking, telemetry and commanding (TT&C) operations, such as the Air Force Satellite Control Network (AFSCN).

The feed network is responsible for distributing and combining radio frequency (RF) signals to and from individual TR modules. It must accommodate two independent transmit and receive beams (a total of four beams) with full duplex operation. Phase I of

the SBIR effort focused on the feed network at the subarray level. The basic architecture of the feed network developed and demonstrated will support a subarray architecture that will be employed in the implementation of a hemispherical phased array antenna for horizon-to-horizon, simultaneous coverage of multi-satellite tracking and communication. The success of such an application rests heavily on the development of a robust feed network, which combines superior RF isolation and interconnect technology in a cost-effective packaging scheme. AOE established the BFN parameters that are necessary for its successful, cost-effective implementation including the shape, material selection, coupler type and stack-up. In addition, interconnects between the BFN and AOE developed radiating elements and Princeton Microwave Technologies (PmT) developed TR modules were established. All of these technology developments underwent detail design and were successfully demonstrated with hardware during the Phase II efforts. The chosen BFN configuration that was implemented is simultaneously consistent with program performance and manufacturability objectives.

The feed network developed under Phase I of this effort was closely related to another SBIR topic, "Omni directional Hemispherical Phased Array Antenna" in which AOE developed dual-band, full duplex, dual-polarized wide-scanning radiating element technology suitable for use in an AFSCN system. The basic radiating element architecture was established along with some basic TR module and subarray architecture concepts. During the course of this Phase II effort, it was determined that the radiating elements (as well as the BFN) must also support operation over the USB as well as the SGLS frequency bands. The original dual band radiating element was not able to support operation over both these frequency bands and hence new broadband radiating elements were developed and demonstrated under this effort and were integrated with the BFN.

The BFN and radiating element technology developed under this effort were designed not only to work together as an integrated subarray antenna panel, but also to integrate with TR modules and beam steering computers that were developed by CME. To this end, AOE worked closely with PMT, CME and Ball Aerospace such that TR modules easily integrated into the panel and were supplied with appropriate RF, power and control signals. AOE generated and supplied all panel interface definitions such that there was no ambiguity when interfacing TR modules and power and control signals with the antenna panels. In total, AOE fabricated six antenna panels that were fully populated with TR modules and successfully tested both by the Air Force and Ball Aerospace. While some problems were encountered during the integration and test process, no failures were due to AOE's antenna panel hardware.

Under this Phase II effort, AOE employed proprietary finite element software to design and predict the performance of the radiating elements that were integrated into the BFN. The resulting radiating element design was then experimentally verified both by waveguide simulator measurements and through element pattern testing of a small passive array. Figure 3 shows the results of the waveguide simulator measurements and Figure 4 shows the small test array used to measure element patterns. Under another task, the BFN underwent a detailed design effort and several prototypes were fabricated. These prototypes were successfully validated by testing them for DC continuity of the

DC and digital lines as well as RF testing them to ensure proper distribution of the RF signals. Subsequent to the BFN and radiating element validation, a complete antenna panel with integrated BFN/radiating elements and accommodation for T/R modules was fabricated and delivered to Hanscom Air Force Base (testing at Ipswich, MA) for TR module integration and testing. After successful testing of the initial panel, two additional panels were fabricated. Figures 5 and 6 show the antenna panel under test in the near field range at the AFRL/SN, Ipswich test facility.
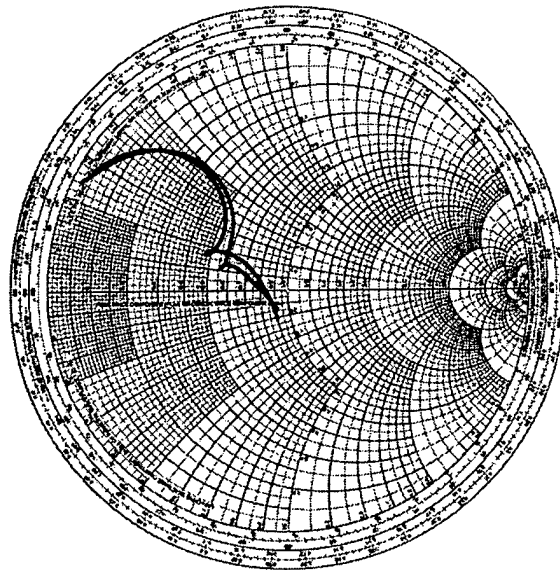
Figure 3. Complex gated simulator reflection data comparison (gray line-measured / black line-AOE FEM unit cell).
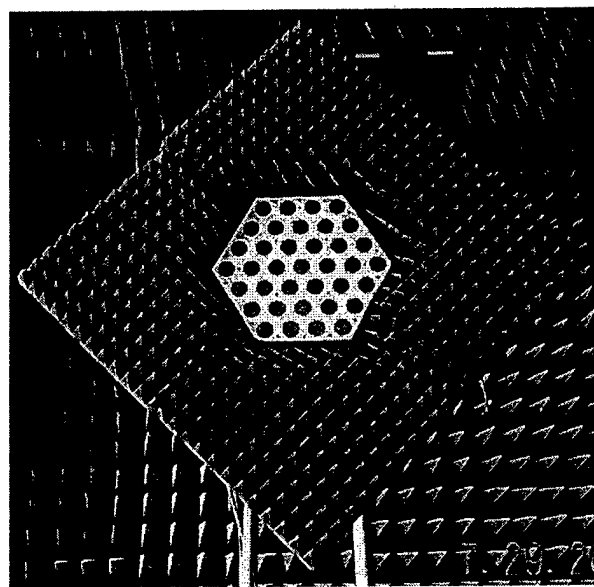
Figure 4. Small test array at the Air Force test facility in Ipswich
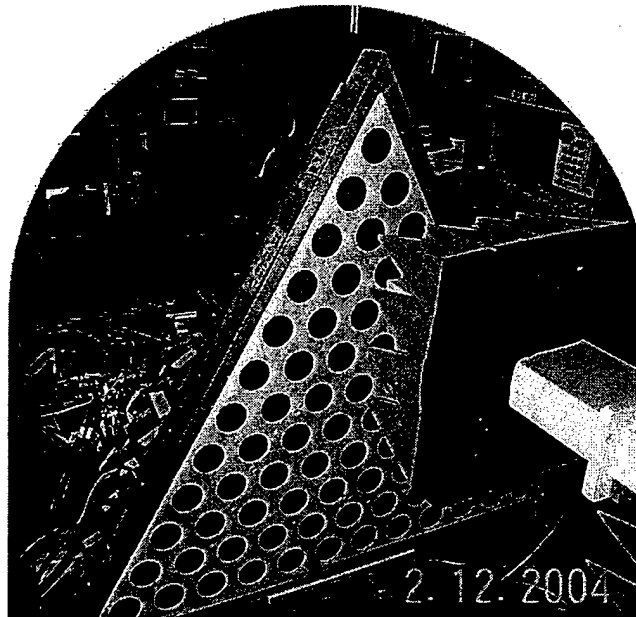
Figure 5: First antenna panel being measured with TR modules installed, at the Air Force Ipswich test facility.

Figure 6: First antenna panel being measured with TR modules installed at the Air Force Ipswich test facility.
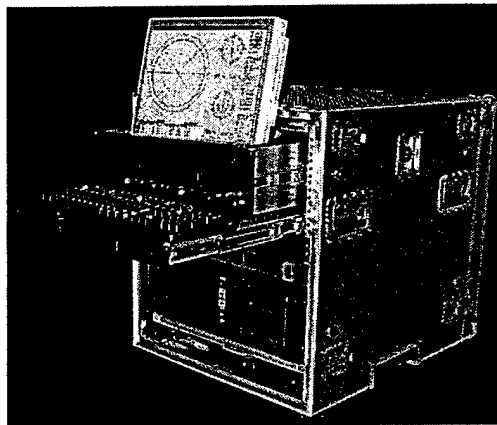
5. Antenna Control Computer for a Phased Array Antenna

Under an Air Force Phase II SBIR effort entitled, "Antenna Control Computer (ACC) for Phased Array Antennas (PAA)," managed by AFRL/SNHA, Custom Manufacturing & Engineering, Inc. (CME), developed an ACC for the geodesic dome, satellite tracking, telemetry, and command (TT&C) phased array antenna architecture to support the modernization of the United States Air Force Satellite Control Network (AFSCN). CME is currently working with the Air Force Research Labs (AFRL) to further enhance the ACC concept. A goal of the TT&C Phased Array Antenna project supported by the CME ACC is to have the ability to be a substitute for existing multiple dish antennas and their Antenna Control Units (ACU) with little or no modifications to the current control and status (C&S) connected computers. To help achieve this goal, the ACC design will retain

253

the electrical requirements and connectors the same as the current ACU/C&S interface. The ACC software commands interface will be a subset of the current commands in the existing C&S computer network. In addition, the current status message format can remain the same from the ACC to the C&S. As part of its ACC enhancement effort under AFRL guidance, CME is developing the algorithms and control software to configure multiple antenna panel facet arrays arranged in a geodesic dome in order to provide multiple, concurrent satellite tracking and steering. This development involves complex mathematical computations for satellite orbital path predictions and panel facet configuring for beam steering.

CME has developed and packaged a comprehensive development and demonstration support workstation using state-of-the-art computer hardware. This enhanced demonstrator will replace the ACU and interface directly to the C&S and the panel facet controllers to provide antenna control and steering functions.

The new geodesic dome system provides higher communications capacity and reliability, replacing multiple dish antennas. The new system provides benefits for both government and commercial antenna control operations. The ACC is shown in figure 7.


Figure 7: Antenna Control Computer for Phased Array Antenna Steering

ACC Features

The ACC will:
- Provide local and remote control of phased array antenna steering
- Offer safety functions for dome power and beam steering (675 panels)
- Supply maintenance functions for panel controller and transmit/receive module reporting (78 transmit/receive modules per panel)
- Provide virtually 100 percent up time through redundancy and hot swap capabilities
- Replace the current ACU and seamlessly interface with one or more existing C&S computers in order to support satellite TT&C operations for the AFSCN

254

6. Portable Universal Ground Processing Unit (PUGPU)

DR70 Front End   Monics Display

FCS   Telemetrix 70/70 XL   Telemetrix 500GT
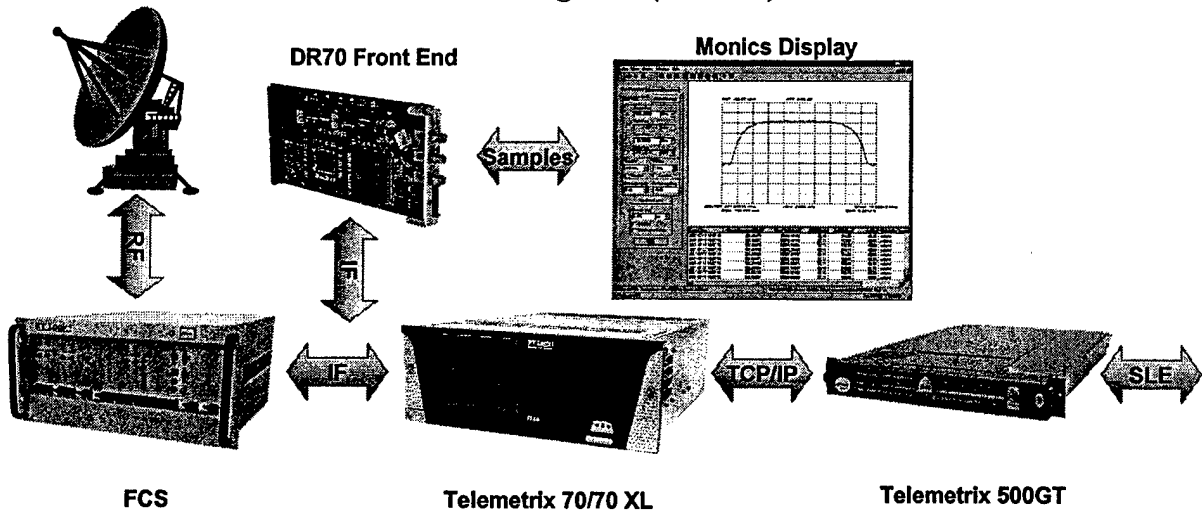
PUGPU Overview

Under an AF Phase II SBIR effort entitled "PUGPU" and managed by AFRL/IFGE Rome, NY, remotely reconfigurable software driven digital signal processing system was developed. The PUGPU system supports the full set of TT&C ground processing functions providing a 'Universal Processor" and supporting the optimal RF, IF interface, and remote software interface functions for effective ground operations. The PUGPU supports frequency conversion through its Frequency Conversion Subsystem (FCS), a digital based TT&C baseband processing system (DBP) using a commercially available Telemetrix XL, spectrum monitoring with a Digital Spectral Analysis (DSA) subsystem, and provides Eb/No measurements that can be used in uplink power control operations. A much fuller implementation of the Consultive Committee of Space Data Systems (CCSDS) protocols is also implemented, including the Space Link Extensions (SLE) utilized for interfacing to the ground networks via Internet Protocol.

Figure shows the configuration of the PUGPU system and its external interfaces with the equipment in the Satellite Control Center. The PUGPU supports both USB and SGLS formats for telemetry and commanding operations.
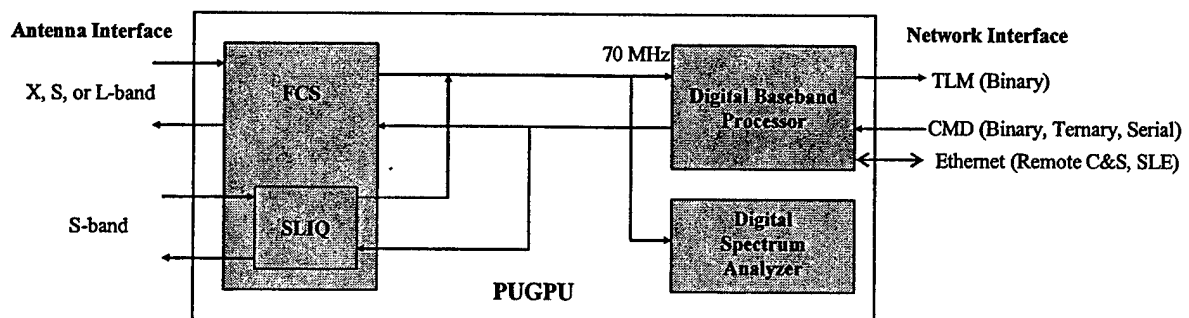

Figure 8. PUGPU System

255

The support of various frequency ranges is a central component of the PUGPU in making it a truly "universal" unit. The different IF ranges imposed by the current AFSCN, NASA, and CCSDS standards are supported by many converter vendors. However, it can be a cumbersome task and a requirement to optimally match the performance parameters of the frequency conversion process as part of a front-end system design to the DSP-based baseband processing functions implemented within the PUGPU. A representation of the FCS implemented as a frequency conversion subsystem is provided in Figure .
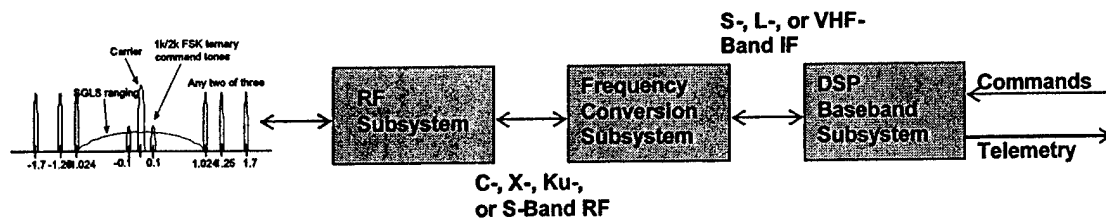
Figure 9: PUGPU FCS RF and IF Conversions

The PUGPU design addresses the following operational issues:

- Design of IF performance parameters to optimally match both the baseband and RF subsystems interfaced by PUGPU. Parameters include frequency range, tuning, dynamic range, spectral emissions, and noise figure.

- Develop a form factor solution that makes minimal use of rack space and mounting resources.

- Provide a PUGPU configuration that is a scalable architecture where different frequency ranges can be readily supported with minimal changes to the fundamental subsystem solution.

- Provide a design with minimal Line Replaceable Units (LRU) and discrete subsystem components to minimize sparing requirements and life cycle costs.

The above issues are resolved by providing a form factor solution for PUGPU that incorporates the frequency conversion process as an integral part of the PUGPU digital baseband processing that provides the traditional Telemetry, Commanding, and Ranging functions.

6.1. Frequency Conversion Subsystem (FCS)

The variety of downlink frequencies supported across the various platforms, increase to higher data throughputs, and the move towards in-band commanding and telemetry has extended the basic S-Band telemetry/L-Band command philosophy to include X-Band, with future expansions for C-Band, Ku-Band, and Ka-Band downlinks. With this range of downlink frequencies and wide bandwidths it is not possible to utilize a single down conversion unit and then process at a low frequency IF. A more cost-effective and technically viable solution is to block-down convert from each specific band to a

common IF. Based upon the block down conversion products available today and the approach taken in implementing tactical terminals, an L-Band IF is used. The L-Band supports a bandwidth of 800 MHz in order to accommodate higher data rate applications. The FCS design consists of a 19" wide rack mounted chassis. The chassis contains 21 CPCI card slots which host processing cards, frequency conversion modules, and the DSA components using both RF and digital backplanes. The processing cards host firmware functions that are modular and tailored specific to the chassis applications. Specifically, tailored applications include spectral analysis and measurement, signal monitoring, and monitoring and control of the frequency conversion 'bricks' that are housed in the chassis. These 'bricks' support the necessary RF and IF frequency ranges (C, X, Ku, S/L, 70MHz) specific to the PUGPU application. The converters slide in and out of the chassis from the front by way of a handle and are blind-mated in the rear for DC power and status. Each converter brick contains a single input and output port specific to the frequency conversion requirement. The converters may translate a fixed range of frequency (block) or be tunable within a frequency range (agile) depending on the application. Redundant power supplies provide the chassis with reliable power. The FCS interface layout is shown in figure 10.
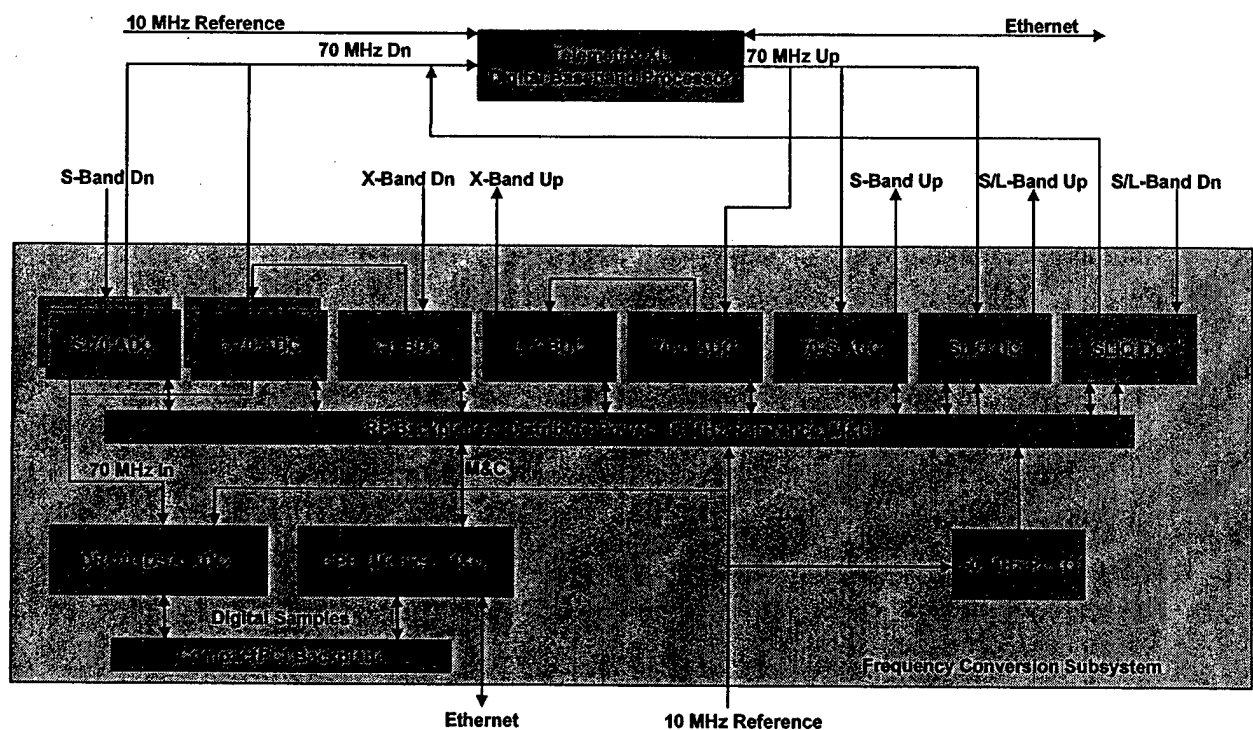
Figure 10: PUGPU FCS Interfaces

The FCS converter bricks are specific in terms of input and output frequency to provide the PUGPU a capability to interface to any AFSCN, NASA, or CCSDS RF/IF interface. This integrated system solution which combines frequency conversion with baseband processing allows a single solution for all current frequency conversion problems and eliminates the technical complexities associated with interfacing, lead times, and compatibility between third party converter vendors. The software control and status task

for the FCS consolidates control of the up-converters and down-converters as well as the spectral analysis, and other signal quality monitoring.

6.2. Digital Baseband Processing System (DBPS) (Telemetrix XL)

RT Logic is working on the Satellite Control Network Contract (SCNC) supporting Honeywell in their implementation of the Remote Tracking Station (RTS) Block Upgrade. Specifically, RT Logic is providing the unit that performs the digital signal processing associated with telemetry, commanding and ranging. This unit, called the Telemetrix XL, supports both SGLS and USB signal structures and is a digital, FPGA-based solution. The Telemetrix XL product is packaged in a rack-mount industrial personal computer and supports both serial and Ethernet interfaces for digital interfaces and uses 70 MHz to receive and transmit telemetry, ranging & commanding signals respectively. Figure 11 shows the chassis view of the Telemetrix-XL product. RT Logic has leveraged off this development to extend the Telemetrix XL to utilize additional functions within the FCS as the PUGPU DBPS. An external software-controlled matrix switch can be used to dynamically assign routing of the signal paths between the FCS subsystem and the DBPS

The Telemetrix hardware is a PCI-based architecture where each of the internal boards communicates via a common backplane bus. Dual Pentium processors control the unit and communicate with each of the Downlink (DL2G) IF and processing boards, the Uplink (UL3) board, and the Signal Conversion Board (SCB) as shown in Figure 12. An external I/O board which is mounted to the back of the chassis rack is used to bring out all external signals and test points for the subsystem. .
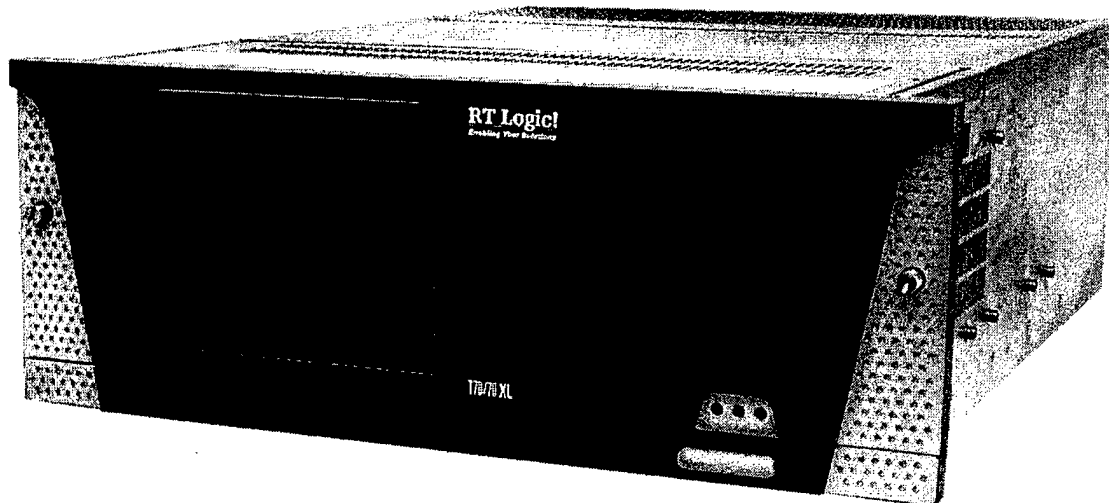
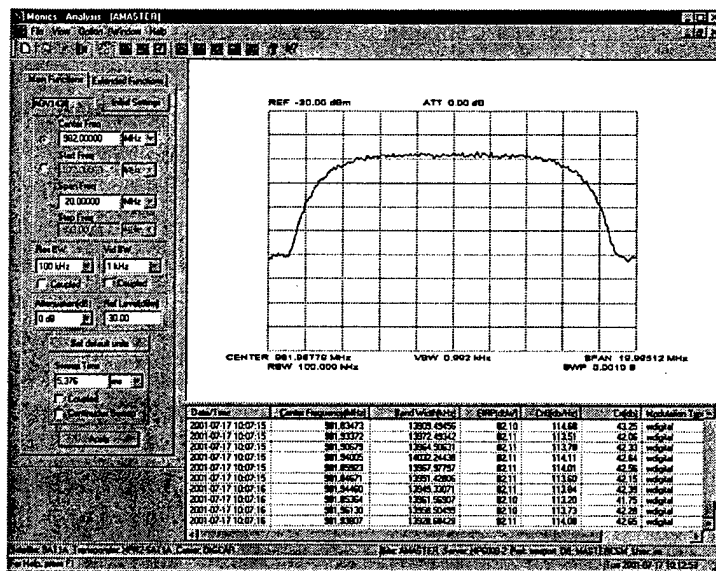
Figure 11: Telemetrix XL Chassis
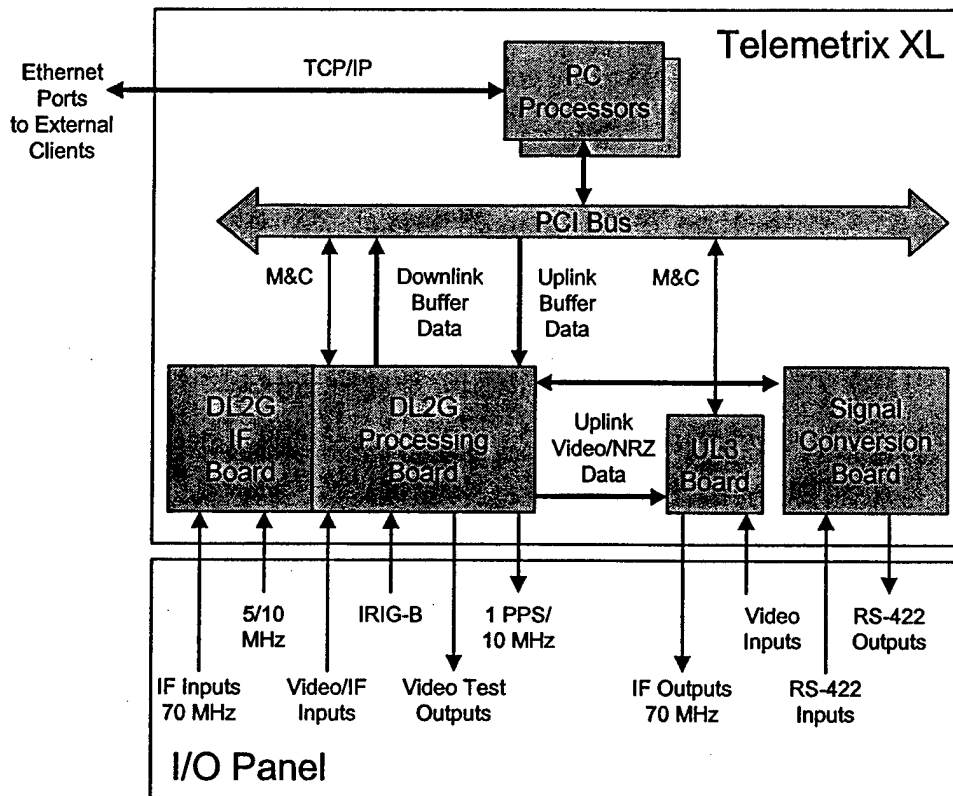
Figure 12. Telemetrix XL Internal Hardware

The PUGPU software controls the local FCS and DBPS elements. This software can run as a Java client on any network-based control workstation. A resource management function is implemented that supports a satellite 'contact-centric' definition of the link to be processed. This allows configuration of the front-end parameters without knowledge of the specific hardware implementation. Additional software on the DBPS supports interfacing to the Satellite Control Center (SOC) via legacy clock and data interface (through a multiplexer) or via Ethernet. Ethernet data can be sent as raw encrypted packets, or if the link is CCSDS with clear headers, using the SLE protocols.

The Telemetrix XL base unit is extended to utilize the additional I/O and processing required for the PUGPU. These extensions consist of a self contained transmit and receiver BERT, signal generation loop-back capability (internal, IF, and RF) to diagnose signal paths, RF and IF patching, a frequency reference source for 10 MHz and 1PPS, and a self contained GUI to monitor and control the rack components. Figure 13 shows the functional capabilities of the DBPS with the additional capabilities.

Figure 13: DBPS Extended Capabilities

6.3. Digital Spectral Analysis (DSA) Subsystem

The DSA is used as an automatic satellite carrier monitoring system designed to monitor satellite uplink and downlink performance and to assure that transponder accesses are properly configured. The monitoring system is designed for applications that necessitate multiple monitoring sites, often from geographically separate areas. The distributed architecture allows monitoring of remote locations from a Network Operations Center (NOC) using communications networks as narrow as 64Kbps. From any point on the WAN, including Web access to individual sites, the DSA can provide monitoring and control.

Using advanced Digital Signal Processing (DSP) techniques, the DSA is able to find and display interfering carriers, even when there is a Carrier-under-Carrier interference. In addition, it is capable of providing distinctive carrier characteristics to assist the operator in determining the source of an interfering signal. A typical DSA monitoring window is shown in Figure 14.

Figure 14: DSA Spectrum Monitoring Window

The automatic monitoring feature provides unattended monitoring of carriers, noise slots and beacons while the operator is free to attend to other activities. These operator initiated monitoring plans will test each carrier in the plan and automatically set the RF switching, and DSP Subsystem to the appropriate values. If an abnormal condition is detected, the system will alert the operator and store the measurement traces along with the measurement results. Stored data and traces can be played-back for any period of time.

Based on the FCS configuration, the PUGPU front-end can be configured for an almost unlimited number of monitoring sites and for any mixture of X, S, C, Ku, and Ka-band uplink and downlink RF monitoring chains. Each monitoring chain is converted to a 70 MHz IF by the agile converter modules. The FCS is used as the DSA front-end tuner assembly utilizing a digitized 70 MHz input. The FCS' Block down converters and optional external RF Switch are used to accommodate any standard satellite frequency band. The Instantaneous measurement bandwidth is 36 MHz and the dynamic range is 60 dB.

The DSA software performs the basic and enhanced measurement capability. Basic monitoring reports EIRP, Occupied Bandwidth, C/N and Center Frequency. Carriers defined by the operator can include Eb/No as an automatic measurement parameter. Any abnormal measurement will generate an alarm. The operator can select the Enhanced Measurements option to display modulation type, Eb/No display a carrier under carrier interference. TDMA analysis software can be added to the DSP software as an option.

261

7. Conclusion

An S-Band Electronically Scanned Antenna (ESA) subarray has been developed for Telemetry, Tracking and Commanding (TT&C) and communications at Unified S-Band (USB) and Space Ground Link Subsystem (SGLS) frequencies to meet the operational needs of the AF Satellite Control Network (AFSCN). The successful demonstration was entitled Phased Array at Wallops Island (PAWS). The six panel subarray was tested to validate the technologies use in a future Geodome Phased Array Antenna (GDPAA) at a NASA Flight Test Facility located on Wallops Island, Va. in August 2004. The PUGPU received telemetry from both Air Force SGLS and NASA USB satellites during the PAWS demonstration. The PUGPU sat next to the legacy SGLS and USB equipment illustrating a 5 time reduction in size. The PUGPU was also remotely reconfigured using a TCP/IP Ether-fiber-Ethernet link. A design to cost exercise will be conducted to provide a low cost GDPAA. With the successful demonstration of the PAWS and lessons learned, the components; Transmit and Receive (TR) modules, beam formers, radiating elements and antenna control software will be optimized as necessary. This paper was submitted during the demonstration. Detailed results and analysis of the antenna evaluation will be available from AF Space Battlelab in Jan 2005. Plans have begun to develop a 54 panel subarray to test satellites as high as Geostationary and demonstrate simultaneous links.

References

[1] S. S. Bharj, M. Thaduri, P. J. Oleski, Lt. R. Patton, B. Tomasic, J. Turtle S. Liu, "Dasiy Chain Controlled Muti-Beam T/R Module for AFSCN", Antenna Applications Symposium, 2004.

[2] S. S. Bharj, P. J. Oleski, A. Merzhevskiy, B. Tomasic, S. Liu and J. Turtle, "Multi-Beam Transmit Receive Module for USB and SGLS Band Satellite Links', Antenna Applications Symposium pp. 1, 2003.

[3] S. S. Bharj, P. J. Oleski, A. Merzhevskiy B. Tomasic, S. Liu, J. Turtle, N. Patel, "Low Cost Transmit/Receive Module for Space Ground Link Subsystem, Antenna Applications Symposium", pp. 1, 2002.

[4] S. S. Bharj, P. J. Oleski, A. Merzhevskiy, B. Tomasic, S. Liu, "Affordable Antenna Array for Multiple Satellites Links", Antenna Applications Symposium" pp. 401, 2000.

[5] TIA/EIA-RS-485, Standard for Electrical Characteristics of Generators and Receivers for Use in Balanced Multipoint Systems

ENHANCED K_a-BAND ELECTRONICALLY SCANNED ANTENNAS WITH MULTI-FUNCTION RF CAPABILITY

R. Dahlstrom, O. Kilic
U.S. Army Research Laboratory
2800 Powder Mill Road
Adelphi, MD 20783
dahlstrom@arl.army.mil

Abstract: An electronic scanning antenna (ESA) that uses a beamformer such as a Rotman lens has the ability to form multiple beams for shared-aperture applications. This characteristic makes the antenna suitable for integration into systems exploiting the Multi-Function Radio Frequency (RF) concept, meeting the needs for a Future Combat System (FCS) RF sensor. An antenna which electronically scans 45 degrees in azimuth has been built and successfully tested at ARL to demonstrate this multiple-beam, shared-aperture approach at K_a band. Subsequent efforts are focused on reducing the component size and weight while extending the scanning ability of the antenna to a full hemisphere with both azimuth and elevation scanning. Primary emphasis has been on the beamformer, a Rotman lens or similar device, and the switches used to select the beams. Approaches described include replacing the cavity Rotman lens used in the prototype MFRF system with a dielectrically loaded Rotman lens having a waveguide-fed cavity, a microstrip-fed parallel plate, or a surface-wave configuration in order to reduce the overall size. Repackaging the cavity Rotman lens in a smaller, multilayer configuration is proposed, as well. This reduction in size of the Rotman lens can facilitate elevation scanning by making possible the addition of one lens at each array port of the current design for elevation beam forming in a reasonably sized package. The desired elevation angle would be selected by using a switch to select the desired beam port. We will discuss the challenges and progress in the development of such an antenna.

1. INTRODUCTION

The U.S. Army Research Laboratory (ARL) is currently pursuing key technologies for low-cost, advanced battlefield sensors for multimode radar and communication platforms as shown in figure 1. These radar and communication functions include active/passive target acquisition, combat identification, weapons
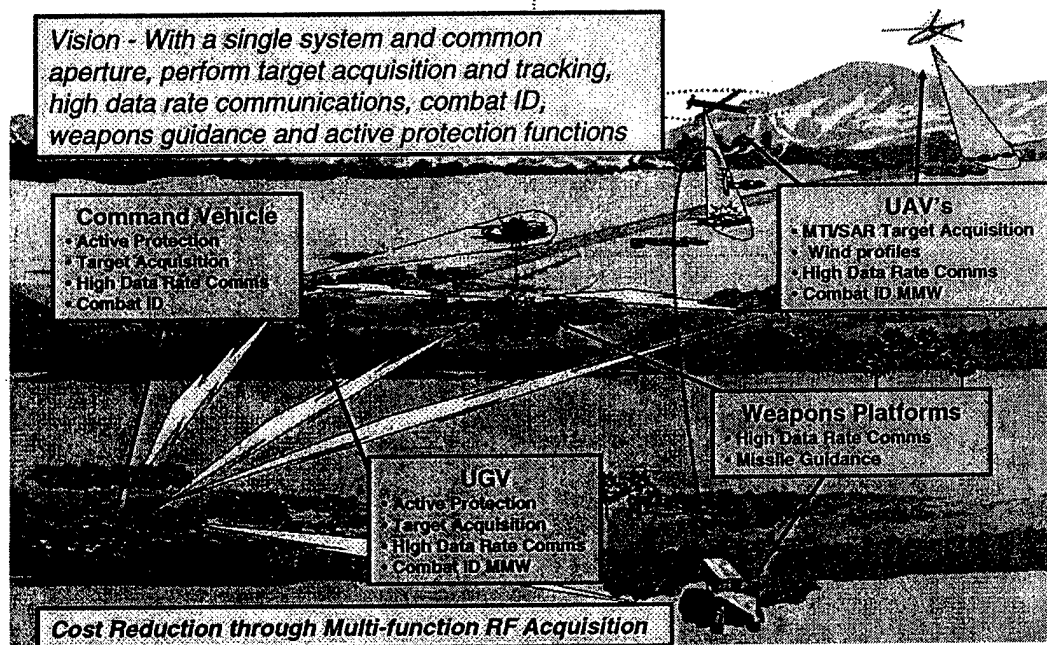
Figure 1. Multi-function RF concept

guidance, secure point-to-point communications, active protection, networks for situational awareness, and signal intercept. Typically, each of these functions is performed by a separate piece of equipment specifically designed for that purpose, with its own electronics package and antenna. As more of these functions are added to a vehicle, the available space suitable for antennas is quickly depleted, and costs and weight increase rapidly. Incorporating multiple-function components into these systems can considerably reduce total system size, weight, and cost. By sharing a single antenna aperture, one can time- and/or frequency-multiplex both radar and communications functions, or, in the case of multiple-beam antennas, perform them simultaneously.

2. SYSTEM DESCRIPTION

In the K_a-band ESA we have developed, we achieve the simultaneous performance of multiple functions by combining a multiple-beam antenna array with a PIN-diode switching network while maintaining a broad overall system bandwidth of better than 36 to 40 GHz. The complete antenna system consists of an 8 (vertical) x 32 (horizontal) array of slot-fed microstrip patch radiators (figure 2) fed by the Rotman lens (figure 3) horizontally, and by microstrip corporate feeds vertically. The Rotman lens has 19 input ports, with the port on each end intended to be terminated to provide a symmetric environment for the remaining
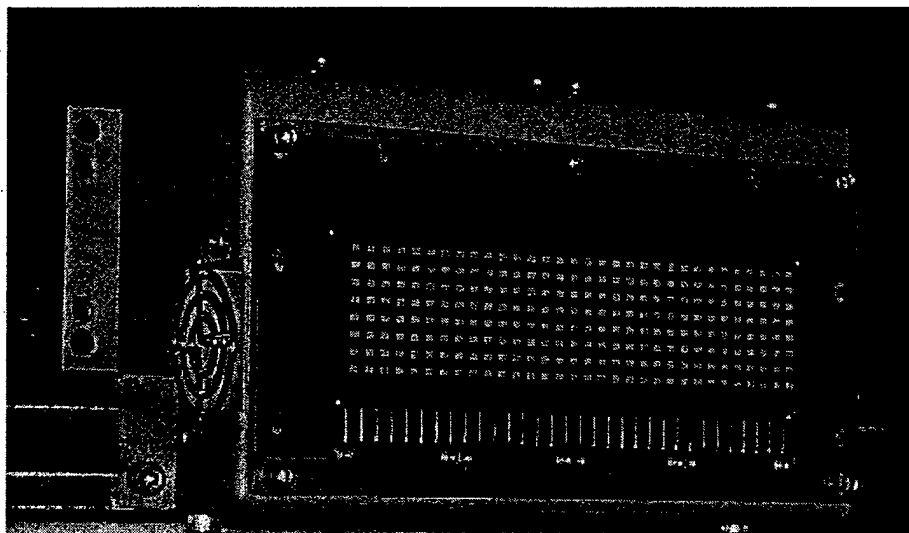
Figure 2. Patch array mounted to antenna/amplifier assembly

ports. The center 17 ports correspond to azimuth beam-scanning positions covering ±22.5 degrees from broadside. A dual-channel beam-switching network (BSN) (figure 4) is used to select one of the beams for each channel. For

Beam ports

Rotman lens

Phase adjustment

Array ports
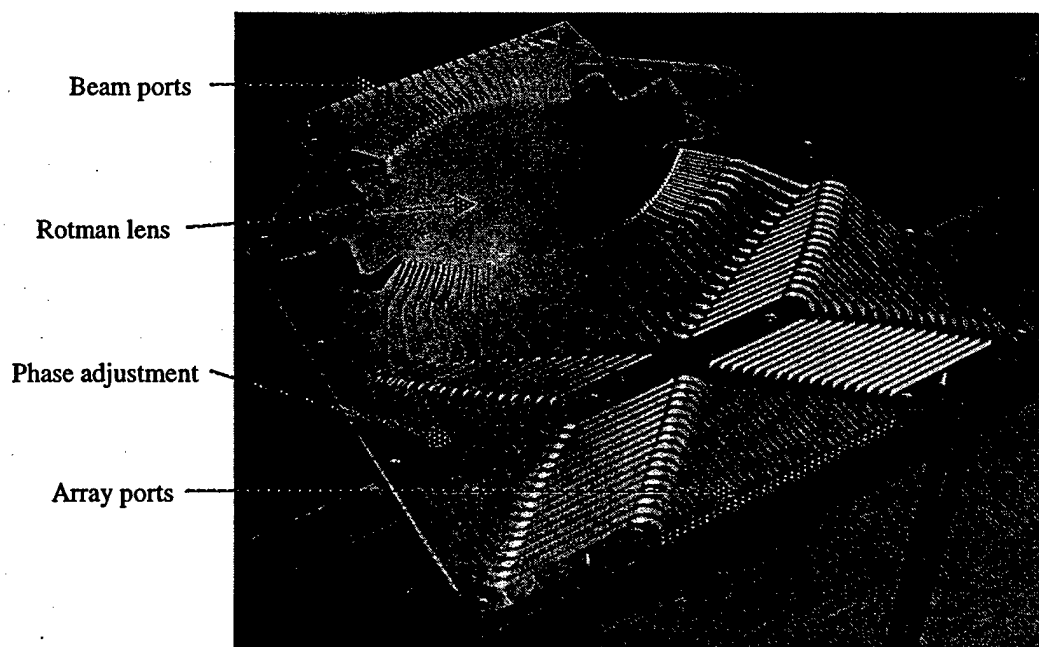
Figure 3. Rotman lens – one half shown, with absorber

266

Two 1x16 port switch
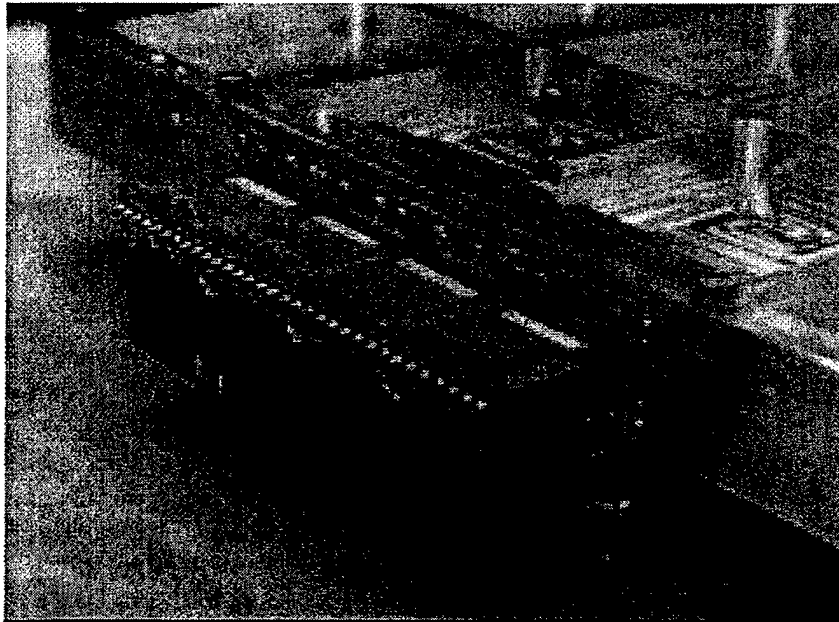assemblies, one for each
channel

Ten 1x4 port switch
modules, five for each
channel

Sixteen 1x2 port
switches to connect the
active channel ports to
the corresponding lens
beam ports

Figure 4. Trex Enterprises 2x16 PIN-diode switch
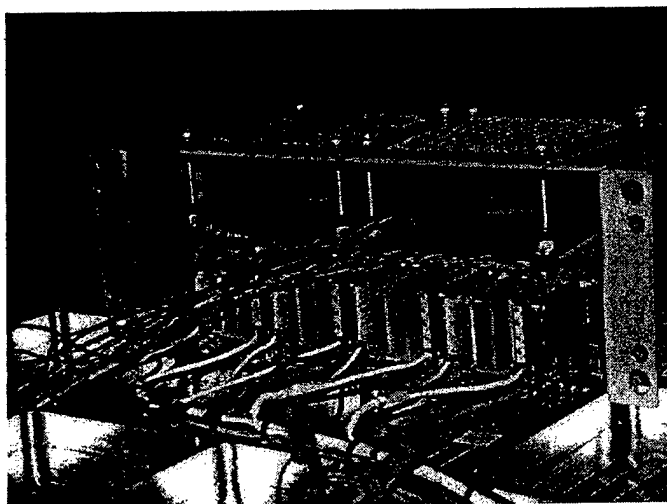
Figure 5. MMIC amplifiers mounted to lens and patch array

Figure 6. Amplifier assemblies mounted on Rotman lens

transmit, 32 power amplifies (figure 5) are inserted between the output ports of the lens and the patch array to increase the power radiated. For receive, low noise amplifiers (figure 6) are used between the lens and the patch array to minimize degradation of receiver noise figure by losses in the Rotman lens and the switch.

3. ESA OPERATION

Operation in an electronically scanned mode involves remotely controlling the BSN to switch either of the signal source inputs to any of the 17 beam ports of the Rotman lens, in a sequential or random scan, as desired. Adding time-multiplexed functions requires only that the appropriate beam selection be made at the same time as the input signal is switched. A fixed-beam communication channel can be added by coupling to the appropriate beam port. In a similar manner, incorporating additional functions merely adds to the complexity of the BSN, not of the antenna itself.

4. WAVEGUIDE ROTMAN LENS

The key to achieving a low-cost, compact, multibeam antenna is the use of a Rotman lens or similar device to provide the appropriate phasing to each element of the array for each desired beam angle. One medium used for this lens is

waveguide, with the E field oriented parallel to the broad walls of the lens to reduce reflections at the input and output ports. In this orientation, the wavelength of the signal traveling through the lens is a function of the wall spacing. The corresponding variation of the velocity of propagation of the signal in the lens causes a shift in beam angle with frequency for angles off broadside. Using an E field oriented perpendicular to the broad walls of the lens could eliminate this effect, but over the limited frequency range typically used, the beam shift is small and acceptable for anticipated applications. Therefore, our current effort has focused on reducing the weight and size of parallel E field waveguide designs to make them more competitive with stripline and microstrip approaches.

5. LIGHT-WEIGHT WAVEGUIDE ROTMAN LENS

Our current waveguide Rotman lens consists of two aluminum plates with half the waveguide pattern machined into each, which are then screwed together to create the lens cavity and associated waveguides. To maintain flatness, each half is relatively thick (with ridges on the outer surfaces to reduce the weight) so that when they are assembled together, the mating surfaces make intimate contact with each other. It is relatively large, also, with the phase adjustment taking considerable space because of being limited to a planar configuration. The parameters of this configuration could be optimized further, but the possible improvement would be relatively small. Therefore, the use of light-weight materials with more compact configurations are being investigated.

6. METALIZED PLASTIC LENS

The use of metalized plastic instead of aluminum results in a substantial reduction in weight even with our current design. Such a lens is currently being fabricated using ULTEM resin from GE Plastics metalized with copper. The pattern of the lens and the phase adjusting waveguide interconnects are unchanged from the aluminum version, but the thickness of the plates is being reduced to 0.375 inch. Test samples of 7-inch lengths of waveguide fabricated in this way have a measured loss of 0.4 dB which is somewhat higher than the 0.1 dB loss of TRG A690 waveguide measured in the same manner. The higher loss is assumed to be due to the greater surface roughness of the metalized plastic. We are investigating ways of reducing the surface roughness, but it is not an immediate concern because the current metallization is considered adequate.

Instead of creating the lens cavity by surrounding an air space with a conductor, an option for future work would be to make the lens cavity itself of plastic which would be metalized on its exterior surface. This lens configuration would be considerably lighter than our current one, and it would be smaller as well, due to

Elevation Scan Microstrip Patch Array

Phasing Layer

Lens Layer

Four Identical Panels

Azimuth Scan
Waveguide Rotman Lens

Waveguide PIN-Diode Switch

Power and Low-Noise Amplifiers
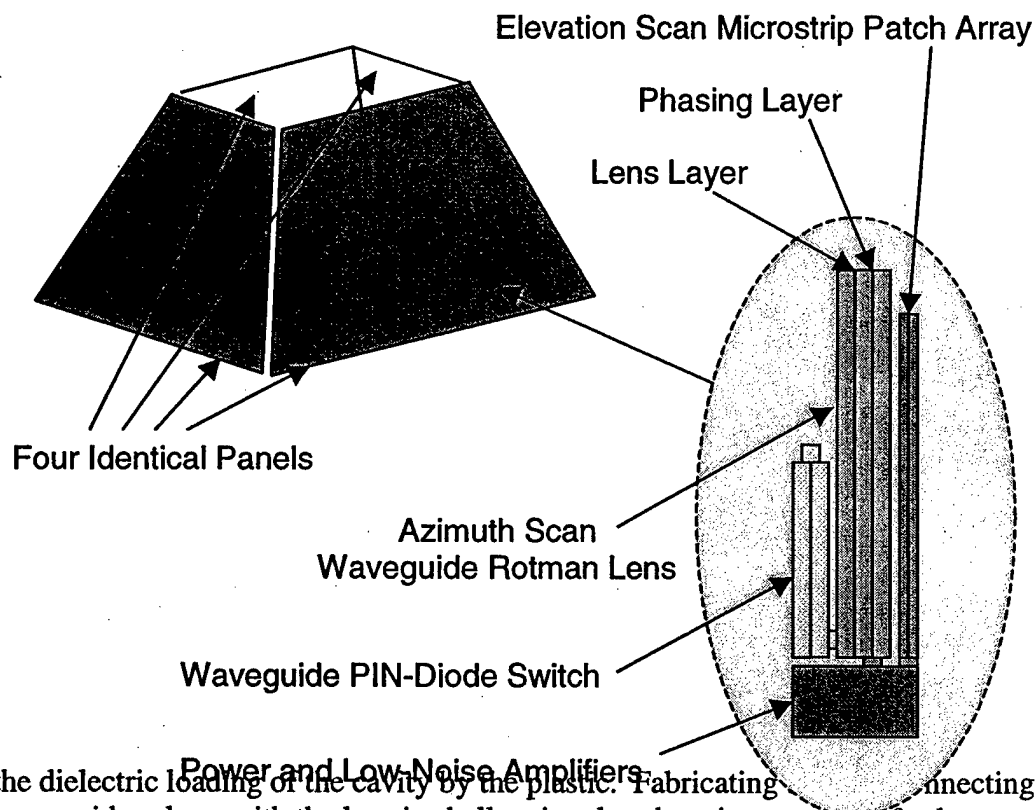
the dielectric loading of the cavity by the plastic. Fabricating connecting
waveguides along with the lens is challenging, but there is a potential for low-cost
proc   **Figure 7.** Folded Rotman lens antenna concept.   to
con

7. FOLDED WAVEGUIDE ROTMAN LENS

The size of our waveguide Rotman lens can be reduced considerably by using a
multi-layer structure, where the lens cavity is on one layer and the phase
adjustment lines fold back alongside the lens in an adjacent layer as shown in
figure 7. If it is adequately supported, each additional layer would only need to
be thick enough to contain the waveguide traces on each side because the
structural rigidity is already provided by the outside plates. For our configuration
with traces that are 0.112 inch deep, a layer thickness of only 0.25 inch would be
adequate. In addition, the ability to choose the location of the pass-through
waveguides to help provide the phase adjustment gives an additional degree of
freedom which considerably reduces the length of those lines and, therefore, the

270

space needed for them. With two circuit layers, the length of the lens assembly could be cut nearly in half with only a 0.25-inch increase in thickness. Using an additional layer to fold the lens cavity itself would reduce the length of the assembly by almost a factor of 4 from our current configuration with only a 0.5-inch increase in thickness. The resulting package could be less than 5 inches long with a thickness less than 1.5 inches. Additional layers could incorporate the switches, amplifiers, and the patch array.

8. ALTERNATIVES TO THE WAVEGUIDE ROTMAN LENS

Alternatives to the waveguide Rotman lens were investigated in order to reduce the overall size and weight of the lens and, therefore, the size and weight of the MFRF system, itself. Also, the current design scans only in the horizontal plane. By miniaturizing the Rotman lenses, stacking them at the output ports of the current design, it could be practical to scan in elevation as well. Initial designs were carried out at Ku band to minimize cost for the prototype design.
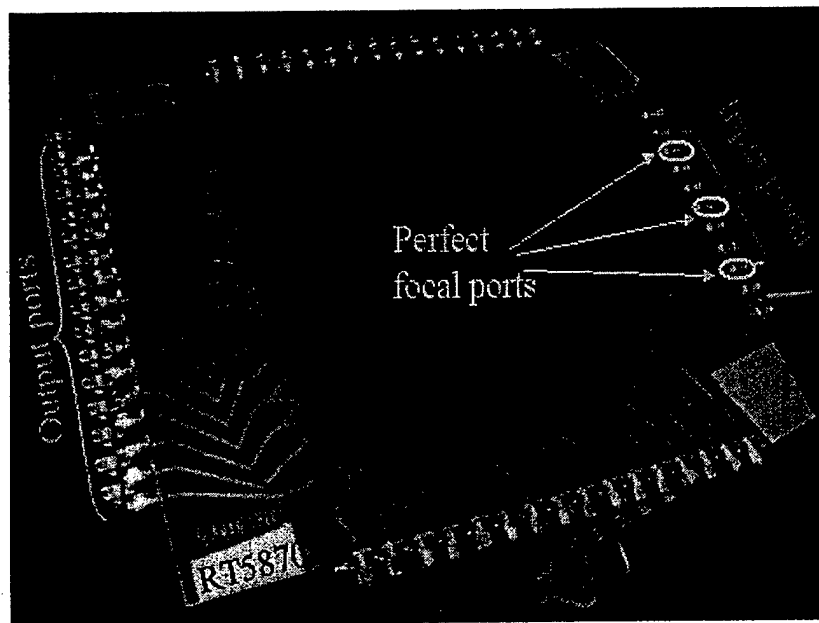
Figure 8. Ku-Band microstrip Rotman lens

Two different approaches are discussed for the design of the dielectric loaded lens in the following sections. The first approach is a microstrip lens design, where the feeds and delay lines are printed on a dielectric with a conductor plate in the back. The second approach launches surface waves in a thicker dielectric medium

271
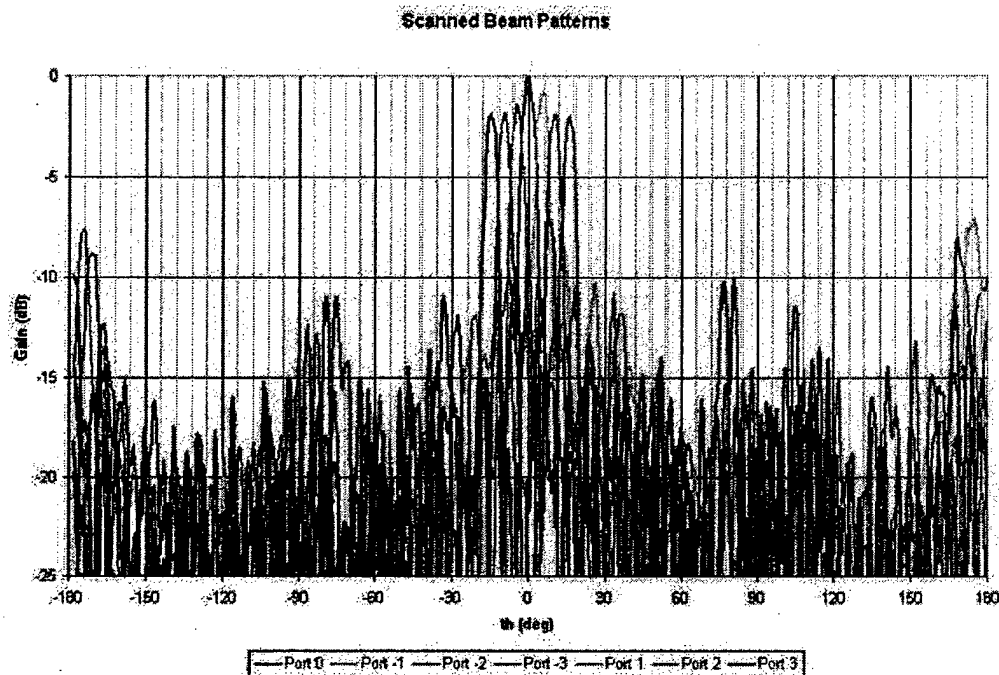
Figure 9. Measured radiation patterns for all beam positions of the microstrip Rotman lens

where the conductor plate in the back is removed. Preliminary simulation results are available at this time. Work is underway in building and testing this alternative approach.

9. Ku-BAND MICROSTRIP ROTMAN LENS

The objective of the development is to miniaturize the two waveguide Rotman lenses used in the current system by dielectric loading. The Rotman lens is a true time delay structure, where the input port locations determine the scan angle. The region between the input and output ports is the parallel plate region where the fields propagate with appropriate delay in phase to allow for the desired scan, [8]. By using a dielectric material instead of air the overall size of the lens can be reduced by a factor of $\sqrt{\varepsilon_r}$, where ε_r is the dielectric constant of the material.

Based on Rotman geometry, a Ku-band microstrip lens was designed and built using a 20-mil thick RT5870 Duroid material, as shown in Figure 8. The lens was designed to scan over 20 degrees with 7 different beam positions. A 1x16 element patch array is connected to the output ports. The overall size of the lens is about 30 cm x 35 cm.

272
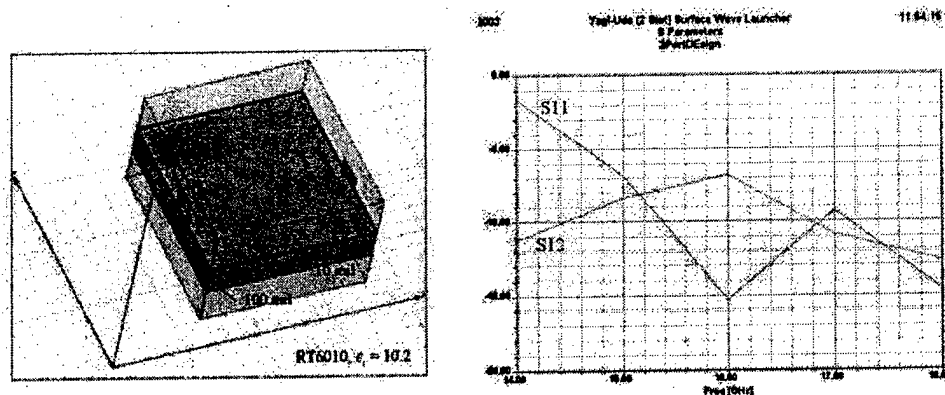
Figure 10. Surface wave launching element design and simulated performance.

Antenna pattern measurements were made at different input beam positions to validate the performance of the lens. Figure 9 shows the scanned beam positions at 17 GHz as the input is switched between the different ports. The back lobes are due to the interaction of the ground plane of the microstrip patch array and the conducting feed and parallel plate structure of the lens. Power measurements compared to a standard horn suggest that the Rotman lens integrated with the 1x16 element patch array has about 9.5 dB loss at 17 GHz. The 1x16 element patch array has a gain of 12 dBi at boresight.

10. SURFACE WAVE ROTMAN LENS

As an alternative to the microstrip design, a dielectric lens using surface waves is being considered by ARL. This approach eliminates any need for the ground plane at the back of the lens, and significantly reduces the use of copper for the parallel plate region in the design. This is expected to reduce the copper loss in the structure. In order to propagate surface waves efficiently, thicker dielectric substrates with higher dielectric constant are preferred. In the first prototype for the surface wave Rotman lens, RT6010 Duroid material ($\varepsilon_r = 10.2$) is used. The surface wave is launched using an element structure similar to a Yagi-Uda element, as shown in Figure 10. Two slots, which act as the driver and the reflector, are used in the design. Previously, Yagi-Uda type elements with three slots, corresponding to the reflector, driver and director, have been demonstrated to effectively launch surface waves on the same Duroid substrate, [9].

273
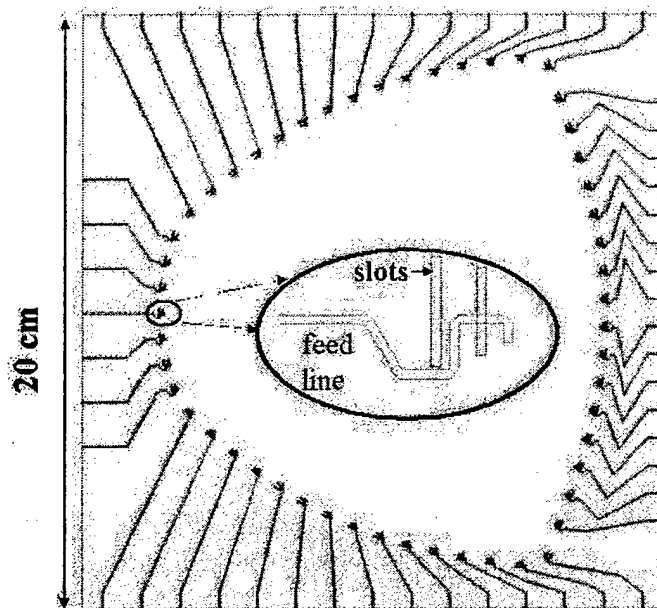
Figure 11. CAD drawing of surface wave Rotman lens
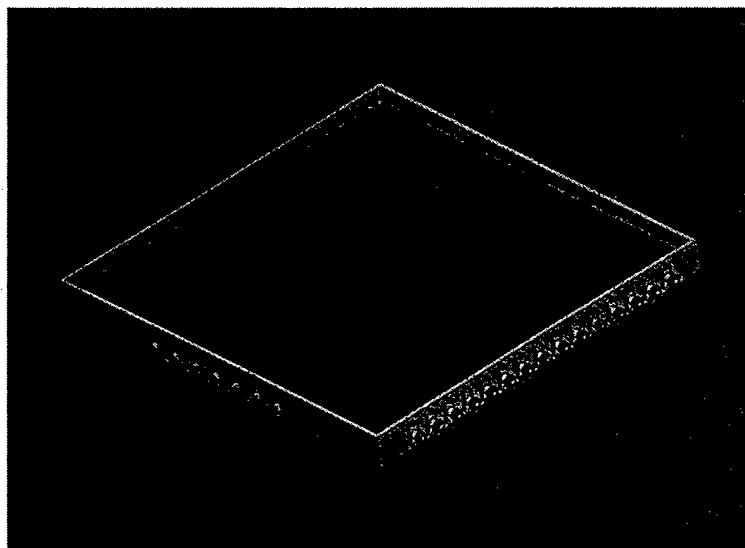
Figure 12. Surface wave lens mounted in supporting frame.

Simulations for the two-slot element have shown that surface waves can be launched effectively in the desired direction as observed in the S-parameter curve.

A drawing of the Rotman lens design using the surface wave element and the RT6010 material is shown in Figure 11. The thicknesses of the Duroid layers are chosen as 10 mils for the feed layer and 100 mils for the parallel plate region, so that only the TM_0 mode is excited in the structure. The lens parameters are determined so that the scan performance is identical to the microstrip lens
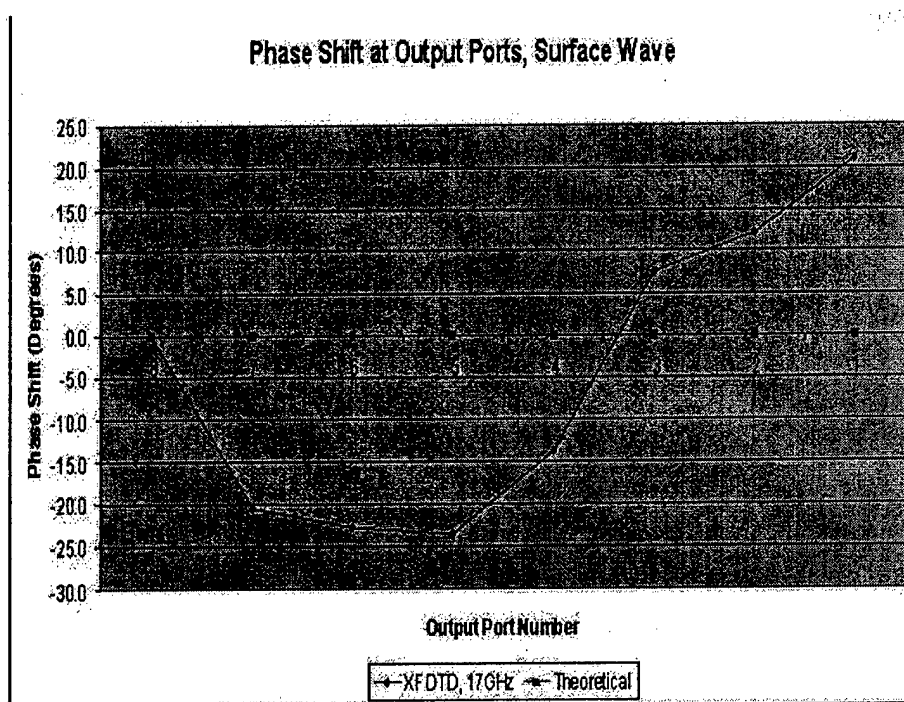
Figure 13. XFDTD predicted output phase for the center beam of the surface wave lens.

discussed before. Since a higher dielectric is used, the overall size for this design is expected to be smaller. The ground plane for the feedlines of this lens is between the two dielectric layers. A frame is being built to accommodate the mounting of the connectors as shown in Figure 12. Measurements of S-parameters for the design will be made when the frame is completed. An initial assessment of the lens performance is shown in Figure 13, for the central input port for which a uniform phase distribution is expected at the output. The results, which are based on simulations using XFDTD, show promise.

275

11. ALTERNATIVES TO THE ROTMAN LENS

An interesting alternative to the Rotman lens, which is limited to a total scan of about 120 degrees, is the 360-degree *R-2R* lens described by Clapp [11]. The *R-2R* lens, a special case of the *R-KR* lens, is a circular cavity which, when fed at a point on its periphery, provides the desired phasing at other points on its periphery for a circular array with a radius twice that of the lens. A single *R-2R* lens is limited to 180 degrees because of the mapping from the lens diameter to the array diameter, but, by using four or six lenses and interconnecting them with hybrid couplers, a full 360 degrees can be scanned horizontally. A cylindrical patch array or similar antenna would then provide beam forming and scanning vertically.

12. FOCAL PLANE ARRAY

The antenna configurations discussed thus far use a lens to achieve multiple-beam scanning horizontally with either single-beam phased array or highly complex Rotman lens scanning vertically. Possible techniques for achieving multiple-beam scanning both horizontally and vertically with minimum complexity involve extending the linear beam ports of the proposed lenses to two dimensions. One configuration would locate the beam ports conformally over a hemispherical lens surface with the lens, such as a Luneburg lens, forming the beam directed opposite the feed point. Another would be to use a focal-plane array with a lens that either augments the degree of scan or has the ability to additionally scan the beam by incorporation variable phasing elements on its surface. The desired beam is then selected by using a switch to connect the appropriate electronics to the desired beam. Switches of the type we are currently using are prohibitively complex when extended to the number of ports required here. Therefore, we are currently pursuing the developing switch technology that would make these approaches practical.

13. CONCLUSION

Several approaches have been presented for further refining the antenna for the MFRF system. Although they are in various stages of development, many of them show promise. A microstrip lens has been designed and built demonstrating suitable performance. Lighter waveguide and surface wave lenses are being fabricated and other designs are being readied for fabrication. As different vehicles present different requirements when mounting the MFRF system and some approaches meet these requirements better than others, more than one of these approaches will likely be pursued to completion.

REFERENCES

1. S. Weiss, R. Dahlstrom, O. Kilic, E. Viveiros, S. Tidrow, F. Crowne, E. Adler, "Overview of the Multifunction RF Effort – An Army Architecture for an Electronically Scanned Antenna," *Proceedings of the 2002 Antenna Applications Symposium*, pp. 119-129.

2. E. O. Rausch, A. F. Peterson, and W. Wiebach, "A Low Cost, High Performance, Electronically Scanned MMW Antenna," *Microwave J.*, vol. 40, no. 1, pp. 20–32, January 1997.

3. E. O. Rausch, A. F. Peterson, and W. Wiebach, "Millimeter Wave Rotman Lens," *Proceedings of the 1997 IEEE National Radar Conference*, pp. 78–81, May 1997.

4. R. Dahlstrom, A. Bayba, "A Rotman Lens Implementation for Multi-Function RF Antenna Applications," *Proceeding s of the 2002 Antenna Applications Symposium.*

5. R. Dahlstrom, S. Weiss, E. Viveiros, A. Bayba, and E. Adler, "A Ka-Band Electronically Scanned Antenna for Multi-Function RF Applications," *Proceeding s of the 2003 Antenna Applications Symposium*, pp. 360-372.

6. T. Katago, S. Mano, and S. Sato, "An Improved Design Method of Rotman Lens Antennas," *IEEE Trans. Antennas and Propagation*, vol. AP-32, no. 5, pp. 524–527, May 1984.

7. H.-H. Fuchs, D. Nüßler, "Design of Rotman lens for beamsteering of 94 GHz antenna array," *Electronic Letters*, vol. 35, no. 11, pp. 854-855, 27 May 1999.

8. W. Rotman and R. F. Turner, "Wide-Angle Microwave Lens for Line Source Applications," *IEEE Trans. Antennas and Propagation*, vol. AP-11, no. 6, pp. 623-632, November 1963.

9. Y. Qian, A. R. Perkons, T. Itoh, "TM Surface-Wave Power Combining by a Planar Active-Lens Amplifier," *IEEE Trans. Microwave Theory and Techniques*, vol. 46, no. 6, June 1998

10. P. S. Hall, S. J. Vetterlein, "Review of Radio Frequency Beamforming Techniques for Scanned and Multiple Beam Antennas," IEEE Proceedings, vol. 137, no. 5, pp. 293-303, October 1990.

11. R. E. Clapp, "Extending the *R-2R* Lens to 360°," IEEE Trans. Antennas and Propagation, vol. AP-32, no. 7, pp. 661-671, July 1984.

12. Y. T. Lo, S. W. Lee, *Antenna Handbook: Theory, Applications, and Design*, Ch. 19, J. S Ajioka, J. L. McFarland, "Beam Forming Feeds," pp. 19-1-122, Van Nostrand Co. Inc., 1988.

IRREGULAR SHAPED SUBARRAYS FOR TIME DELAY CONTROL OF PLANAR ARRAYS

R.J. Mailloux, S.G. Santarelli, and T.M. Roberts
Sensors Directorate, Air Force Research Laboratory
80 Scott Drive, Hanscom AFB MA 01731-2909

Abstract: This paper investigates the use of several types of small subarrays (four or eight elements each) that are rotated or flipped and rotated to completely fill (tile) the active region of planar arrays. The subarrays in any one array are identical, but introduce an aperiodicity in the phase center location (and radiated subarray pattern) as they are rotated or flipped and rotated. Phase shift is presented at every element of the arrays, with time delay inserted behind each subarray.

The paper will illustrate the reduced peak quantization lobe levels achievable with such subarrays, and will present average sidelobe levels for various size subarrays.

1. Introduction

It is well known that large ground and space based array antennas suffer limited instantaneous bandwidth when they are scanned by phase shifters instead of time delay devices. At present, time delay units are expensive, lossy and often are too large to fit within the inter-element array cell distance, and so it is established practice to insert time delay units at the input to subarrays while using element level phase shifters. Time delayed arrays of contiguous subarrays unfortunately produce significant quantization lobes, and these impact radar or communication system design and performance. Recent progress in constrained overlapped subarrays has led to improved pattern performance, but these networks have loss and so require amplification at the subarray level or within the subarray network.

One alternative to these subarray approaches is the use of a thinned aperiodic array, perhaps with random element distribution to prevent the formation of the quantization lobes. The disadvantages of such distributions are that they still have higher average sidelobe distributions, require an oversize aperture and are difficult to feed.

This paper investigates the properties of simple irregularly shaped subarrays that can be "tiled" to completely fill an array aperture without leaving any gaps.

Although there are many ways to combine various shapes to tile rectangular apertures, the goal here was to use only a single subarray shape in an aperture that could be rotated to tile the whole aperture.

2. Irregular Subarrays

The use of irregularly shaped subarrays instead of rectangular subarrays brings several advantages. The act of rotating subarrays by 90 degrees makes the periodicity vary and makes the phase center move with each rotation.

Although there are a huge number of possible geometric configurations that will tile a surface, we considered it important to choose subarrays (tiles) that could be fed by lossless orthogonal power dividers, namely subarrays of 2^n elements. One of the simplest of these is the four element subarray of Figure 1, called an L-tetromino, and this is one of the shapes chosen for this study. This figure, rotated by multiples of ninety degrees becomes four very different subarrays. The asterisks on each figure mark the chosen point at which there is perfect time delay. The remaining four cells have the same time delay but use phase shift to provide the proper phase tilt at center frequency. These simple shapes can be combined, as in a puzzle, to tile a surface and fill an aperture with contiguous time-delayed subarrays, but without any evident residual quantization lobes for large subarrays.

Before discussing the electromagnetic properties of scanned arrays of these subarrays, it is relevant to introduce some shapes that result from studies of combinatorial mathematics. There is a developing literature [1-4] of special shapes called polyominoes, which are shapes made from connected square unit cells that all have their vertices at integer points. An n-omino is a union of 'n' cells whose interior is connected by cells that touch along sides. Figure 2 shows the simplest polyomino shapes [1] including the four basic tetromino shapes. Figure 3 shows the 12 basic pentomino shapes. The number c(n) of such possible shapes grows exponentially with n, and the first dozen of these are given in the table below, which is in all of the references.

Table 1			
n	c(n)	n	c(n)
1	1	7	108
2	1	8	369
3	2	9	1285
4	5	10	4655
5	12	11	17073
6	35	12	63600

A more complete table and listing numbers of other types of polynominoes are given by Redelmeier[4]. Of these, an important group can be obtained from the above by flipping the figures over.

This study is limited to the L tetromino and the octomino shown in Figure 4. We have not studied polyominoes larger than 8 cells because these have larger phase error, more significant subarray pattern squint and are thus more appropriate for narrower bandwidth array applications. We do not present results here for figures that are flipped and rotated, although our findings are that that procedure makes it much simpler to tile a region, especially with the L-octomino.

The concept of "tiling" a rectangle with polyominoes is an interesting avenue of mathematical research, but in this study we have taken exception to the rigorous definition of tiling that involves filling every cell within the rectangle with no shapes extending beyond the chosen rectangle. In our study we let parts of the figures fall outside of the boundary of the array and assume that these elements are simply not excited, but terminated in matched loads. This corresponds to accepted engineering practice, and involves very little wasted signal since the elements in question are at the edges of the array and usually carry reduced power.

3. Results from the several polyomino studies

The polyomino subarrays investigated in this paper are compared with rectangular subarrays that completely fill the apertures. Thus, Figure 5 is the pattern of an array of 256 (16 x 16) square 4-element subarrays filling an array of 1024 elements using 256 time delays and 1024 phase shifters at frequency 1.15 times the center frequency and scanned to $u_0 = v_0 = 0.5$. There is assumed to be a cosine element pattern but no other losses except the effect of amplitude tapering using a − 40dB Taylor taper. Subarray quantization lobes are at approximately the −20dB level. Losses into the quantization lobes are small and neglected.

Figure 6 shows the tiling of the same array using L-tetrominos. These are located to fully tile the aperture, and if there were no truncation of the subarrays at the edges of the array it would have the same center frequency gain as the array of Figure 5. As it is, only a small percentage of the subarrays are truncated, and these are in the heavily tapered region of the array.

Figure 7 shows the pattern of the array of Figure 6, and reveals significant randomization of the sidelobe energy, with only one sidelobe at the −30dB level, and all others below −40dB.

Figure 8 shows the average sidelobe level of this subarray relative to the isotropic level to be about −10dB, and since the array has about 1000 elements, this corresponds to an average sidelobe level about 40dB below the main beam.

To test the dependence of array size on sidelobe level, a central section of the same filled aperture was investigated by truncating the array using the central 144 (12 x 12) subarrays. Figure 9 illustrates the truncation, and Figures 10 and 11 show that the results of filling the 576 element array with the contiguous 2 x 2 subarrays leads to −20dB quantization lobes as expected, while the array of irregular subarrays has many more sidelobes at the −30dB and −35dB level because the array gain is reduced by about 3dB. This result is significant, because for the rectangular array the quantization lobe locations or peak values are not a function of the array size, only of subarray size and bandwidth. The remaining peak sidelobes of the array of irregular subarrays are reduced for the larger array, and so do not behave like quantization lobes. One can expect that they continue to decrease (relative to the main beam) as the array is made larger.

Figure 12 shows the radiation pattern of an array of 256 eight-element (4 x 2 element) subarrays, with the expected quantization lobes at the −20dB level. Figure 13 shows the L-octomino filled array and Figure 14 shows its pattern. It
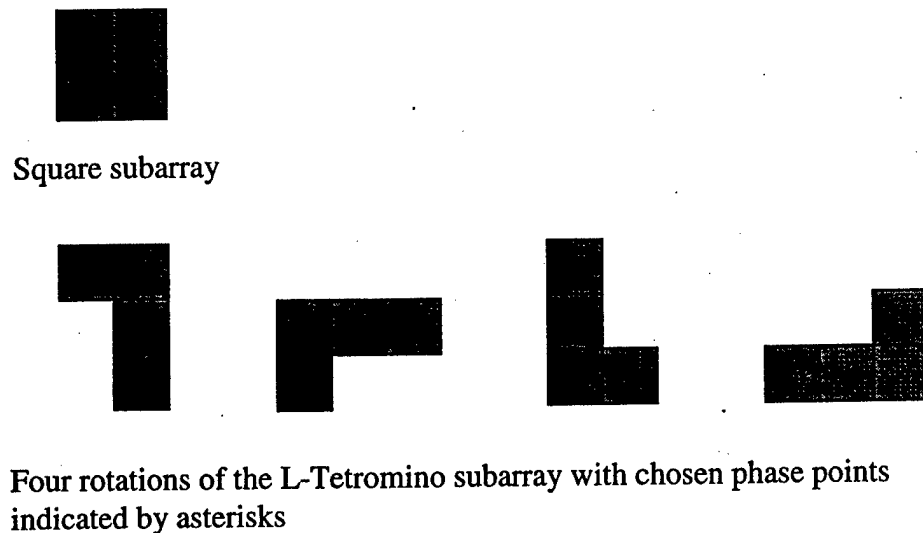
has some sidelobes larger than the tetromino array even though the octomino array is larger. Figure 15 shows that the average (isotropic) error sidelobe of the octomino array differs by only a few dB from that of the tetromino array, Figure 8. At present, we believe that the cause of these extra peak sidelobes is the periodicities we have built into the tiled surface when composing the tiling. We have found the octomino array difficult to tile without building areas of the rectangle with repeated multiple structures, and it is these repeated structures that seem to cause specific larger sidelobes. Using flipped polyominoes is an approach that we will explore to make the structure simpler to tile.

4. Conclusion

The paper has compared the radiation patterns of rectangular subarrays and two irregularly shaped polynomino subarrays, one with four and one with eight elements. In the examples presented the arrays only used one type of polynomino, and achieved significant suppression of quantization lobes. It also appears that average sidelobe level and peak sidelobe levels continue to decrease (relative to the main beam peak) as the array is made larger. The technique thus has significant potential for eliminating the quantization lobes of phase steered time delayed subarrays without sacrificing array gain at center frequency.

5. References

[1] S.W. Golomb, Polyominoes, Second edition, Princeton University Press, Princeton, NJ, 1994, Chapter 1

[2] D. Klarner, "My life among the polyominoes" Nieuw Archief voor Wiskunde (3), XXIX, (1981), p. 166; also The Mathematical Gardner, Wadsworth International Group, 10 Davis Drive, Belmont, CA 94004

[3] D.A. Klarner, "Polyominoes" Chapter 12 in Handbook of Discrete and Computational Geometry, Edited by J.E. Goodman and J. O'Rourke, CRC Press, New York, 1997

[4] D.H. Redelmeier, "Counting Polyominoes: Yet another attack" Discrete Math. vol. 36, no. 2, (1981) 191-203

Square subarray

Four rotations of the L-Tetromino subarray with chosen phase points indicated by asterisks

Figure 1: Square subarray and L-tetromino subarray with same area

Monomino

Domino

Straight Tromino

Right Tromino

Straight Tetromino

Square Tetromino

T Tetromino

Skew Tetromino
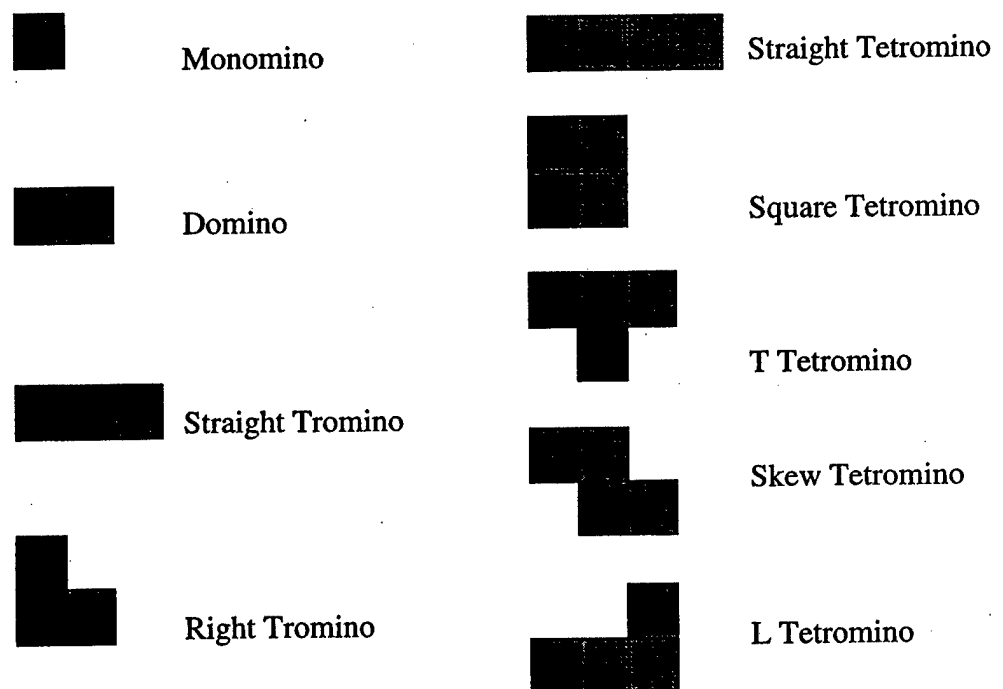
L Tetromino

Figure 2: Simple polyomino shapes (after Golomb [1])
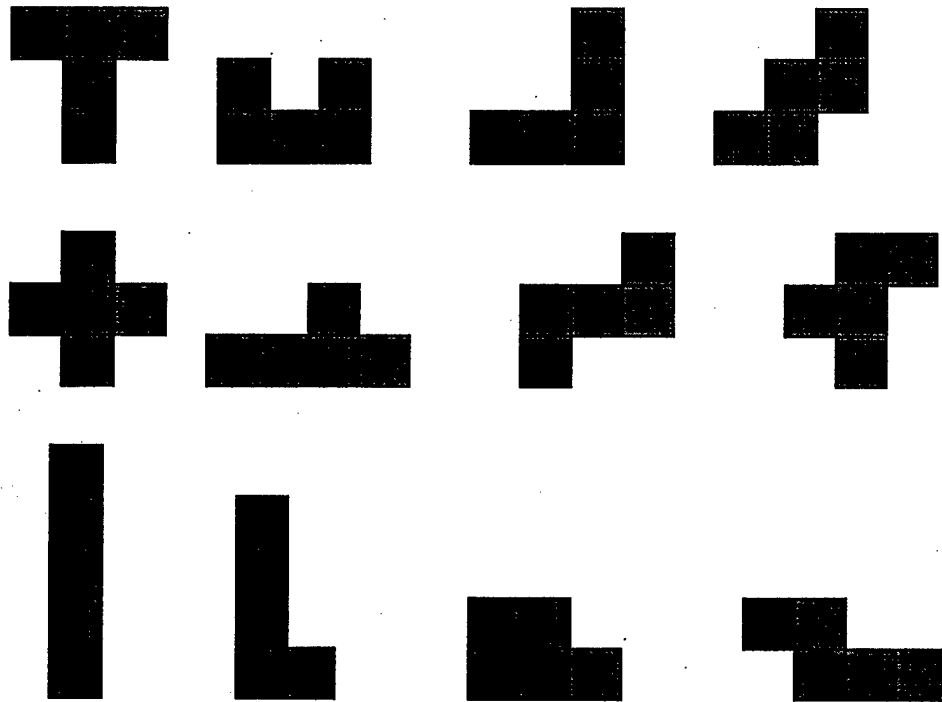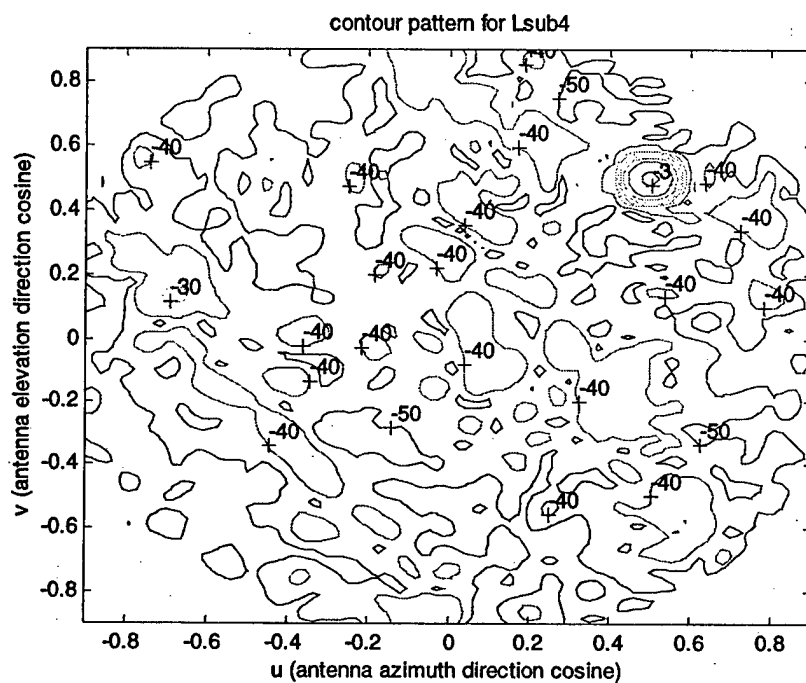
Figure 3: The twelve pentominoes (after Golomb [1])
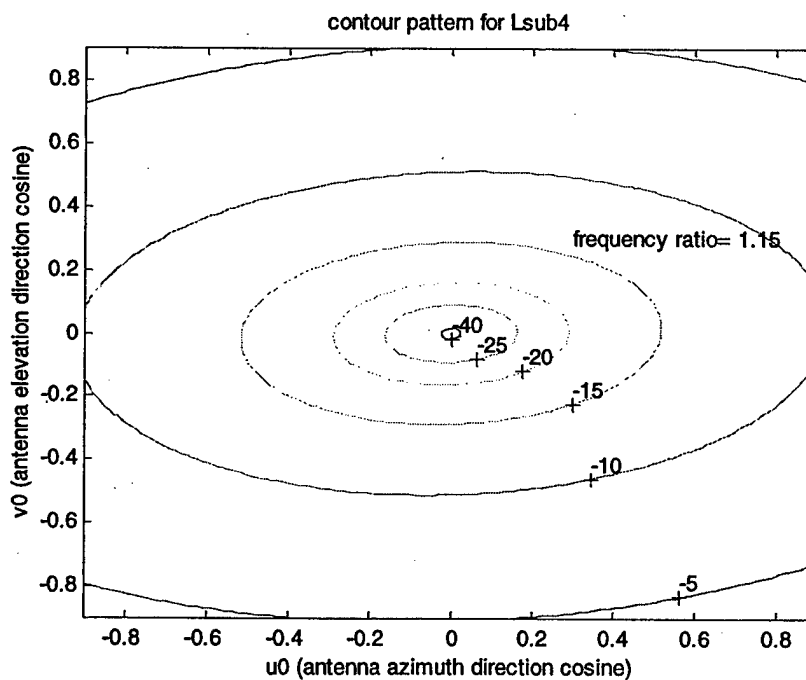

Figure 4: Four rotations of the L- Octomino
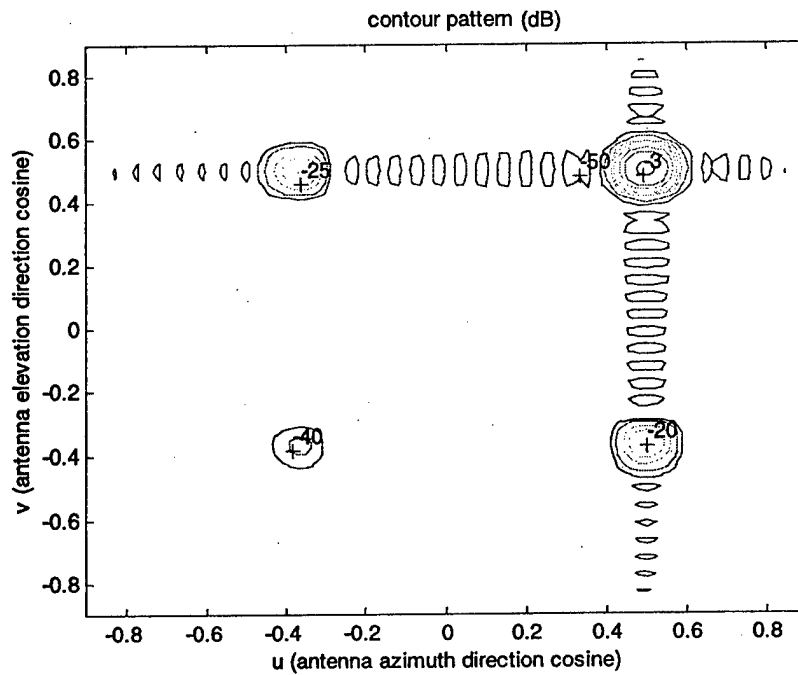
Figure 5: Array of 256 (2 x 2) subarrays at 1.15f₀
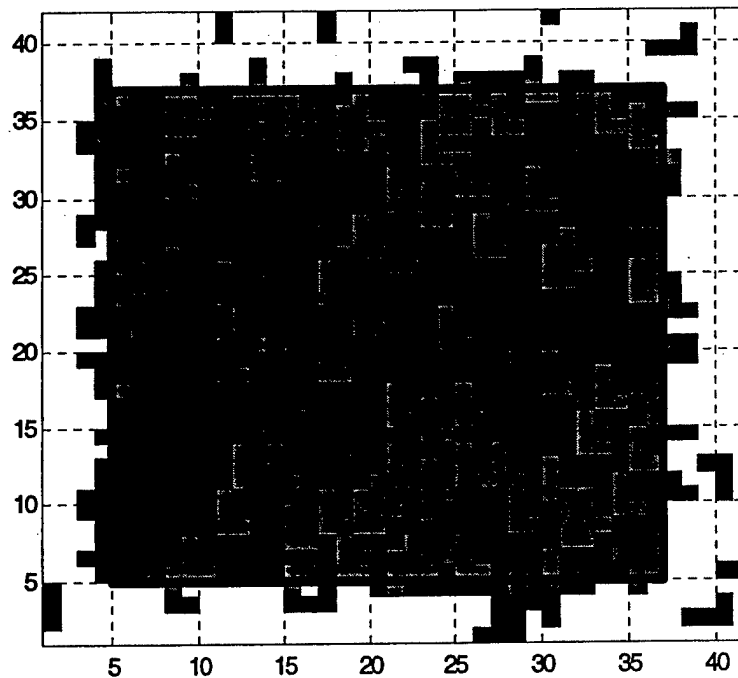
Figure 6: Array of 256 L-tetromino subarrays (elements outside of square array truncated)

contour pattern for Lsub4

Figure 7: Pattern of the array from Figure 6

contour pattern for Lsub4

Figure 8: Average sidelobe level of the L-tetromino subarray
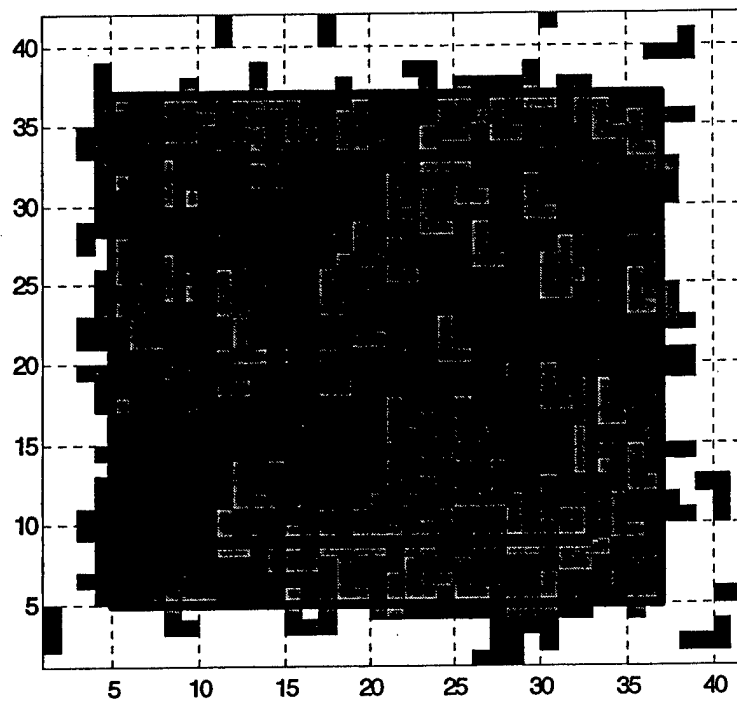
Figure 9: tetrominoes on 12 x 12 subarray grid
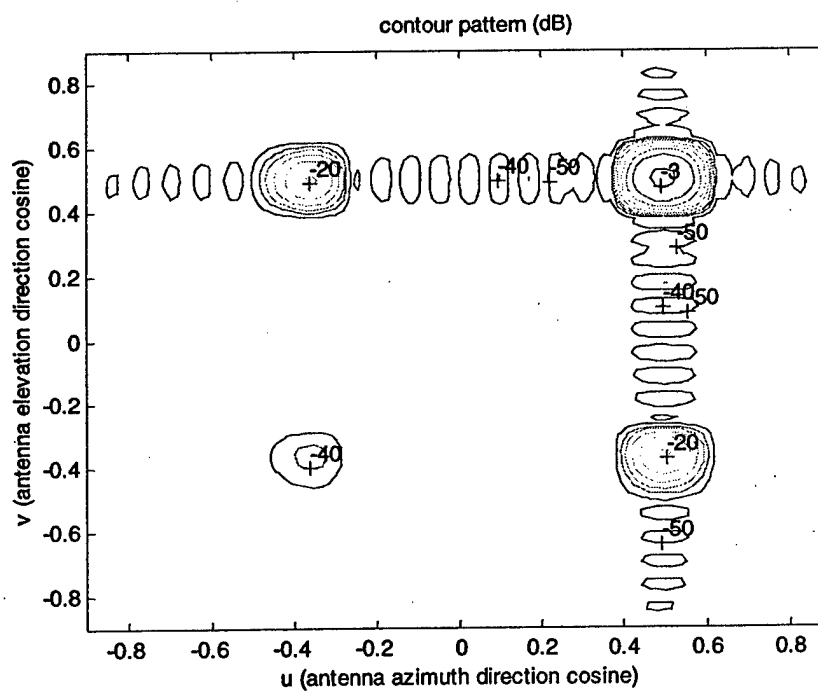
Figure 10: Pattern of array of 12 x 12 subarrays
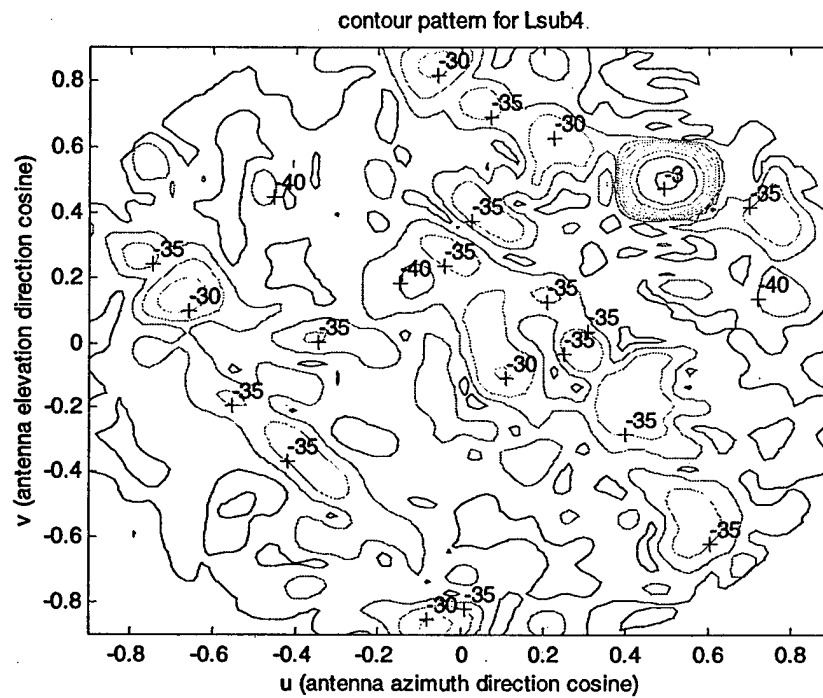
Figure 11: Pattern of array of Figure 9
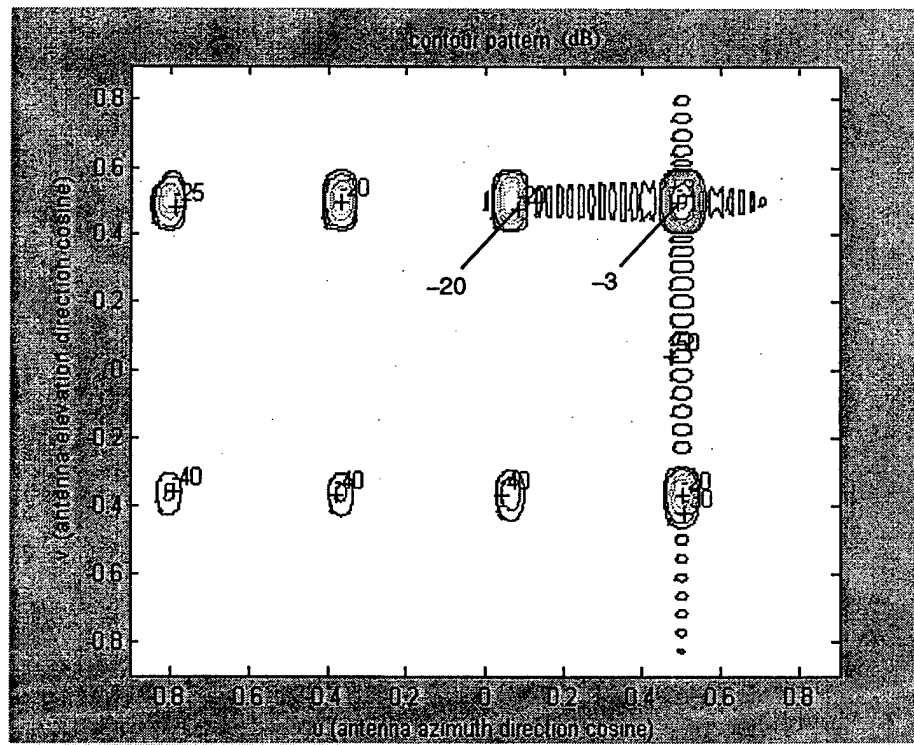
Figure 12: Pattern of array of 256 rectangular subarrays at 1.15 f_0

290
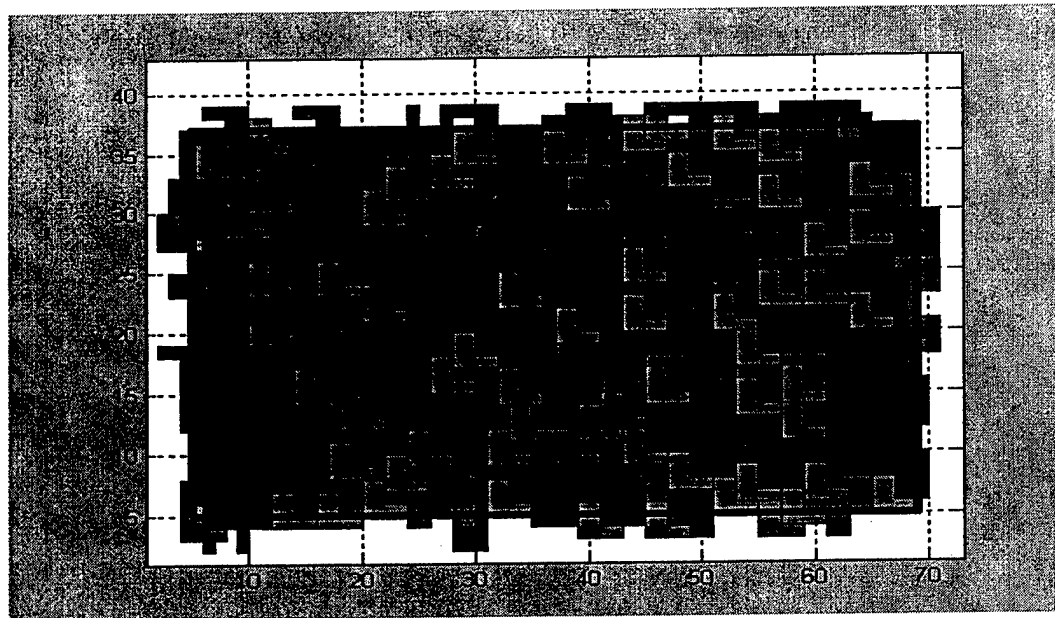
Figure 13: Array of 256 octominoes
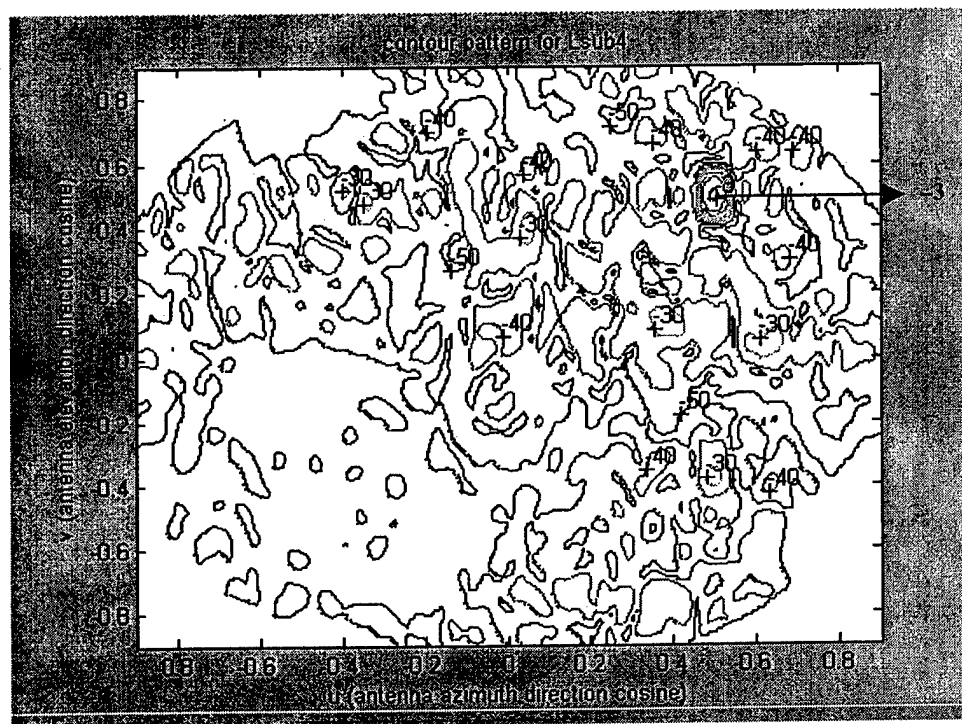
Figure 14: Pattern of array of figure 13 at 1.15 f_0
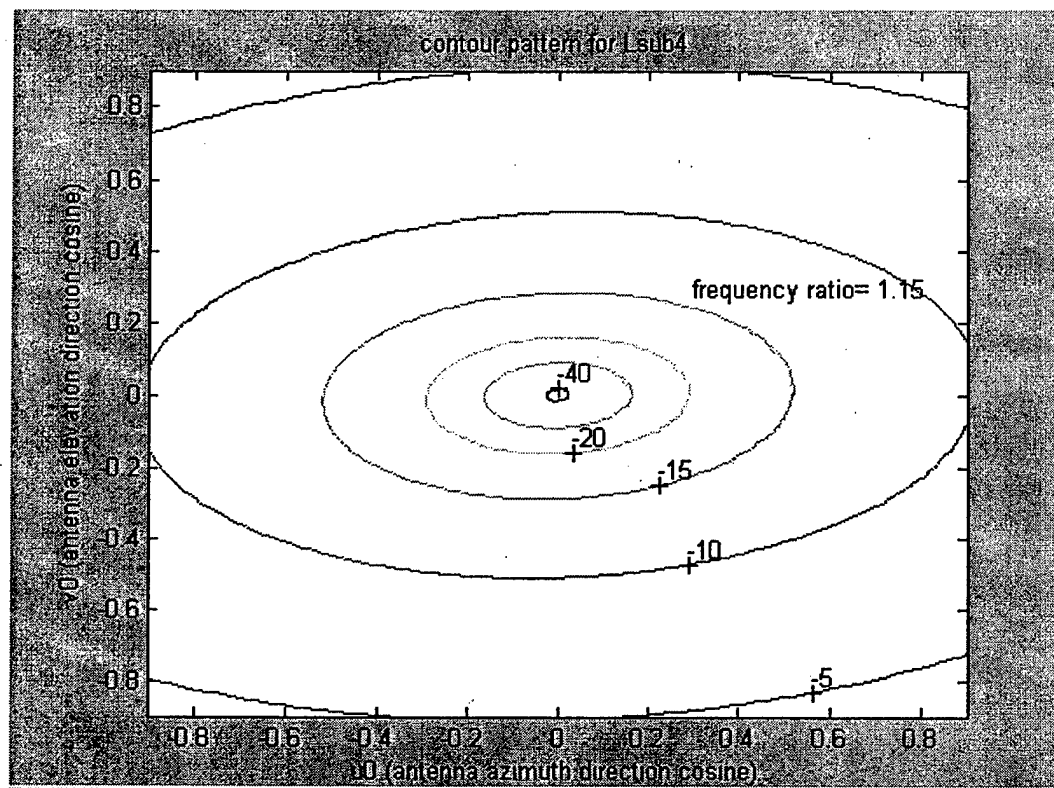
Figure 15: Average error sidelobes of octomino array

ARRAY OF ROTATED RANDOM SUBARRAYS

K. C. Kerby and J. T. Bernhard
Electromagnetics Laboratory
Department of Electrical and Computer Engineering
University of Illinois at Urbana-Champaign
Urbana, IL 61801
http://antennas.ece.uiuc.edu/

ABSTRACT: This work investigates the properties of an array of periodically rotated identical random subarrays. Pattern multiplication indicates that, like the non-rotated array previously investigated, this array has improved bandwidth response and avoids the grating lobes of a periodic array. Additionally, it will be more cost effective to manufacture than a fully random array. The random pattern function of a 2x2 block of subarrays with a set pattern of rotation is characterized and compared to that of an array whose subarrays are not rotated. The expected broadside patterns are very similar. However, the rotation pattern chosen is a special case that changes the probability distribution of the sidelobe level to normal rather than chi-squared. The variance is also reduced. The result is a significantly improved ability to achieve low side lobe levels. These results may be extended to larger arrays with the same rotation pattern.

1. INTRODUCTION

Aperiodicity is generally recognized as one effective way to extend the useful bandwidth of antenna arrays. Periodic arrays develop grating lobes when the spacing in wavelengths between elements is large, which sets an upper frequency bound for operation. In periodic arrays, one way to work around that upper bound is to place elements closer together, a practice that is obviously limited by the size of the elements themselves. Aperiodic arrays do not develop grating lobes because all of the individual element patterns will only interfere constructively at the main beam – at other points in the visible range some elements' fields will add constructively and some destructively. The result is a relatively uniform random sidelobe level away from the main beam, though higher sidelobes sometimes occur close to the main beam where more elements' contributions still add in phase. This principle is most effective when there are many elements.

One common type of aperiodic array is the random array, developed in the 1960s [1]. Initially, more attention was paid to the reduction in the number of elements required, as compared to periodic arrays, for comparable sidelobe level and beamwidth. However, the behavior of interest in this case is random arrays' very stable pattern behavior over wide bandwidths. Other suitable types of aperiodic arrays exist, but random arrays were chosen for use in this study because algorithmic design methods are not often effective enough to yield significant improvements in performance over the random method without some method of optimization or dynamic programming [2].

This work builds on a previous study of periodic arrays of random subarrays (PARS) [3], the objective of which was to simplify the geometry of random arrays while preserving their wideband properties. This is a continuation of that work, attempting to further lower the maximum sidelobe level by rotating the subarrays in a pattern. This rotation results in averaging of the sidelobes to a more uniform level – thus the largest sidelobes are reduced. The rotation pattern chosen is a special case that also affects the probability distribution of the sidelobe level in an advantageous way. Most possible rotation patterns would not have this effect.

This paper first reviews the properties of the periodic array of random subarrays. The next section contains an analytical treatment of the array of rotated random subarrays (ARRS) and its behavior. A comparison is then made of the two types of arrays, from which conclusions are drawn about their relative effectiveness.

2. BACKGROUND

The new array of rotated random subarrays will be compared with a periodic array of random subarrays (without rotations) that has been discussed previously [3]. Here we review the behavior of that array. The PARS consists of small rectangular random subarrays arranged periodically (Fig. 1). The PARS's sidelobe level was very similar to that of a single one of its subarrays. A larger, purely random array with the same total number of elements as the PARS had a lower sidelobe level. For an array of a given aperture size and number of elements, the robust wideband performance of a random array was preserved in a geometrically simpler design, but with somewhat higher sidelobes than a purely random array of the same size. As a result, from a performance standpoint a purely random array was more effective, and the reason to use a PARS would be that one wanted to use a certain number of elements to achieve some desired gain in a geometrically simpler package than the purely random array.

Since the subarray is a standard random array, the sidelobe level at any given observation angle follows a chi-squared distribution with two degrees of freedom. The probability that all of the subarray's sidelobes are less than some fraction, r, of the main beam can be approximated as a joint probability that the sidelobe levels at a number of observation points are all less than r:

$$\Pr\{P_{sub}(u) < r\} \approx (1 - e^{-Nr^2})^{16ab} \quad [1].$$ (1)

In the above equation, P_{sub} is the array factor for the subarray, N is the number of elements per subarray, and a and b are the subarray dimensions in wavelengths.

By comparison, the sidelobe level of the total array factor has a slightly different probability distribution. Because the random subarray factor is being multiplied by a periodic superarray factor, the variance is no longer approximately invariant with position. Since a simple approximation was desired, it was necessary to choose one of two methods of simplifying the problem to be solved. One was to choose a method of averaging the variance, and use the average value to determine the probability distribution. The other method made use of the fact that the number and locations of the largest sidelobes are essentially known – they will appear in the same locations as the superarray factor's grating lobes, of which there are $4ab$ instead of $16ab$. At these locations, the variance of the array factor's value outside the main beam was the same as that for the subarray. Thus the total array factor's sidelobe level probability distribution could be approximated by

$$\Pr\{P_{NR}(u) < r\} \approx (1 - e^{-Nr^2})^{4ab}.$$ (2)

This second method is much more conservative than the first, and in general overestimates the sidelobe level. Figure 2 shows a graph of the probability that all sidelobes are less than –13 dB for three different values of N in a PARS of four arrays as well as in a single square subarray as the subarray side length (in wavelengths) varies. This illustrates the array's behavior as frequency changes.

3. ARRAY PROPERTIES WITH ROTATION

This section will derive the properties of a 2 x 2 segment of the ARRS. For larger arrays, this group may be used as a building block. The group is composed of four square subarrays in the x-y plane with side length d in meters, and the coordinates of the subarrays' centers are $(-d/2, d/2)$, $(d/2, d/2)$, $(d/2, -d/2)$, $(-d/2, -d/2)$. The subarrays are rotated in ϕ by 0, 90, 180, and 270 degrees, respectively.

It is assumed that the elements on all subarrays have rotationally symmetric radiation patterns. Because the arrays are required to fit together after being rotated, the side lengths a and b are no longer allowed to be different. Figure 3 illustrates the layout of this array. The array factor for this small array is given by the sum of the subarray factors, including phase changes due to position. Equations 3-6 show expressions for the array factors of each of the subarrays, modified for phase shifts due to rotation and position. The total array factor is given in Equation 7. In these equations, F_{rot} is the subarray factor corresponding to the subarray rotated by the angle rot, in degrees. N is the number of elements per subarray. θ and ϕ are the polar and azimuthal angles, respectively. P_R is the total array factor for the array with rotations. The independent random variables x_n and y_n represent individual element positions in the aperture, and may take any value between -½ and ½. Their probability distributions are $f(x)$ and $g(y)$. The probabilistic analysis methods used in the following section follow those in [4].

$$F_0 = \frac{1}{N} e^{j\frac{kd}{2}\sin\theta(-\cos\phi+\sin\phi)} \sum_{n=1}^{N} e^{jkd\sin\theta(x_n\cos\phi+y_n\sin\phi)} \tag{3}$$

$$F_{90} = \frac{1}{N} e^{j\frac{kd}{2}\sin\theta(\cos\phi+\sin\phi)} \sum_{n=1}^{N} e^{jkd\sin\theta(-x_n\sin\phi+y_n\cos\phi)} \tag{4}$$

$$F_{180} = \frac{1}{N} e^{j\frac{kd}{2}\sin\theta(\cos\phi-\sin\phi)} \sum_{n=1}^{N} e^{jkd\sin\theta(-x_n\cos\phi-y_n\sin\phi)} \tag{5}$$

$$F_{270} = \frac{1}{N} e^{j\frac{kd}{2}\sin\theta(-\cos\phi-\sin\phi)} \sum_{n=1}^{N} e^{jkd\sin\theta(x_n\sin\phi-y_n\cos\phi)} \tag{6}$$

$$P_R = \frac{1}{4}\left(F_0 + F_{90} + F_{180} + F_{270}\right) \tag{7}$$

This analysis considers the real and imaginary parts separately in order to easily compare the results to those of the non-rotated array, where the same approach was used. Let the real part be denoted by P_{R1} and the imaginary part by P_{R2}. One notices that P_R has only a real part; due to the rotation pattern the imaginary part is 0. For comparison, the non-rotated array's imaginary part is not identically 0, but its expected value is 0. Because the imaginary part is not a random quantity, the ARRS's sidelobe level will have only one degree of freedom in its chi-squared distribution, which reduces it to a normal distribution.

For mathematical simplicity, define the reduced observation angle variables $u_c = kd \sin\theta \cos\phi$ and $u_s = kd \sin\theta \sin\phi$. The probability distributions for x_n and y_n are assumed to be even. Also, because these expressions show up in various forms in the expected value and variance, let

$$\varphi_x(u) = \int_{-1/2}^{1/2} f(x)e^{jux}dx \qquad (8)$$

$$\varphi_y(u) = \int_{-1/2}^{1/2} g(y)e^{juy}dx \qquad (9)$$

The expected value and variance of the real part of the rotated array factor are:

$$E(P_{R1}) = \frac{1}{2}\left(\cos\left(\frac{u_c}{2} - \frac{u_s}{2}\right)\varphi_x(u_c)\varphi_y(u_s) + \cos\left(\frac{u_c}{2} + \frac{u_s}{2}\right)\varphi_x(u_s)\varphi_y(u_c)\right) \qquad (10)$$

$$\sigma_{R1}^2 = \frac{1}{8N}(1 + \frac{1}{2}\cos(-u_c + u_s)\varphi_x(2u_c)\varphi_y(2u_s)$$
$$+ \frac{1}{2}\cos(u_c + u_s)\varphi_x(2u_s)\varphi_y(2u_c)) - \frac{1}{4N}E^2(P_{R1}) \qquad (11)$$

Using the Riemann-Lebesgue lemma to approximate these expressions for large values of u (that is, outside the main beam), all instances of $\varphi_x(u)$ and $\varphi_y(u)$ approach 0. Therefore the expected value of the real part outside the main beam is 0, and the variance is given by

$$\sigma_{R1}^2 \approx \frac{1}{8N}. \qquad (12)$$

By the central limit theorem, for large values of N the real part of the array factor has an approximately normal distribution, so the probability that the array factor in the region of large u is less than some fraction r of the main beam can be approximated by

$$\Pr\left(\left|P_R(u_c, u_s)\right| < r\right) \approx \mathrm{erf}(4r\sqrt{N}) \qquad (13)$$

297

Since the probability distribution, mean, and variance approximately do not vary with observation angle over the entire visible range outside the main beam, the average sidelobe level for this array, r_{avg}, can be obtained using

$$\text{erf}(4r_{avg}\sqrt{N}) = 0.5 \qquad (14)$$

The probability of a sidelobe at one location being less than r can be applied to the entire visible range outside the main beam by taking the joint probability that, observing the sidelobe level at a certain number of locations, it is less r at all of them. This is reasonable because the magnitudes of the array factor at adjacent values of u are closely related [4]. The observations will be at $64a^2$ locations rather than $16a^2$ because the larger total aperture results in faster variation in the sidelobe region.

$$\Pr\left(|P_R(u_c,u_s)| < r, \forall u_c : \psi_c < |u_c| < 2a, \forall u_s : \psi_s < |u_s| < 2a\right) \approx \left(\text{erf}(4r\sqrt{N})\right)^{[64a^2]} \qquad (15)$$

The variable a is the subarray side length in wavelengths. The brackets around the $64a^2$ exponent on the right hand side of the equation above indicate rounding to the next highest integer. ψ_c and ψ_s refer to the width of the main beam in terms of u_c and u_s – thus the bounds on u_c and u_s above refer to the visible region outside the main beam.

If an ARRS of more than one of these groups of four subarrays were to be designed, one would expect the known locations and number of superarray factor grating lobes to result in a change in the exponent of the peak sidelobe probability as occurred in the PARS analysis. However, since the repeated element is a square with side length $2a$, there are $16a^2$ grating lobes in the superarray pattern rather than $4a^2$.

In the next section, these results will be compared with the previously characterized behavior of the array without rotations.

4. COMPARISON

The goal of both the array of rotated random subarrays and the periodic array of random subarrays is to achieve low sidelobe levels over a large bandwidth while maintaining a more repetitive geometry than a purely random array. In this section we will compare the probabilistic behavior of the two arrays, followed by an example design process that illustrates the tradeoffs between them.

Figure 4 shows the probabilities versus r of a PARS and ARRS, each with four subarrays, 400 total elements, and 3600 square wavelengths total area. Since we are only considering the array factor and assuming the elements to be isotropic at all frequencies, the particular frequencies of these graphs are arbitrary, since the array behavior depends on the relationships between r, the number of elements, and the aperture size in wavelengths. The important feature here is that the ARRS levels off at a high probability at a much lower value of r than the PARS's. The value at which an array's probability function exhibits this leveling-off behavior will be referred to as the threshold value. In both types of arrays, for a particular r there is a threshold value of N, and for a given N there is a threshold r. As a result of its threshold at a lower value of r, an ARRS can achieve a better sidelobe level with the same aperture size and number of elements.

Another comparison may be made between the number of elements required per subarray to achieve a desired probability and sidelobe level. Figure 5 graphs the number of elements required to achieve a –20 dB sidelobe level with 85% probability against the square root of the aperture area, which is proportional to frequency. For this sidelobe level, the PARS requires far more elements than the ARRS, the PARS's required N being in the neighborhood of 500 while the ARRS's required N is less than 42.

Lastly, for several fixed values of N, the peak sidelobe probability is graphed against the square root of the aperture area, which allows the graph in Figure 6 to show the way a PARS or ARRS behaves over a wide frequency range. If N is chosen so that it is beyond the threshold region for the entire frequency range, both arrays have very stable array factors and can easily be designed so that their sidelobes remain below a specified r value over the entire range. However, the ARRS has a lower threshold value of N, resulting in lower element density and consequently an extended lower frequency limit. Using fewer elements will result in lower gain, but in general low-noise amplifiers can be added at lower cost than hundreds more elements and their accompanying feed lines and phase shifters.

As an example of the design process and tradeoffs for the PARS and ARRS, suppose an array of four square subarrays is desired that operates from 3 GHz to 30 GHz with peak sidelobe level of –13 dB or less over the entire range. To limit the effect of coupling and in order that our approximations hold, it is also desired that at all frequencies the average element density is no more than one element per ten square wavelengths of aperture area. The assumption that the expected value of the array factor is 0 in the region of large u is accurate over more of the visible range if u is large over more of the visible range. This occurs when the aperture is large. The ten square wavelength requirement here is larger than is

always necessary, but low element density will increase the aperture size and improve the accuracy of sidelobe level predictions. We will require that the probability of success be at least 85%, to reduce the likelihood of having to test more than one array designed with these parameters. Since the probability is lower at higher frequencies, this amounts to a requirement of 85% probability at 30 GHz.

The element distributions in x and y may be any even probability distribution. When the desired sidelobe level is not too low, the choice of element distribution essentially does not matter except in the region very near the main beam. If an array with a very low sidelobe level is to be designed, one must account for more than just the $\frac{1}{8N}$ term of the ARRS variance. The full expression for the variance, given in Equation 11, includes $\varphi_x(u)$ and $\varphi_y(u)$, which depend on the element distribution. Since the variance in these cases is small, it may no longer be acceptable to approximate the expected value of the array factor in the sidelobe region as 0, as has been done here. The expected value also depends on $\varphi_x(u)$ and $\varphi_y(u)$. In Figures 1 and 3, the element distribution is normal. In the solutions to examples in this section, the element distribution will also be normal, because in general normal distributions appear to result in lower sidelobes near the main beam, where the expected value is larger compared to the variance and accounts for a larger proportion of the sidelobe level.

Upon solving this problem with a required probability of 85%, the probability equations derived previously result in only 18 elements in each subarray of the ARRS, 72 elements total, and a subarray area of 180 square wavelengths. This result is slightly problematic because the analysis in the previous section depended on the central limit theorem, and therefore is prone to error when N is small. Lo's investigation [5] suggests that this central limit theorem-based type of characterization of random arrays is still usable for relatively small N, but the N it refers to is in the neighborhood of 50 to 80 elements, not 18. Here, the number of elements in the subarrays is small enough that the central limit theorem will definitely result in some inaccuracy when the array factor is calculated.

Solving this problem for a PARS results in 329 elements per subarray, 1316 total. In this case the smallest subarray allowed measures approximately 57.4 wavelengths on a side at 3 GHz, which corresponds to a total array with dimensions 11.5 by 11.5 meters. Comparatively, the approximation that was derived earlier predicts that an ARRS with the same parameters has a sidelobe level less than −25 dB with 85% probability.

One issue that must be avoided in this design process is that, if the subarray factor's main beam is wide enough, superarray grating lobes can overlap with it and thus not be reduced to the random sidelobe level. This effect can be observed in the lower-frequency array patterns of the second sample ARRS. This can usually be prevented by enlarging the subarray aperture, thus narrowing its main beam.

Array factors have been calculated for all three arrays mentioned, and they are graphed at several frequencies for each. Figures 7, 8, and 9 show the $\phi = 0$ plane of the array factor of the ARRS with 18-element subarrays at 3, 15, and 30 GHz. Interestingly, the resultant array pattern is fairly close to the prediction despite the small size of the subarrays. Over the whole visible range, few sidelobes exceeded the −13 dB design goal; those that did had magnitudes of at most about −10 dB. Figures 10, 11, and 12 show the PARS's array factor at 3, 15, and 30 GHz., and Figures 13, 14 and 15 show that of the second ARRS (329 elements per subarray) at those frequencies. Other planes of the array factors were observed and found to be qualitatively similar to the examples shown.

5. CONCLUSION AND REMARKS

As is evident from the example in the previous section, the ARRS achieves some improvement in performance over the PARS with minimal increase in geometric complexity. The ARRS has a slightly extended lower frequency bound relative to a PARS with the same aperture and number of elements. The number of elements required to achieve a specified sidelobe level is reduced, which results in arrays with fewer elements and feed lines for the same sidelobe level, or in lower sidelobe levels for the same number of elements.

The behavior of the ARRS is similar to that of a symmetric array briefly considered by Lo [6]. Both have array factors outside the main beam characterized by a normal distribution rather than chi-squared. This is to be expected, since the arrangement of the ARRS is symmetric along diagonal axes. It also has 90-degree rotational symmetry.

Because this characterization and the resultant design process depend on the central limit theorem and should only be accurate for large numbers of elements, it is interesting that the performance of the ARRS with 18-element subarrays was relatively close to predictions. It may be useful to investigate random arrays, PARSs, and ARRSs with small numbers of elements and characterize how the accuracy of the characterization used here is affected.

The ARRS and PARS could be constructed using special types of random subarrays, including binned arrays [7] or arrays with a nearest-neighbor constraint [8]. These in particular are interesting because purely random arrays have no built-in safeguards against element clustering, which can introduce coupling and may decrease the effectiveness of the array. It may be wise for practical ARRS and PARS implementations to use some such method of ensuring that individual elements are not too near one another. Binned and nearest-neighbor constrained arrays also exhibit the possibly useful trait of suppressing the random sidelobes nearest the main beam by reducing the array factor variance in that region.

An array of rotated random subarrays has been probabilistically characterized and its performance compared to that of an array of non-rotated random subarrays. Rotation resulted in some improvement in sidelobe level and lower frequency range without greatly increasing the complexity of the array's geometry. A sample design demonstrated the effectiveness of this class of array, and it is suggested that some existing refinements to the purely random array should be implemented in the subarrays of the ARRS in order to increase its practicality for real applications.

ACKNOWLEDGMENT

REFERENCES

[1] Y. T. Lo, "A Mathematical Theory of Antenna Arrays with Randomly Spaced Elements", *IEEE Trans. Ant. Propagat.*, vol. 12, pp. 257-268, May 1964.

[2] B. D. Steinberg, "Comparison Between the Peak Sidelobe of the Random Array and Algorithmically Designed Aperiodic Arrays", *IEEE Trans. Ant. Propagat.*, vol. 21, pp. 366-370, May 1973.

[3] K.C. Kerby and J. T. Bernhard, "Wideband Periodic Array of Random Subarrays", *Proc. IEEE Ant. Propagat. Soc. Int. Symp*, vol. 1, pp. 555-558, June 2004.

[4] Y. T. Lo, "On the Theory of Randomly Spaced Antenna Arrays", Antenna Lab., Dept. of Elec. Engrg., Univ. of Illinois, Urbana, Tech. Rept. No. GI4894, 1962. Sponsored by Natl. Science Foundation.

[5] Y. T. Lo, "Sidelobe Level in Nonuniformly Spaced Antenna Arrays", *IEEE Trans. Ant. Propagat.*, vol.11, pp. 511-512, July 1963.

[6] Y. T. Lo, "A Probabilistic Approach to the Problem of Large Antenna Arrays", *Radio Science*, vol. 68D, pp. 1011-1019, Sept. 1964.

[7] W. J. Hendricks, "The Totally Random Versus the Bin Approach for Random Arrays", *IEEE Trans. Ant. Propagat.*, vol. 39, pp. 1757-1762, Dec. 1991.

[8] R. L. Fante, G. A. Robertshaw, and S. Zamoscianyk, "Observation and Explanation of an Unusual Feature of Random Arrays with a Nearest-Neighbor Constraint", *IEEE Trans. Ant. Propagat.*, vol. 39, pp. 1757-1762, July 1991.
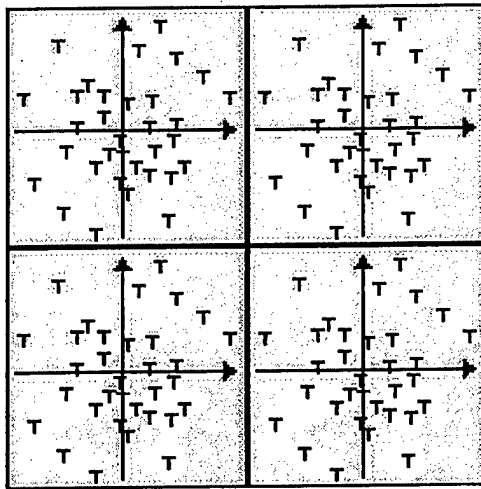
Fig. 1: Layout for periodic array of random subarrays, including subarray boundaries and orientation axes. Elements are randomly placed using a normal distribution.
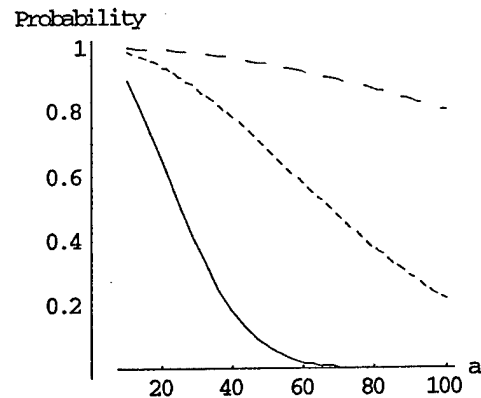
Fig. 2: Probability that all sidelobes are less than −13 dB for 3 different values of N in a PARS of 4 subarrays as a varies with frequency. Solid line: N=170. Short-dashed line: N=210. Long-dashed line: N=250.
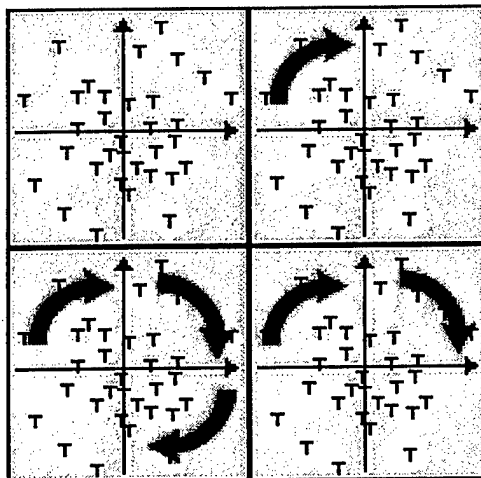
Fig. 3: Layout and rotation pattern for array of rotated random subarrays. Elements are randomly placed using a normal distribution. After rotation, individual elements all have the same orientation.
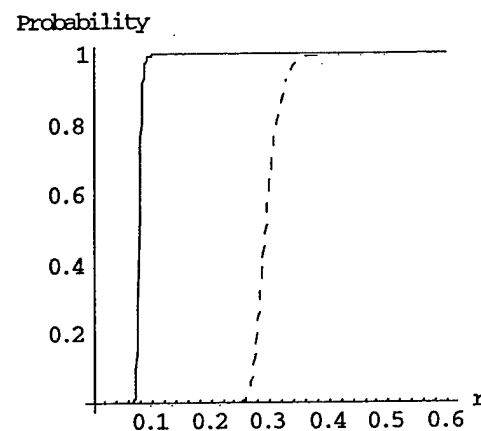
Fig. 4: Probabilities vs. r of an ARRS (solid line) and PARS (dashed line), each with 400 elements and 3600 square wavelengths total area.

304
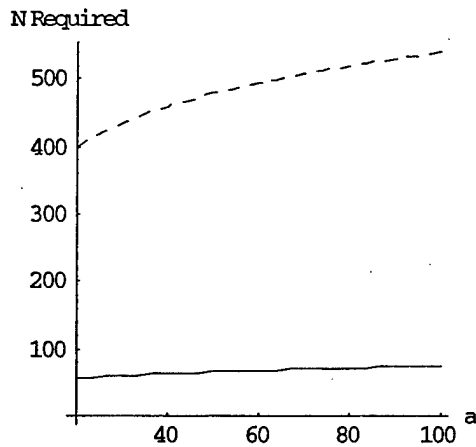
Fig. 5: Number of elements required to achieve a −20 dB sidelobe level with 85% probability vs. a, which depends linearly on frequency, for an ARRS (solid line) and a PARS (dashed line) with four subarrays each.
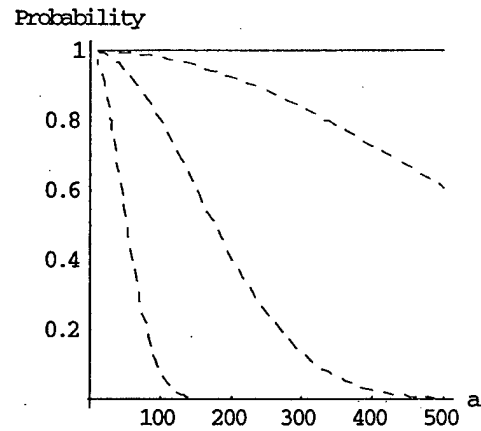
Fig. 6: For N = 300, 250, and 200, the probability of −13 dB sidelobe level is graphed against the square root of the aperture area, which shows the way a PARS (dashed lines) or ARRS (solid lines) behaves over frequency.
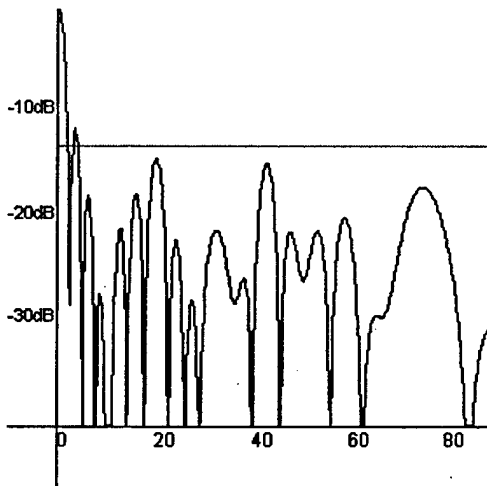
Fig. 7: Calculated $\phi = 0$ plane of the 72-element ARRS array factor at 3 GHz. Solid line is the −13 dB design requirement.
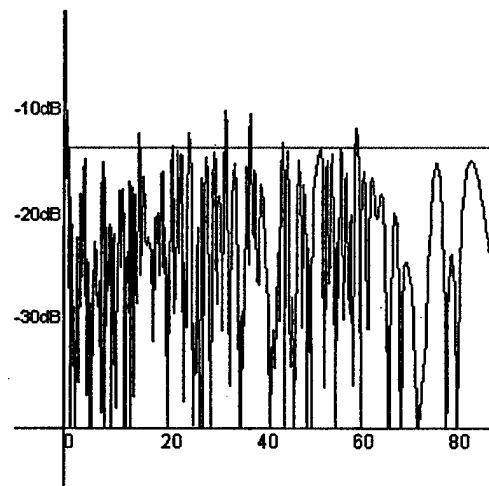
Fig. 8: Calculated $\phi = 0$ plane of the 72-element ARRS array factor at 15 GHz. Solid line is the −13 dB design requirement.

305
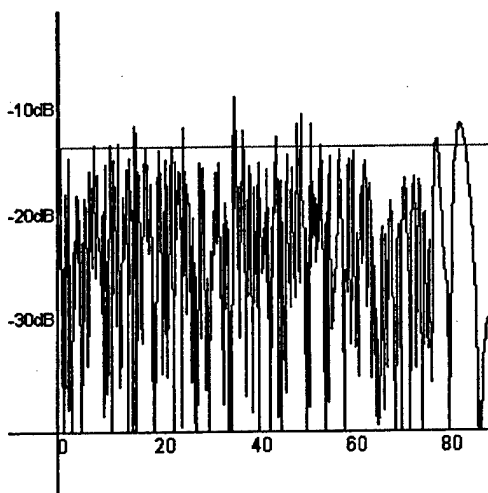
Fig. 9: Calculated $\phi = 0$ plane of the 72-element ARRS array factor at 30 GHz. Solid line is the –13 dB design requirement.
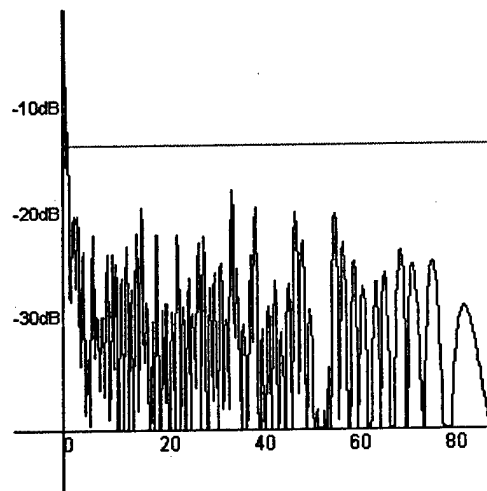
Fig. 10: Calculated $\phi = 0$ plane of the 1316-element PARS array factor at 3 GHz. Solid line is the –13 dB design requirement.
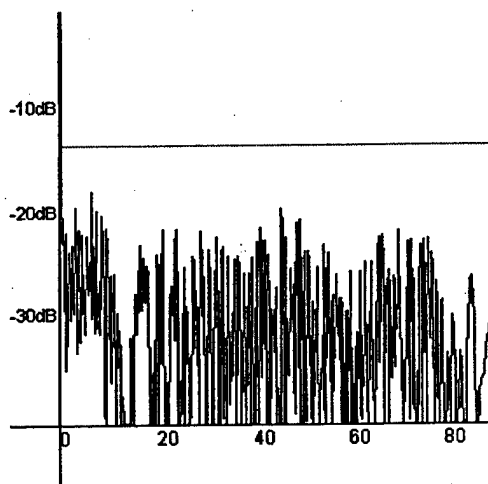
Fig. 11: Calculated $\phi = 0$ plane of the 1316-element PARS array factor at 15 GHz. Solid line is the –13 dB design requirement.
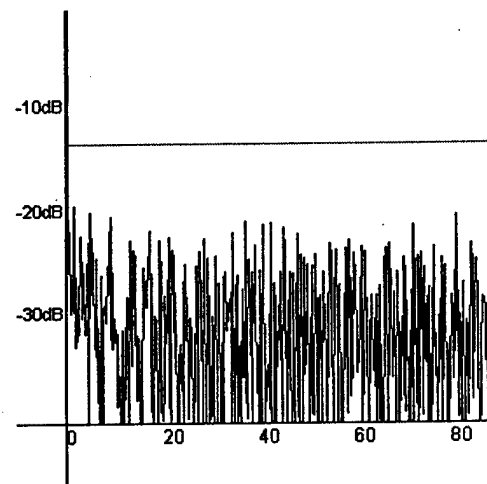
Fig. 12: Calculated $\phi = 0$ plane of the 1316-element PARS array factor at 30 GHz. Solid line is the –13 dB design requirement.

306
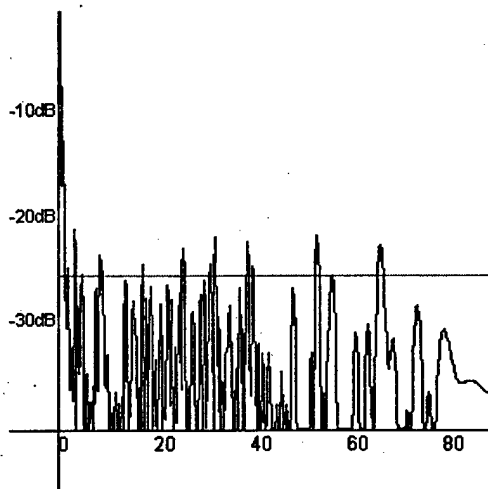
Fig. 13: Calculated $\phi = 0$ plane of
the 1316-element ARRS array factor
at 3 GHz. Solid line is the –25 dB
predicted sidelobe level.
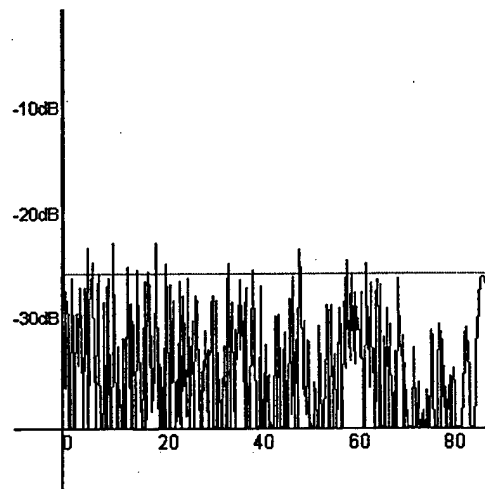
Fig. 14: Calculated $\phi = 0$ plane of
the 1316-element ARRS array factor
at 15 GHz. Solid line is the –25 dB
predicted sidelobe level.
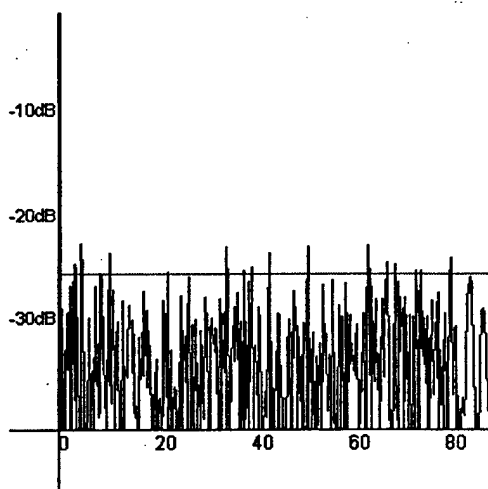
Fig. 15: Calculated $\phi = 0$ plane of
the 1316-element ARRS array factor
at 30 GHz. Solid line is the –25 dB
predicted sidelobe level.

DAISY CHAIN CONTROLLED MULTI-BEAM T/R MODULE FOR AFSCN

Sarjit S. Bharj – Princeton Microwave Technology
Madan Thaduri – Princeton Microwave Technology
Paul J. Oleski – Air Force Research Laboratory, Rome, NY
Lt. Robert Patton – Air Force Research Laboratory, Rome, NY
Dr. Boris Tomasc – Air Force Research Laboratory, Hanscom, AFB, MA
John Turtle – Air Force Research Laboratory, Hanscom, AFB, MA
Dr. Shiang Liu – Aerospace Corp, LA AFB, CA

1. ABSTRACT

A Transmit/Receive (TR) module for Unified S-Band (USB) and Satellite Ground Link Subsystem (SGLS) frequencies has been developed and fabricated for a Phase Array Antenna (PAA) demonstration. The TR module has the unique features of an on board daisy chain control using a Complex Programmable Logic Device (CPLD) and a Built in Test (BIT) circuit using a micro controller for reporting health status of power amplifier and low noise amplifiers. The feedback information is provided via telemetry in packet format. The RF section includes two transmit channels capable of transmitting 30 dBm in each, and two receive channels with low noise amplifiers with 1.0 dB noise figure. The dual transmit and receive channels are separated by ceramic based dielectric resonator filters that uses a band pass response for the receive band of 2200 – 2300 MHz and a notch filter for the transmit section which provides a rejection of 60 dB in the receive band. Each channel incorporates a 4-bit phase shifter, a 5-bit attenuator, gain blocks and on-off switch. In addition, each of the receive channels and transmit channels are connected via a polarization circuit to allow LHCP and RHCP. The format of the TR allows two independent transmit and two independent receive beams. The insertion of the module has been designed to handle hot switching and circuits are incorporated for full protection of the beam former in case of module failure. This paper will detail the format, functionality and performance of the TR module.

2. INTRODUCTION

Low cost component design and implementation issues are critical in developing a practical phased array antenna. Combined RF, Digital and monolithic circuits are important but not the only critical issue.

Affordable antenna arrays operating at microwave frequencies are envisioned to consist of active modules that employ microwave integrated circuits located at each radiating element of the aperture. The antenna system consists of a separate receiver and transmit aperture capable of rapid beam motion. The transmitter antenna should be capable of high radiation power levels and the receiver antennas must achieve high G/T ratios. Beam agility and high-radiated power levels in association with the close spacing between the radiators drive the antenna design. The requirement for fast beam switching will require digital control circuits to calculate phase shift settings. A high RF radiated power level developed from closely spaced RF amplifiers generates very large heat densities. This forces the transmit antenna to increase in area to where beam pointing accuracy limits the array size. The great number of elements in the array emphasizes the need to develop a practical method of distributing control signals throughout the array. A Geodesic Dome Phase Array Antenna (GDPAA) is considered for the Air Force Satellite Communication Network (AFSCN). Implicit in the system function array is the need to operate the array in full duplex operation. Additionally the array should be capable of controlling fundamental radiation characteristics such as beam width, beam size, side lobe levels and radiated power, in order to realize different antenna characteristics required by the various satellites. The array aperture consists of a large number of radiating elements that are spaced approximately half a wavelength at the upper end of the operational frequency band. The frequency response and excitation of each element in the aperture can be independently controlled. The aperture can be fully or partially utilized either to direct energy over a large volume or intentionally directed in a certain direction. The capability of the array to provide transmit and receive functions simultaneous and to rapidly alter the set of configurations is possible due to active element control circuit. The active circuits allow for the control of the radiation characteristics of the PAA. The aperture can be uniformly illuminated to achieve maximum gain or tapered illumination and to achieve low side lobes or beam shaping. The combination of the variable attenuator and phase shifter permits the array Illumination to be modified and the antenna beam to be scanned in any direction. The filter specifies the portion of the aperture used by a particular system. The phase shifter, the variable attenuator and the amplifier are components that have been developed in Microwave Monolithic Integrated Circuit (MMIC) technology in the last decade.

The requirement for high isolation between transmit and receive channels focused the effort to investigate the exact performance that can be achieved from the low-cost ceramic filters and traditional filters. In addition, low cost MMIC based power amplifiers for the transmit channel have also been located. Effort was also directed towards the design of a low-cost phase shifters.

Other important factors that were considered in the development of the TR module were:
- TR module's interface with beam former
- Hot condition Operation
- Polarization Diversity
- Dual Transmit and Receive Channels
- Low Cost with Justification
- High Isolation between Transmit and Receive Channels
- Digital Control on Board
- Ruggedness and Reliability

3. SYSTEM BLOCK DIAGRAM

Each transmit/receive module consists of an RF board and a DC control unit controlling the MMIC's on the RF board. The RF board has four channels comprising of two transmit and two receive channels. Figure 1 shows the block diagram of the RF board of the T/R Module.

The transmitter path is shown by a dotted line to distinguish it from the receiver path. The transmit frequency of operation is 1.75 – 2.1 GHz. The receiver frequency of operation is 2.2-2.3 GHz. The transmit path consists of an input at Tx1/Tx2 and output from one of the two antenna ports (A1/A2). The transmitter signal passes through a four-bit phase shifter (ϕ shift of 22.5^0, 45^0, 90^0, 180^0), a SPDT switch to open/close the RF path, a five-bit attenuator (attenuation levels of 1dB, 2dB, 4dB, 8dB, 16dB), a pre amplifier and then through another absorptive type SPDT switch before reaching the embedded power combiner. The absorptive SPDT switch is used to induce left hand circular polarization (LHCP) and right hand circular polarization (RHCP) in the signal. A 90-degree hybrid is used to provide quadrature phase in the input signal. The quadrature output of the hybrid is amplified using MMIC amplifiers to a power output in excess of 30 dBm before transmitting through a high rejection low pass ceramic filter. The overall gain of the transmitter channel is 20 dB.
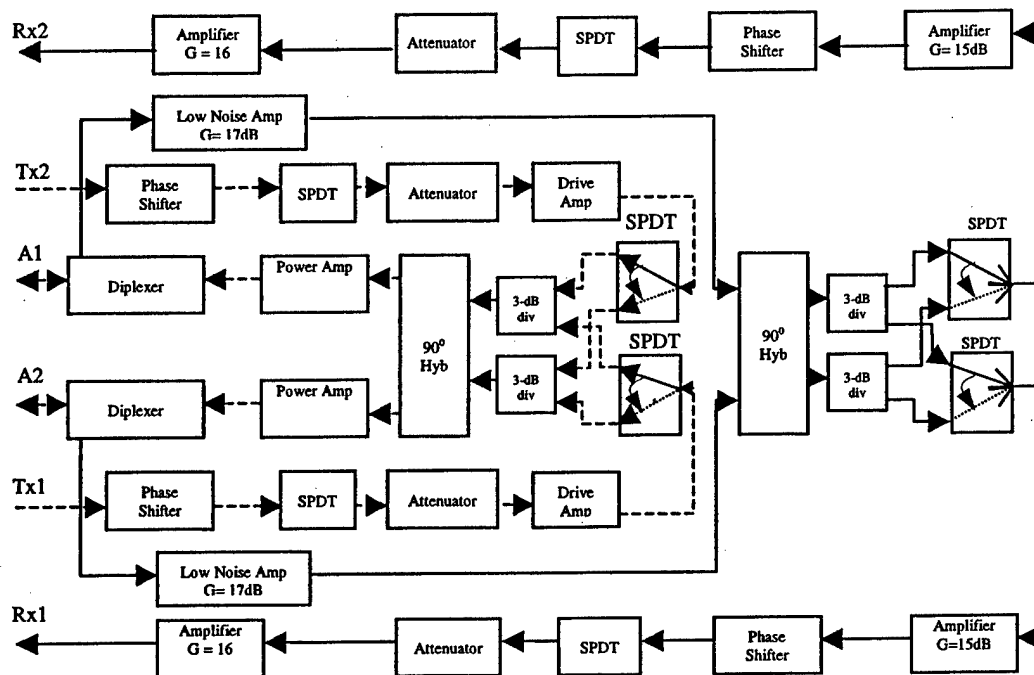
Figure 1. Block diagram of the T/R Module

For the downlink (receiver), the input signal is fed to a high rejection band pass ceramic filter using A1/A2 port. The input signal passes through a series of amplifiers, phase shifters, attenuators, and SPDT switches before reaching the receiver ports (Rx1/Rx2). The total gain across the receiver band is 30 dB. The specifications for the transmit and receive sections of the TR module are detailed in Table I and Table II.

Table I. Transmit channel specification

PARAMETER	SPECIFICATIONS
Frequency	1.75-2.1GHz
Gain	20dB
Power output per channel	30dBm
Phase shift	360°
Control	Electronics
Retrofit	Hot swap
Efficiency	> 40 %

Spurious	<-85
Attenuation	3 to 10 dB

Table II. Receive channel specification

PARAMETER	SPECIFICATIONS
Frequency	2.2-2.3 GHz
Gain	30dB
Noise Figure	1.2dB
Phase shift	360°
Attenuation	30dB min

The main components of the Transmit-Receive (TR) module are:
- Ceramic diplexer with high rejection
- Low noise MMIC amplifiers
- High Power MMIC driver and Power MMIC Amplifiers
- Quadrature and in phase hybrids
- 4-Bit Transmit and Receive digital Phase Shifter
- 5-Bit Digital Control Attenuators for Transmit and Receive channels
- Polarization selection
- Xilinx digital controller (Cool Runner II CPLD)
- PIC micro controller for Built-In-Test
- RS-485 and SPI interface

3.1. DIPLEXERS

Two diplexers are required to maintain optimum performance. The transmit side of the diplexer filter, inserted after the transmit amplifier, prevents wideband noise from entering the receiver, and degrading performance. The receive section of the diplexer, prevents the coupled transmit signal from degrading the linearity of the receive Low Noise Amplifier (LNA). The diplexer filters are made of high Q ceramic resonators. Two types of diplexers were investigated. The first consisted of a band pass type of response to provide at least 60 dB of rejection at the crossover point between the bands. This filter provided a loss of 1 dB in the transmit pass band and 1.5 dB in the receive path. We then investigated a band stop band pass type of diplexer. This filter that produces an insertion loss of 1 dB in the receive band consists of ten resonators in a coaxial structure. The transmit section loss was 0.5 dB with a rejection of 65dB at the crossover frequency. The band stop filter consisted of three sections of notch filtering using ceramic technology.

Table III. Transmit filter specification

PARAMETER	SPECIFICATIONS
Frequency	1.75-2.1 GHz
Insertion loss	1.0 dB Max
Return loss	<-15 dB
Rejection at 2.15 GHz	<-50 dB

TABLE IV. Receive filter specification

PARAMETER	SPECIFICATIONS
Frequency	2.2-2.3 GHz
Insertion loss	1.0 dB Max
Return loss	<-15 dB
Rejection at 2.15 GHz	<-50 dB

3.2. LOW NOISE MMIC AMPLIFIER

A low noise MMIC amplifier developed for the satellite and the radio market for the frequency of 2.2 to 2.3 GHz has been used. The device provides a gain of 18 dB with an associated noise figure of 1 dB. It is based on E-D MESFET process and consumes very low current.

3.3. FOUR BIT TRANSMIT AND RECEIVE PHASE SHIFTERS

A phase shifter design based on the MMIC switch incorporating a single pole double throw was procured from Marconi. This device essentially replaces two single pole double throw switches. The component count reduced from 10 devices per phase shifter, (Total 40 for TR module) to 5 devices per phase shifter (20 per TR module). The design of the Transmit and Receive channel phase shifters was detailed in Ref 1. The insertion loss of the phase shifter was measured at 8 dB with a total change in insertion loss of 0.4 dB in all phase states.

The transmit phase shifters were designed based on low-pass, high-pass filter sections switched between paths. The phase shifter provided 22.5, 45, 90 and 180-degree phase shifts with an error of 10 degree for the 180 degree bit. Total amplitude change for the phase shifter was less than 1 dB for all phase states. The receive phase shifters were based on the switch line approach and exhibited an insertion loss of 6 dB. Again the total amplitude change was less than 1 dB for all phase states.

3.4. POLARIZATION SWITCHING

A scheme for polarization switching has been incorporated into the TR module. The details are shown below.
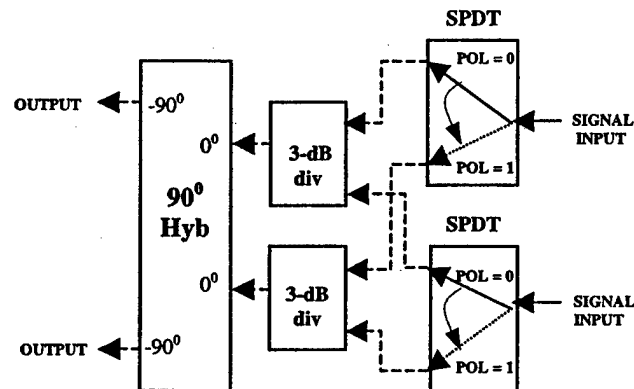
Figure 2. Polarization switching schematic

Both LH and RH circular polarization is achieved in the transmit and receive section of the module. Incorporation in the receive section is detailed in Figure 2.

4. DC CONTROL BOARD

In the simplest terms, in a phase array system, a number of TR modules are used to steer the beam in the required direction. This is programmatically done by selectively controlling each Transmit/Receive module by sending synchronous command signals (e.g. data, clock and enable) to each module from the controller. Different techniques are used to send the control signals from the controller to the modules. In AFSCN system, the synchronous serial signals are sent from the controller to the TR modules in a daisy chain sequence. This is done until all the modules in the array have data in their shift registers. So the address of each module in the array is implied by the modules position in the array.

Xilinx Cool Runner II CPLD is used to provide the control signals to the four channels. The DC control board is made as a stand-alone board so that the boards could be easily detached from the module if found defective. The block diagram of the control board is shown and a description of the signal level interface is given. Following this, the final post place and route simulations of the Xilinx controller are shown. Figure 3 shows the control board on the right side of the Rx section of the TR module.
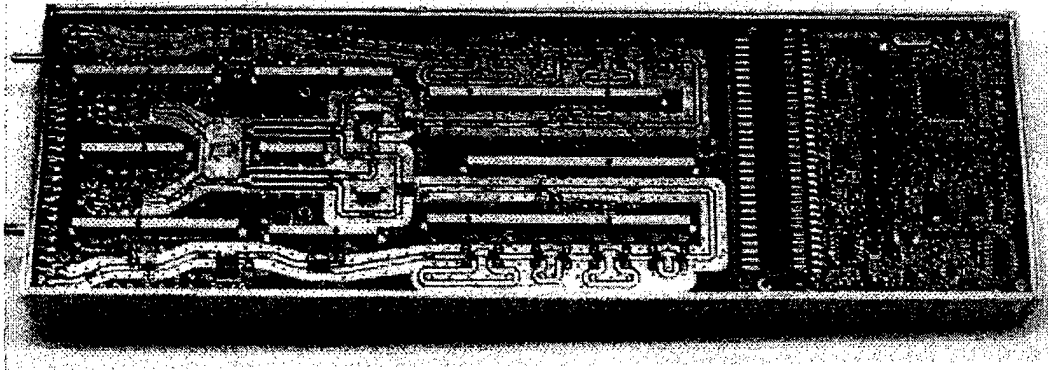
Figure 3. The T/R Module is controlled using a DC control board

4.1 BLOCK DIAGRAM OF THE BOARD

Figure 4 shows the simplified block schematic of the DC board. As can be seen, synchronous serial signals are sent to the module from the controller. The major components on the board are the PIC micro controller and cool runner II.

One of the advantages of using the cool runner II device is its low power consumption. The board has the capability of constantly monitoring the currents going to the RF power amplifiers on the TR module. Also the module temperature is constantly recorded using a precise temperature sensor. This information is collected and stored in the PIC and sent to the controller upon request for further processing. The asynchronous data from the PIC to the controller is sent using differential RS485 format [4]. The RS485 driver is disabled after sending the data.

315

Figure 4. Simplified block diagram of DC control

Table V shows the DC board specifications. Final place and route simulation for the on board Xilinx controller were performed to verify the functionality of the design.

Table V. Specification for the DC board

PARAMETER	VALUE
Operating Voltage	+5V
Power Consumption	40 mA
Operating Frequency	4MHz
Data Transfer Time	4uSec

Based on timing simulations, the maximum frequency of operation for the Xilinx controller is estimated to be 140 MHz. But the PIC device, which is relatively slow device, receives the same synchronous signals from the interface that are also sent to the Xilinx controller. To synchronize both these devices, the final operating frequency of the board is set at 4 MHz. The total system is done at this frequency and very reliable board operation is achieved. Both sides of the control board are shown in figure 5.

Figure 5. Top and bottom view of the control board

5. TR MODULE LAYOUT

The original TR module layout was conducted in a manner where the Inputs/Outputs (I/O) from the beam former were on the opposite end, to the antenna Output/Input (O/I) respectively. Later, it was clear that the I/O from the beam former to the antenna O/I needed to be on the same side to allow module exchange in the hot condition. The width of TR module was restricted to a maximum of 3 inch. The RF board was fabricated using grounded coplanar technology to reduce coupling and grounding effects. The control board was fabricated on Multilayered FR-4 substrate.

The completely assembled Transmitter section of the TR module with the associated control circuitry is 9.25 inches long and is shown in Figure 6. The receiver board is shown in Figure 7. The combined thickness including housing is 1.0 inch thick.
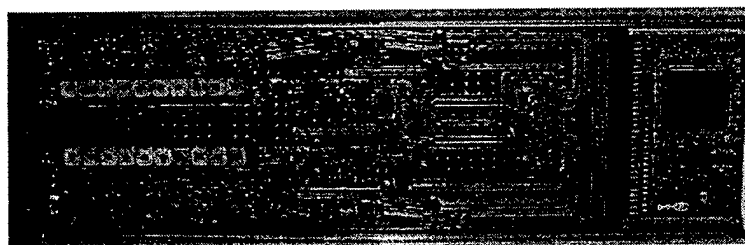
Figure 6. TX section of the TR module

317
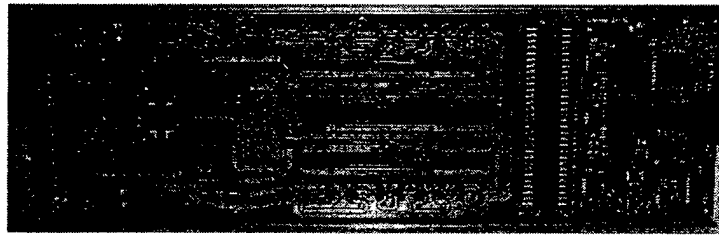
Figure 7. RX section of the TR module

6. DESIGN TO COST

The design to cost of the TR module has been conducted from project initiation. From onset, the cost associated with the components without compromise in the performance has been the guiding rule. The availability of the active devices for the PCS market has greatly influenced the cost of amplifiers and phase shifters. Added with novel design and layout, the design to cost goal is near reality.

7. MEASURED DATA

Measured data for the TR module is detailed below. Figure 8 and Figure 9 show the measured response of the receive channel polarization and attenuator circuit respectively.
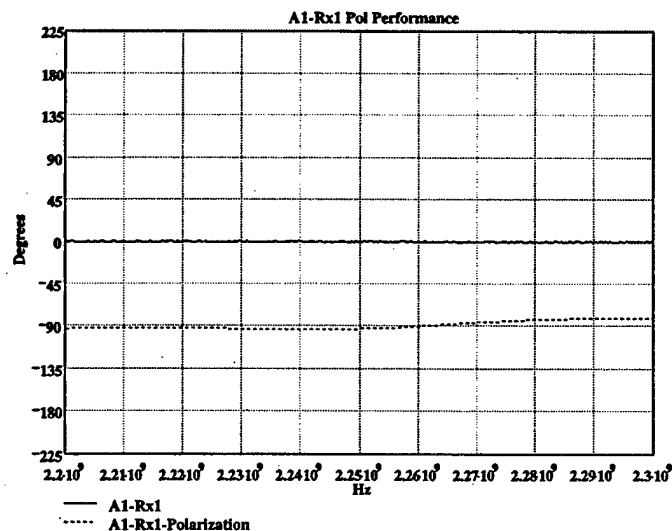
Figure 8. Receive polarization performance

318
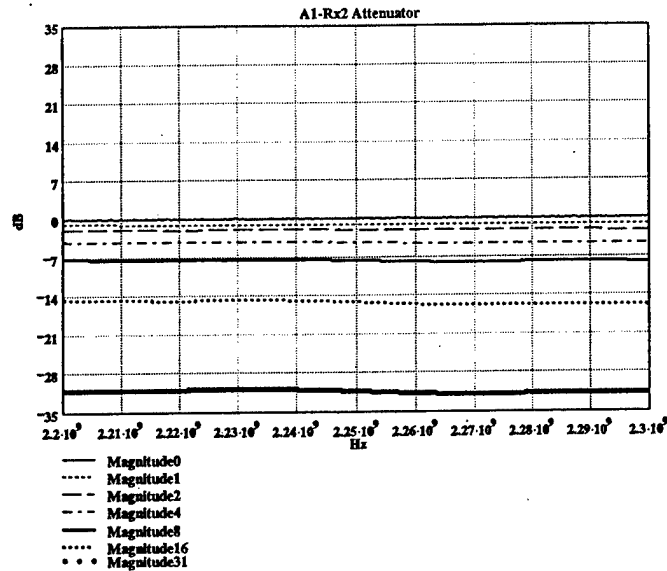
Figure 9. Attenuator response from the receive section

Figure 10 and Figure 11 show the transmit channel attenuator and polarization performance result. Figure 12 shows the measured performance of the phase shifter over the transmitter band. Figure 13 shows the diplexer performance over transmit and receive band. For frequency and amplitude measurements, the reference is set at 0^0 and 0 dB respectively.
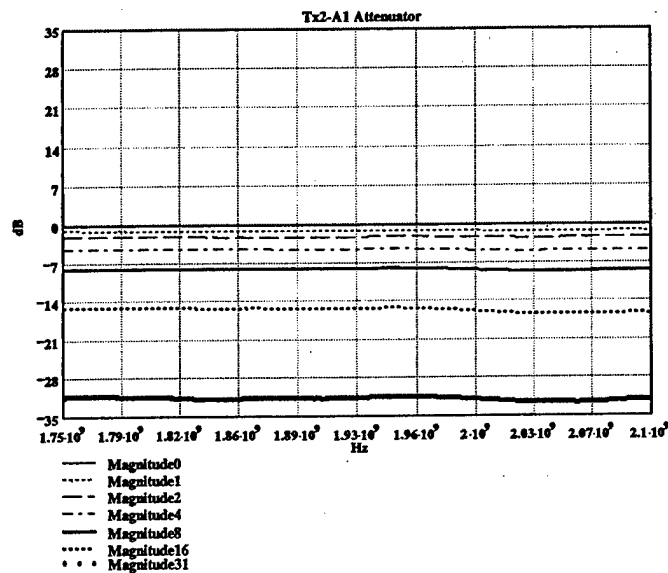
Figure 10. Transmit channel attenuator response
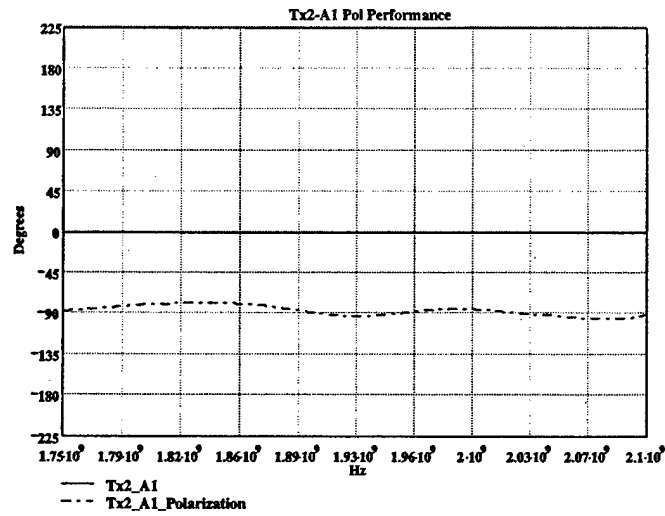
Figure 11. Polarization performance over the transmit band
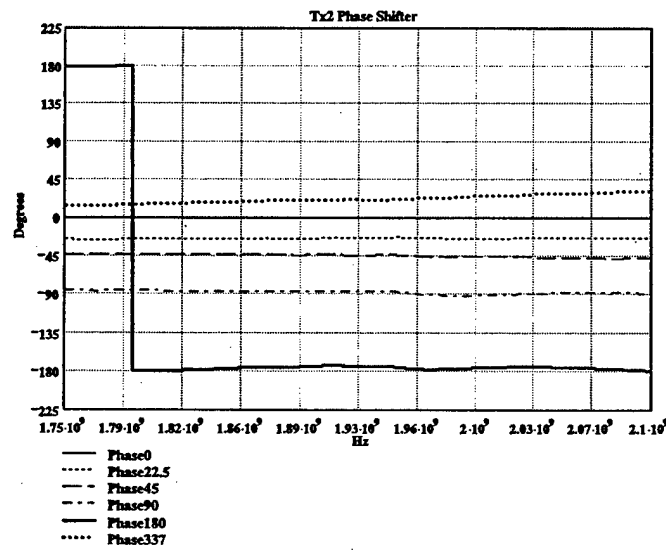
Figure 12. Transmitter phase shifter performance
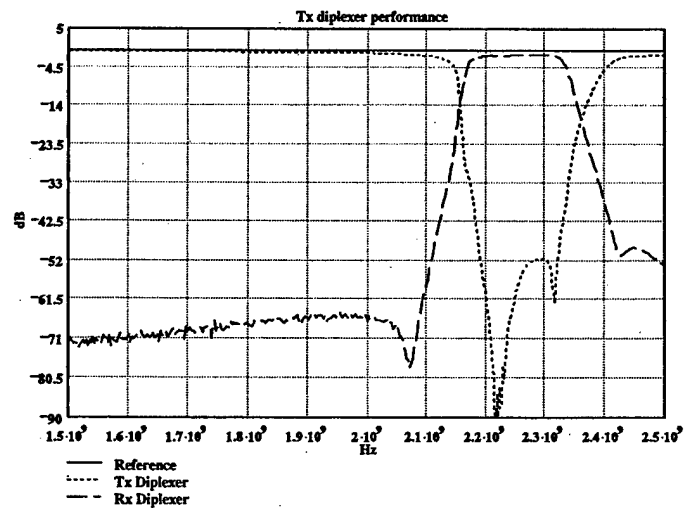
Figure 13. Rx/Tx diplexer performance

CONCLUSIONS

An S-Band Transmit and Receive (TR) module has been developed for Telemetry, Tracking and Commanding (TT&C) and communications at Unified S-Band (USB) and Space Ground Link Subsystem (SGLS) frequencies to meet the operational needs of the AF Satellite Control Network (AFSCN). An efficient DC control board for the TR module has been developed, fabricated and tested. A design to cost exercise was conducted to ensure a low cost product. In the transmit section of the TR module a power output of 30 dBm per channel with an overall TX gain of 20 dB was achieved. The Tx section also includes a 4-BIT phase shifter, a 5-BIT attenuator and polarization switching. In the receive channel a noise figure of 2 dB was measured with an overall gain of 30 dB. The dual Rx channels also include a 4-BIT phase shifter and a 5-BIT attenuator. In its present form, the TR module is reproducible. A subarray of 78 elements (one panel) has been successfully tested at the AFRL/SN Antenna Measurements Facility, Ipswich, MA. A six-panel subarray was assembled by Ball Aerospace for the testing of TT&C functions with NASA and DOD LEO satellites. This Air Force Space Battlelab (AFSB) demonstration took place in August 2004 at the NASA Flight Test Facility, Wallops Island, VA. Detailed results will be published by AFSB in January 2005.

REFERENCES

[1]   "Affordable Antenna Array For Multiple Satellites Links", 2000 Antenna Applications Symposium. P 401, Sarjit S Bharj, Paul J. Oleski, A. Merzhevskiy, B. Tomasic, S. Liu

[2]   "Low cost Transmit/Receive module for space ground link subsystem, 2002 Antenna Applications Symposium. P 1, Sarjit S Bharj, Paul J. Oleski, A. Merzhevskiy B. Tomasic, S. Liu, John Turtle, Narendra Patel

[3]   "Multi-Beam Transmit Receive Module for USB and SGLS Band Satellite Links', 2003 Antenna Applications Symposium P 1, Sarjit S. Bharj, Paul J. Oleski, A. Merzhevskiy B. Tomasic, S. Liu, J. Turtle

[4]   TIA/EIA-RS-485, Standard for Electrical Characteristics of Generators and Receivers for Use in Balanced Multipoint Systems.

MILLIMETER-WAVE BEAMFORMER FOR SHORT-DISTANCE PROBING

V. A. Manasson, L. Sadovnik, M. Aretskin, M. Felman
WaveBand Corporation
17152 Armstrong Ave.
Irvine, CA 92614

Abstract: Testing results for a new beam-steering antenna are presented. The antenna is capable of focusing electromagnetic energy in a small spot located at short distances from the antenna, distances that for conventional antennas fall into the near-field radiation region. One application for the new antenna can be millimeter-wave based screening for concealed weapons.

Most beam-steering antennas designed for operation in a radar or in an imaging sensor form slightly diverging beams. The beam cross-section is always larger than the antenna size in the respective plane. However, some applications require the antenna to form a beam that has a cross-section much smaller than the antenna size. The straightforward way to decrease the beam cross-section is to use a converging lens as an adjunct to the beam-steering antenna. Such a system is usually cumbersome, heavy, bulky, and suffers from extra absorption and reflection losses. We describe a new beam-steering antenna that is capable of forming converging beams with a spot size much smaller than the size of the antenna.

We will present the design and testing results of a new beam-steering antenna that is capable of focusing electromagnetic energy in a small spot located at short distances from the antenna, distances that for conventional antennas fall into the near-field radiation region. One application for the new antenna can be millimeter-wave based screening for concealed weapons.

The new antenna is a modification of the leaky-wave beam-steering antenna developed at WaveBand Corporation. That antenna typically comprises a single mode dielectric waveguide and a variable diffraction grating load. The diffraction grating covers a surface of a spinning cylinder and rotates with the cylinder. A conventional diffraction grating represents a periodic structure with a fixed period (the grating constant). In our antennas, the diffraction grating pattern is not uniform. The grating period varies along the drum circumference. The antenna beam originates from the interaction between the feeding dielectric waveguide and the active portion of the diffraction grating, the portion which is at the

moment close to the dielectric waveguide. The remainder of the diffraction grating is passive. As the drum rotates, at different instants different portions of the diffraction grating, with different periods, become active and produce beams propagating in different directions.

The specific feature of the new antenna presented here is that the cylindrical diffraction grating has a period that varies not only in one direction (along the circumference) but also along the cylinder's axis. Thus, different portions of the antenna form beam fronts in different directions. Proper selection of the grating period as a function of distance along the feeding waveguide can provide a converging beam, as well as a beam of a more complex shape.

We have built an antenna with H-plane scanning capability. The active aperture size in the H-plane is 18". The antenna operates in the W-band. We tested it at a frequency of 94 GHz. The spinning drum diffraction grating was designed to provide a narrow beam spot at a distance of 60 in (H-plane). To form the antenna beam in the V-plane we used a cylindrical lens. The antenna architecture diagram is shown in Fig. 1.
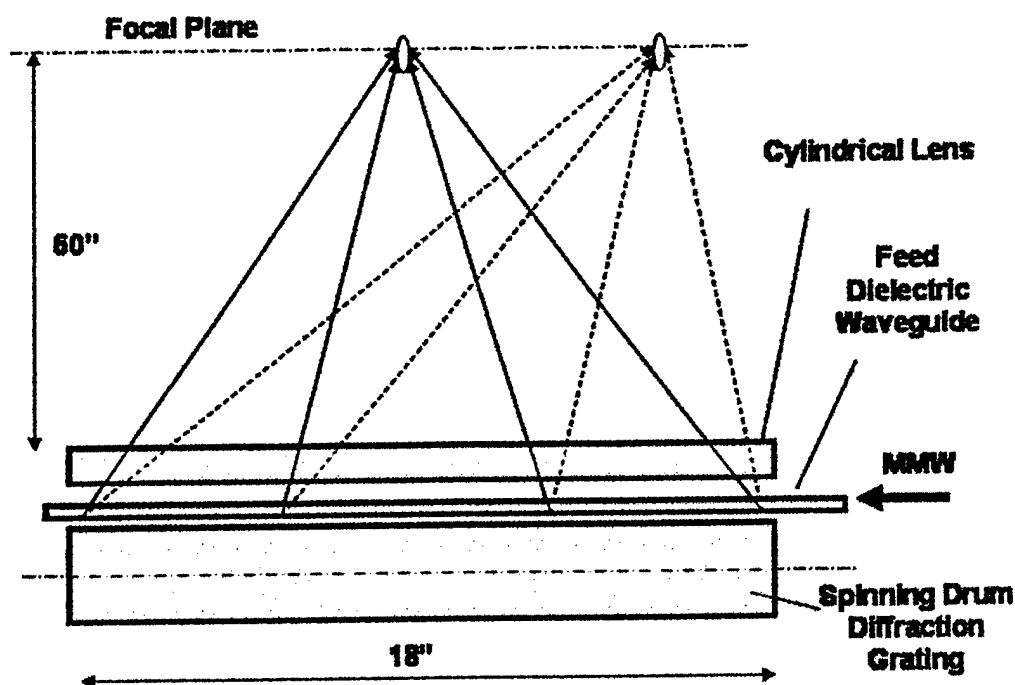
Fig. 1. Focusing beam steering antenna diagram (H-plane)

The variable diffraction grating was designed to focus the beam in the H-plane at a distance of 60 in (focal plane). The grating period varies continuously along the drum circumference. This provides true continuous scan as the drum rotates. Two examples of the grating period variations for two randomly selected instant beam positions are shown in Fig.2. According to our simulations, those gratings produce beam patterns shown in Fig.3.
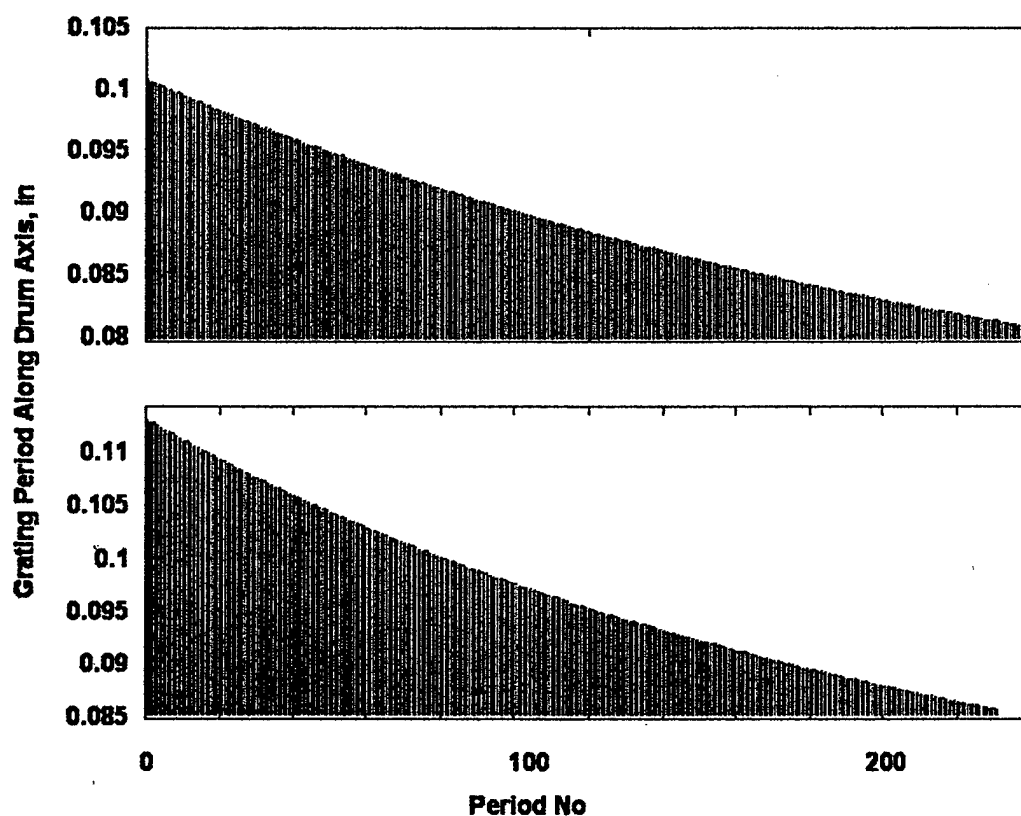
Fig.2. Examples of grating period variation for two positions of the beam.
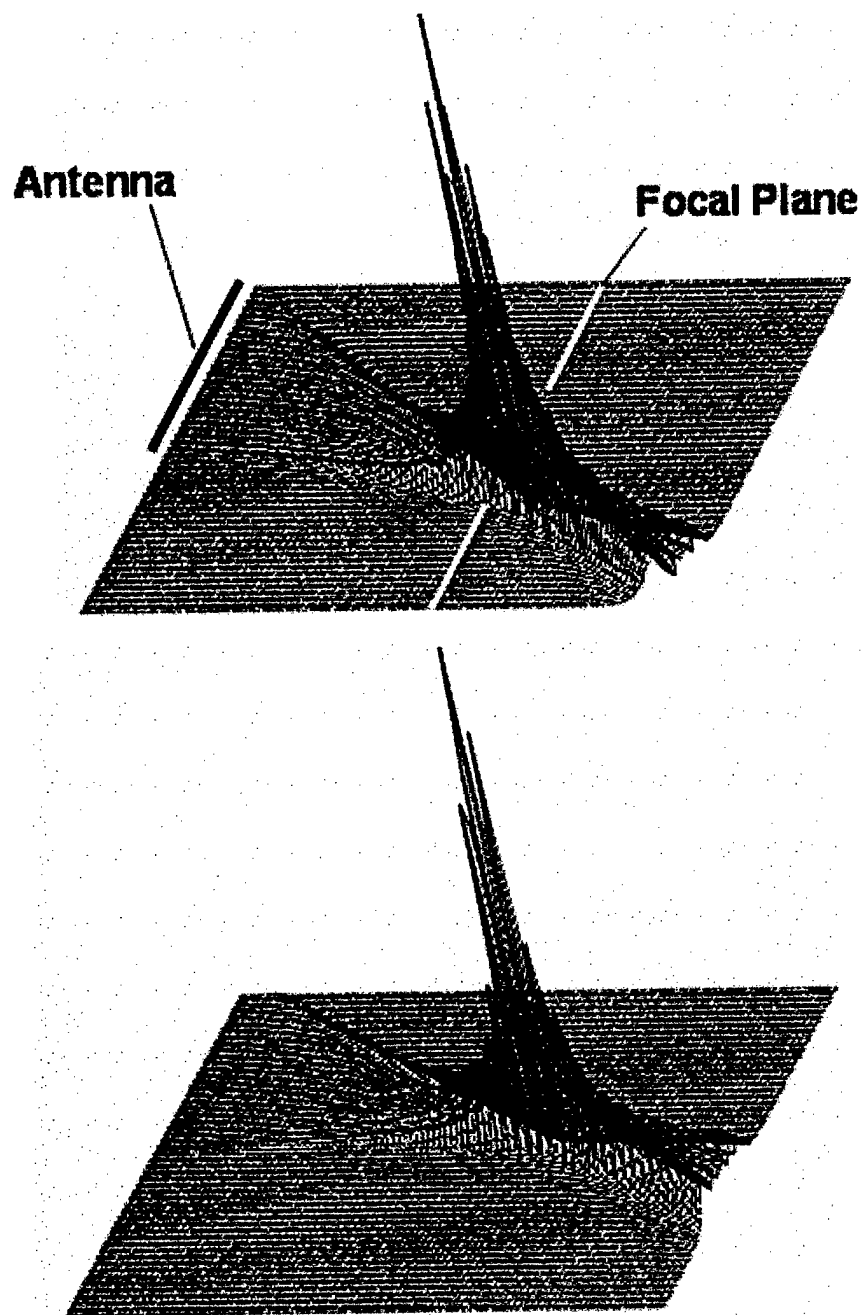
Fig.3. Simulated power distribution within the H-plane for two converging beams formed by an antenna with grating period variations shown in Fig.2.

We tested the new antenna using a near-field antenna measurement system. Rather than measure amplitude and field distribution in the near-field regions, we placed the antenna at a distance of 60 in from the scan plane of the system. This allowed us to directly measure the energy distribution in the antenna focal plane. The measurement results for 10 different drum (beam) positions are shown in Fig.4.
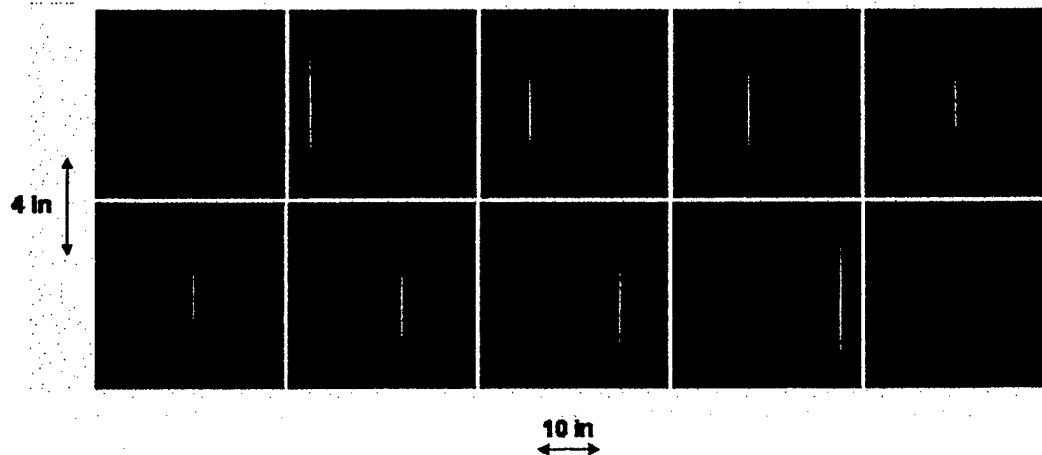
Fig. 4.   Focal plane 2D-beam profile for 10 different drum (beam) positions.

Within the entire scan region (30 in) the antenna provides a narrow spot in the H-plane. The spot size at the level of -3 dB is smaller than 0.5 in, or 4 wavelengths (see Fig.5).
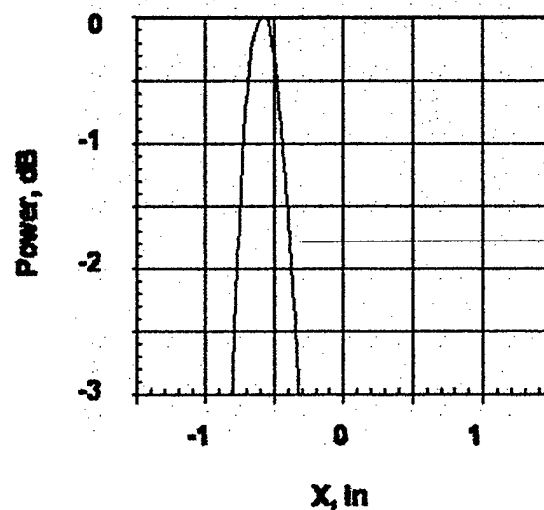
Fig.5.   Focal beam spot in the H-plane is on the order of 4 wavelengths (0.5 in).

The full-scale focal plane beam profile in the H-plane for 10 beams is shown in Fig.6.
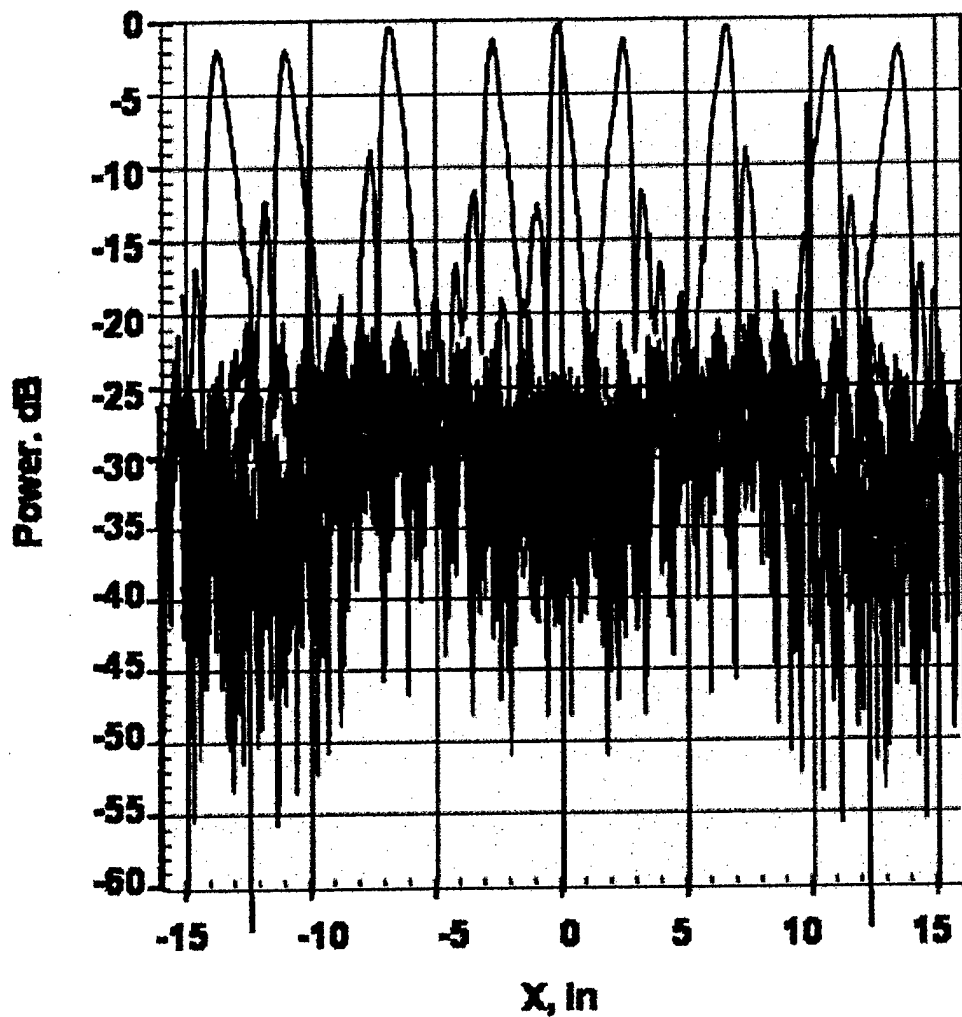
Fig.5. Focal plane beam profile in the H-plane.

In the orthogonal plane (the V-plane), the beam profile is determined by the cylindrical lens. The H-plane focal plane (60 in from the antenna) lies in the far field of this lens, which starts at the distance of 4 in from the antenna. The focal plane beam profile in the V-plane is shown in Fig.6. At the -3 dB level it is ~ 4 in high.
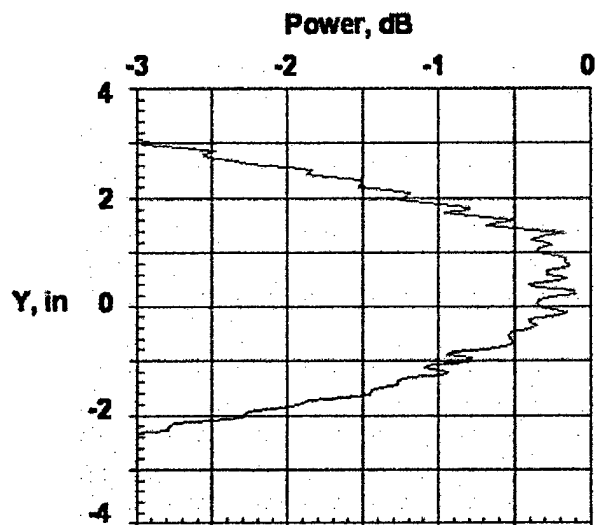
Fig. 6. Focal plane beam profile in the V-plane.

Using the hologram technique, we have also reconstructed the H-plane beam profile in planes parallel to the focal plane. The results are shown in Fig.7.
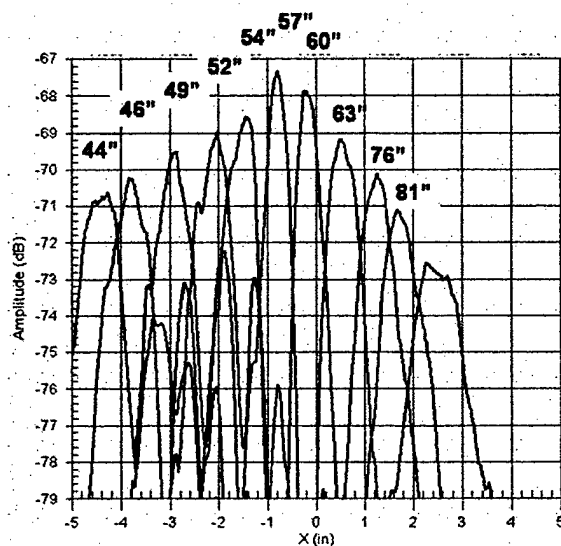
Fig.7. H-plane beam profiles for a single beam at different planes parallel to the focal plane. Numbers indicate distance between the antenna and the profile plane.

The data shown suggest that the actual focus is located at a distance of 57 in from the antenna, which is a little closer than the designed focal distance, 60 in.

The new antenna is designed for operation as a millimeter-wave sensor in imaging scanners whenever the scanning plane is located at rather short distances from the antenna, which can be the case, for example, in concealed weapon screening systems.

Pages 330-349
A Study on a Transmission Feeding Method for Mobile Handset Using a Circulator
Yuta Takgi, Ryo Yamguchi and Shinji Uebayashi
Paper not included no clearance submitted.

A New Antenna and Rectifier Circuit for Long Range Passive RFID Tag Using 2.45 GHz ISM Band

Hitoshi Kitayoshi   and   Kunio Sawaya
Hatchery Square 7th R&D, Tohoku University
04 Aoba, Aramaki, Aoba-ku, Sendai 980-8579, Japan
kitayoshi@hsq.niche.tohoku.ac.jp

Abstract: **This paper presents a novel long range passive RFID tag with 10 m reading distance under ISO/IEC 18000-4 specification. The base-station transmit average power is 1 W, operating in the 2.45 GHz ISM band with an antenna gain is 6 dBi. The proposed RFID tag size is a 70x25x4 mm. We developed a divided microstrip antenna and a voltage multiplying rectifier circuit for passive RFID tag. The divided microstrip antenna can handle a receiving power port and a transponding modulation port separately by 3-terminal structure. When comparing the receiving signal level of transponding from RFID tag, the proposed antenna is 10 dB efficient to conventional dipole antenna. And the proposed voltage multiplying rectifier circuit is configuration of short stub tank circuit and modified Cockcroft-Walton circuit. The proposed rectifier is able to convert from 0.07 Vrms 2.45 GHz CW to more than 1 V DC and the power conversion efficiency is about 40%.**

1. Introduction

Recently, popularity of the RFID system as identification and tracking technology has been growing rapidly. The RFID system is composed of the base station (reader) and the transponder (tag). Since the RFID tag is required to be compact, low price and long life without any the maintenance, passive RFID tag without battery used at 2.45 GHz ISM band is most suitable. However, the distance between the reader and the tag is limited because the field strength of the responding signal from the tag is proportional to the inverse of the square of the distance and becomes weak as the distance increases. Therefore, it is important to develop an RFID tag applicable for a long reading range.

In this paper, a novel passive RFID tag for a more than 10 m reading range is proposed, where the transmitted RF power of the reader is 4 W EIRP at the operating frequency of the 2.45 GHz ISM band. The proposed tag is composed of a divided microstrip antenna and a passive voltage multiplying circuit, and the size is about $0.6\lambda \times 0.2\lambda \times 0.03\lambda$ where λ is the wavelength. The received level at the reader for the case of the proposed tag is about 10 dB greater than that for the case of the dipole antenna of the conventional tag [1]. Since antenna is a microstrip type antenna having a ground plane, it can be used in the vicinity of a metal structure. The proposed rectifying circuit is composed of a tank circuit of a $\lambda/4$ short stub and modified 3-stage Cockcroft-Walton [2] circuit and can convert from -10 dBm(Z_O=50 Ω) RF input of 2.45 GHz CW to more than 1 V DC voltages at R_L=33 kΩ which corresponds to the RF/DC power conversion efficiency of about 40%.

2. Geometry of tag antenna

Fig.1 shows the structure of the conventional passive RFID tag [1]. Variable impedance Z_v for the modulation of the transponding signal is connected to the feeding terminal A-B of the tag antenna. A rectifying circuit for receiving the power is also connected in parallel to the terminal A-B. Fig. 2 shows the structure of the proposed passive RFID tag. The tag antenna is a divided microstrip antenna. PIN diodes as the variable impedance element for the modulation and a rectifying circuit are connected to the terminals A-B and B-C, respectively.
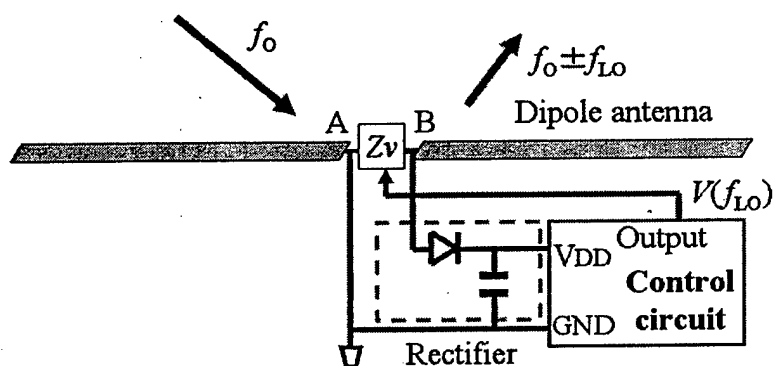
Fig.1 Structure of conventional passive RFID tag.
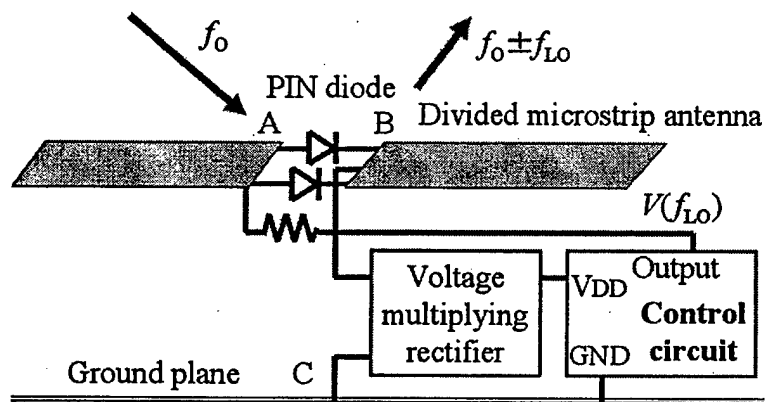
Fig.2 Structure of proposed passive RFID tag.

Fig. 3 shows the schematic diagram for evaluating the received signal level from the tag at the reader. The received signal level at the frequency of $f_0 + f_{LO}$ are calculated by using the method of moments (MoM), where f_0 is the RF frequency and f_{LO} is the local frequency of the modulation of the RFID tag. The modulation is performed by the PIN diode in the tag. Fig. 4 shows the received signal power normalized by the transmitted power of the reader antenna as a function of the length of the tag antenna L for the cases of the conventional RFID tag having planer dipole antenna without ground plane and the proposed tag with divided microstrip antenna. The actual gain of the reader antenna is assumed to be 6 dBi according to the ISO/IEC 18000-4 specification. The series resistance and the junction capacitance of the PIN diodes are supposed to be $R_s = 1\ \Omega$ and $C_0 = 2$ pF, respectively and the distance between the tag and the reader antennas is $z = 83\ \lambda$ (10 m). It is noted that the received power level of the proposed tag is about 10 dB higher than that of the conventional tag by selecting an appropriate antenna length.
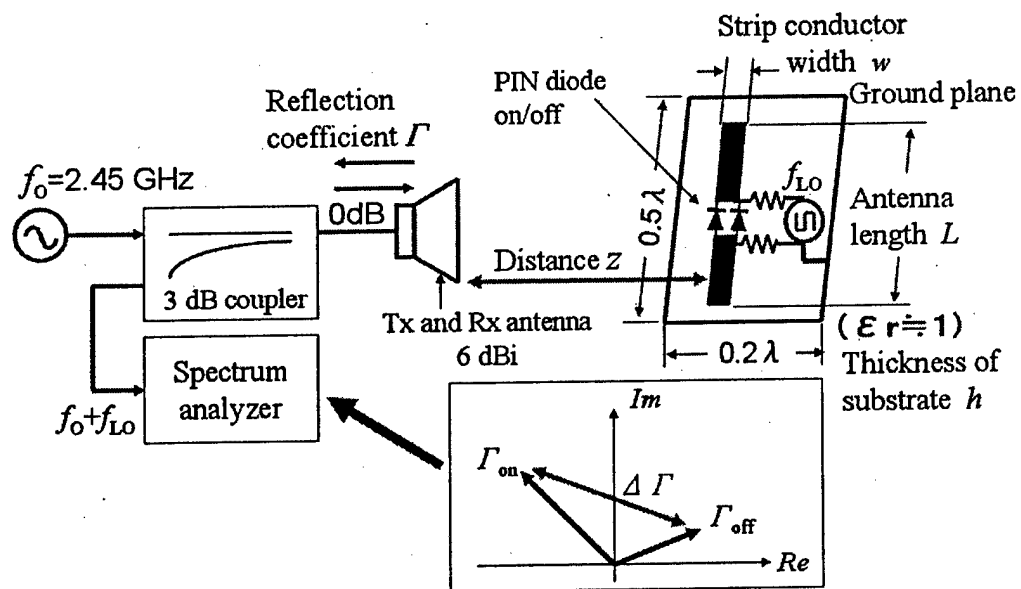
Fig.3   Schematic diagram for evaluating received signal level at reader.
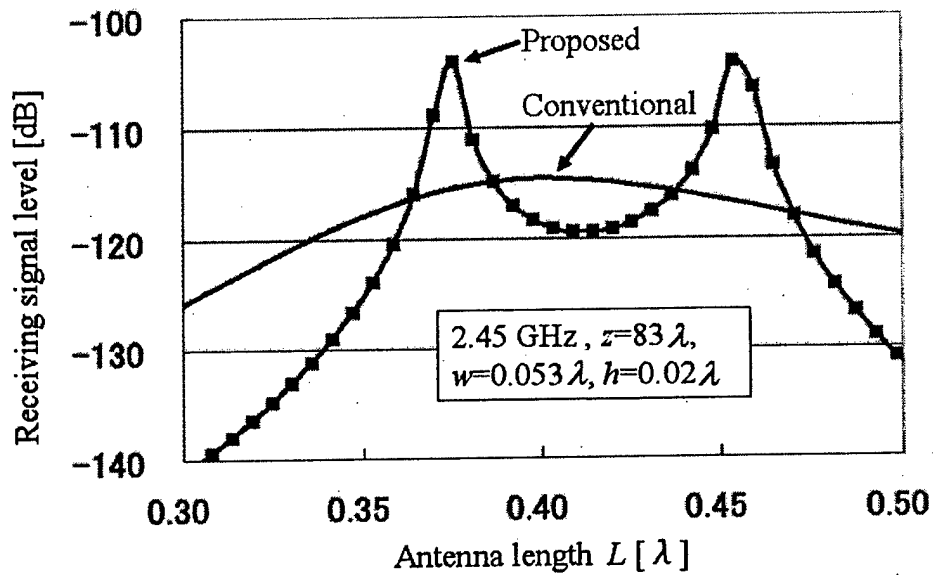
Fig.4   Received signal level of reader antenna as a function of length
        of the tag antenna L.

Fig. 5 shows the received signal level of reader antenna as a function of the normalized frequency for the cases of the proposed RFID tag versus thickness h and strip conductor width w. The series resistance and the junction capacitance of the PIN diodes are supposed to be R_s=0 to 6 Ω and C_0=1 pF, respectively and the distance between the tag and the reader antennas is z=83λ. It is noted that the received power level of the proposed tag is strongly dependence of the series resistance value of the PIN diodes in case of small size tag which is a low resonance frequency type.
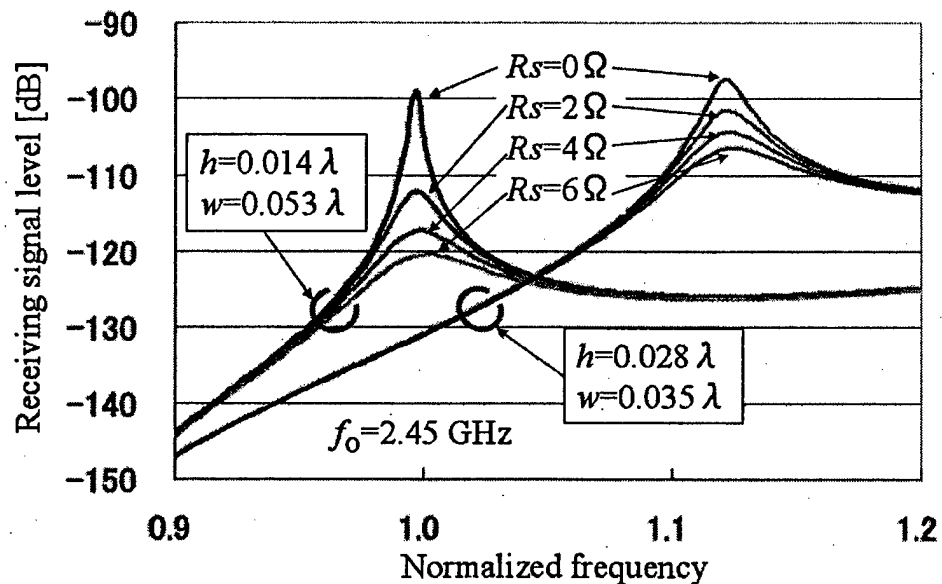
Fig.5 Received signal level of reader antenna versus thickness h and strip conductor width w in case of proposed RFID tag (z=83λ, L=0.364λ, Co=1 pF).

Fig. 6 shows the received signal level of the proposed tag with varying the values of the series resistance R_s and the junction capacitance C_0 of the PIN diodes. The value of the junction capacitance does not affect the received signal level significantly, while the value of the series resistance strongly changes the received level, and a small series resistance is desirable to increase the distance between the reader and the tag.
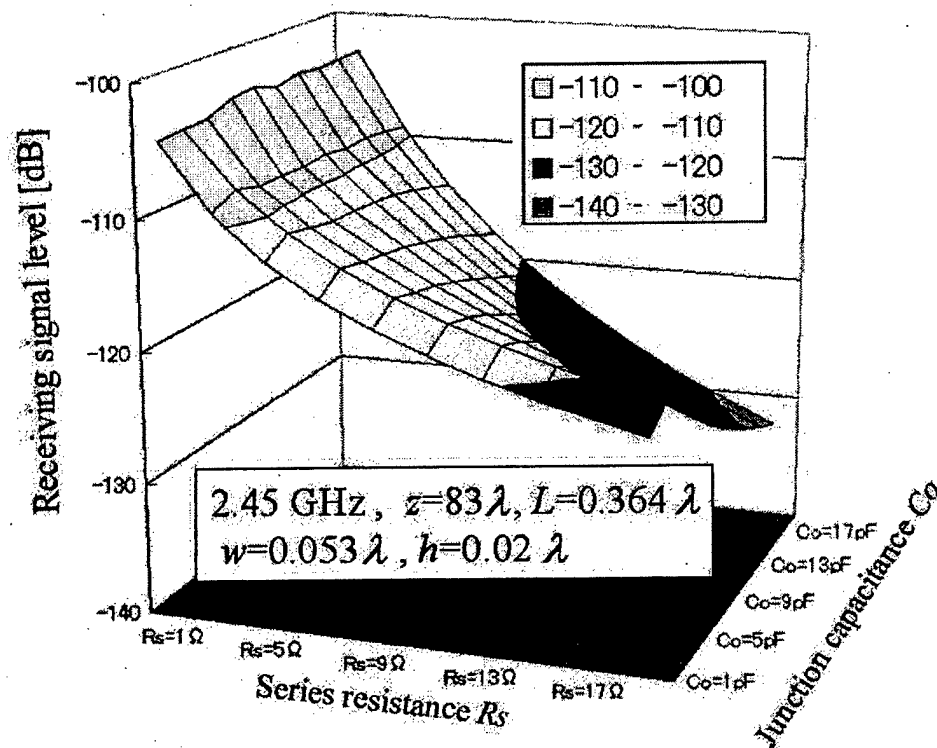
Fig.6   Received signal level of reader antenna versus series resistance and junction capacitance of PIN diode in case of proposed RFID tag.

Fig. 7 shows the received signal level of the conventional RFID tag having planer dipole antenna without ground plane with varying the values of junction capacitance C_0 and the series resistance R_s of the PIN diodes. In this case the value of the series resistance R_s does not affect the received signal level significantly, while the value of the junction capacitance C_0 strongly changes the received level, and a small junction capacitance is desirable to increase the distance between the reader and the tag.
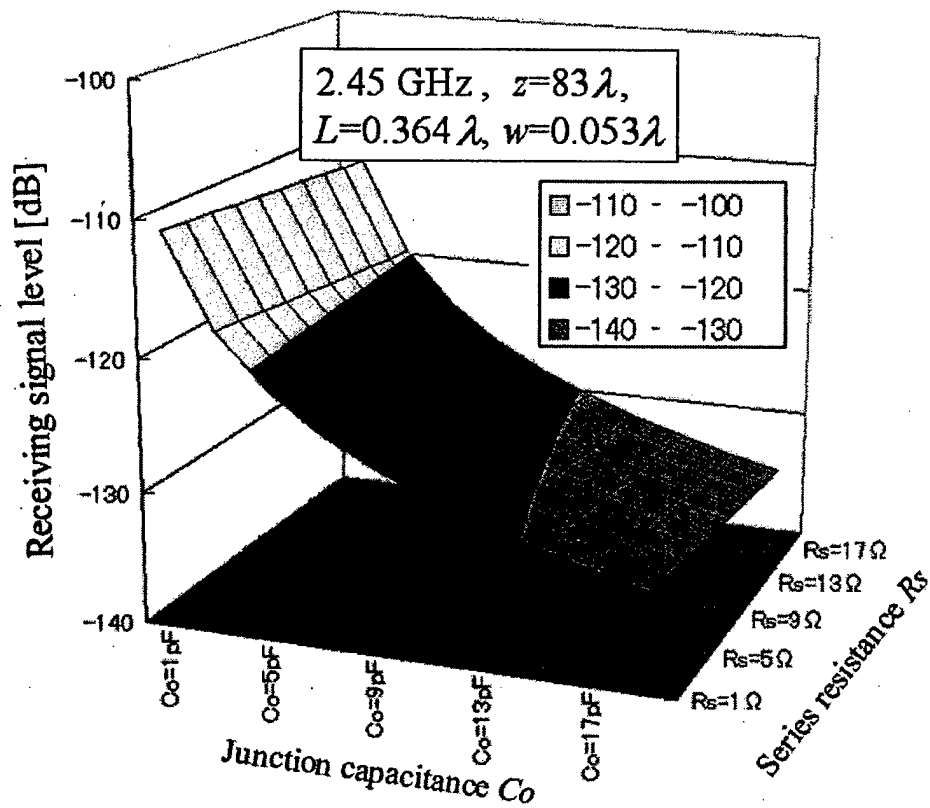
Fig. 7 Received signal level of reader antenna versus series resistance and junction capacitance of PIN diode in case of conventional RFID tag.

3. Rectifying circuit

For the case of the rectifying circuit of the conventional tag shown in Fig. 1, a high impedance of the tag antenna is desirable to obtain the high DC voltage. However, required power to generate 1 V for the control circuit is more than 0 dBm even when a high impedance antenna such as the folded dipole antenna is used, because a simple diode rectifying circuit is used.

The received power of the microstrip antenna of the proposed tag is estimated to be about -10 dBm at the distance of z=4 m assuming that the transmitted average power is 1 W and the gain of the reader antenna is 6 dBi. This power is enough to operate the control circuit of the RFID tag. However, the estimated value of the received DC voltage is as low as 0.1 V assuming 50 Ω load, which is too small to operate the control circuit. Therefore, a rectifying circuit boosting DC voltage more than 10 times and working at 2.45 GHz band is required to obtain the DC voltage higher than 1 V with 30 μW power consumption.

Fig. 8 shows the proposed rectifying circuit composed of a tank circuit of a 3 λ/4 short stub and modified 3-stage Cockcroft-Walton circuit. The first diode of the original Cockcroft-Walton circuit [2] is removed. The uniform values of the capacities in the original Cockcroft-Walton circuit are also changed as lower capacitance of the input side capacities. The rectifying diode used in this study is HSMS-286 (C_0=0.25 pF). DC output of the proposed rectifying circuit is numerically analyzed by using the SPICE transient simulator. Fig. 9 shows the frequency response of the proposed rectifying circuit when the input RF power is -10 dBm and load resistance is R_L=33 kΩ. DC voltage of about 1.15 V is obtained which is considered to be enough to operate the control circuit. The conversion efficiency of the proposed rectifying circuit is about 40%, which is much greater than the conventional Cockcroft-Walton circuit.
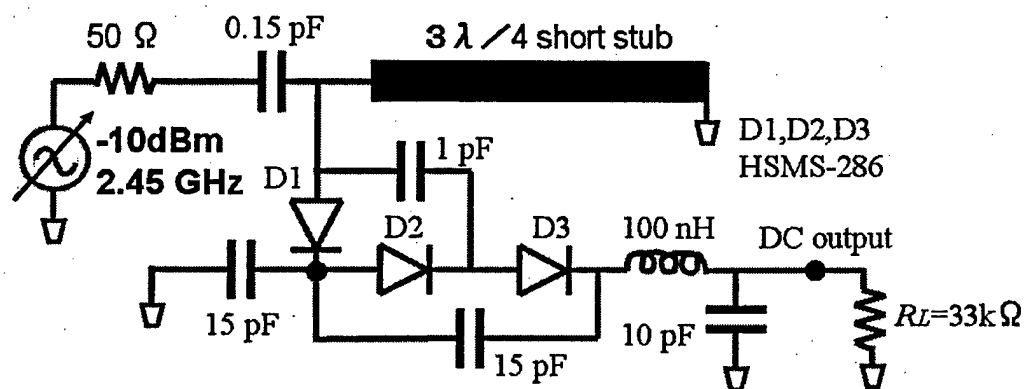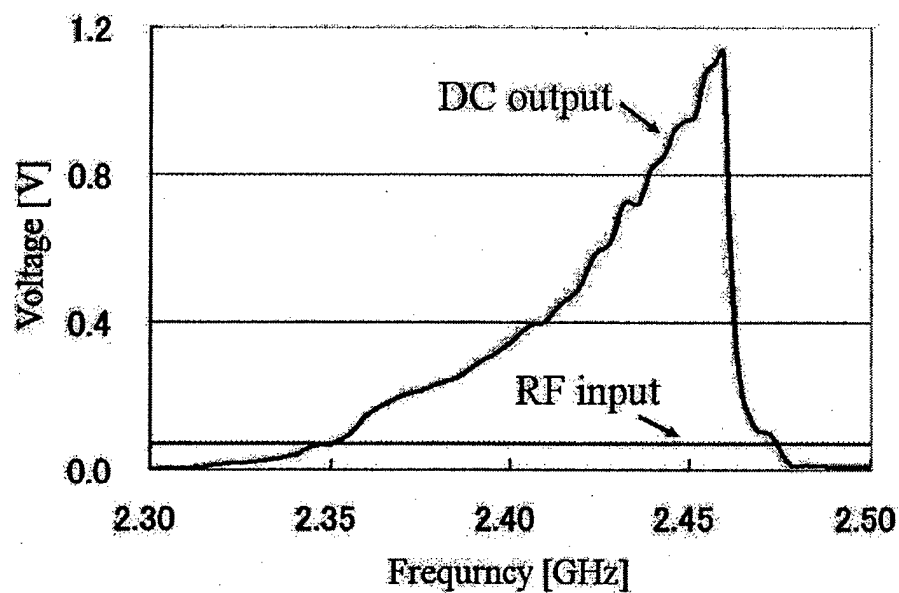
Fig.8 Proposed rectifying circuit.

Fig.9 Frequency response of proposed rectifying circuit.

358

4. System design

Traditionally, passive RFID tags operate at 915 MHz or 2.45 GHz using dipole antennas, and their reading distance is typically limited to less than 10 m or 4 m, respectively, e.g., 9.25 m with a conventional Cockcroft-Walton circuit operate at 915 MHz [3], and 3.3 m with SAW temperature sensor operate at 2.45 GHz [4]. In this section, propose a system for the multipoint temperature indication by using passive RFID tags under operating ISO/IEC 18000-4 specification.

The configuration block diagram of multipoint temperature indication system to propose to Fig. 10 is shown. The purpose of this system is monitor of the equipments for high-voltage power transmission and distribution. The reader transmit average power is 1 W, operating in frequency hopping spread spectrum (FHSS) method used at 2.400-2.427 GHz with an antenna gain is 6 dBi. And the transmit spread spectrum generated by FH-CW and pulse modulation is effect to increase the crest factor of the receiving RF signal at the RFID tag. The received power of the microstrip antenna of the proposed tag is estimated to be about -18.5 dBm at the distance of z=10 m assuming that the reader transmitted power is 4 W EIRP. Therefore, the problem of the RFID tag is the reduction of the power consumption and the operating voltage.

The RFID tag had a temperature sensitive X'tal oscillator circuit for generate f_{LO}, and the operation temperature range is from -40$°C$ to +85$°C$ and the measurement accuracy is $\pm 0.3°C$, and the transponding signal to the reader with temperature information f_{LO} is modulated with the ID code. The receiving signal level at the reader from the RFID tag is about -100 dBm. The receiver circuit of the reader composed of a narrow band filter for the high accuracy of frequency measurement. The reader has a data base and the temperature is changed from the analyzed FFT frequency spectrum of transponding signal of the RFID tag by it, and the ID code is demodulated from the spectrum. The reader indicates are ID codes and temperatures of RFID tags.
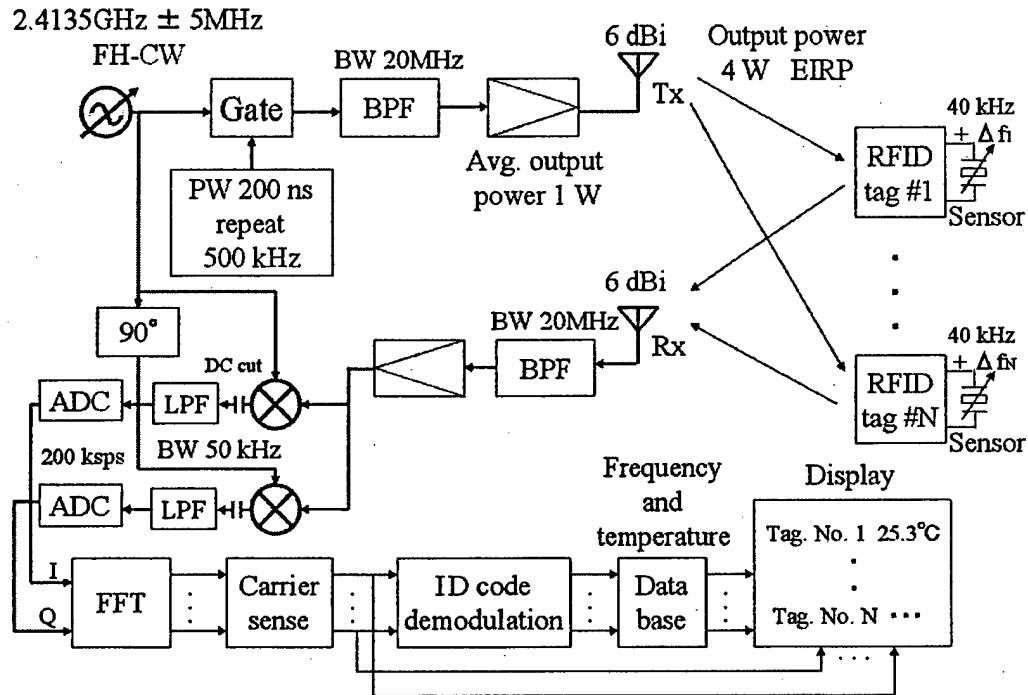
Fig. 10 Configuration block diagram of multipoint temperature indication system.

5. Experimental results

The circuit diagram of temperature sensing passive RFID tag for the proposed multipoint temperature indication system is shown in Fig. 11. With this circuit, proposed divided microstrip antenna is used for the RF power reception and transponding operation. However, it used varactor diodes as the variable impedance element Z_v for the modulation with low consumption power than PIN diodes. And the RFID tag used X'tal sensor oscillation circuit by an advanced ultra-low-voltage CMOS gate IC for the transponding modulation control of it.

Fig. 12 is consumption current characteristics at the transponding modulation control circuit of proposed temperature sensing passive RFID tag. In this figure, the voltage and the current which the transponding modulation control circuit begins in the oscillation about are 0.4 V and 1 µA, respectively.

Divided microstrip antenna
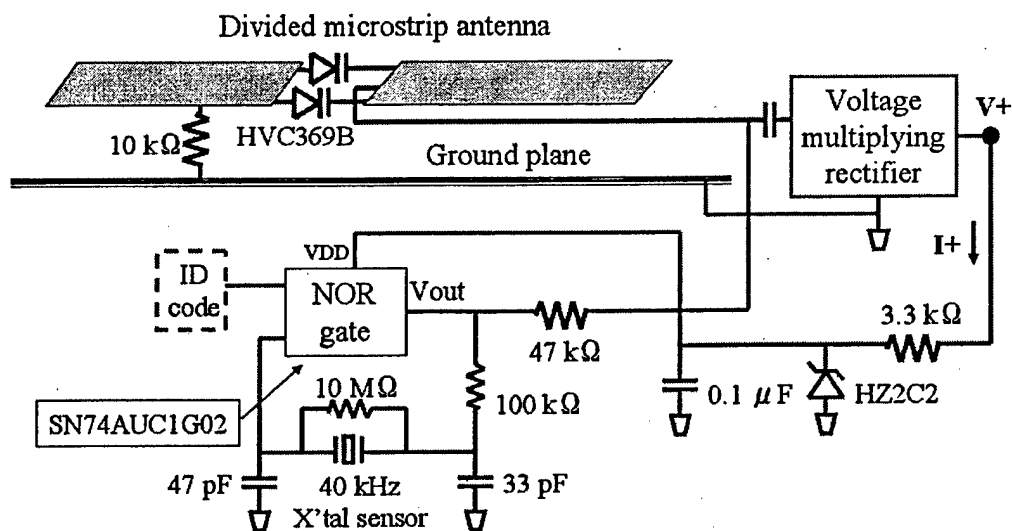
Fig. 11 Circuit diagram of temperature sensing passive RFID tag.
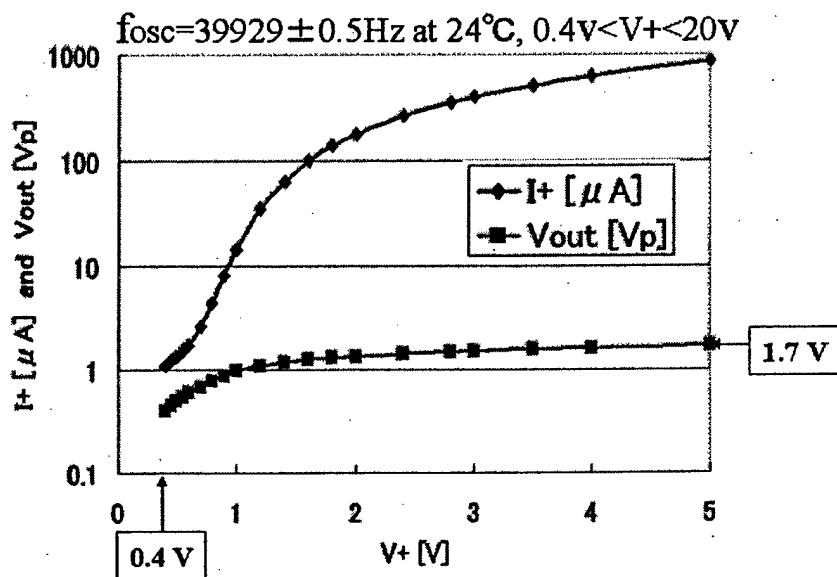
Fig. 12 Current consumption characteristics of RFID tag.

The circuit diagram of voltage multiplying rectifier for the proposed temperature sensing passive RFID tag is shown in Fig. 13. This rectifying circuit modified the circuit which was shown with Fig. 8 because it matched to the FHSS method.

Fig. 14 is V+ DC output frequency response of the experiment with the transponding modulation control circuit load in Fig. 13. In this experiment, the input RF power and the output DC voltage are -20 dBm and 0.56 V, respectively and the V+ DC output is exceeds the minimum operation voltage of the transponding modulation control circuit. But, the RF/DC power conversion efficiency is about 10 %. The cause of this efficiency decline lowered the Q value of the rectifying circuit because it matched to the FHSS method.

Fig. 15 shows the input reflection coefficient S11 frequency responses of the divided microstrip antenna loaded varactor diodes versus impressed DC bias voltage Vout. Proposed divided microstrip antenna can change a resonance frequency by the small impressed DC bias voltage, which can be understood by seeing this figure. Also, the phase change of the S11 influences a transponding signal level.

Fig. 16 is the photograph of passive RFID tag to have used for the experiment.
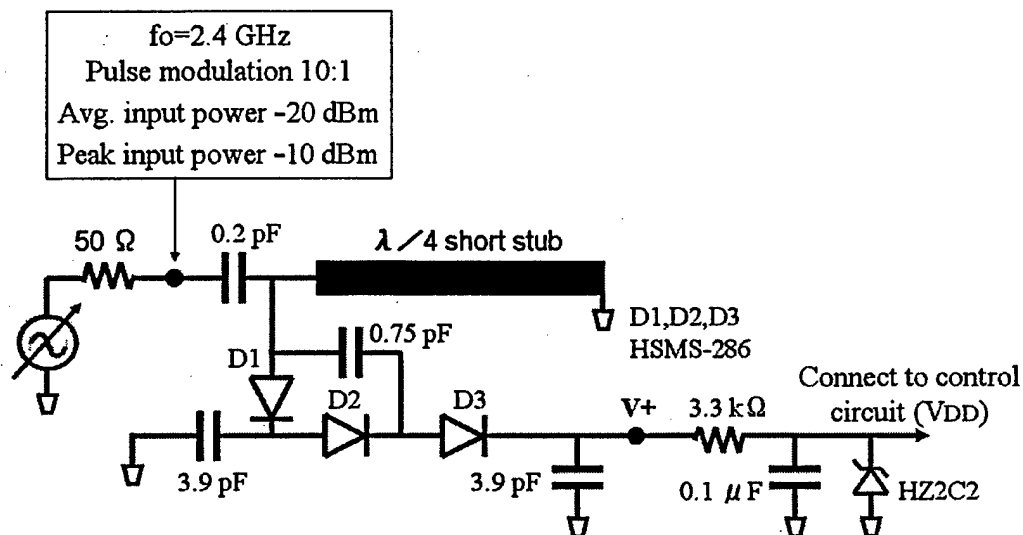
Fig. 13 Circuit diagram of voltage multiplying rectifier.
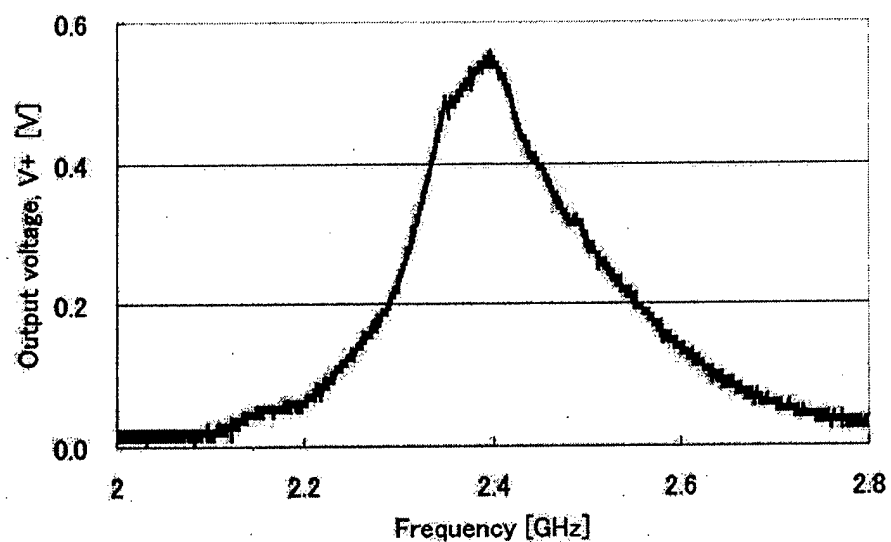
Fig. 14 Experimental result of V+ frequency response in case of control circuit loaded.
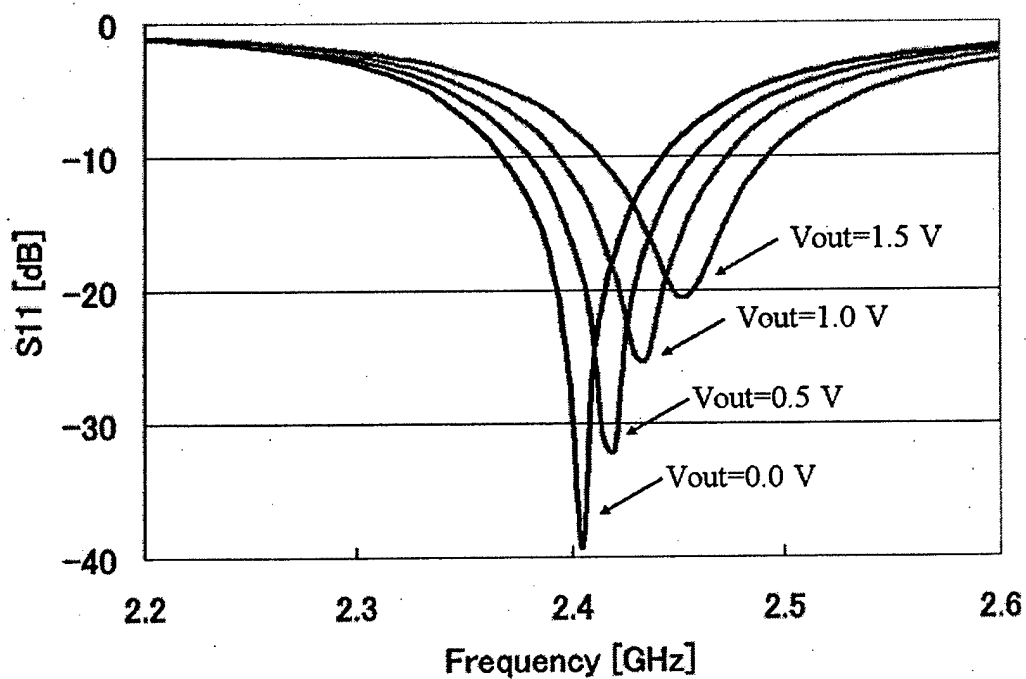
Fig. 15 Frequency response of divided microstrip antenna.
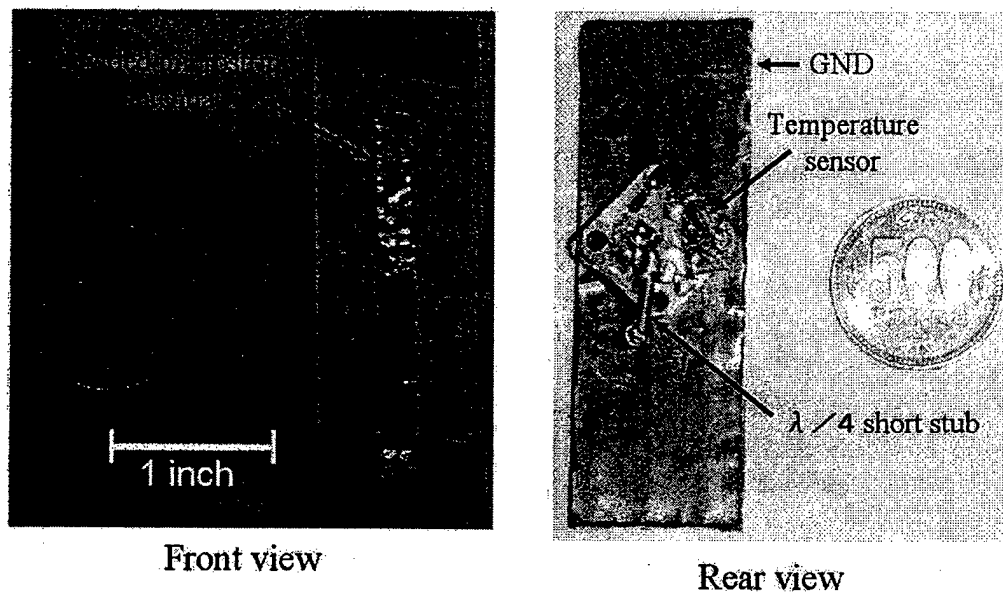
Front view   Rear view

Fig. 16 Photograph of temperature sensing passive RFID tag.

Fig. 17 shows the block diagram of experimental setup for multipoint temperature measurement by using proposed passive RFID tags. In this experiment, the reader transmit power is 1 W EIRP and used a pulse modulation RF signal generator and a RF power amplifier and a 10 dBi double-ridged guide antenna, respectively for the airing. And the receiver is composed of a RF spectrum analyzer and a 10 dBi double-ridged guide antenna.

The photograph of the situation of the experiment is shown in Fig. 18 and 19. In this experiment, the distance from the reader to the RFID tag No. 1 and No. 2 is 3 m and 3.5 m, respectively and the observed frequency spectrum is shown in Fig. 20. The frequency spectrum observed three times, i.e. the 1st is the condition of Tag #1=27°C and Tag #2=27°C, and the 2nd is the condition of Tag #1=44°C and Tag #2=27°C, and the 3rd is the condition of Tag #1=44°C and Tag #2=53°C. The temperature of each of the two tags can be evaluated as the frequency of the observation spectrum, which can be understood by seeing Fig.20. By the way, the accuracy of the oscillation frequency of the temperature sensor can be evaluated is better than ±0.1 Hz, because the RF signal generator and the RF spectrum analyzer of the reader are phase locking by using 10 MHz reference frequency.
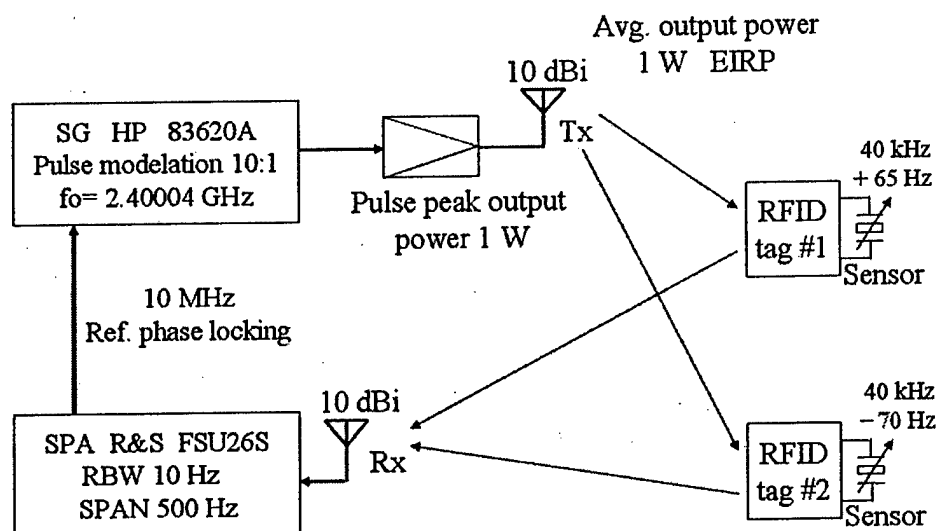
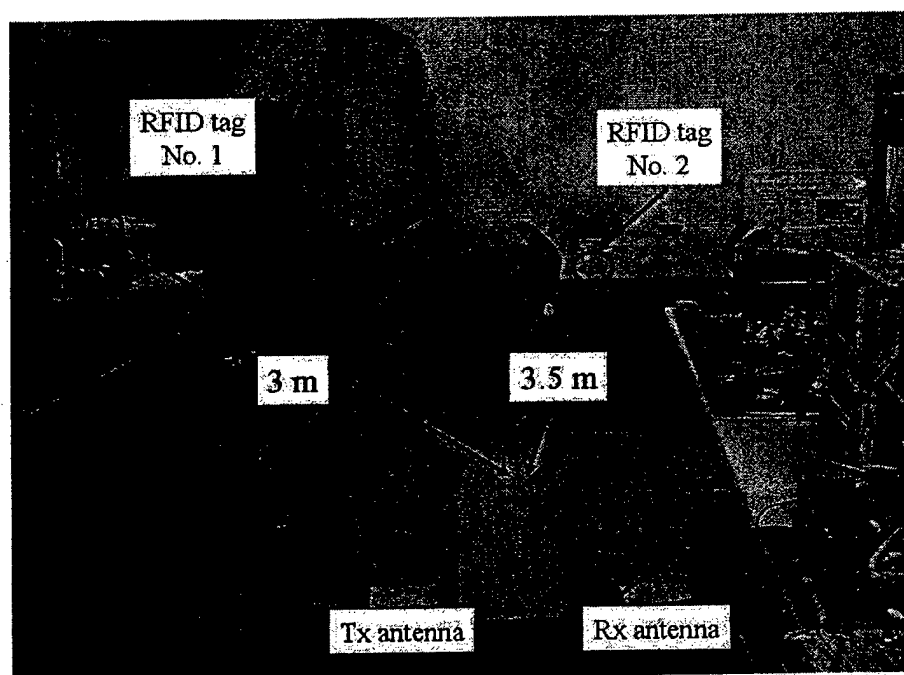Fig. 17 Block diagram of experimental setup.

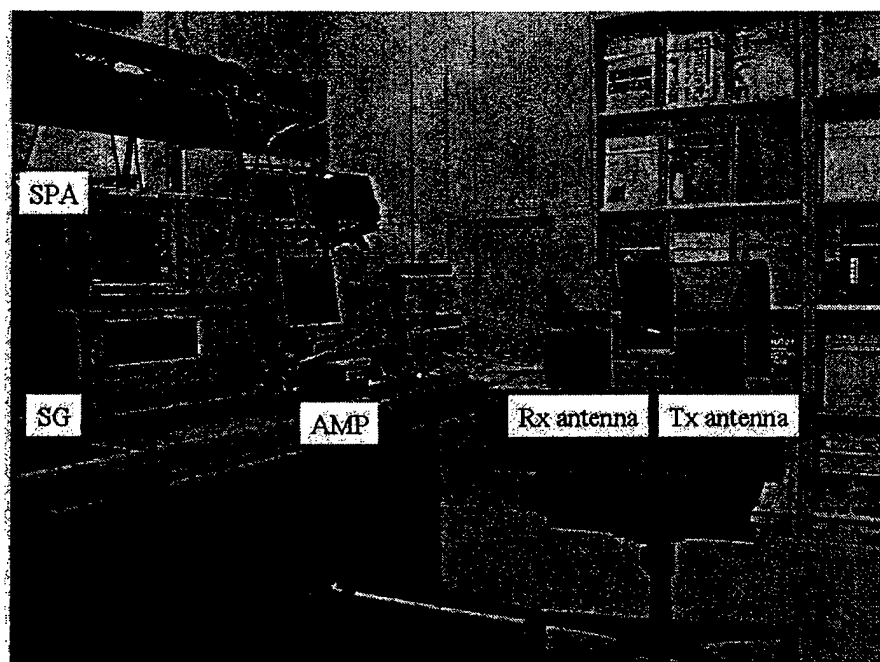Fig. 18 Photograph of experimental setup of RFID tags.

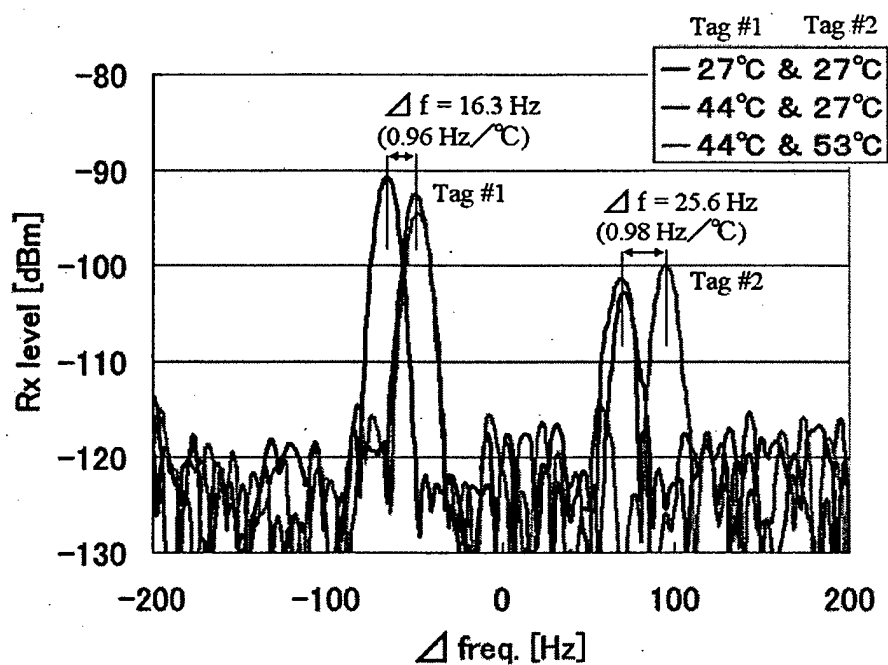Fig. 19 Photograph of experimental setup of base-station.

Fig. 20 Received signal frequency spectrum from RFID tags at reader.

366

6. Conclusion

A novel passive RFID tag for a long reading range composed of a divided microstrip antenna and a rectifying circuit boosting the DC voltage has been proposed. It has been shown that the received level at the reader for the case of the proposed tag is about 10 dB greater than that for the case of the dipole antenna of the conventional tag. Since antenna is a microstrip type antenna having a ground plane, it can be used in the vicinity of a metal structure. The proposed rectifying circuit is composed of a tank circuit of a $\lambda/4$ short stub and modified 3-stage Cockcroft-Walton circuit and can convert from 0.07 Vrms RF voltages of 2.45 GHz to more than 1 V DC voltages which corresponds to the efficiency of about 40%. Also, long range passive RFID tag with 10 m reading distance under ISO/IEC 18000-4 specification showed to be possible because the proposed RFID tag worked at the reception 2.45 GHz band RF power of -20 dBm by the experimental result. Moreover, experimental results were shown of the multipoint temperature measurement system by using proposed long range passive RFID tags.

References

[1] Raj Bridgelall, "Bluetooth/802.11 Protocol Adaptation for RFID Tags", Proceedings of European Wireless 2002, Feb. 2002.

[2] "Cockcoft-Walton Voltage Multipliers", e.g;
http://www.wenzel.com/pdffiles/voltmult.pdf and
http://deutsche.nature.com/physics/16.pdf

[3] Udo Karthaus and Martin Fischer, "Fully Integrated Passive UHF RFID Transponder IC With 16.7-μW Minimum RF Input Power", IEEE Journal of Solid-State Circuits, vol. 38, no. 10, pp.1602-1608, Oct. 2003.

[4] G. Scholl, C. Korden, E. Riha, C.C.W. Ruppel, U. Wolff, G. Riha, L. Reindl, R. Wwigel, "SAW-Based Radio Sensor Systems", IEEE Microwave Magazine, vol. 4, no. 4, pp. 68-76, Dec. 2003.

HIGH EFFICIENT WIDEBAND DIRECTIONAL PANEL ANTENNA

O.Sulima
AVS Microwaves
10 Crown Hill Place, Toronto, ON, CANADA
avs@sympatico.ca

1. ABSTRACT

A new type of a cavity-backed slot antenna is presented and discussed. The new antenna is extremely efficient and has a wide bandwidth of operation. It can be used as a directional panel antenna with low side-lobe level and high front to back ratio.

2. INTRODUCTION

Over the past few years, there has been a rapidly growing interest in high efficient antennas with enhanced electrical characteristics in the communication industry, especially for high-speed, high capacity service delivery. The conventional directional panel antenna design, based on a microstrip patch or a printed dipole antenna, does not allow to design a high efficient antenna operating in a specified waveband with desired electrical characteristics, especially with low return loss, low side-lobe level and high front-to-back ratio.

In this paper the results of a theoretical modeling and experimental study of a novel high efficient directional panel antenna are presented and discussed. The elementary radiating element of the proposed antenna array is a cavity-backed slot operating on its lowest H_{00} mode. Experimental studies of the antenna indicate that the antenna is well balanced and has a very low return loss in a wide frequency range.

The proposed antenna has a low side lobe level and a high front to back ratio. The radiated field of the antenna is linearly polarized with a low cross polarization level, which is illustrated by a series of experimental data and results of numerical modeling.

3. THEORETICAL MODEL

The theoretical model of a cavity-backed radiating slot is based on a rigorous solution of a corresponding 2D scattering problem and a transmission line model of a radiating element.

Consider a 2D geometric figure, as shown in Fig.1.The cavity-backed slot is excited by a line magnetic current placed at the point P in the upper half-space. The problem can be formulated as a singular integral equation [1] for an unknown electric field on the slot

$$\int_{-c}^{+c} E(x)\{G_1(x,x') + G_2(x,x')\}dx = -2\psi(x'),$$
(1)

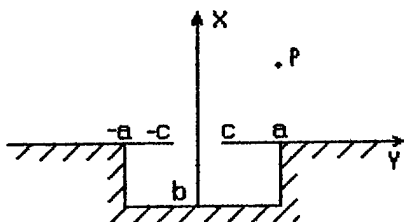where $E(x)$ is the unknown tangential component of the electric field on the slot, G_1 and G_2

Fig.1 Cavity-Backed slot.

are Green functions of the upper half-space and the cavity respectively:

$$G_1(x',x) = -\frac{k}{2w} H_0^{(2)}(k|x'-x|),$$
(2)

$$G_2(x',x) = -i\frac{k}{2w}\sum_{n=0}^{\infty}\frac{\delta_n}{\gamma_n 2a}\coth(\gamma_n b)\cos(\frac{n\pi}{2a}(x-d))\cos(\frac{n\pi}{2a}(x'-d)),$$
(3)

where $w = \sqrt{\frac{\mu}{\varepsilon}}$ is the free space impedance, $\gamma_n = \sqrt{\left(\frac{n\pi}{2a}\right)^2 - k^2}$, $\delta_0 = 1$, $\delta_n = 2$.

Taking into account the fact that G_1 and G_2 possess logarithmic singularity, the kernel of the equation (1) can be expressed in the form

$$G_1 + G_2 = i\frac{2k}{\pi w}\ln(\eta|x'-x|) + K(x',x),$$
(4)

where η is a constant defined by the geometrical parameters of the cavity, the slot width and the frequency of incident field, while $K(x',x)$ is a continuous function of

two independent variables. The fact that $G_2(x,x')$ can be given in the form of (4) stems from the asymptotic behavior of coefficients of (3), and the formula [2]:

$$\sum_{k=1}^{\infty} \frac{\cos(kt)}{k} = -\log\left|2\sin\frac{t}{2}\right|, \quad t \in [-2\pi, 2\pi]. \tag{5}$$

We seek the unknown function $E(x)$ in the form of:

$$E_x(x) = \frac{\displaystyle\sum_{k=0}^{\infty} x_k T_k\left(\frac{x}{c}\right)}{\sqrt{1 - \left(\frac{x}{c}\right)^2}} \tag{6}$$

where $T_k(x)$ are the Tchebyshev polynomials. Presentation of the unknown field in the form (6), together with a weight function to account for the singular behavior of $E_x(x)$ at edges of the aperture, and consideration of the orthogonal properties of the Tchebyshev polynomials on the interval $[-c,c]$, allows the transformation of (1) into a system of linear equations

$$x_m + \sum_{n=0}^{\infty} x_n a_{n,m} = b_m \tag{7}$$

here $a_{n,m}$ and b_m are the Tchebyshev coefficients of the K(x,y) and the incident field, respectively . It is possible to show [3] that the following estimates for the coefficients $a_{n,m}$ are valid:

$$|a_{n,m}| \le \frac{\eta^6 \, const}{(m^2 - 1)(n^2 - 1)} \tag{8}$$

$$\sum_{n=1}^{\infty} |a_{n,m}| \le \infty, \quad m = 1,2. \quad N, \tag{9}$$

here N is the order of the truncation of (7). In the assumption of a narrow slot, the solution of (7) can be given as

$$x_0 = i \frac{2w}{kc} \frac{J_0(kc\sin(\varphi))}{i\frac{\pi}{2} + \pi\frac{\cot(kb)}{2ka} + \ln(\frac{\gamma\pi(kc)^2}{8ka}\sin(\frac{\pi d}{2a})) - 2\pi\sum_{n=1}^{\infty}\left(\frac{\coth(\gamma_n b)}{\gamma_n 2a} - \frac{1}{n\pi}\right)\cos^2(\frac{n\pi d}{2a})J_0^2(\frac{n\pi c}{2a})} \tag{10}$$

$J_0(x)$ - is the Bessel function of the zero order, γ =1.7810 - Euler constant. It is necessary to note that coefficients in the infinite series in the denominator decay as $O(n^{-5/2})$ as $n \to \infty$. It is assumed that all other coefficients x_i for $i > 0$ are negligible small.

Numerical studies showed that the narrow slot approximation and exact solution agree well if the slot width is less then one tenth of a wavelength. The narrow slot solution does not depend upon cavity size or slot position. The only factor which can effect the accuracy of calculation of cutoff frequencies is a truncation order in the series in (10), but as it was already indicated above, the series terms decay fast enough to ensure numerical stability of the summation process.

Expression (10) readily provides information about resonant characteristics of a cavity-backed slot, including the lowest H_{00} -mode and all cavity modes. The denominator in (10) also contains a term responsible for a quarter wave resonance in a groove.

4. TRANSMISSION LINE MODEL

At the next step the cavity-backed slot antenna is presented as a short-circuited cavity-backed slot line with the line impedance Z_0 as shown in Fig.2.
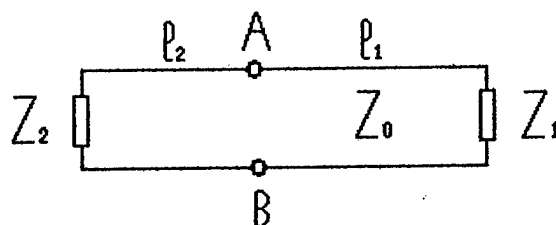

Fig.2 Transmission line model of the Cavity-Backed Slot Antenna.

Here AB defines points of excitation of the antenna. Te slot length l is equal to the sum of the right and left antenna shoulders. As the slot is shunted at its ends, it is natural to assume that $Z_1=Z_2=0$, in this case the input impedance at AB can be defined as

$$Z_{inp} = Z_0 \frac{\tanh(hl_1)\tanh(hl_2)}{\tanh(hl_1)+\tanh(hl_2)}. \tag{11}$$

Formula (11) accounts for cavity and slot parameters: cavity width and depth, slot width and length and allows to calculate input impedance of the antenna for any combination of their values as a function of frequency. The propagation constant of

371

the line $h = h' + jh''$ is a complex function where h'' represents radiation losses of a leaky cavity-backed slot wave. Typical characteristics of input impedance at points AB defined by (11) is given on Fig.3.

Input impedance of the cavity-backed slot antenna tends to infinity in the neighborhood of a cut-off frequency of the cavity-backed slot wave $f \sim 2.65$GHz. At the second resonance at 5.8 GHz the input impedance is equal to 50 Ohm. Results of numerical modeling of the input impedance of the cavity-backed slot antenna indicate that the second resonance is the most suitable for designing of a wideband antenna. The input impedance at this point can assume values from several to a hundred Ohm, depending on cavity and slot dimensions.
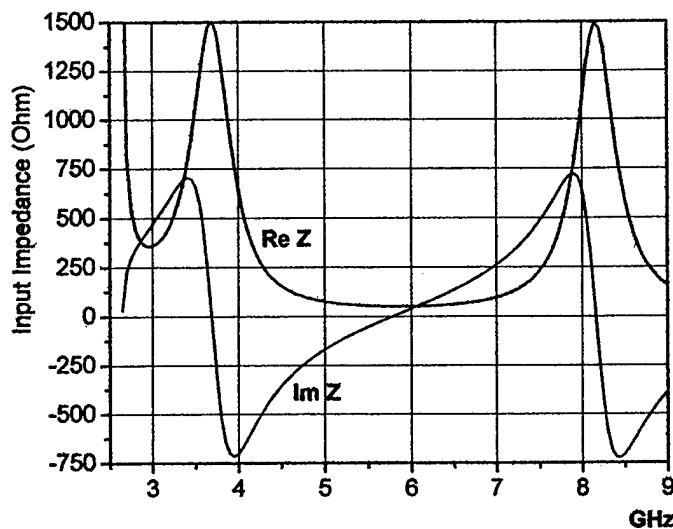
Fig.3 Input impedance of a Cavity-Backed Slot Antenna.

The lowest possible value of the input impedance at the first resonance $f \sim 3.75$ GHz is 200-300 Ohm.

5. EXPERIMENT

Results of numerical modeling of the cavity-backed slot antenna were used in a design of a directional panel antenna for operation at 5.8 GHz.

372
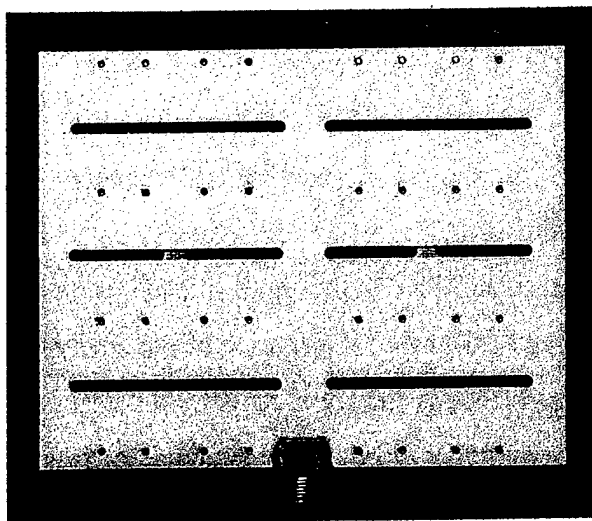
Fig. 4 The front view of the antenna.

The main objective of the design was to achieve a maximum possible efficiency and bandwidth of operation and to decrease the ground plate edges effect on a radiation pattern in the H plane. The photograph of the antenna prototype is shown on Fig.4. The antenna dimensions are 8.5*10.5cm. The ground plane is manufactured from a Teflon copper laminate. A copper foil, forming backing cavities, is electrically connected to the upper copper layer by means of copper rivets. The antenna has an edge mount SMA connector. The antenna has
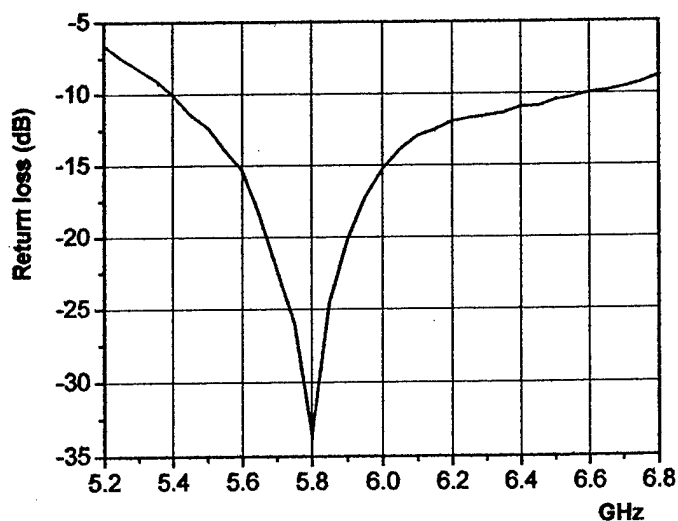
Fig.5 Return loss of the antenna versus frequency.

two active slots excited by microstrip lines and four passive slots. Active slots parameters: width and lengths and backing cavity size are chosen to resonate at 5.8GHz. Results of experimentally measured return loss of the antenna are presented on Fig. 5.
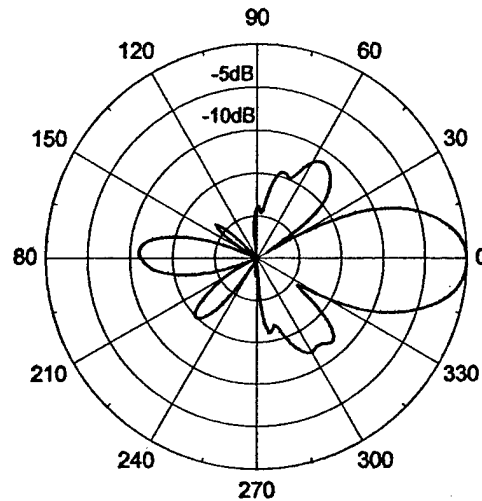
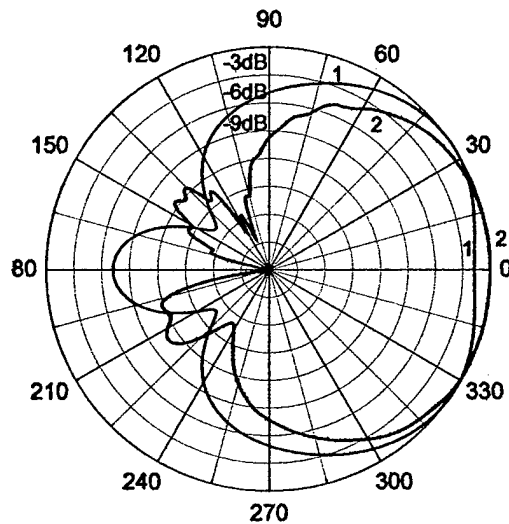Fig. 6 E-plane field pattern at 5.8 GHz.

Fig.7 H-plane field patterns at 5.8 GHz. 1 – single slot, 2- one active and two passive slots.

The –14dB bandwidth of the antenna is equal to 3.5% of the resonant frequency (200 MHz). Experimentally measured field patterns of the antenna in the E and H

planes are given on Fig.6 and Fig.7 (curve 2). On the Fig. 7 it is also shown the field pattern of a single slot (curve 1) on a ground plane of the same size as the antenna. Passive slots significantly reduce the edge effect on a field pattern. The HPBW of the antenna in the H plane is equal to 115^0 and 145^0 without passive slots. Passive slots also significantly reduce radiation in the backward direction. The coupling effect between two neighboring slots can be either enhanced or suppressed by changing resonant frequencies of passive slots, which gives an opportunity to control the amplitude of a magnetic current on the slot and consequently influence the far field pattern. The HPBW of the antenna in the E plane is equal to 30^0 and the antenna gain is 10.7dBi. The idea to use a quarter wave groove near an edge to reduce its effect on a field pattern is well known and often used in antenna design. The main difference between a resonant groove and a cavity-backed slot is the bandwidth of operation. Quarter wave grooves are narrowband, the use of grooves instead of cavity-backed slots in the antenna will result in a significantly narrower bandwidth of operation of the antenna.

6. CONCLUSSION

A new design of a cavity-backed slot antenna is proposed and discussed. Experimental studies showed a good agreement between predicted and experimentally observed antenna characteristics. The proposed antenna is extremely efficient and has a wide bandwidth of operation. Incorporation of passive resonant slots in the antenna design significantly reduces the edge effect and decreases radiation in the backward direction.
The proposed design can be effectively used in a design of a high efficient directional panel antennas and antenna arrays.

7. ACKNOWLEDGMENT

8. REFERENCES

[1] A. Sulima, " Input Impedance and Scattering Cross Section of a Cavity-Backed Slot", IEEE Trans. On Antennas and Propagation in print
[2] I.S. Gradstein, I.M. Ryzik, Table of Integrals, Series and Products, San Diego, CA, Academic,1980
[3] V.M. Aleksandrov, V.A. Kucherov, "Method of Orthogonal Polynomials in Mixed problems of the Theory of Elasticity", Journal of Applied Mathematics and Mechanics (Moskow), v.34, N4, 1970.

Calculation of Mutual Coupling Between Axial Magnetic Dipoles on Circular Cylinders with Applications to Tactical Missile Systems

Deb Chatterjee

Computer Science and Electrical Engineering Division,
University of Missouri Kansas City (UMKC)
Kansas City, MO 64110, USA

Abstract

Conformal phased array antennas, flush-mounted on future generation tactical missiles, have been envisaged to provide high data rate of transmission and in flight retargeting, adding to mission flexibility, in terms of improved battle damage assessment/indication (BDA/BDI) through enhanced target imagery. For such defense communication systems, it is critical that the antenna performance be accurately characterized. The main purpose of this investigation is to seek quantitative information on antenna locations, flush-mounted on the curved part of the missile structure, and, their subsequent influence on the antenna radiation behavior. The mutual coupling is a function of antenna location pairs on a convex structure, and manifests itself in terms of active element gain pattern of the antenna. In this paper the mutual coupling between a pair of short, axial, narrow slots is represented by the surface magnetic field and on canonical topologies that are structurally close to that of Raytheon MIM 104 (Patriot) missiles, for frequencies around 10 GHz. For this typical missile geometry, since its fuselage can be modeled by a circular cylinder, a host of high-frequency (asymptotic) solutions to the canonical problem are readilly applicable to model mutual coupling. At high-frequencies, the phenomenon of mutual coupling is electromagnetically modeled by *creeping wave* propagation over the curved, convex part of the missile structure. In this paper, the mutual coupling is studied by numerical comparison of three asymptotic (high-frequency) creeping wave formulations for the surface magnetic field for cylinder radii ka $\approx$ 10 and 43, and, for axial offsets of 0 and 3λ. For small (ka $\approx$ 10) cylinders, the three creeping wave formulations were compared against the rigorous results obtained via FDTD (*Finite Difference Time Doman*) technique. The preliminary comparison of rigorous and asymptotic techniques show marked differences in the neighborhood of the *paraxial* region, suggesting the need for further investigations into the creeping wave mechanism of mutual coupling in conformal phased arrays.

I. INTRODUCTION

Future-generation tactical missiles, may be envisaged to need more technical sophistication for rapid transmission and reception of critical information. In some specific combat scenarios, it maybe necessary to inflict severe and complete damage to the enemy targets, and rapidly convey the same information via secure, high data rate communication links between the missile and a remote (military) location. One of the essential conditions is thus to ensure the survivability of such comminication links [1, p. 232]. Consequently, it turns out that the proper functioning of the antenna system, which is the front end of the physical layer in a communication link, is a key feature for reliable performance of such systems. Electromagnetic characterization of such flush-mounted antennas, and an understanding of the relationship between their radiation behavior and the survivability of communication links, is the main subject of this paper.

Application of arrays to military and commercial communication systems is well known [2],[3]. Recent interest in conformal arrays [4]-[6], following the early work [7],[8], suggests scope for further investigations for new applications. It has been observed in [3, ch. 9] that degradation of channel SINR occurs when strongly coupled (or weakly isolated) antennas are used as an array for transmission/reception. Furthermore, for conformal phased arrays, prediction of coupling is extremely important, necessiating use of accurate mathematical models [2, ch. 4].

For conformal arrays it has been shown in [8] that element gain pattern (in an array environment) is significantly different from the corresponding isolated element pattern. The mutual coupling, which is a manifestation of traveling electromagnetic waves guided along the curved part of the missile structure, can cause vanishing of such element gain patterns for certain physical observables. A typical situation of antenna-to-antenna coupling, for a pair of physical locations on a tactical missile structure, is shown in Fig. 1. The purpose of this investigation is to identify the detrimental effects of mutual coupling for such scenarios via numerical modeling. Such predictions are aimed at identifying coupling paths which would cause directive antenna gains to vanish, causing catastrophic link failures. To that end, mutual coupling between antennas has also been studied from an EMI/EMC point of view [9].

Calculation of mutual coupling for missile structures at radar frequencies $\geq$ 10 GHz is a computaionally challenging problem. As discussed in [10], the various state-of-art modeling tools/techniques, based on rigorous/exact approaches (or solutions) such as in [11],[12,ch. 2], are of little use due to severe convergence problems.

High-frequency/quasi- or ray-optic [13, ch. 12]-[22] techniques are employed in situations where the frequency is high enough. These techniques are typically asymptotic expansions of the exact solutions to the canonical electromagnetic boundary value problem. The numerical accuracy of such solutions increases as the wavenumber (or frequency) increases.

Another advantage of employing the ray-optic or high-frequency solutions is their amenability to physical interpretation in terms of extension of the laws of classical geometrical optical optics. Referring to Fig. 1, such implies that at sufficiently high frequencies electromagnetic energy from antenna A is coupled to B via paths, that essentially obey the Fermát principle of least time (or shortest path). It follows that such short-
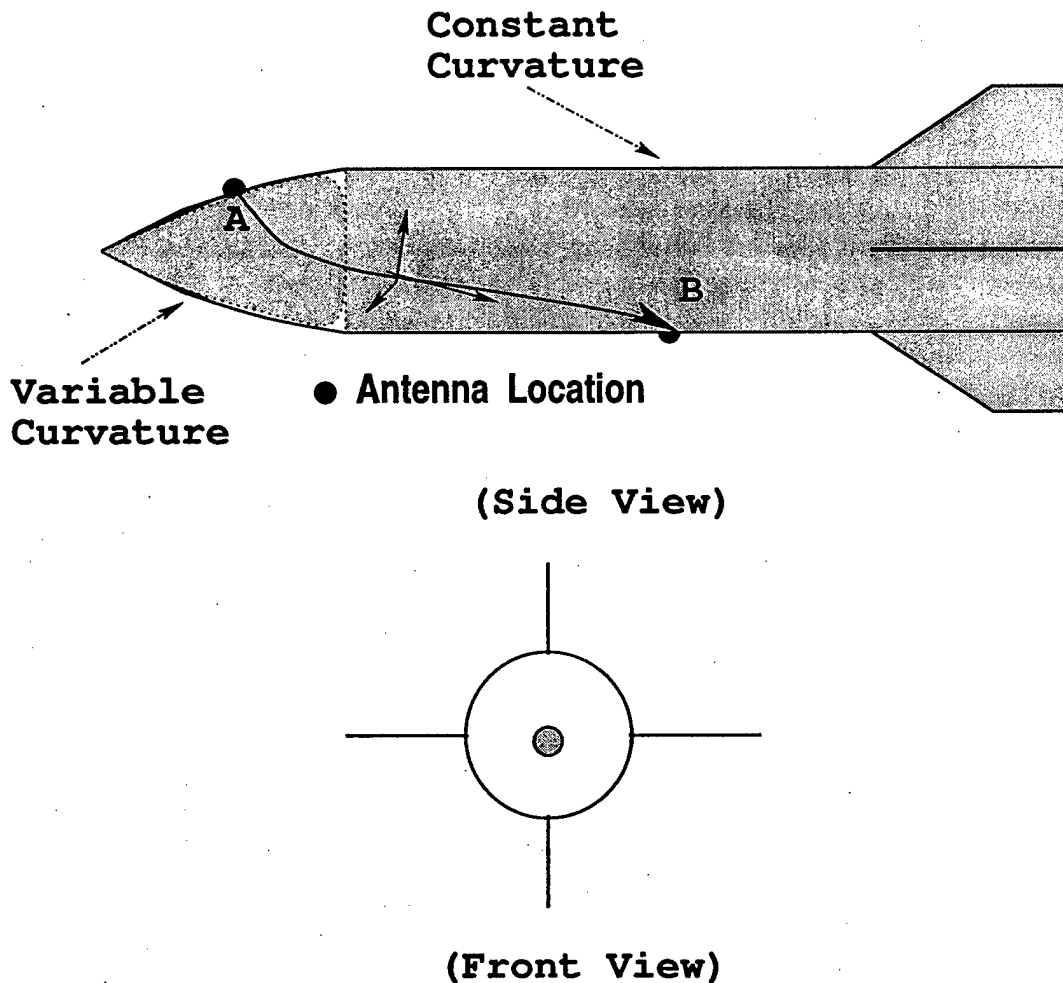
Fig. 1. Coupling phenomenon between antennas located on a tactical missile structure such as the Patriot MIM 104 shown in [1, p. 30, Fig. 2.16]. The coupling path shown here is taken to the *shortest* distance between A and B on the curved, convex surface part of the missile. The shortest path on a curved, convex surface is known as a *geodesic*. The fuselage section of such a tactical missile can be modeled by a circular cylinder.

est paths between two points on a curved, convex surface are *geodesics*, and the waves traveling along geodesic paths are known as *creeping waves*.

It must be remarked that experimental verification of creeping wave formulations in [16], are available in the recent works in [23],[24]. This important validation suggests the application of the theory to new applications. Extension of the creeping wave theory to model antennas on missile structures made from composite materials has recently been addressed in [25]. A computer analysis code, used primarily for EMI prediction for aircraft antennas, has been developed and described in [26].

In this paper the creeping wave theory is employed to study the mutual coupling between antennas. The results, and the ensuing conclusions are therefore valid at high frequencies. The missile fuselage, as shown in Fig. 1, is modeled by a circular cylinder. To examine the effect of curvature and axial offsets on the creeping wave coupling, the

antennas are considered to be far away from the missile nose-cone. This simplifies the calculations, since, to the first order the effects of diffraction from the tip of the nose cone and wings/stabilizers can be ignored. Thus our results include effects of the curvature of the missile fuselage only similar to an earlier study [27].

In section II, relevant formulas for creeping wave theory from [16],[19] and [22] are presented. The mutual admittance (Y_{12}) for two axially oriented magnetic current elements (point sources) is shown to be directly proportional to the H_z component of the surface magnetic field. The creeping wave representation for H_z from the three (UTD, T.S.Bird and Boersma-Lee) asymptotic techniques are include in this section. The importance of mutual coupling and how it affects the array antenna gain pattern is discussed in some detail with relation to creeping waves. Numerical results are presented in section III, followed by a description of ongoing future work in section IV, and a summary in section V. Two appendices are included; appendix I presents relevant formulas related to geodesic paths summarized from [28], and appendix II includes the formulas for the various hard (TE) surface Fock functions calculated from the formulas available in [20, Appendix I]. Some of the numerical results on Fock functions are not widely known, and are included here for for the first time. To that end, these results for the Fock functions should serve as a benchmark for any future calculations. A selective list of references is included.

II. CREEPING WAVE THEORY AND MUTUAL COUPLING

As explained earlier, the mutual coupling is studied here for a pair of antenna locations on a missile fuselage that is modeled by a perfect, electrically conducting (PEC) circular cylinder. The general scattering model si shown here in Fig. 2, and its *specialization* to antennas located directly on the cylinder is shown in Fig. 3. Furthermore, for identifying the first order (or dominant) effects, the antennas on the fuselage are situated such that the nose-cone and wings/stabilizers effects are not included. These considerations suggest the general canonical model involving an infinite circular cylinder shown in Fig. 3. For this model the appropriate mathematical formulation is developed in[15],[16],[18]-[20] and [22]. The descriptions in these figures are complete enough for understanding the geometrical features of creeping wave propagation.

Consider two narrow, axial, short slot radiators, A and B as shown in Fig. 3. Mathematically, these sources can be represented in cylindrical coordinates, without any loss of generality, as

$$d\vec{p}_m(A) = \hat{z}' V_1 \frac{\delta(\rho - a)\delta(\phi)\delta(z)}{a}, \tag{1}$$

at location A, and,

$$d\vec{p}_m(B) = \hat{z} V_2 \frac{\delta(\rho - a)\delta(\phi - \phi_d)\delta(z - z_{\text{offset}})}{a}, \tag{2}$$

and at location B, with (complex) excitations $V_{1,2}$, respectively. The three formulations in [16],[19],[22] allow one to calculate the surface magnetic field excited by either of the slot antennas. More importantly, [16, Eq. (167)] has been shown in [23] to apply to

(ii) "Unfolded" or Developed Cylinder

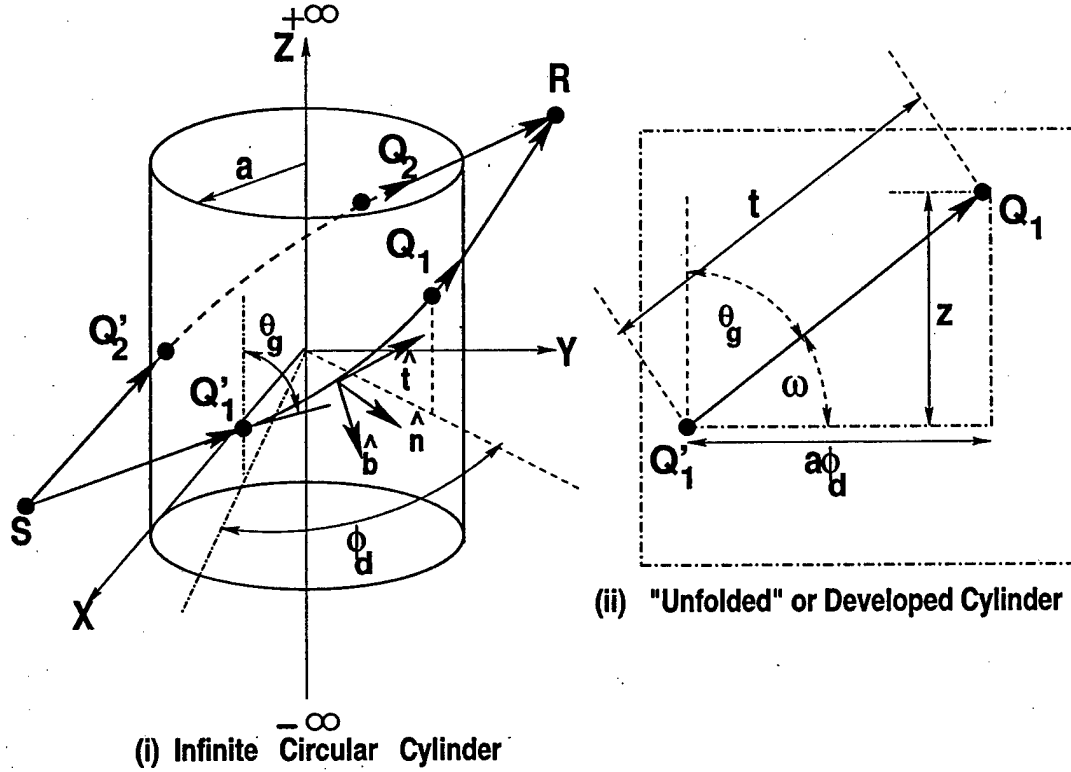**(i) Infinite Circular Cylinder**

Fig. 2. Scattering by a perfectly conducting circular cylinder in terms of two dominant creeping wave (ray) paths. The unfolded cylinder corresponds to the high-frequency planar limit when $ka \rightarrow \infty$. The *moving trihedron* (along the geodesic path length, t, for $Q_1' \rightarrow Q_1$) is defined by the unit vectors, $\hat{b}$ (binormal), $\hat{n}$ (normal) and $\hat{t}$ (tangent) such that, $\hat{n} = \hat{b} \times \hat{t}$. For source $S \rightarrow Q_1'$, and, $R \rightarrow Q_1$, is the canonical case for mutual coupling betwen antennas on a smooth convex surface, and, $\theta_g \rightarrow 0$ defines the paraxial region. The general topology shown here applies to the calculation of shadowing of wing-mounted antennas by the aircraft/missile fuselage. A special case of this scenario is shown explicitly in Fig. 3, below.

surfaces with variable radii of curvature in Fig. 1. The result for a perfect, electrically conducting (PEC) circular cylinder follows from the general result [16, Eq. (167)] as a special case. In contrast, [19, Eq. (1)] is specific to the canonical case of a PEC circular cylinder only. Expressed in terms of the geodesic ray parameters, this surface magnetic field, at location B due to a source at A, reads:

$$\vec{H}_m(B|A) = \overline{\overline{G}}_m(B|A) \cdot d\vec{p}_m(A). \tag{3}$$

In (3) the subscript m refers to magnetic field or excitations (sources). The surface dyadic Green's function, from [19, Eq. (2)], in cylindrical systems read

$$\overline{\overline{G}}_m(B|A) = \hat{z}\hat{z}' G_{zz}(B|A) + \hat{\phi}\hat{z}' G_{\phi z}(B|A) + \hat{\phi}\hat{\phi}' G_{\phi\phi}(B|A) \tag{4}$$

All the components in (4) lie on the cylinder, *i.e.*, there are no components normal to the cylinder curved surface. For two axially oriented slots in Fig. 3, $z' \equiv z$. This results in the single component of the surface magnetic field, $\vec{H}(B|A) = \hat{z}H_z(B|A)$. The final

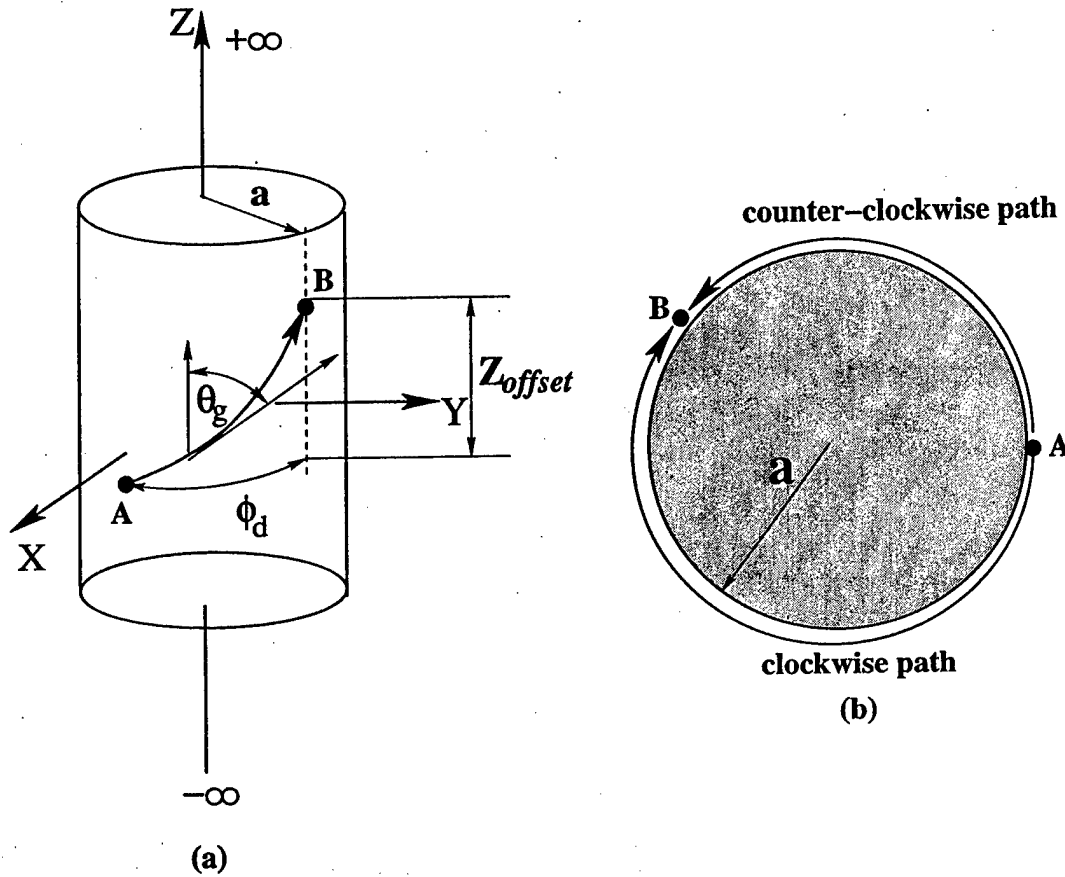380

Fig. 3. Illustrating the specific issue of mutual coupling between antennas **A** and **B** on a PEC circular cylinder through creeping wave propagation. The creeping wave travels along the *geodesic* or shortest path from source $(A) \rightarrow$ receiver (B). At high-frequencies, $ka \rightarrow \infty$, the total field can be considered as a superposition of the fields on the clockwise and counter-clockwise paths.

expression for H_z from [16, Eq. (167)], specialized for a PEC circular cylinder, reads:

$$H_z(B|A) = C_o G_o(kt)[\sin^2\theta_g \tilde{C}(\xi) + v_0(\xi)\{\sin^2\theta_g + \tilde{Q}(1 - \tilde{Q})(2 - 3\sin^2\theta_g)\}]. \tag{5}$$

Equation (5) is the UTD *Uniform Theory of Diffraction* formulation for the creeping wave field. In (5)

$$\tilde{C}(\xi) = \frac{4}{3}\cot^2\theta_g \tilde{Q}\xi v_0'(\xi). \tag{6}$$

From [19] one can obtain the corresponding expression for the surface magnetic field that reads

$$
\begin{aligned}
H_z(B|A) &= C_o G_o(kt)\left\{ v_0(\xi)[\sin^2\theta_g + \tilde{Q}(1 - \tilde{Q})(2 - 3\sin^2\theta_g)] \right. \\
&\quad + \left. \tilde{Q}\left[v_0(\xi)\left(\frac{31}{72}\cos^2\theta_g - \frac{5}{24}\right) + v_1(\xi)\left(\frac{11}{64} - \frac{17}{36}\cos^2\theta_g\right)\right. \right.
\end{aligned}
$$

381

$$+ \; v_2(\xi)\left(\frac{1}{24}\cos^2\theta_g + \frac{1}{40}\right) + \frac{\jmath\xi}{5}v_0^{(1)}(\xi)\bigg]\bigg]\bigg\}.$$

(7)

(Equation (7) is referred to as the TSB formulation, in view of [19].) From [19] one can also obtain the Boersma-Lee formulation [22] expressed as below:

$$\begin{aligned}
\mathbb{H}_z(\mathbb{B}|\mathbb{A}) &= C_o\mathbb{G}_o(kt)\Big\{ v_0(\xi)[\sin^2\theta_g + \tilde{\mathcal{Q}}(1-\tilde{\mathcal{Q}})(2-3\sin^2\theta_g)\}] \\
&\quad - \; \tilde{\mathcal{Q}}\xi v_0'(\xi)\left(\frac{11}{12}\sin^2\theta_g + \tilde{\mathcal{Q}}\bigg[\frac{11}{6} - \frac{187}{64}\sin^2\theta_g\bigg]\right)\Big\} \\
&\quad - \; \frac{2}{3}C_o\mathbb{G}_o(kt)\tilde{\mathcal{Q}}^2\xi v_0'(\xi)\cot^2\theta_g.
\end{aligned}$$

(8)

In (5) to (8), one has the following terms defined as:

$$\mathbb{G}_o(kt) = \frac{e^{-\jmath kt}}{t},$$

$$\tilde{\mathcal{Q}} = \frac{\jmath}{kt}, \text{ and the } complex \text{ constant,}$$

$$C_o = \frac{-\jmath k \mathbb{V}_1}{2\pi\eta_o}.$$

(9)

The various hard (TE) surface Fock functions in (5) to (8) are defined in Appendix II. The Fock parameter

$$\xi = \left(\frac{ka}{2}\sin\theta_g\right)^{\frac{1}{3}}\phi_d,$$

(10)

for a circular cylinder. (For variable curvature convex surfaces, the general form for the Fock parameter is given in [16, Eq. (113)]). With the knowledge of $\mathbb{H}_z(\mathbb{B}|\mathbb{A})$, from (5),(7) or (8), one can calculate the mutual admittance between the two slots via the relationship [16, Eq. (191)], as:

$$\begin{aligned}
\mathbb{Y}_{\mathbb{AB}}(\theta_g, \phi_d; k) &= -\frac{1}{\mathbb{V}_1\mathbb{V}_2^*}\iint\limits_{\Omega_B} d\tau_b \\
&\quad \times \iint\limits_{\Omega_B} d\tau_a\{d\vec{\mathbb{p}}^*_m(\mathbb{B})\cdot\vec{\mathbb{H}}_m(\mathbb{B}|\mathbb{A})\} \\
&= \mathbb{Y}_{\mathbb{BA}}(\theta_g, \phi_d; k), \\
&\quad \text{via reciprocity theorem} \\
&\quad [13, \text{pp. } 404\text{-}409].
\end{aligned}$$

(11)

For two magnetic point sources with strengths $V_{1,2}$, it follows that

$$|Y_{AB}(\theta_g, \phi_d; k)| \propto |H_z(\theta_g, \phi_d; k)|.$$

The UTD, TSB and B-L formulations for the axial component of the surface magnetic field $|H_z|$ are available in (5),(7) and (8), respectively.

It is important to point out that of the three creeping wave formulations, the UTD (or equation (5))has been most widely used [9],[11],[23],[24]. However, in all these investigations the paraxial term $\tilde{C}(\xi)$ in (6) was not considered. Its effects have been included, for the first time, in the present paper.

In (11):

(i) V_1 and V_2 are the equivalent mode voltages of excitation associated with the dominant electric field in the slot apertures

(ii) the differential elements $d\tau_{a,b}$ and areas $\Omega_{A,B}$ refer to antennas A and B, respectively.

The calculation of θ_g and geodesic path length, t, have been defined in eqs. (15) and (16), respectively. Therefore, with these equations and (10), one can compute the $H_z(B|A)$ via eqs. (5) and (7) for a single creeping wave path in Fig. 3(a). To calculate the *total* creeping wave field as in Fig. 3(b), it is merely necessary to re-calculate all the necessary parameters in (15), (16) and (10) for the counterclockwise path, by replacing $\phi_d \rightarrow 2\pi - \phi_d$ in these equations. The total $H_z(B|A)$ is then a superposition of the fields from these two paths.

Following [13, p. 125, Eq. (3-103)], one can write its corresponding dual relationship:

$$Y_m^a = Y_{m1}\frac{V_1}{V_m} + Y_{m2}\frac{V_2}{V_m} + \cdots + Y_{mm} + \cdots + Y_{mN}\frac{V_N}{V_m} \tag{12}$$

for the active input admittance Y_m^a in a general array environment. The various Y_{mp} are the mutual admittances and are calculated from the knowledge of the surface magnetic field as shown in [15]. This relation applies to arbitrary arrays, and hence if the surface magnetic field due to slots on an arbitrary convex surface is known, the active input admittance can be calculated. It is emphasized that *only* [16] provides formulas to calculate surface fields due to the sources on general convex surfaces. This is accomplished primarily by introducing torsion factors and calculation of the geodesic radius of curvature and geodesic lengths on such general surfaces. Some indications on how to calculate such parameters have been made available in [28].

Once the geodesic and other curved surface parameters are known, one calculates the all important Fock parameter ξ from a more generalized formula available in [16, p. 4-53, Eq. (113)]. This is the most important step; because calculation of ξ then readily allows computation of the surface magnetic field through the various surface Fock functions, which themselves are function of ξ only. In this sense the formulations in [16] are remarkable because the ray optical principles allows calculation of array performance parameters on general convex surfaces. In [24] the Green's function for slots on a doubly-curved surface has been taken from [16] and shown to agree with experiments.

It follows from our discussions that the active input admittance in a N-element array is dominated by the creeping wave field. It has been shown in [8] that the radiation
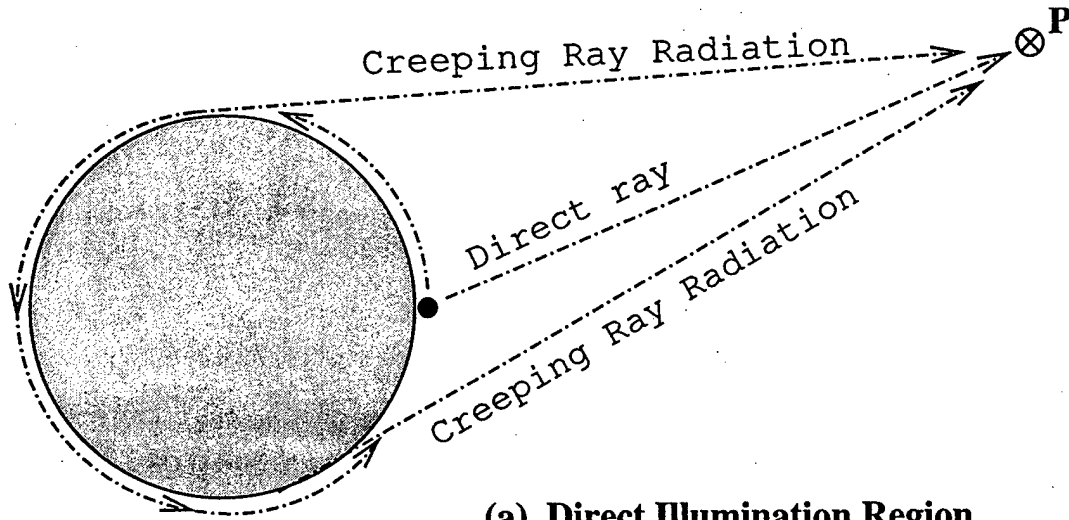
(a) Direct Illumination Region
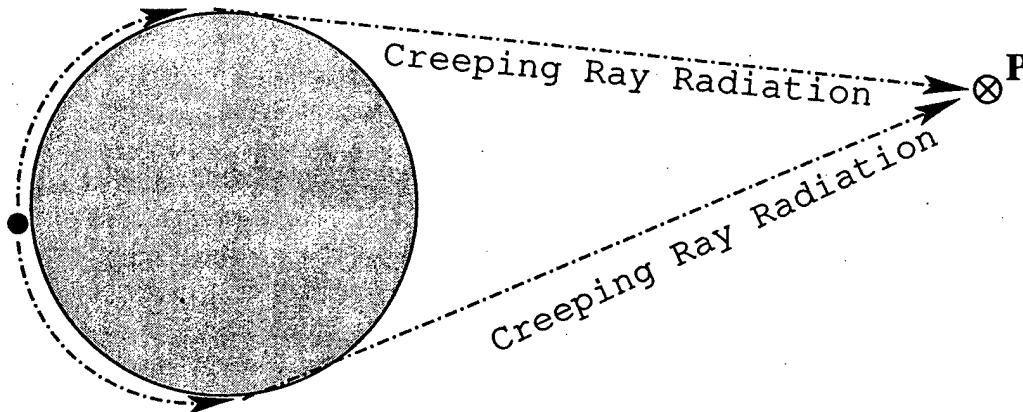
(b) Shadow Illumination Region

Fig. 4. Radiation pattern calculation in various regions as the observation point **P** moves around the cylinder. In the direct illuminated region, the creeping wave and direct source ray interferences play a dominant role. In the shadow region, the radiation pattern is dominated by creeping ray radiation only. The radiation fields can be calculated from the formulations in [17].

field from a conformal array can be expressed as Floquet wave modes. So, when the propagation constant of the Floquet mode equals that of a creeping wave then one might expect a null in the active element pattern. This could be expressed following [12, p. 135, Eq. (3-120)] as:

$$g_e^{A,B}(\theta, \phi) \approx g_{iso}^{A,B}(\theta, \phi)[1 - |\Gamma_{A,B}(\theta_g, \phi_d; k)|^2].$$ (13)

Equation (13) thus underscores the importance of the study of the creeping waves, where the active reflection coefficient $|\Gamma_{A,B}(\theta_g, \phi_d; k)|$ is calculated using the various preceding creeping wave formulas as in (5),(7) and (8).

For a slot on a PEC cylinder the isolated element gain pattern, $g_{iso}^{A,B}(\theta, \phi)$, is calcu-

lated via superposition of the fields from the appropriate ray paths as shown in Fig. 4(a) and (b). For these regions the radiated field can be found in [16] or [17]. (Incidentally, [17] has more improvements to the original form given in [16].) The appropriate (high-frequency) analytical expressions for these radiated fields are not included here for brevity, as they have not been employed in any following calculations in section III.

III. NUMERICAL RESULTS AND DISCUSSIONS

The results for this section are shown in Figs. 5 to 8. It is emphasized that these are preliminary comparisons. (Additional numerical investigations are in progress and will be presented at the time of the presentation.)

In general, all the results show the variation of the surface magnetic field calculated from (5) and (7) with respect to the azimuth angle ϕ_d, and for various axial separations, z_{offset}. For the calculations shown in Figs 7 and 8, a cylinder of radius 20.75 cms, and a frequency of 10 GHz was chosen from [1, p. 132,, Fig. 6.4]. The geometry corresponds closely to the data available for Raytheon MIM 104 (Patriot) tactical missile.

The numerical data for these results are contained in the respective figures themselves and hence are omitted here for brevity. The FDTD technqiue was used for comparison (Fig. 6) because it is evident from [8] that the exact calculations via the eigenfunction method requires substantial analytical effort in the deep shadow regions.

The FDTD calculations, shown in Fig. 6, are very preliminary in nature. This is because for ideal comparisons, one needs to eliminate the edge diffraction of the creeping waves in order to compare the results for a finite cylinder vs. the results from (5),(7) or (8), all of which are for infinite cylinder geometries. To understand the effects of the edge contributions, results the same topology are currently being investigated for cylinders of length 7λ and for same electrical size $ka \approx 10$. In this case the dipoles will be about 2λ away from the edges, and hence these results are expected to be slightly accurate. Furthermore results from the FDTD technique are also being investigated for dipole separations of 1λ and 2λ.

One may summarzie the major conclusions from the preliminary results. It appears that the three creeping wave formulations disagree for large axial offsets and for smaller electrical radii ($ka \approx 10$). Far from the paraxial region, the results from the three are in agreement. The agreement improves substantially for large and no axial offsets for $ka \rightarrow \infty$, as evidenced by the results from Figs. 7 and 6, for $ka \approx 43$.

IV. FUTURE WORK

Current efforts are primarily aimed at further validation of the creeping wave surface magnetic field against the FDTD calculations on longer cylinders to eliminate the effects of edge diffractions. Additionally, investigations are underway to calculate the Y_{12} for slots on cylinders via (5), (7) and (8) and compare these against the FDTD (or other exact) calculations.

It must be pointed out that [25] presents a formulation for the coated cylinder and its extensions to arbitrary convex surfaces. However, no numerical results are available in [25]. Therefore the validity of the results in [25] are unknown. It appears that the best
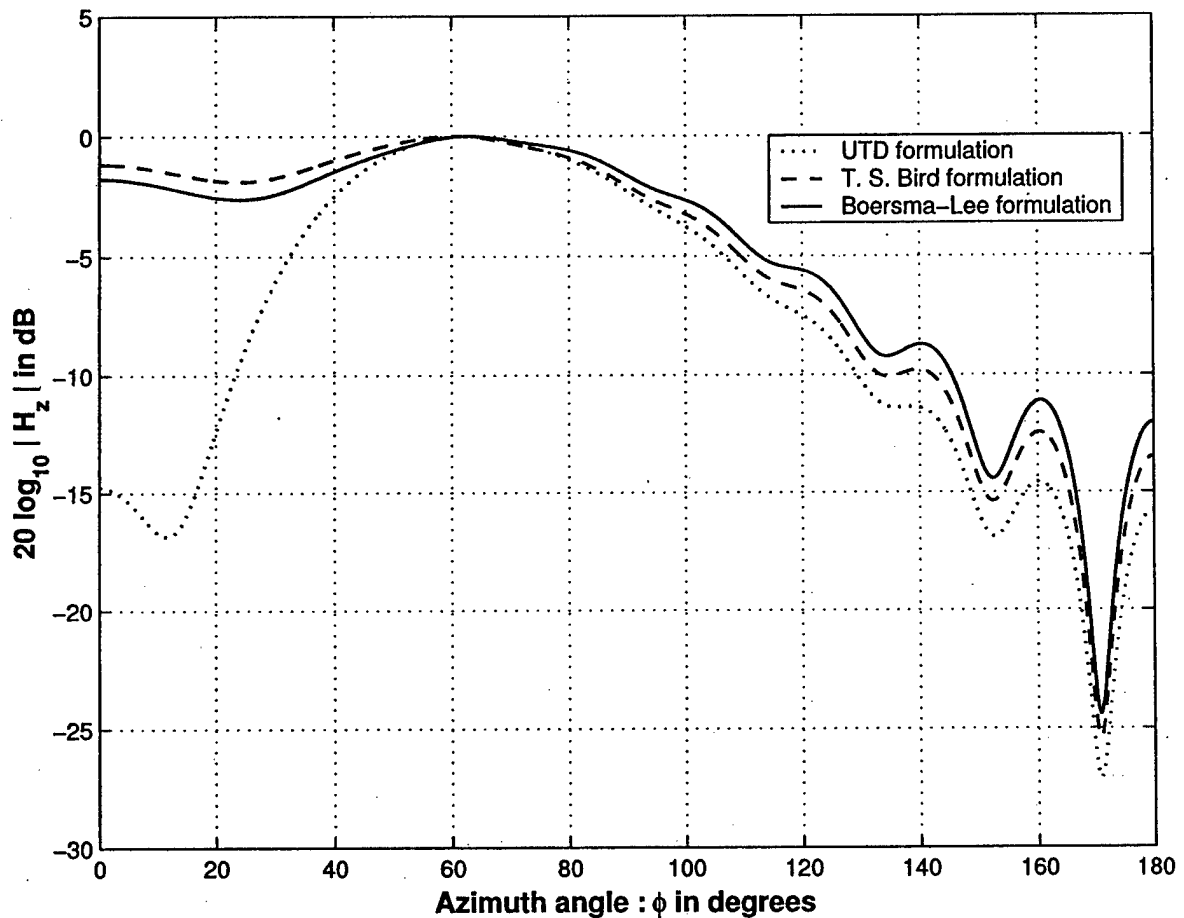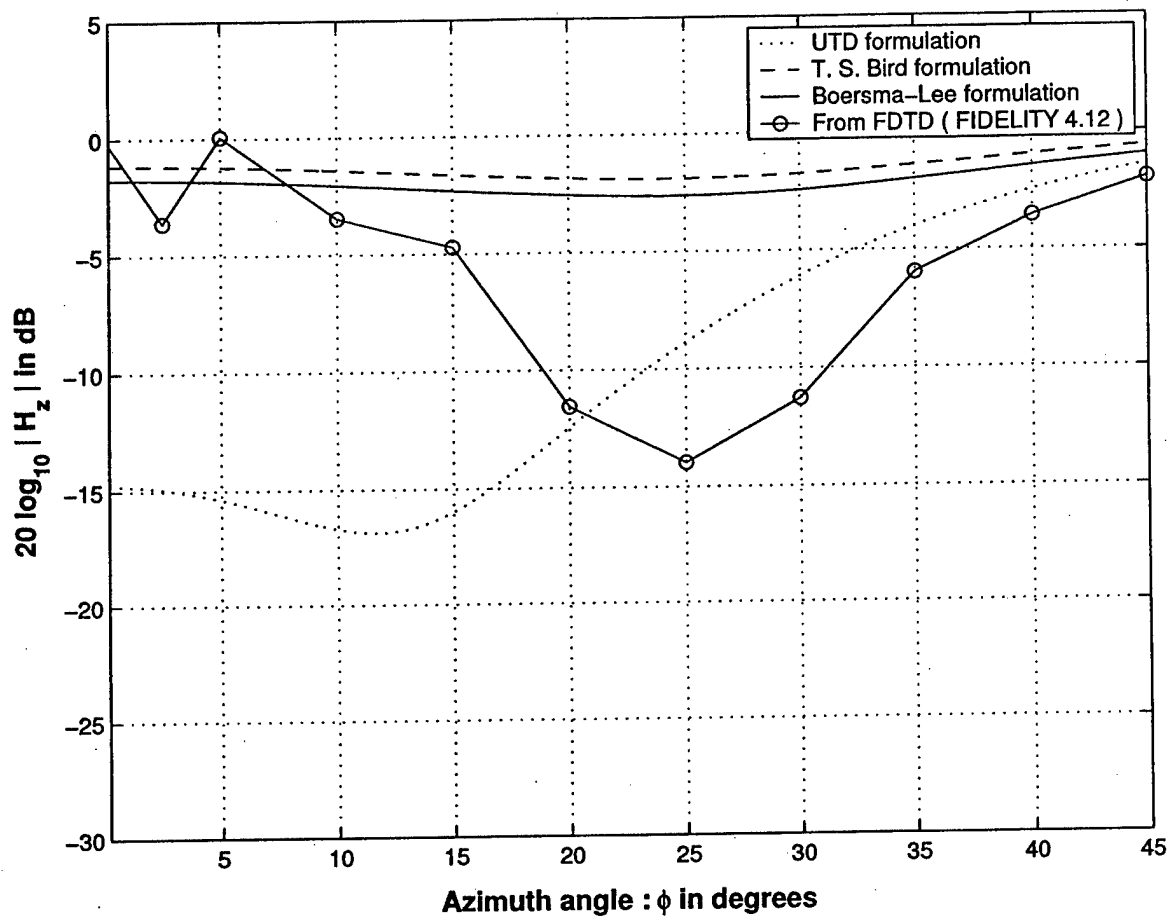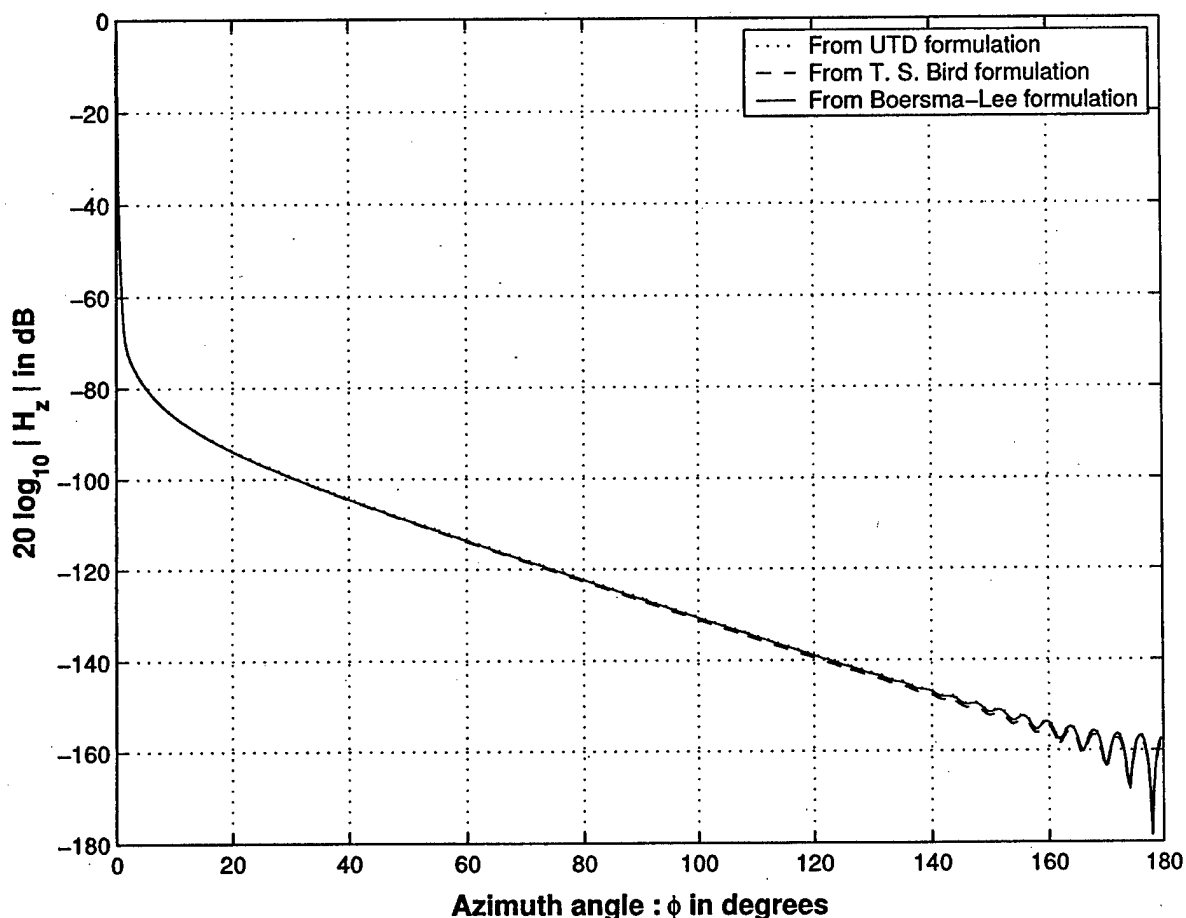
Fig. 5. Comparison of creeping wave surface magnetic field, H_z, for $ka \approx 10$ and $Z_{offset} = 3\lambda$ at 5 GHz. One notices a difference of ≈ 12 dB in the paraxial region, defined by $\phi \leq 60°$.

way to improve the existing creeping wave formulations is to examine the limitations of the canonical models, and then procced towards the more general geometries as in [25]. The reason for this is that the original asymptotic formulations in [15]-[22] were developed from the exact solutions to the *canonical* problem, and hence are analytically tractable and more readily numerically verifiable.

V. SUMMARY

Conformal array antennas on future tactical missile systems can provide enhanced battle damage assessment and indication through improved target imagery via high data rate communication links. At high frequencies the coupling of electromagnetic energy between a pair of antenna locations can be accurately modeled via propagation of creeping waves that travel along the shortest (geodesic) path between the location pair. The analysis presented here indicates that creeping wave coupling can cause complete vanishing of the antenna gains for some specific situations.

Fig. 6. Comparison of creeping wave surface magnetic field, H_z, for $ka \approx 10$ and $Z_{offset} = 3\lambda$ at 5 GHz in the paraxial region $\phi \leq 40°$ against the FDTD calculations. For FDTD calculations a cylinder of length 5λ was selected. The short, magnetic dipoles were selected of length $\frac{\lambda}{20}$ and with constant excitations. The discretization (cell size) used in the FDTD calculations was $\approx \frac{\lambda}{15}$. The dipoles were 1λ away from the curved edge of the cylinder.

For some select geometries the influence of mutual coupling (or antenna-to-antenna isolation) was numerically studied using three different creeping wave formulations. The preliminary results presented here indicate that the for small cylinders ($ka \approx 10$) the UTD coupling formulation differs significantly from the other two across the paraxial regions.

ACKNOWLEDGEMENT

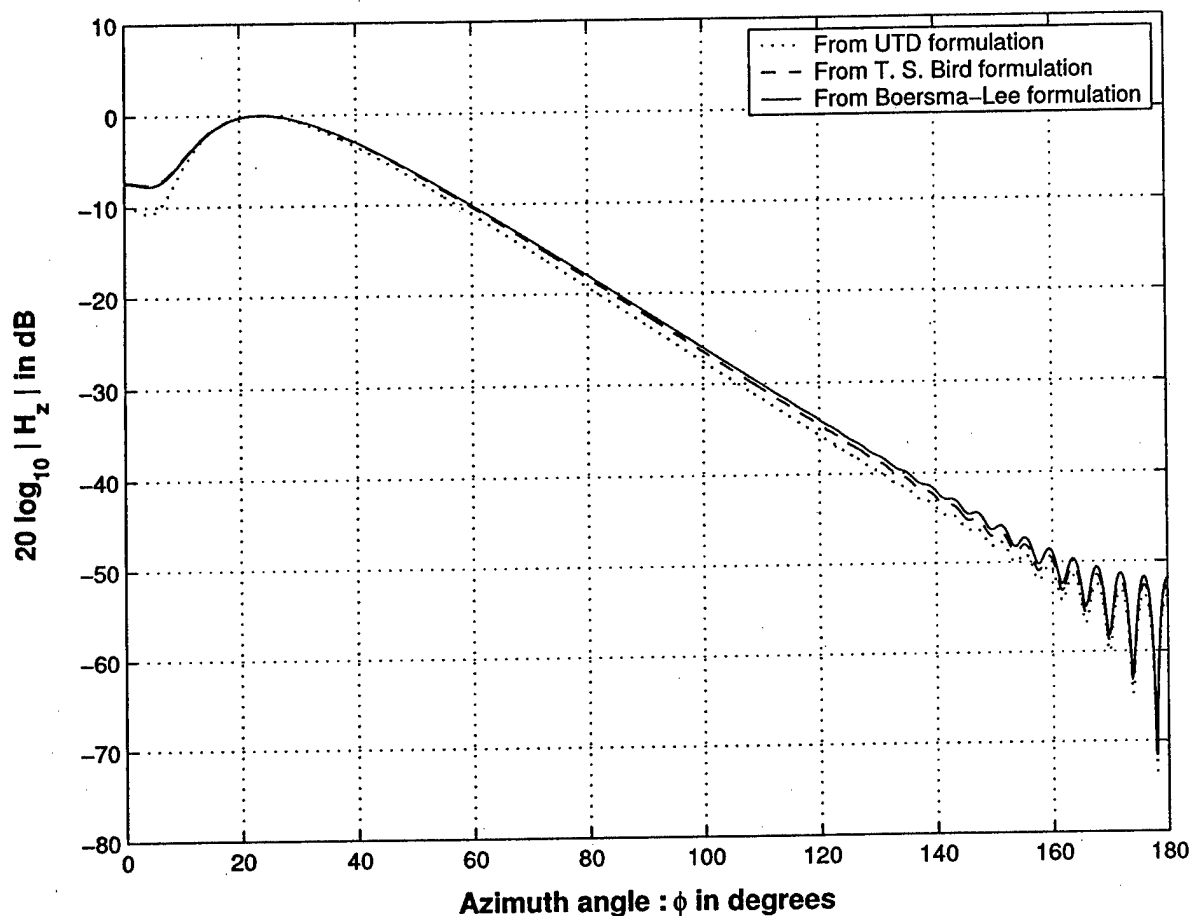**Fig. 7.** Comparison of creeping wave surface magnetic field, H_z, for $ka \approx 43$ and $Z_{offset} = 0\lambda$ at 5 GHz. The data refers to the Raytheon MIM 104 Patriot missile geometry.

REFERENCES

[1] E. L. Fleeman,*Tactical Missile Design*. Reston, VA, USA: AIAA, Inc., 2001.

[2] R. J. Mailloux, *Phased Array Antenna Handbook*. Boston, MA, USA: Artech House, 1994.

[3] K. Fujimoto and J. R. James, *Mobile Antenna Systems Handbook*. Boston, MA, USA: Artech House, 2001.

[4] G. Gerini and L. Zappelli, "Phased Arrays of Rectangular Apertures on Conformal Cylindrical Surfaces: A Multimode Equivalent Network Approach,"*IEEE Trans. Antennas and Propagat.*, vol. 53, no. 7, pp. 1843-1850, July 2004.

[5] B. Thors and L. Josefsson, "Radiation and Scattering Tradeoff Design for Conformal Arrays,"*IEEE Trans. Antennas Propagat.*, vol. 51, no. 5, pp. 1069-1076, May 2003.

[6] A. J. Sangster and R. T. Jacobs, "Mutual Coupling in Conformal Microstrip Patch Antenna Arrays," *IEE Proceedings: Microwave, Optics and Antennas*, vol. 150, no. 4, pp. 191-196, August 2003.

[7] G. V. Borgiotti and Q. Balzano, "Mutual Coupling Analysis of a Conformal Array of Elements on a Cylindrical Surface,"*IEEE Trans. Antennas and Propagat.*, vol. 18, no. 1, pp. 55-63, January 1970.

[8] J. C. Herper, A. Hessel and B. Tomasic, "Element Pattern of an Axial Dipole in a Cylindrical Phased Array, Part I: Theory,"*IEEE Trans. Antennas and Propagat.*, vol. 33, no. 3, pp. 259-272, March 1985.

[9] S. A. Davidson and G. A. Thiele, "A Hybrid Method of Moments-GTD Technique for Computing Electromagnetic Coupling Between Two Monopole Antennas on a Large Cylindrical Surface,"*IEEE Trans. Electromagnetic Compatibility*, vol. EMC-26, no. 2, pp. 90-97, May 1984.

[10] J. S. Asvestas, *Future Directions in Antenna Analysis and Design Software*; (a survey conducted by the Technical Working Group on Antennas (TWGA) of the Electromagnetic Code Consortium (EMCC)). October 2000.

Fig. 8. Comparison of creeping wave surface magnetic field, H_z, for $ka \approx 43$ and $Z_{offset} = 3\lambda$ at 5 GHz. Interestingly, in the paraxial region the difference between UTD, and, the TSB,B-L solutions is about 2 dB. The data refers to the Raytheon MIM 104 Patriot missile geometry.

[11] C.-W. Wu, L. C. Kempel and E. J. Rothwell, "Hybrid Boundary Element Integral Method for Cavities Recessed in an Elliptic Cylinder,"*IEEE Trans. Antennas and Propagat.*, vol. 51, no. 8, pp. 1829-1836, August 2003.

[12] J. J. Bowman, T. B. A Senior, P. L. E. Uslenghi, *Electromagnetic and Acoustic Scattering by Simple Shapes.* NYC, NY, USA: Hemisphere Publisshing, Inc., 1987.

[13] W. L. Stutzman and G. A. Thiele, *Antenna Theory and Design.* NY, USA: John-Wiley and Sons, Inc., 1998.

[14] J. Shapira, L. B. Felsen and A. Hessel, "Ray Analysis of Conformal Array Antennas,"*IEEE Trans. Antennas Propagat.*, vol. 22, no. 1, pp. 49-63, January 1974.

[15] S. W. Lee, "A Review of GTD Calculation of Mutual Admittance of Slot Conformal Array,"*Electromagnetics*, no. 2, pp. 85-127, 1982.

[16] P. H. Pathak, 'Techniques for High Frequency Problems', chapter 4 (pp. 4-3 to 4-117) in *Antenna Handbook: Theory, Applications and Design*, Y. T. Lo and S. W. Lee (eds.). NY, USA: Van Nostrand Reinhold Co., 1988.

[17] H.-T. Chou, P. H. Pathak and M. Hsu, "Extended Uniform Geometrical Theory of Diffraction Solution for the Radiation by Antennas Located Closse to an Arbitrary, Smooth, Perfectly Conducting, Convex Surface,"*Radio Science*, vol. 32, no. 4, July-August 1997, pp. 1297-1317.

[18] T. S. Bird,"Mutual Coupling Analysis of Radiation From Finite Waveguide Arrays Conforming to Cylindrical Structures,"Research Report, Department of Electrical and Electronic Engineering, James Cook University of North Queensland, February 1983.

[19] T. S. Bird, "Accurate Asymptotic Solution for the Surface Field Due to Apertures in a Conducting Cylinder," *IEEE Trans. Antennas and Propagat.*, vol. 33, no. 10, pp. 1108-1117, October 1985.

[20] T. S. Bird, "Comparison of Asymptotic Solutions for the Surface Field Excited by a Magnetic Dipole on a Cylinder,"*IEEE Trans. Antennas and Propagat.*, vol. 33, no. 10, pp. 1237-1244, November 1984.

[21] S. O. Rice, "Diffraction of Plane Radio Waves by a Parabolic Cylinder: Calculation of Shadows Behind Hills,"*Bell Syst. Tech. Jour.*, vol. XXXIII, part I, pp. 417-504, 1954.

[22] J. Boersma and S. W. Lee, "Surface Field Due to a Magnetic Dipole on a Cylinder: Asymptotic Expansion of Exact Solution,"technical report no. EM 78-17, Electromagnetics Laboratory, Department of Electrical Engineering, University of Illinois at Urbana Champaign, prepared under contract no. N00019-78-C-0064 for Department of Navy, Naval Air Systems Command, Washington DC, December 1978.

[23] P. Persson and L. Josefsson,"Calculating the Mutual Coupling between Apertures on a Convex Circular Cylinder Using the Hybrid UTD-MoM Method," *IEEE Trans. Antennas and Propagat.*, vol. 49, no. 4, pp. 672-677, April 2001.

[24] P. Persson, L. Josefsson and M. Lanne, "Investigation of the Mutual Coupling Between Apertures on Doubly Curved Convex Surfaces: Theory and Measurements,"*IEEE Trans. Antennas and Propagat.*, vol. 51, no. 4, pp. 682-692, April 2003.

[25] P. E. Hussar and E. M. Smith-Rowland, "An Asymptotic Solution for Boundary-Layer Fields Near a Convex Impedance Surface,"*Journal of Electromagnetic Waves and Applications*, vol. 16, no. 2, pp. 185-202, 2002.

[26] P. E. Hussar, V. Oliker, H. L. Riggins, E. M. Smith-Rowland, W. R. Klocko and L. Prussner, "An Implementation of the UTD on facetized CAD Platform Models",*IEEE Antennas and Propagation magazine*, vol. 42, no. 2, pp. 100-106, April 2000.

[27] D. Chatterjee, S. Chakrabarti, K. Shanmugan and G. E. Prescott, "Performance Simulation Studies for a Class of 'Smart', Conformal Array Antenna Architectures",*Proceedings of the IEEE Phased Array Systems and Technology Symposium*, pp. 251-254, May 21-25, 2000, Dana Point, CA, USA.

[28] S. W. Lee, *Differential Geometry for GTD Applications*, technical report # EM 77-21, Electromagnetics laboratory, University of Illinois Urbana-Champaign, prepared under contract # NSF ENG 73-08218 for National Science Foundation, October 1977.

APPENDIX I

GEODESIC PATH AND CURVATURE PARAMETERS ON A CIRCULAR CYLINDER

The geometry of the geodesic path shown in Figs. 2 and 3 require the knowledge of the unit vectors along the geodesic. Since the geodesic is the 'shortest' path on the cylinder, unfolding the cylinder would cause the geodesic to be a straight line between two points on a plane surface as shown in Fig. 2 (b). These unit vectors can be simply expressed in terms of familiar cartesian coordinates as

$$
\begin{aligned}
\hat{b} &= -\hat{x}\cos\theta_g \sin\phi_d + \hat{x}\cos\theta_g \cos\phi_d - \hat{z}\sin\theta_g \\
&= \hat{\phi}\cos\theta_g - \hat{z}\sin\theta_g, \underline{\textit{binormal}}, \\
\hat{t} &= -\hat{x}\sin\theta_g \sin\phi_d + \hat{x}\sin\theta_g \cos\phi_d + \hat{z}\cos\theta_g \\
&= \hat{\phi}\sin\theta_g + \hat{z}\cos\theta_g, \underline{\textit{tangent}}, \text{ and,} \\
\hat{n} &= \hat{x}\cos\phi_d + \hat{y}\sin\phi_d, \underline{\textit{normal}}
\end{aligned}
$$

(14)

unit vectors, respectively. The angle

$$
\theta_g = \tan^{-1}\left(\frac{a\phi_d}{Z_{\text{offset}}}\right),
$$

(15)

and the geodesic path length

$$
t = \sqrt{(a\phi_d)^2 + (Z_{\text{offset}})^2}.
$$

(16)

The Fock parameter is calculated for both clockwise and counterclockwise paths. If the counter-clockwise path corresponds to an azimuthal angular span of ϕ_d, then the clockwise path corresponds to $2\pi - \phi_d$ as shown in Fig. 3(b). The geometric parameters in equations (14) to (16) are calculated by replacing $\phi_d \longrightarrow 2\pi - \phi_d$ for the counter-clockwise and clockwise paths, respectively. More details can be found in [28].

The following manipulation, using the relationship [14, Eq. (5-5)],

$$
\begin{aligned}
\frac{\xi}{k} &= \frac{t}{k}\left(\frac{k}{2\rho_g^2}\right)^{\frac{1}{3}} \\
&= \frac{t}{(2^{\frac{1}{2}})^{\frac{2}{3}}k^{\frac{2}{3}}\rho_g^{\frac{2}{3}}} \\
&= \frac{t}{\sqrt{2}k\rho_g^{\frac{2}{3}}}.
\end{aligned}
\tag{17}
$$

was used to simplify the generalized form for $C(\xi)$ in [16, p. 4-90] for circular cylinders. In addition, one notes that [16, p. 4-91, Eq. (189b)] can be simplified for a *circular cylinder* as

$$
\begin{aligned}
\tilde{\tau} &= \left[\frac{kt}{2m(Q')m(Q)\xi}\right]^{\frac{1}{2}} \\
&= \left[\frac{kt}{2m^2\xi}\right]^{\frac{1}{2}} \\
&= 1.
\end{aligned}
\tag{18}
$$

For a circular cylinder one has the following parameters, that appear in (16) and (17). These are as given below from [15].

$$
\rho_g = \frac{a}{\sin^2\theta_g}
\tag{19}
$$

where a is the physical (principal) radius of the circular cylinder. Here ρ_g is the radius of curvature of the geodesic path as shown in Fig. 3, and is tangent to the geodesic. The quantity

$$
\rho_b = \frac{a}{\cos^2\theta_g}
\tag{20}
$$

is also associated with the geodesic, and is defined as the binormal radiuus of curvature. This is normal to ρ_g and lie in the tangent plane containing ρ_g and ρ_b. Finally, the quantity

$$
m = \left(\frac{k\rho_g}{2}\right)^{\frac{1}{3}}
\tag{21}
$$

APPENDIX II
HARD (OR TE) SURFACE FOCK FUNCTIONS

In this appendix relevant information regarding the hard (TE) surface Fock functions are furnished. This presentation includes both small argument and residue series representations of the various surface Fock functions denoted generically by $v_n^m(\xi)$. These forms are available in [16]-[18], but no numerical or graphical data are available. The plots of the Fock functions are obtained here for m = 0 and n = 0, 1, 2, and, m = 1 and n = 0. The contour integral form from [17, Appendix I] reads:

$$v_n^{(m)} = \frac{e^{j(n+\frac{1}{2})\frac{\pi}{2}}}{2\Gamma(n+\frac{1}{2})} \int_{C_1} e^{-j\xi\tau} \tau^n \left\{ \frac{w_2(\tau)}{w_2'(\tau)} \right\}^{m+1} d\tau. \tag{22}$$

Bird has evaluated the above integral following the convergent series expansion and the residue series forms. The various forms for the various m and n values are given next from [17, Eqs. (43)-(46)]. The results for the phase of the Fock functions show a discontinuity. However, the phase was calculated using the standard intrinsic (ATAN2(Y, X)) function available on FORTAN 77 or 90, and this function returns a value between $-\pi \le \theta \le +\pi$. To conform to the standard notation of defining the angles, the negative values were converted to their positive counterparts via: $\theta = 2\pi - |\theta|$, whenever $\theta \le 0$.

$$v_0 \approx \begin{cases} 1.0 + \sum_{m=1}^{10} A_m(-j\xi)^{\frac{3m}{2}}, & \text{when } \xi \le 1.25 \\ (-j\pi\xi)^{\frac{1}{2}} \sum_{m=1}^{10} \frac{\exp(-j\xi\tau_m')}{\tau_m}, & \text{when } \xi > 1.25. \end{cases} \tag{23}$$

The other surface Fock functions are given next.

$$v_1 \approx \begin{cases} 1.0 - \sum_{m=1}^{10} B_m(-j\xi)^{\frac{3m}{2}}, & \text{when } \xi \le 1.25 \\ 2(j\pi\xi^3)^{\frac{1}{2}} \sum_{m=1}^{10} \exp(-j\xi\tau_m'), & \text{when } \xi > 1.25, \end{cases} \tag{24}$$

$$v_2 \approx \begin{cases} 1.0 + \sum_{m=1}^{10} C_m(-j\xi)^{\frac{3m}{2}}, & \text{when } \xi \le 1.25 \\ \frac{4}{3}(\pi\xi^5)^{\frac{1}{2}} \exp(j\frac{3\pi}{4}) \sum_{m=1}^{10} \tau_m' \exp(-j\xi\tau_m'), & \text{when } \xi > 1.25, \end{cases} \tag{25}$$

$$v_0^{(1)} \approx \begin{cases} \sqrt{-j\pi\xi} \left\{ 1.0 + \sum_{m=1}^{10} D_m(-j\xi)^{\frac{3m}{2}} \right\}, & \text{when } \xi \le 1.25 \\ (\pi\xi)^{\frac{1}{2}} \exp(j\frac{3\pi}{4}) \sum_{m=1}^{10} (1 + j\xi\tau_m') \frac{\exp(-j\xi\tau_m')}{\tau_m^3}, & \text{when } \xi > 1.25. \end{cases} \tag{26}$$
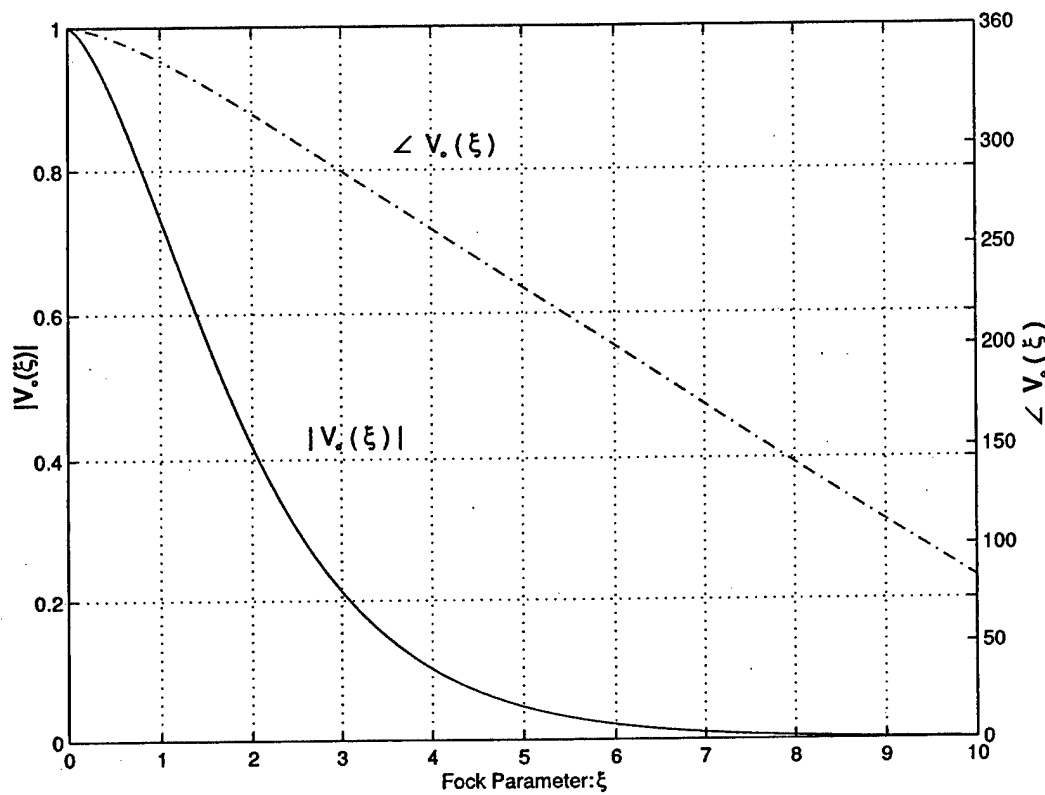
Fig. 9. Magnitude and Phase (in degrees) of the TE surface Fock function $v_0(\xi)$ given by (23).

The first derivatives are given by:

$$v_0' = \frac{1}{2\xi}\{v_0(\xi) - v_1(\xi)\}$$

$$v_1' = \frac{3}{2\xi}\{v_1(\xi) - v_2(\xi)\} \tag{27}$$
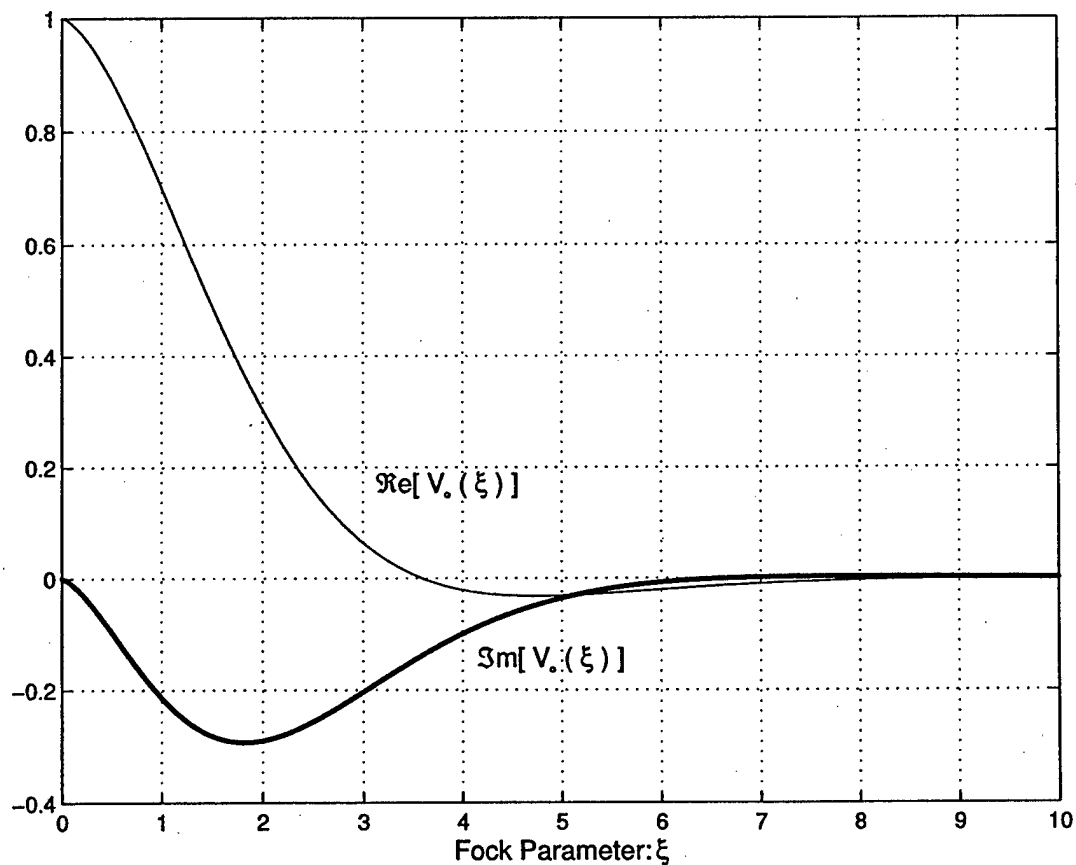
Fig. 10. Real and Imaginary parts of the TE surface Fock function, $v_0(\xi)$, given by (23).

In (22) to (27), the first ten complex roots of the first derivative of the Airy function are defined as $\tau_p = |\alpha_p| \exp(-j\frac{\pi}{3})$ and lie in the 4$^{\text{th}}$ quadrant. The various values of $|\alpha_p|$ are given ihe following table, below. The coefficients A_m, B_m, C_m and D_m in (22) to (27), necessary for calculating the convergent representation in the '*lit*' region ($\xi \leq 1.25$), read:
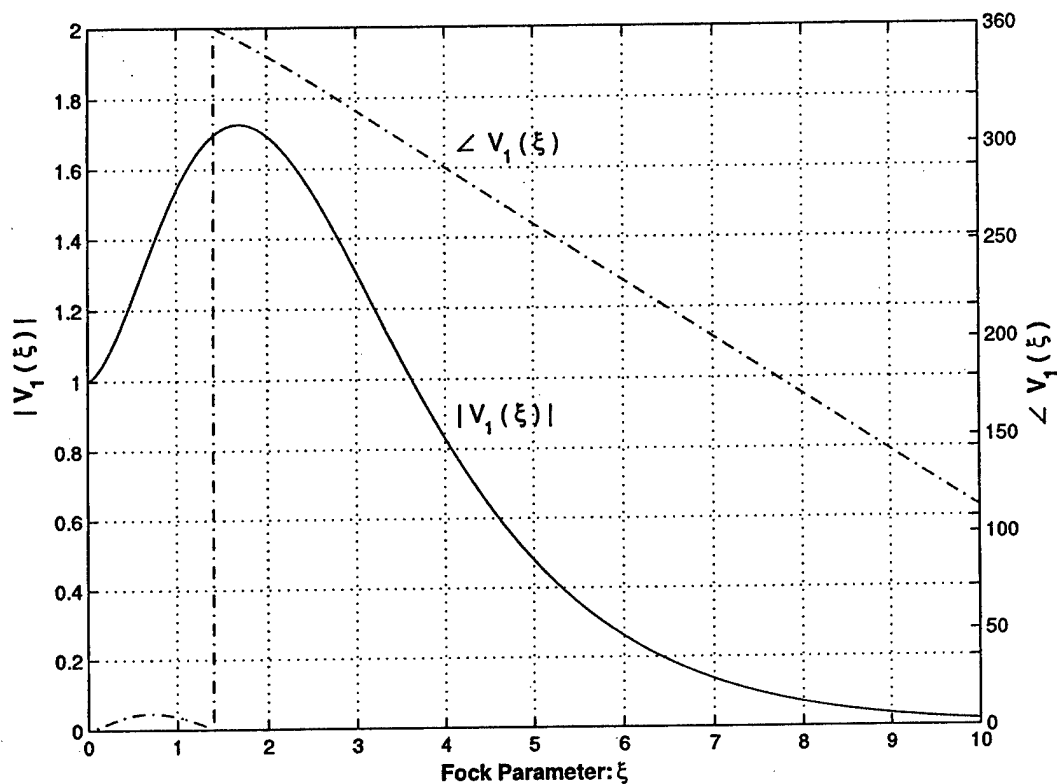
Fig. 11. Magnitude and Phase (in degrees) of the TE surface Fock function $v_1(\xi)$ given by (24).

TABLE I

MAGNITUDE OF THE ROOTS OF $\mathrm{Ai}'(z) = 0$

Index: p	$|\alpha_p|$
1	1.018792797
2	3.24819758
3	4.82009921
4	6.16330736
5	7.37217726
6	8.48848673
7	9.53544905
8	10.5276604
9	11.47505663
10	12.38478837
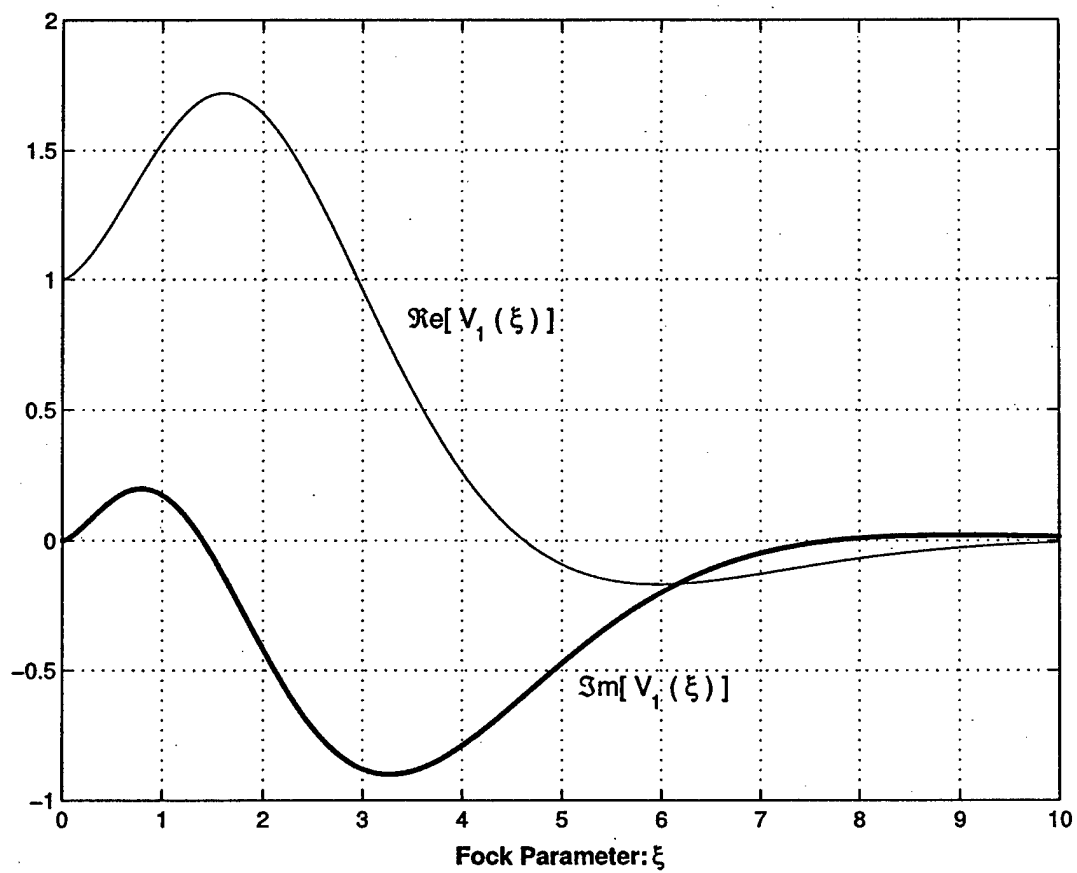
Fig. 12. Real and Imaginary parts of the TE surface Fock function, $v_1(\xi)$, given by (24).
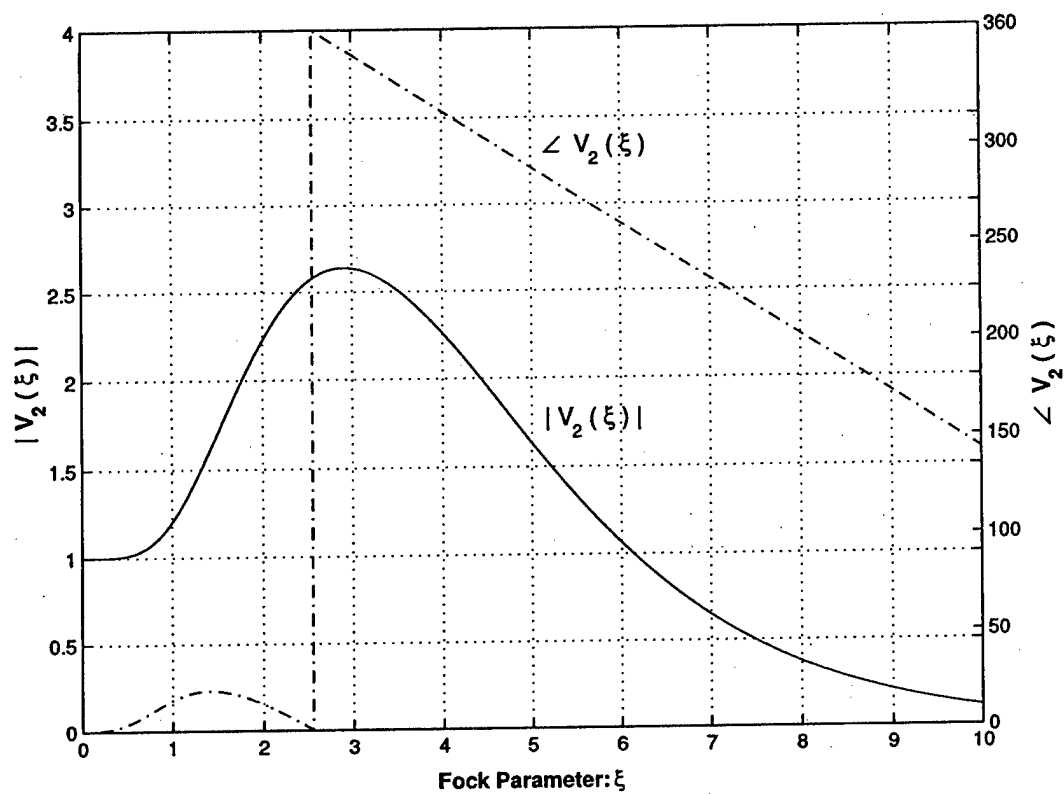
Fig. 13. Magnitude and Phase (in degrees) of the TE surface Fock function $v_2(\xi)$ given by (25).
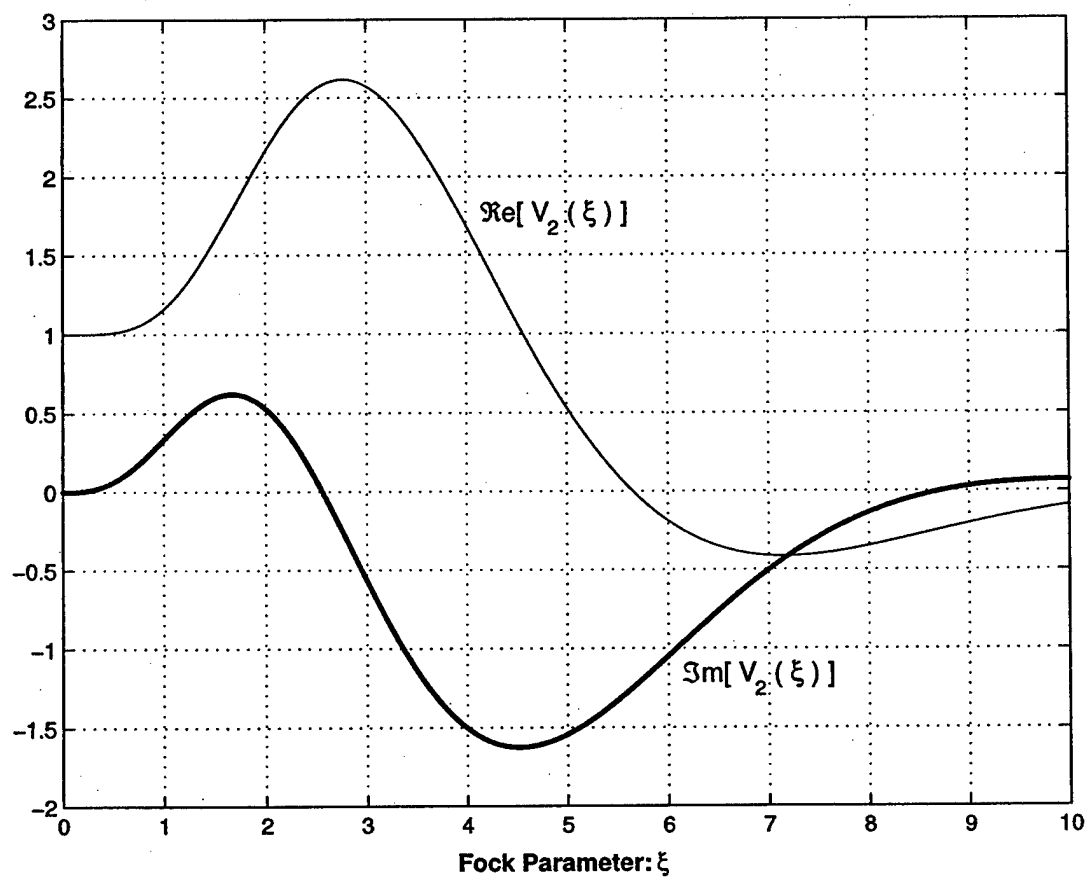
Fig. 14.   Real and Imaginary parts of the TE surface Fock function $v_2(\xi)$ given by (25).
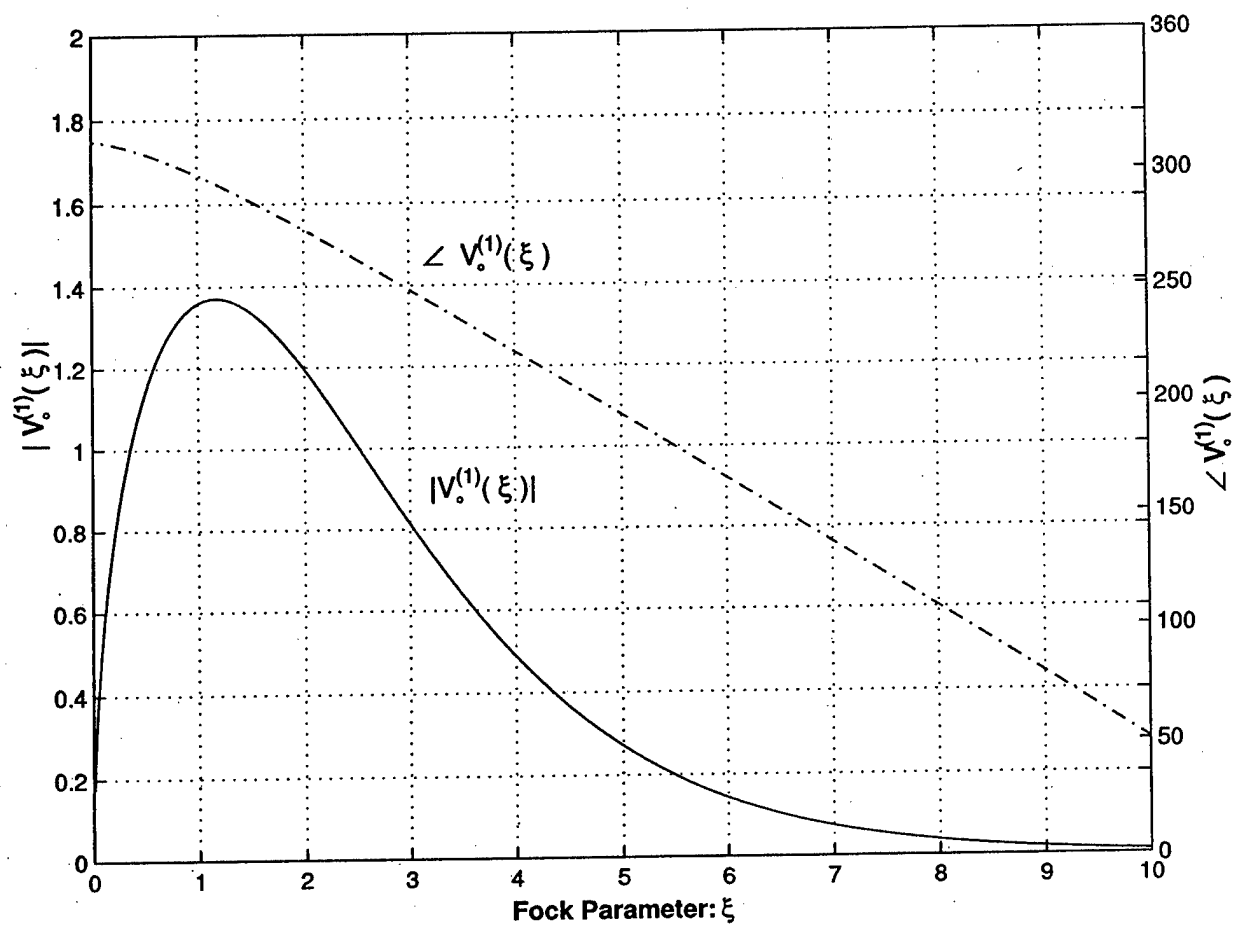
Fig. 15. Magnitude and Phase (in degrees) of the TE surface Fock function $v_0^{(1)}(\xi)$ given by (26).
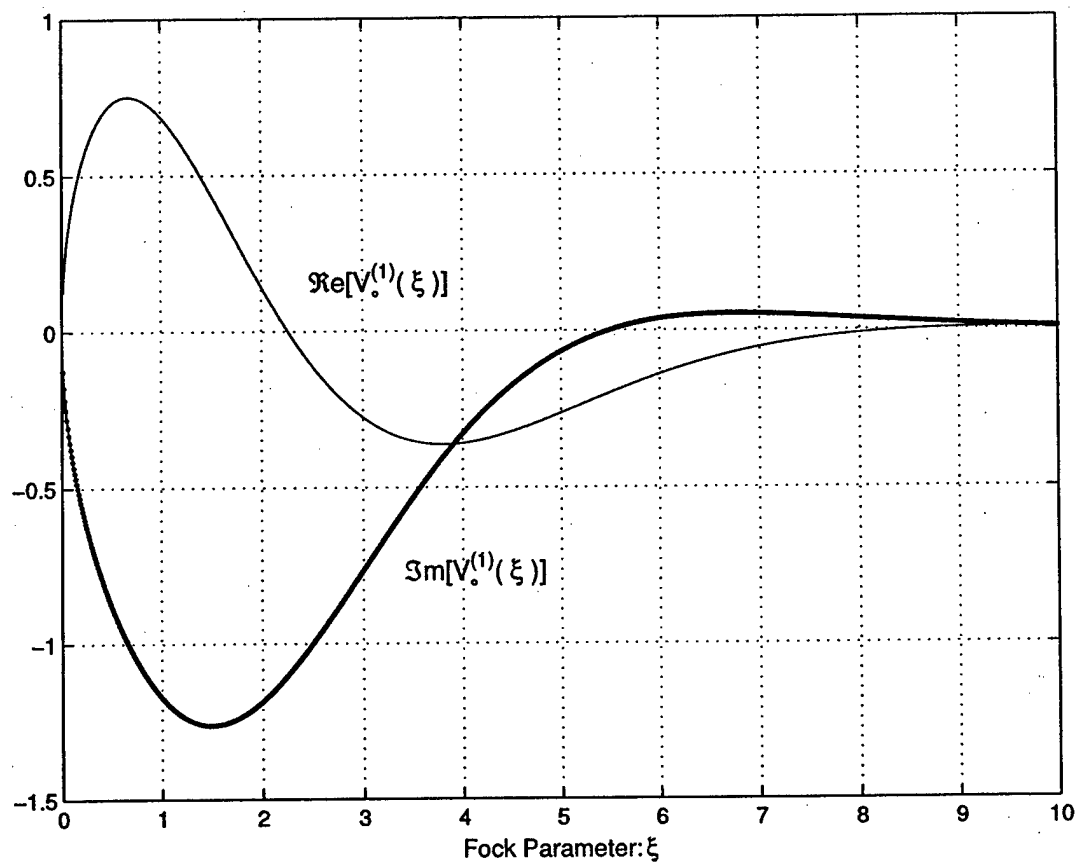
Fig. 16. Real and Imaginary parts of the TE surface Fock function $v_0^{(1)}(\xi)$ given by (26).
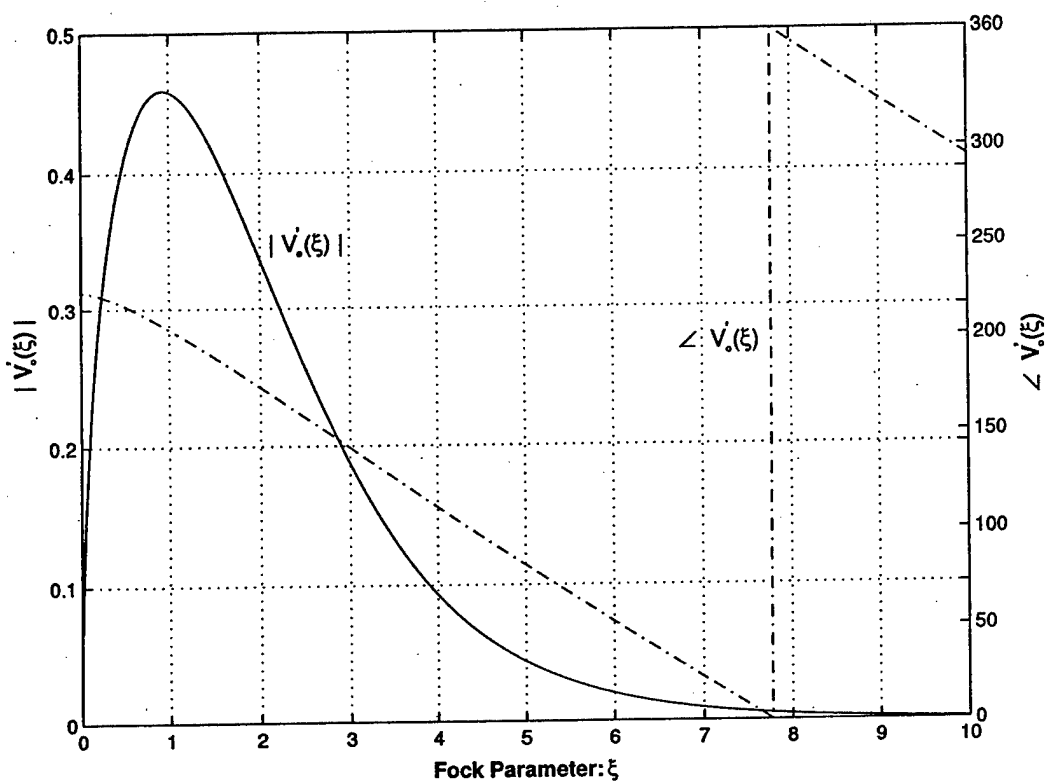
Fig. 17. Magnitude and Phase (in degrees) of the TE surface Fock function $v_0'(\xi)$ given by (27).
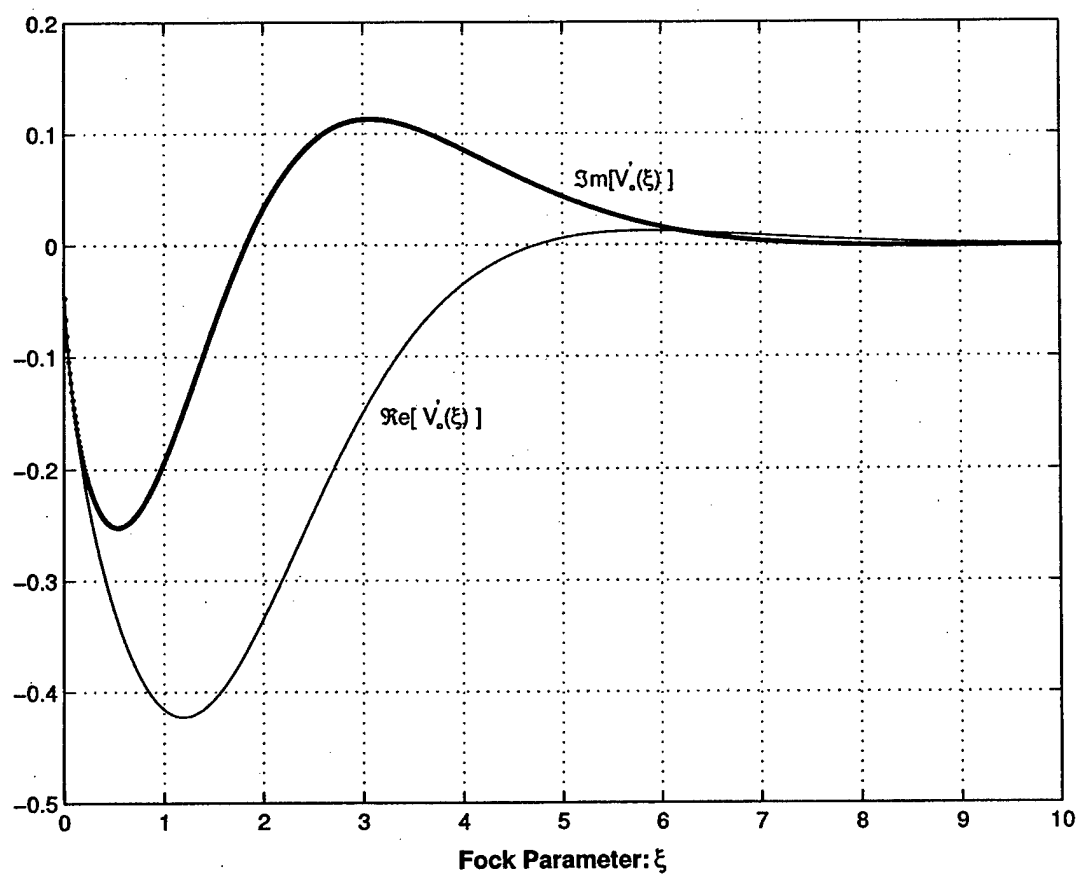
Fig. 18. Real and Imaginary parts of the TE surface Fock function $v_0'(\xi)$ given by (27).
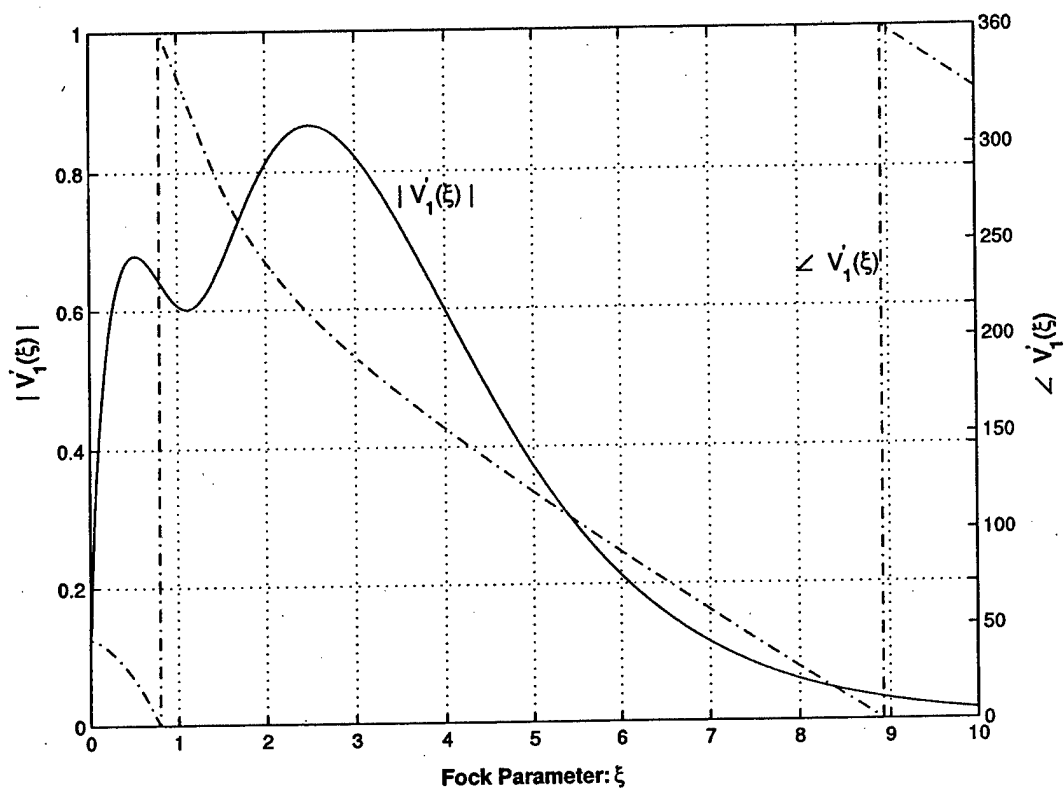
Fig. 19. Magnitude and Phase (in degrees) of the TE surface Fock function $v_1'(\xi)$ given by (27).
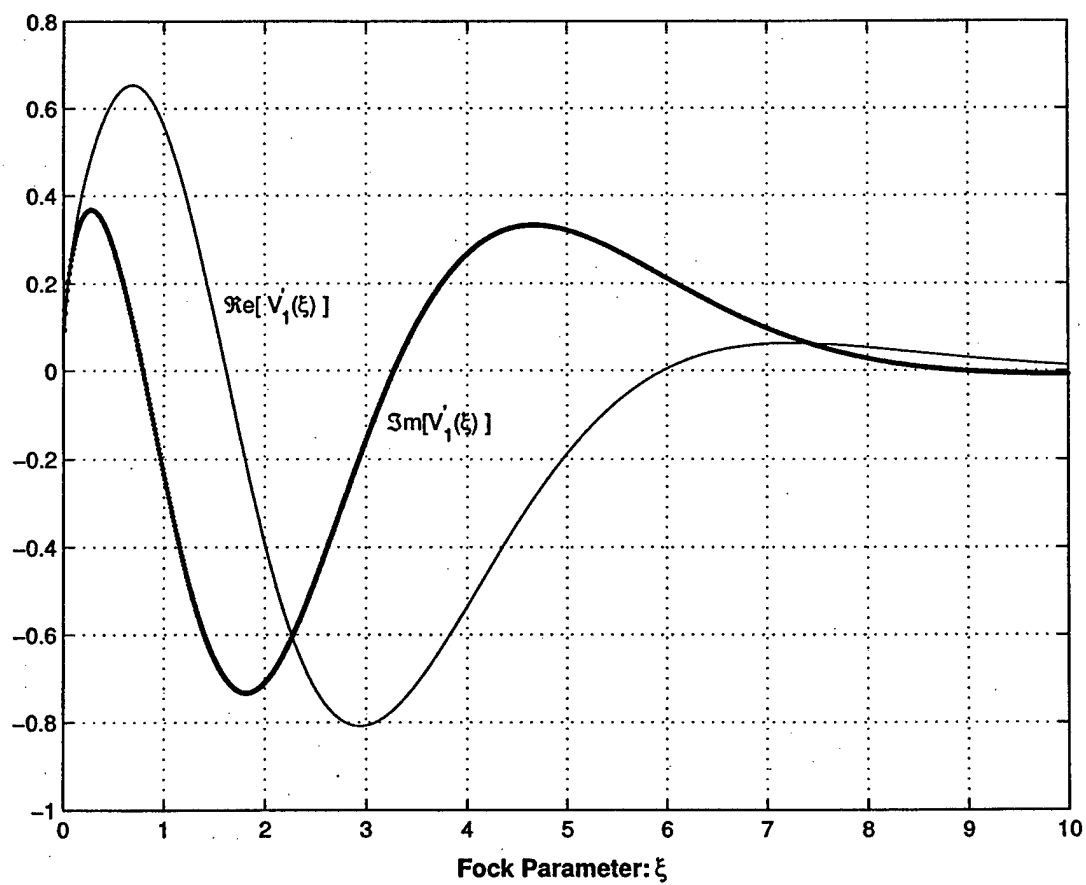
Fig. 20.   Real and Imaginary parts of the TE surface Fock function $v_1'(\xi)$ given by (27).

TABLE II

Coefficients of the Convergent Series in Lɪᴛ Region

m	A_m	B_m	C_m	D_m
1	$4.43113462726 \times 10^{-01}$	$8.86226925453 \times 10^{-01}$	$0.00000000 \times 10^{-00}$	$3.76126389032 \times 10^{-01}$
2	$1.1666666667 \times 10^{-01}$	$5.833333333 \times 10^{-01}$	$5.8333333333 \times 10^{-01}$	$8.3333333333 \times 10^{-02}$
3	$2.42327674928 \times 10^{-02}$	$1.93862139943 \times 10^{-01}$	$3.87724279886 \times 10^{-00}$	$1.46271373512 \times 10^{-02}$
4	$4.39814814815 \times 10^{-03}$	$4.83796296296 \times 10^{-02}$	$1.4513888889 \times 10^{-01}$	$2.27864583333 \times 10^{-03}$
5	$7.28425451422 \times 10^{-04}$	$1.01979563199 \times 10^{-02}$	$4.07918252796 \times 10^{-02}$	$3.30851916278 \times 10^{-04}$
6	$1.12285816943 \times 10^{-04}$	$1.90885888803 \times 10^{-03}$	$9.54429444013 \times 10^{-02}$	$4.56633391204 \times 10^{-04}$
7	$1.62748797057 \times 10^{-05}$	$3.25497594114 \times 10^{-04}$	$1.95298556468 \times 10^{-03}$	$6.03337983082 \times 10^{-06}$
8	$2.23225280182 \times 10^{-06}$	$5.13418144419 \times 10^{-05}$	$3.59392701093 \times 10^{-04}$	$7.65176466954 \times 10^{-07}$
9	$2.91130735093 \times 10^{-07}$	$7.56939911241 \times 10^{-06}$	$6.05551928993 \times 10^{-05}$	$9.32899095284 \times 10^{-08}$
10	$3.62483587817 \times 10^{-08}$	$1.05120240467 \times 10^{-06}$	$9.46082164204 \times 10^{-06}$	$1.09501952127 \times 10^{-09}$

MULTI-BAND, MULTI-POLARIZED SINUOUS ANTENNAS FOR SATELLITE AND TERRESTRIAL APPLICATIONS

Michael C. Buck[1], Tom Cencich[2], Jason Burford[2], and Dejan S. Filipović[1]

[1]Department of Electrical and Computer Engineering
University of Colorado
Boulder, CO 80309-0425
[2]Lockheed Martin Space Systems—Aeronautics Operations
12257 State Hwy. 121
Littleton, CO 80127

ABSTRACT

Four and two arm multi-band slot sinuous antennas are proposed. The four arm geometry produces a split-beam or conical radiation pattern whereas the two arm geometry radiates with the maximum gain at broadside. These radiation patterns are well suited for terrestrial and satellite applications, respectively. Both antennas have narrow bandwidth regions of concurrent good axial ratio (< 4 dB for circular polarization), VSWR (≤ 1.8:1 without complex feed network), good azimuth symmetry (omnidirectionality / WOW < 3 dB), and gain (≥ 5 dBic). A distinctive feature of the proposed antennas is their multi-polarized nature. This is a result of the "folded" arm geometry and the inability of the aperture to perform polarization filtering when ambiguous phase progression between neighboring arms is applied. As a result, both right- and left-handed circular polarizations are possible on the same antenna, appearing in different frequency bands. Additionally, when power is equally split between RHCP and LHCP modes, regions of linear polarization occur (between circularly polarized bands). Each antenna is fabricated on a RT/Duroid® 5880 (ε_r = 2.2) substrate and has a metallic backed, non-absorptive cavity. Measured and simulated data are presented and discussed.

1. Introduction

In 1982, Raymond H. DuHamel, the co-inventor of the log-periodic principle, conceived yet another frequency independent structure, the sinuous

antenna. Though the first realization was planar, DuHamel gave thorough descriptions of conical and pyramidal projections of the basic sinuous curve with additional functionalities and restrictions [1]. A planar sinuous curve is defined by the following:

$$\varphi(r) = (-1)^p \alpha_p \sin\left[\frac{\pi \cdot \ln\left(\frac{r}{R_p}\right)}{\ln\left(\tau_p\right)}\right]$$ (1)

where r is the radial distance from the origin to a point on the sinuous curve with azimuthal coordinate, φ. R_p is the larger radius of the pth cell with angular width denoted as α_p and growth rate as τ_p. These and other parameters important for the description of the sinuous antenna, such as the angular between sinuous arms (δ), are depicted in Fig. 1. As shown, the inner and outer radius of the pth cell define the sinuous growth rate, $\tau_p = R_p/R_{p+1} = r_p/r_{p+1} < 1$. Note that the indexing of cells and arms begins with the outermost cell or arc as $p=1$ and increases toward the center. Additionally, a self-complementary arrangement results in the most consistent impedance and pattern behavior and is typically utilized in sinuous antennas.

For a truly log periodic structure, α_p and τ_p are independent of the cell number p, i.e. they are constant throughout the entire structure. A variation of a log periodic design is a quasi-log periodic design where α_p and/or τ_p vary with each cell. Examples of log periodic and quasi-log periodic structures, shown in Fig. 2, are both self-complementary and with identical defining parameters, with one exception, (a) has a constant growth rate ($\tau_p = \tau = 0.85$), and (b) has a varying growth rate ($0.70 \leq \tau_p \leq 0.93$). A simple transform of the polar coordinates of the structure, $\varphi(r) \rightarrow \varphi(ln(r))$ [2], produces shapes in which the periodicity and self-complementarity of a sinuous antenna can easily be seen.

Another variation of the sinuous structure defined by Eq. (1) is the folded spiral. The folded spiral is defined as a continuous line of the same growth rate but oppositely wound log (equiangular) spirals. Given below are the parametric equations for generating a normal logarithmic spiral (Eq. (2)), a folded spiral (Eq. (3)), and the polar conversion including the sinuous parameter, α_p (Eq. (4)). A constant (r_0) is the starting radius for the curve. The sinuous and folded spiral structures are very similar when formed with the same geometric values of growth rate (τ_p) and angular width ($2(\alpha_p+\delta)$). The largest deviation between the two occurs at the inflection points, or tips, where the curve reverses direction (see Fig. 3).

While there is little difference in the overall geometry as well as in the performance, numerical simulations often needed not only for the design but also for improving our understanding of the antenna behavior, tend to favor the folded spiral. Excessive manual effort in generating an FE mesh of a sinuous structure is needed in order to achieve consistent convergence. Shown in Fig. 4 are conjugate-gradient reached lowest tolerances within 8000 iterations for two antennas with approximately the same number of finite elements. Since performance of the two geometries is very similar (at points where the tolerance was < 0.1), the subsequent studies and design were performed on a folded spiral. Note that the obtained conclusions are valid for both geometries.

$$
\left.
\begin{aligned}
x &= r_0 \cdot \tau_p^{\frac{-\varphi}{\pi}} \cdot \cos(\varphi) \\
y &= r_0 \cdot \tau_p^{\frac{-\varphi}{\pi}} \cdot \sin(\varphi)
\end{aligned}
\right\}
\tag{2}
$$

$$
\left.
\begin{aligned}
x &= r_0 \cdot \tau_p^{\frac{-\varphi}{\pi}} \cdot |\cos(\varphi)| \\
y &= r_0 \cdot \tau_p^{\frac{-\varphi}{\pi}} \cdot \sin(\varphi)
\end{aligned}
\right\}
\tag{3}
$$

$$
\left.
\begin{aligned}
r &= \sqrt{x^2 + y^2} \\
\varphi &= \frac{2}{\pi}\alpha_p \cdot \arctan\left(\frac{y}{x}\right)
\end{aligned}
\right\}
\tag{4}
$$

A traditional sinuous antenna is broadband and can provide two orthogonal senses of polarization from a single aperture. High frequency operation limits are determined by the radial distance at which the sinuous structure begins (feeding region transition) and similarly, low frequencies are limited by outer diameter of the antenna. However, the finite width of the radiating regions should be taken into account when determining the frequency range. Sinuous antenna research has been primarily oriented toward broadband four-arm printed/wire structures. They require additional feeding circuitry to achieve the proper phasing of the individual arms, which adds substantial cost and complexity to the overall antenna. Also, an absorbing cavity is required for proper broadband operation [1, 3-4].

The sinuous antennas proposed here are unique in both operation and realization. Both two- and four-arm antennas are excited in a way to support a traveling wave within slots, with significant difference (as will be demonstrated later) between a dual-linear broadband slot sinuous antenna [7]—the only slot sinuous antenna publication the authors are aware of. In addition, non-absorptive

cavities are used to enhance performance [8, 9]. Use of a lossless cavity (unlike traditional sinuous antennas with lossy, absorptive cavities) contributes to matched efficiencies over 95% for both two- and four-arm geometries while the axial ratio is reduced by more than 5 dB. The four- and two-arm geometries produce a split-beam with a gain null at broadside (mode 2) and a single pencil beam with maximum gain at broadside radiation patterns (mode 1), respectively. The former is fed with a single grounded CPW line feed and the latter by a balanced 0°/180° feed. Antennas like these may be a good choice for applications requiring flush or conformal mounting as well as multi-band and multi-polarized performance from a single antenna. The "folded" nature of the slot line and the inability of the aperature to perform polarization filtering when an ambiguous phase progression is applied between sinuous arms produce this, previously not investigated, behavior. That is, there is no physical difference in having a phase progression that proceeds clockwise or counter-clockwise; the end result remains the same. For instance with the four arm antenna, a phase progression of (0°, 180°, 360°, 540°)≡(0°, 180°, 0°, 180°) is synonymous with the progression of (0°, -180°, -360°, -540°)≡ (0°, 180°, 0°, 180°). Without the ability to filter out one of the available polarizations (as the wrapping sense does for a spiral antenna), both circularly polarized modes co-exist (modes +2 and -2). The same is true with the two arm antenna and phase progressions of (0°, 180°) and (0°, -180°). Two circularly polarized modes (+1 and -1) are possible but no filtering occurs so they both are sustained. Because of this ambiguity, a unique multi-band and multi-polarized signature is observed with these antennas.

2. Antenna Realization

2.1 Four-Arm Slot Sinuous Antenna

The four-arm slot sinuous geometry realized in this work consists of seven bends and six and one half arcs. A constant slot width is maintained by choosing a variable growth rate (quasi-log periodic structure) for the antenna ($\tau = 0.75$ at innermost arc and $\tau = 0.89$ at outermost arc). The angles α and δ which define the angular width of the sinuous arm are 45° and 22.5°, respectively, for all cells. The antenna is chemically etched upon a RT/Duroid® 5880 ($\varepsilon_r = 2.2$) substrate and backed by a flat 5 mm deep lossless, air-filled cavity. The maximum diameter of the radiating aperture of the antenna is approximately 5 cm (cavity diameter ≈ 5.3 cm).

Ambiguous phase progression is accomplished through the use of a non-radiating co-planar waveguide (CPW) mode excitation at the center of the antenna as shown in Fig. 5. A pair of metallic pins positioned through vias and connected to a small, circular metallic disk on the back of the antenna insures correct

phasing and grounding. This feeding scheme generates 180° phase progression between adjacent arms of the antenna (0°, 180°, 0°, 180°), or a total phase progression of 720° with a single port. As discussed above, due to the reversing direction of the geometry it is possible for both RHCP and LHCP polarizations to concurrently exist. Because of this and the inability of the aperture to filter one set of circularly polarized modes, a mixture of oppositely polarized modes occurs. In this case, the phasing is like that of the ±2 modes of a four-arm spiral antenna, resulting in a modal ambiguity and a unique multi-band, multi-polarized behavior. The actual realized antenna can be seen in Fig. 6.

The active regions for each operating band are determined by the same equation as for a sinuous antenna operating in the 2nd mode (note that this antenna must have at least five arms) [1, 4]:

$$r \cdot 2(\alpha + \delta) \approx \lambda \qquad (5)$$

TABLE 1 - DETERMINATION OF ACTIVE REGION OF FOUR-ARM SINUOUS ANTENNA BY ANALYZING INDIVIDUAL SETS OF ARMS.

Section # (p)	Slot Center Radius (cm)	Theoretical Active Radius (cm) From (4)
1	2.2	2.1
2	1.9	1.9
3	1.6	1.7
4	1.4	1.4
5	1.1	1.1
6	0.9	0.9

where $2(\alpha + \delta)$ is, as before, the angular width of a single arm, r is radial distance outward from the center of the antenna, and λ is the wavelength of the resonant band. To numerically verify this equation, sets of arcs are examined separately. More specifically, the circular array of four slots, for each band, is excited with the same phase progression as the composite (or original) antenna. The FE-BI model is used to compute their performance at the center of the band was associated with the minimum value for axial ratio in this frequency swept, numerical experiment. Simulated results show excellent agreement between the

central frequency of the composite sinuous structure and each set of four slot arms. Shown in Table 1 are the radial distances of the slot centers (where the excitation is applied) and theoretical values for the radiating ring radii of the composite sinuous antenna obtained from Eq. (5). Although this equation predicts the theoretical location of the active regions, in simulations of the full composite geometry, we see that additional resonances can also occur, degrading the azimuthal symmetry of the far-field pattern (see Fig. 7).

2.2 Two-Arm Slot Sinuous Antenna

The two-arm slot sinuous antenna geometry is composed similar to the four-arm, but with four bends and four and one half arcs. The realized antenna is shown in Fig. 8. For the previously stated convergence reasons, a folded spiral geometry was used rather than the true sinuous (see Fig. 9). The angles α and δ are 90° and 45°, respectively (twice the values for the four-arm). A constant growth rate ($\tau_p = \tau = 0.62$) was used to allow the slot width to increase logarithmically toward the outermost arc of the antenna. This is similar to the traditional printed sinuous antennas with the difference being the printed antennas are built with at least three arms since the necessary number of arms for broadband operation is equal to $2m+1$. Here m is the total number of desired modes of operation. Thus for single mode broadband operation we need three arms, and for dual-mode we need five arms, etc. RT/Duroid® 5880 was again used as the substrate. The two-arm antenna is backed by an air-filled "stepped" depth cavity with a smaller cavity depth for the higher frequency radiation regions (inner regions of the antenna) and a deeper cavity for the lower frequency regions (outer regions of the antenna). The cavity diameter is approximately 6 cm and 4 cm is left for mounting and termination of the last arc. Resistors are used on the outer open-end termination to potentially allow for an additional band. Of course, if this band is excited it would have reduced efficiency. Note that resistors are not required for printed structures.

Feeding is accomplished with balanced, dual port, 0°/180° feeds. The modal ambiguity also exists on this antenna—(0°, 180°) phase progression undistinguished from (0°, -180°)—and we again have a multi-band, multi-polarized operation. Since, the number of broadband modes for an n-armed antenna is ½(n - 1), none can exist for the two-arm antenna.

3. Discussion of Results

Antenna pattern measurements were taken within a finite, untreated, circular ground plane (diameter ≈ 30 cm for four-arm and ≈ 50 cm for the two-arm). Thus, some diffraction effects are expected. Numerical results for both

two- and four-arm geometries were obtained from an in-house finite element-boundary integral (FE-BI) code [9].

3.1 Four-Arm Slot Sinuous Antenna

Measured and simulated VSWR are compared, with good agreement between them. There is an approximate 3% frequency shift which is likely due to discrepancies between the actual fabricated antenna and the model used to simulate it (Fig. 10). For example, numerical results using a dielectric constant of about 10% higher produced almost perfect agreement with measurements. To increase efficiency of the antenna and improve axial ratio, a lossless, air-filled cavity was used. As can be seen in Fig. 11, an absorptive cavity cannot be used as it degrades antenna performance dramatically.

There are several bands with return loss better than 10 dB, total antenna efficiencies greater than 90% (Fig. 12), axial ratios < 5 dB (Fig. 13), and good azimuthal symmetry (WOW) taken at peak gain elevation angles. For realized structure these bands occur at normalized frequencies of 1, 1.2, 2.1, and 2.6 and can be tuned by changing the growth rate, τ_p. There is another band at 1.6 but due to effects of the cavity resonance, WOW>6 dB and return loss > 6 dB. The measured polarization signature of this antenna can be seen in Fig. 14, where RHCP and LHCP are represented by the white and black colors, respectively.

Fine tuning can be performed by slight variations in the cavity shape and dimensions. The elevation angle of maximum gain varies from the theoretical value of 38° for this mode (for a spiral antenna) by only 1° at all but the third band. The third band is affected by its close proximity to the cavity resonance and thus has a larger deviation, about 6°, from the theoretical value. Far-field patterns for these bands can be seen in Figs. 15 and 16.

3.2 Two-Arm Slot Sinuous Antenna

Using the same numerical and measurement methods, the muilt-band, multi-polarized two-arm antenna is analyzed. Again we can see specific frequency bands at which axial ratio, gain, and omnidirectionality are satisfactory. These bands are clearly related to the sinuous growth rate as can be observed in Fig. 17 where absorber cavity backed antenna is simulated. As with its four-arm counterpart, it is also necessary to have a lossless cavity backing with this antenna. From Fig. 18 it is clear that although the axial ratio trend is much smoother with an absorber backing, circular polarization hardly exists as the axial ratio is greater than 8 dB, even at the resonant bands. But with an air-filled cavity, circularly polarized bands with axial ratio < 3 dB appear. Shown in Fig. 19 is the measured polarization signature of this antenna demonstrated as a

difference in gains between RH and LH components. Note that, without an absorptive cavity, resonances can occur and antenna performance degrades. For the realized structure, this can be seen at a normalized frequency of around 2 in Figs. 18 and 19. The cavity can also be treated as a series connection of two coaxial transmission lines with different characteristic impedances. Knowing the depths of the cavity (length of coaxial line) we can use conventional transmission line equations to determine at what frequency the shorted load of the cavity backing becomes an open. The result of this analysis can be seen in Fig. 20. Note that the frequency of the cavity resonance as determined from the transmission line model corresponds approximately to the resonance location as determined from the FE-BI model.

Circularly polarized and narrow bands are obtained at normalized frequencies of 1.0, 1.8, and 2.3. In addition, linearly polarized bands occur between these CP bands at normalized frequencies of 1.4 and 2.0. The far-field patterns at each band can be seen in Fig. 21a-b. The maximum gain for each band is at broadside with cross-polarizations at $\theta=0°$ of at least 15 dB for CP bands. Also shown in Fig. 21c are the patterns of LP bands (between CP bands) for both E and H planes.

As with the four-arm antenna, the band frequencies can be tuned by changing the positions of the arms, i.e. by modifying the growth rate, τ, and fine-tuned by changing the dimensions of the cavity. One example is shown in Fig. 22. Here, the depth of the cavity is varied between 2 and 4 mm and the result on matched gain and axial ratio can be seen. The cavity resonance location can be shifted by about 13% whereas the axial ratio for the middle band only shifts by about 1%.

4. Conclusions

Two unconventional slot sinuous antennas are proposed. One with four arms and a conical radiation pattern and the other with two arms and a broadside beam pattern. Applications requiring orthogonal polarizations in separate bands from a single conformal or flush-mountable antenna can benefit form these designs. The split-beam pattern would be favorable for terrestrial uses and likewise, the normal mode pattern for satellite and space applications. With physical scaling of these antennas as well as careful designing of the locations of the slots (specifically the growth rate, τ), many frequency ranges can be accommodated.

High efficiency, multiple resonant bands with good axial ratio and omnidirectionality, and alternating polarization between bands are common in both the two- and four-arm geometries. Additionally, the linearly polarized bands

occurring between the circularly polarized bands provide additional functionality for this configuration.

5. Future Work

While neither design is optimized for a specific application, the potential for further progress exists. For instance, a cavity depth with a logarithmic growth, to match that of the antenna, has the prospect to improve performance. For easier modeling and fabrication, the cavity should be initially conical (linear growth). The use of absorptive cavity walls in numerical analyses has been shown to eliminate effects of the cavity resonance. This can also be easily incorporated into the fabricated design using commercially available absorber material or other techniques typically used with spirals.

The sinuous structure-to-feed transition is another aspect of design that needs further investigation. Rather than arbitrarily choosing a convenient geometrical transition at the center, a specifically designed region to match the sinuous structure should be considered. One technique is to design this structure in logarithmic space to match the period of the sinuous geometry but slowly reduce the angular width of the arm (by reducing α_p) and then reverse transform it back to physical space. The reduced arm width should allow for easy placement of the feed in the realized antenna while still maintaining some pre-defined log-periodic characteristics.

REFERENCES

[1] R. H. DuHamel, "Dual Polarized Sinuous Antennas," U.S. Patent 4658262, April 14, 1987.

[2] R. DuHamel and D. Isbell, "Broadband Logarithmically Periodic Antenna Structures," *IRE International Convention Record*, Vol. 5, March 1957, pp. 119-128.

[3] T. Chu and H. G. Oltman, Jr., "The Sinuous Antenna," *Microwave Systems News and Communications Technology*, vol. 18, pp. 40-48, June 1988.

[4] R. DuHamel and J. Scherer, "Frequency-Independent Antennas," *Antenna Engineering Handbook*, R.C. Johnson, Ed. New York: McGraw-Hill, 1993, Chapter 14.

[5] FEMLAB® v3.0a, *Comsol, Inc.* http://www.comsol.com.

[6] T. Ozdemir, J. L. Volakis, and M.W. Nurnberger, "Analysis of thin multioctave cavity-backed slot spiral antennas," *Inst. Elect. Eng. Proc. Microwaves, Antennas, Propagat.*, vol. 146, pp. 447–454, Dec. 1999.

[7] X. Begaud, P. Poey, J. P. Daniel, and G. Dubost, "Design of Wideband Dual Polarized Slot Antenna," in *Proc. of Millennium Conference on Antennas and Propagation*, 2000, CD-ROM.

[8] M.C. Buck and D.S. Filipović, "Split-Beam Mode Slot Sinuous Antenna," *IEEE Antennas and Wireless Propagation Letters*, vol. 3, No. 6, pp. 83-86, 2004.

[9] M.C. Buck, J. Burford, and D.S. Filipović, "Multiband Two-Arm Slot Sinuous Antenna, *Proc. 2004 IEEE AP-S USNC/URSI Symposium*, June 2004.
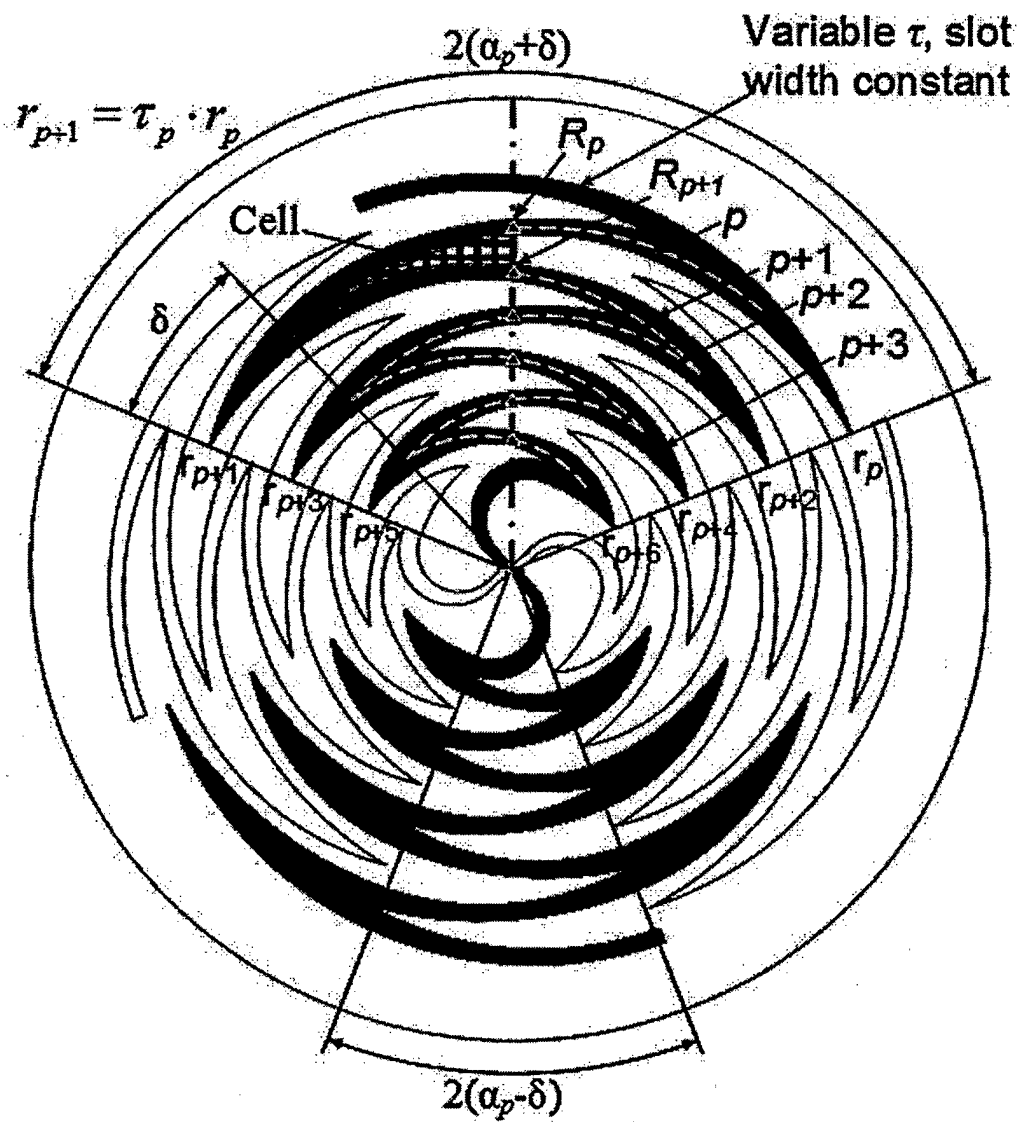
Fig. 1 - Four-arm slot sinuous antenna with description of geometric parameters.

(a)   (b)
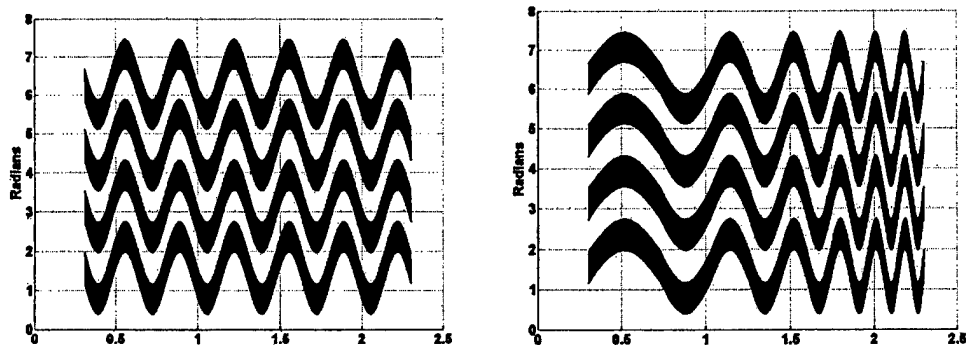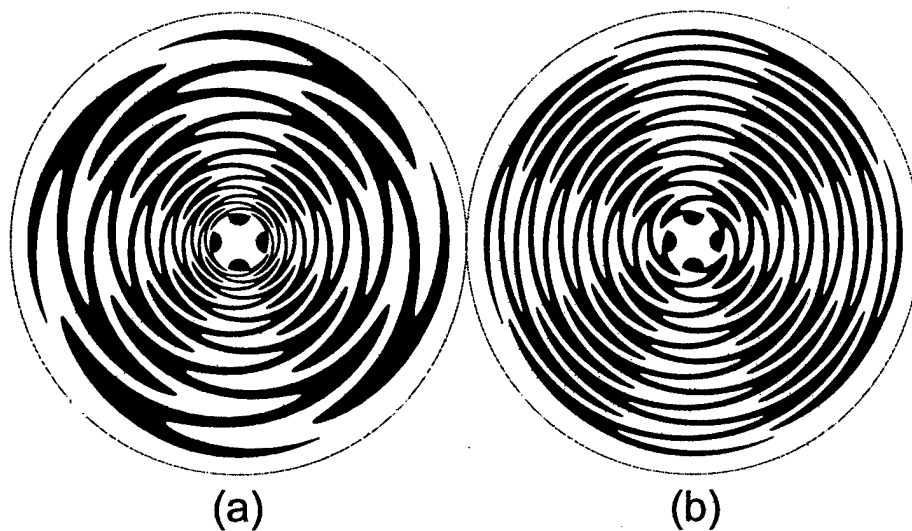
Fig. 2 – Identical four-arm printed sinuous antennas except for: (a) constant growth rate of 0.85 (b) varying growth rate from 0.70 (inner-most) to 0.93 (outer-most) to maintain constant slot width. Periodicity and self-complementarity can be seen in the bottom figures where x-axis is *ln(r)* and y-axis is φ [2].
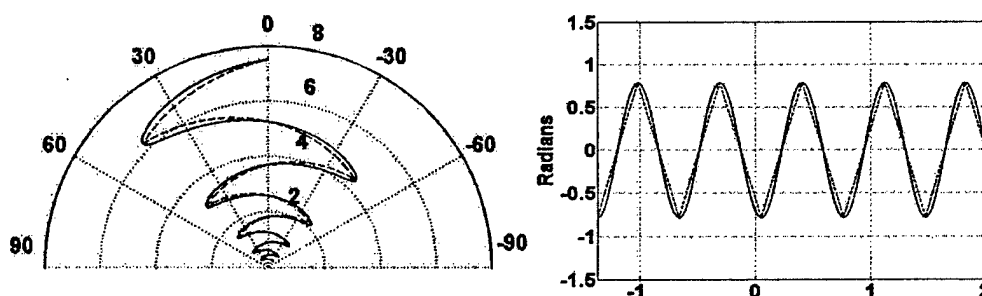
Fig. 3 - Comparison between sinuous curve and folded spiral curve. Essentially main difference is at each bend, the sinuous has smooth transitions between neighboring arcs as opposed to sharp corners associated with the folded spiral.

417
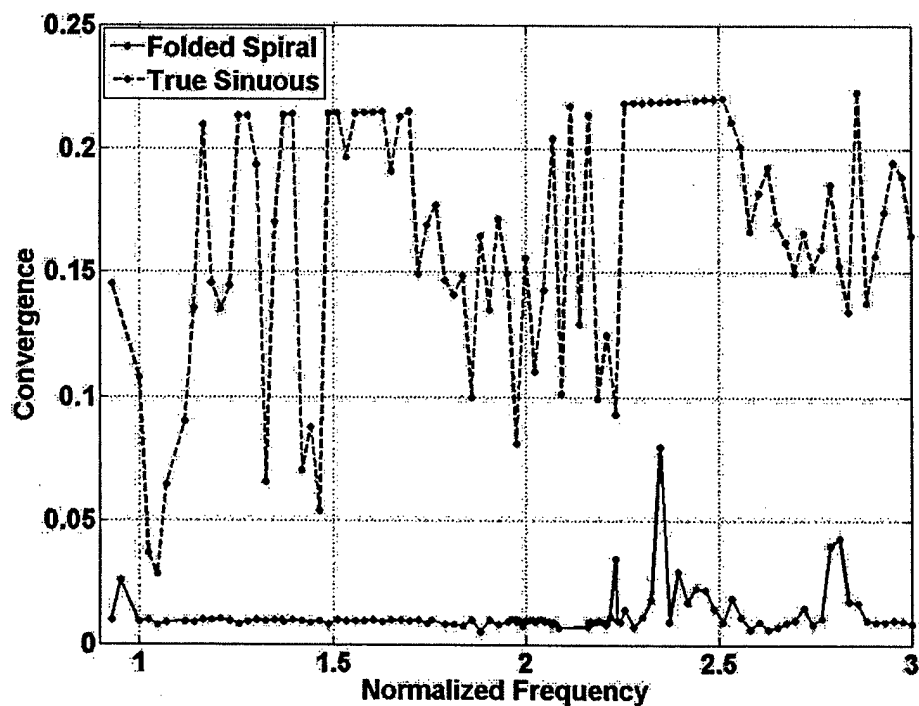
Fig. 4 – The simulation convergence history of the two-arm folded spiral and true sinuous geometries. Plotted are the minimum tolerances that iterative solver converged to within the first 8000 iterations. Total number of finite elements was approximately 9500 per layer for the folded spiral and approximately 9700 per layer for the sinuous. Automatic meshing of Comsol's FEMLAB® [5] was used to generate appropriate meshes. Simulations were performed with FE-BI code [6].
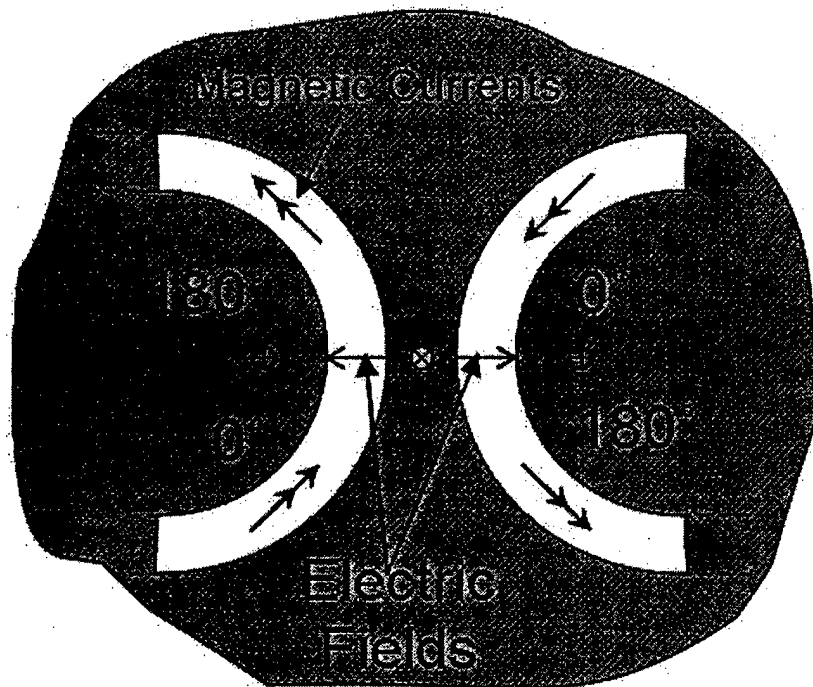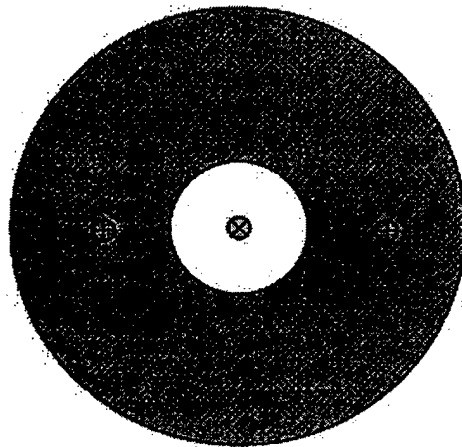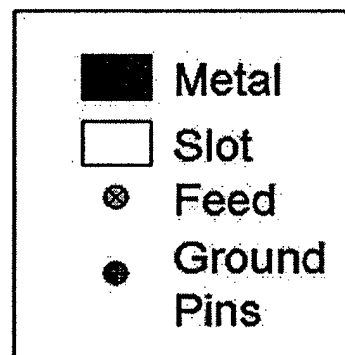
Fig. 5 - Feeding method of four-arm slot sinuous antenna.
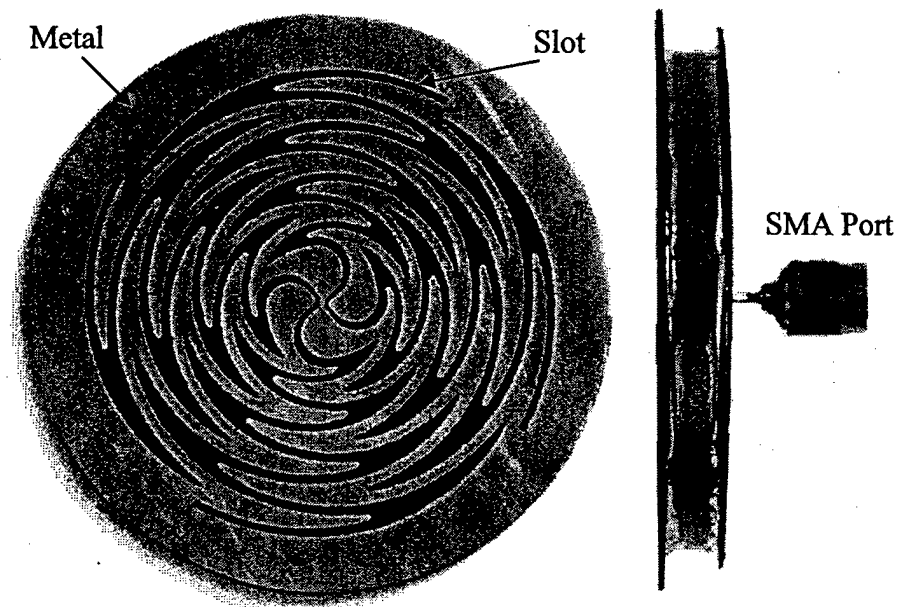
Fig. 6 - Realized four-arm slot sinuous antenna.
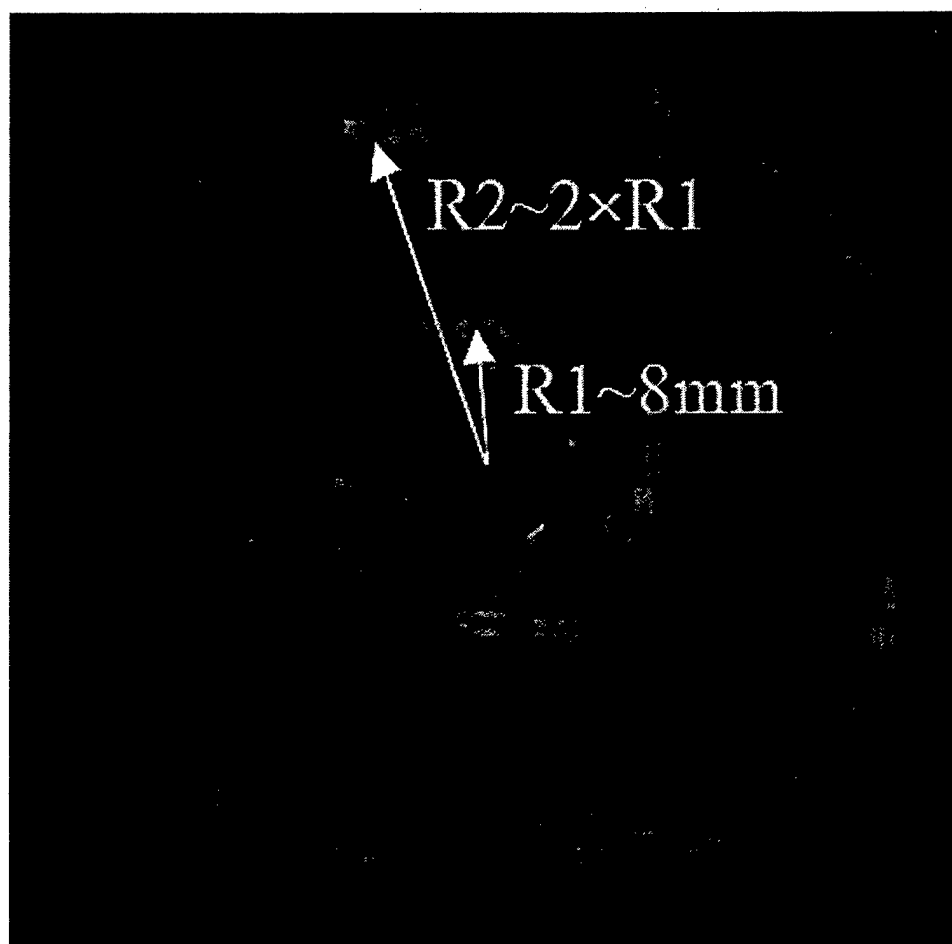
Fig. 7 - Electric field magnitudes within the slots of the four-arm antenna showing finite width active region as well as additional regions when slot fields (magnetic currents) strongly radiate.
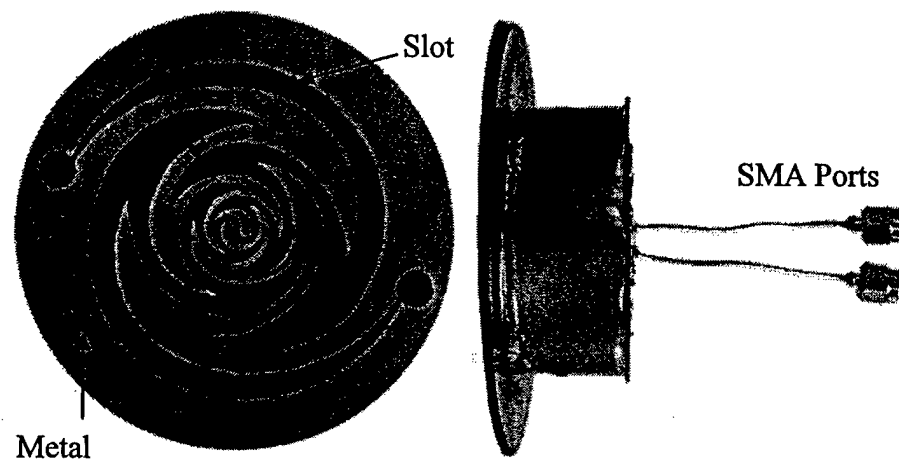
Fig. 8 - Realized two-arm slot sinuous antenna.
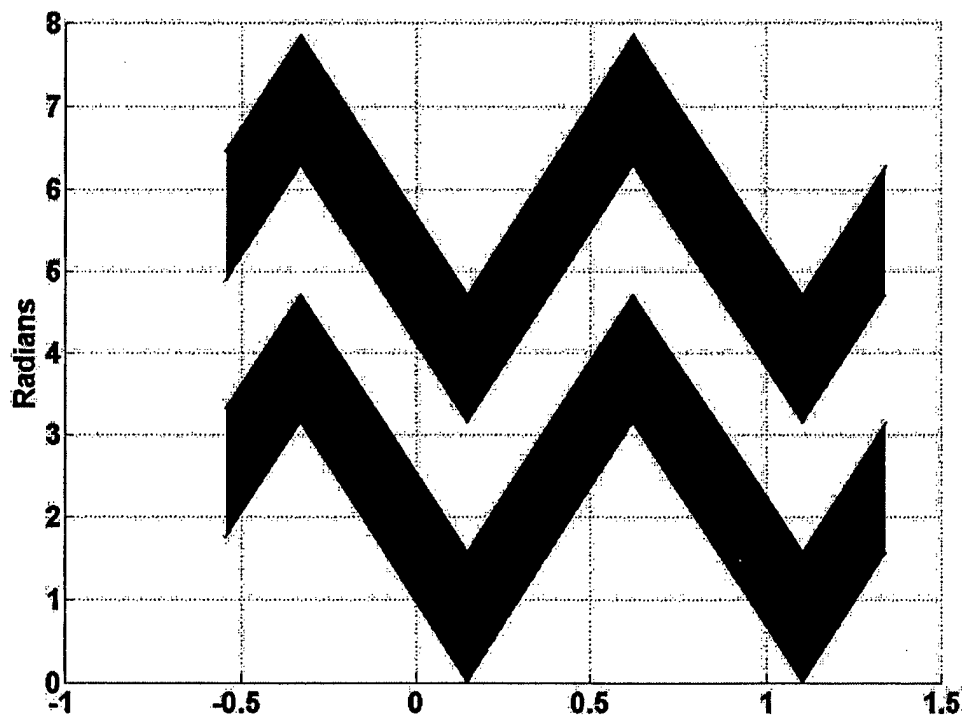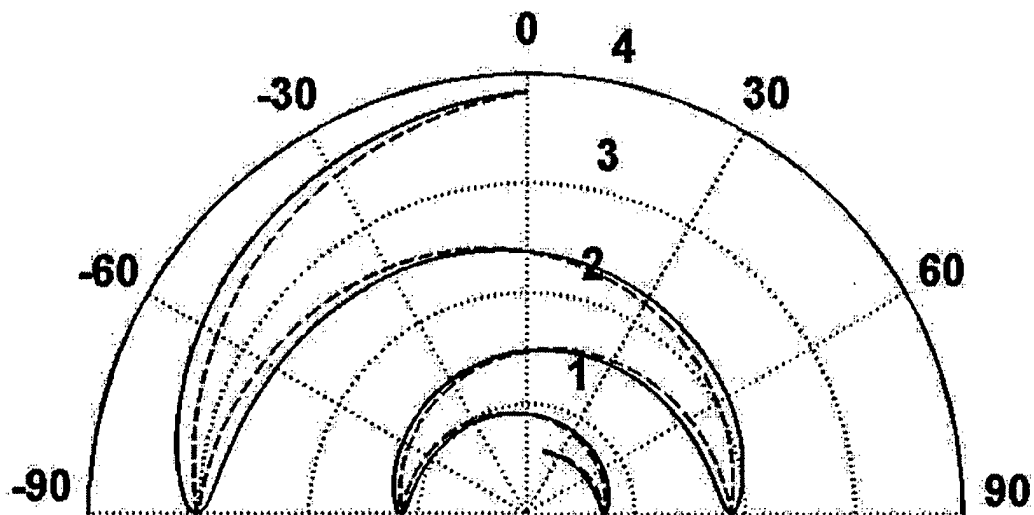
Fig. 9 - (top) Defining sinuous curve and associated folded spiral curve for the two-arm
sinuous antenna. (bottom) Logarithmic space transform for the realized antenna using
folded spiral geometry to facilitate good numerical computation convergence.
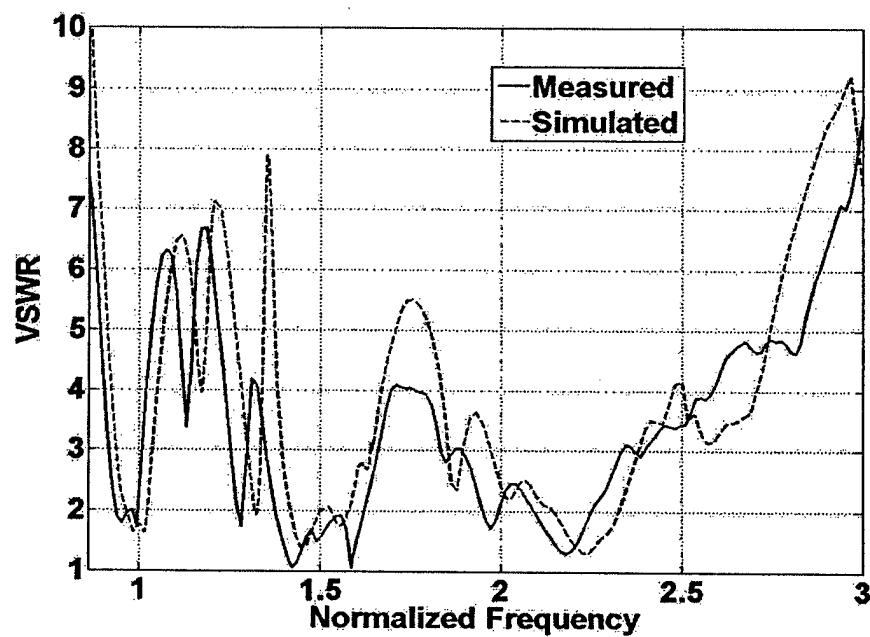
Fig. 10 - Simulated and measured VSWR for the four-arm antenna.
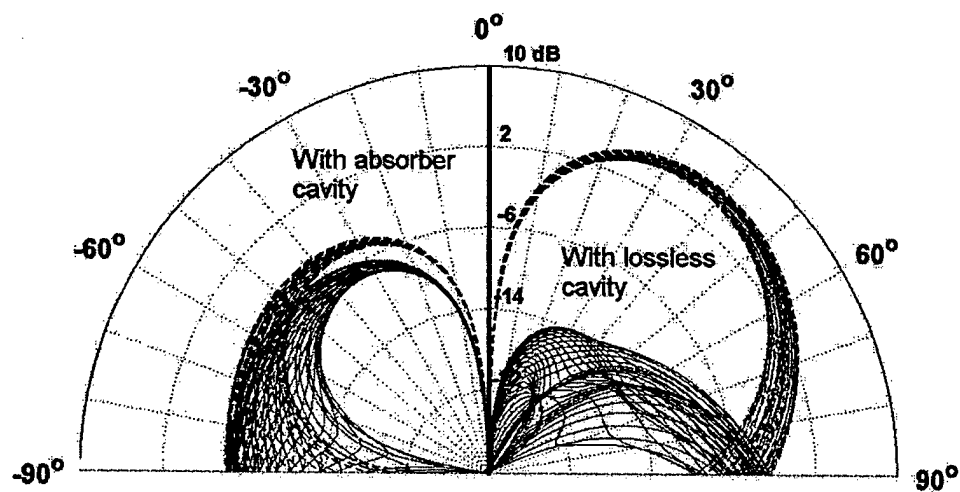
Fig. 11 - Far-field patterns for an individual band for the four-arm slot sinuous antenna. Dashed lines denote RHCP, solid lines are LHCP.
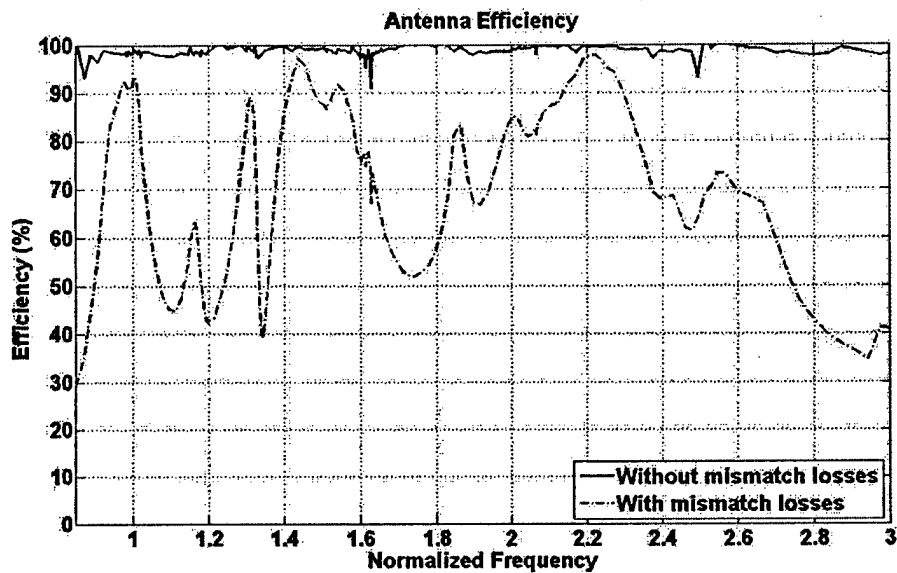
Fig. 12 - Mismatch losses account for a majority of the total losses in the four-arm antenna. Without taking into account these losses antenna efficiency is > 90% over the entire bandwidth.
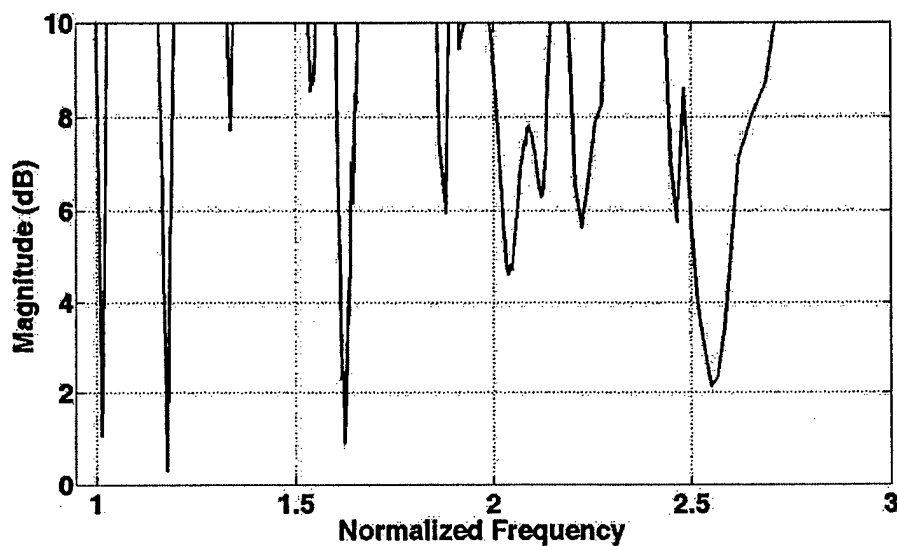
Fig. 13 - Axial ratio at an elevation of 45° for the four-arm antenna.
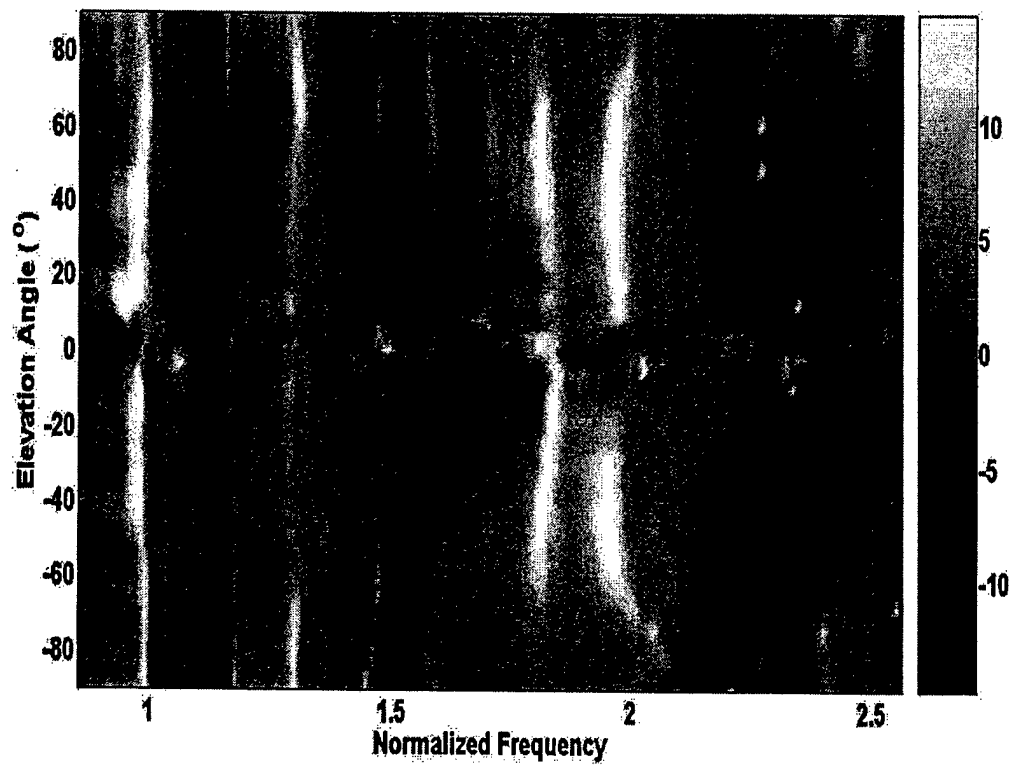
Fig. 14 - Measured polarization signature of the four-arm antenna. Cross polarization difference is plotted with RHCP as white and LHCP as black.
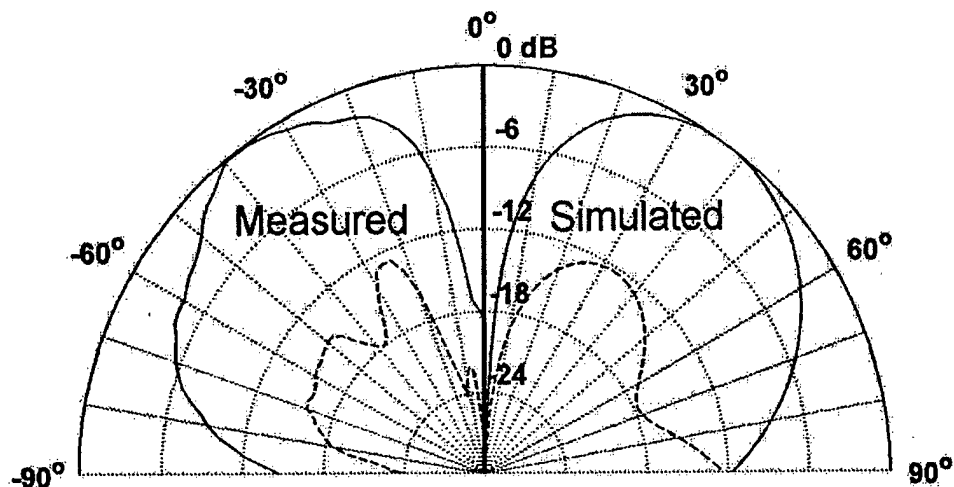
Fig. 15 - Comparison of simulated and measured pattern for RHCP and LHCP for the first resonant band at normalized frequency of 1.0.
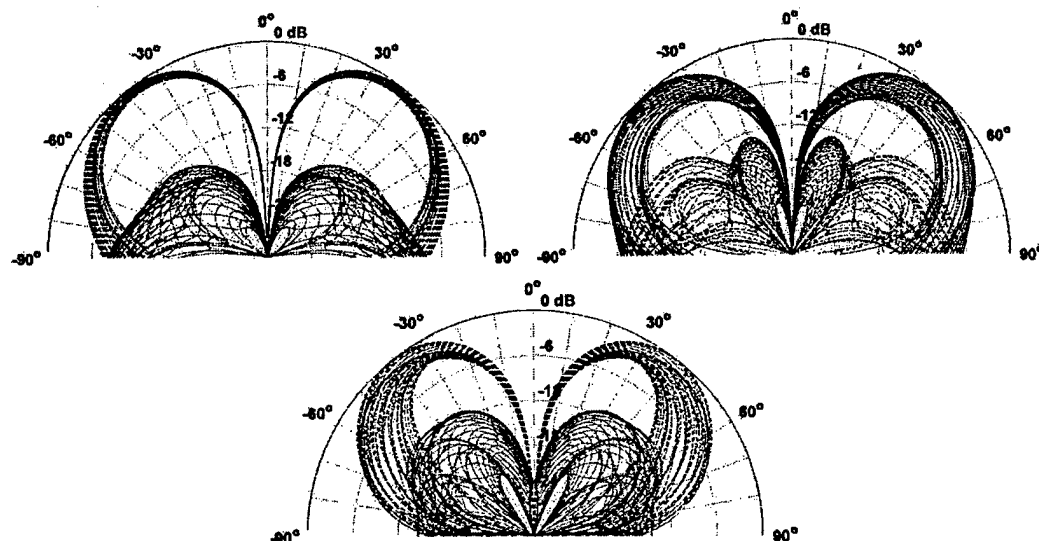
Fig. 16 - Simulated far-field patterns for the four-arm antenna for each band in normalized frequency, clockwise for top left: 1.2, 2.1, 2.6. Note the reversing polarization handedness with adjacent bands. Dashed lines correspond to LHCP and solid lines correspond to RHCP.
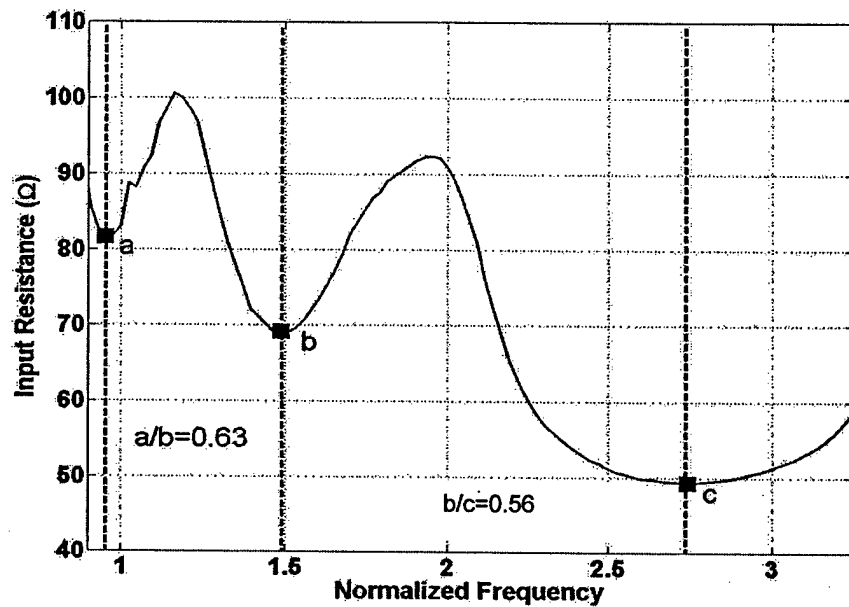
Fig. 17 – Log-periodic nature of the input resistance (top) and axial ratio (bottom) can be seen on the two-arm slot sinuous. The ratio of adjacent bands (signified by dashed vertical lines) are approximately equal to the sinuous geometric growth rate, $\tau = 0.62$.
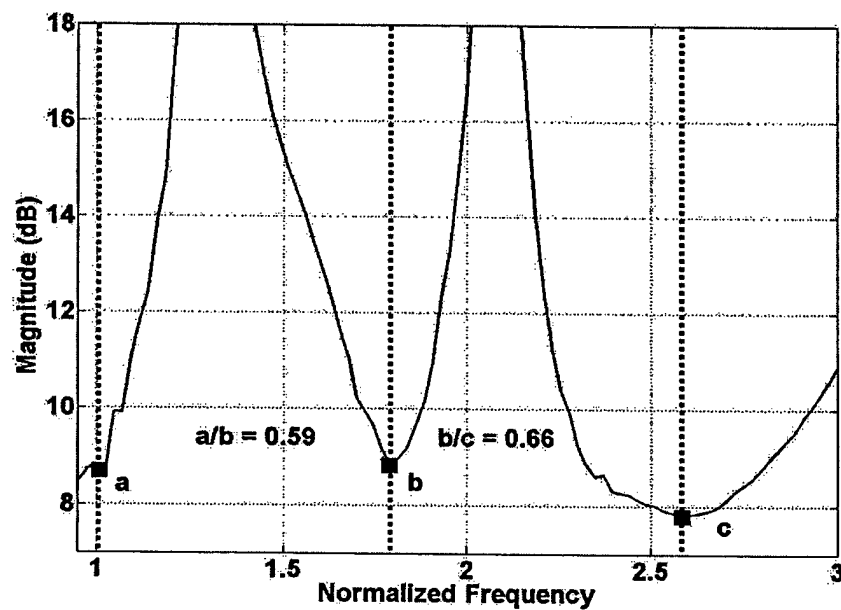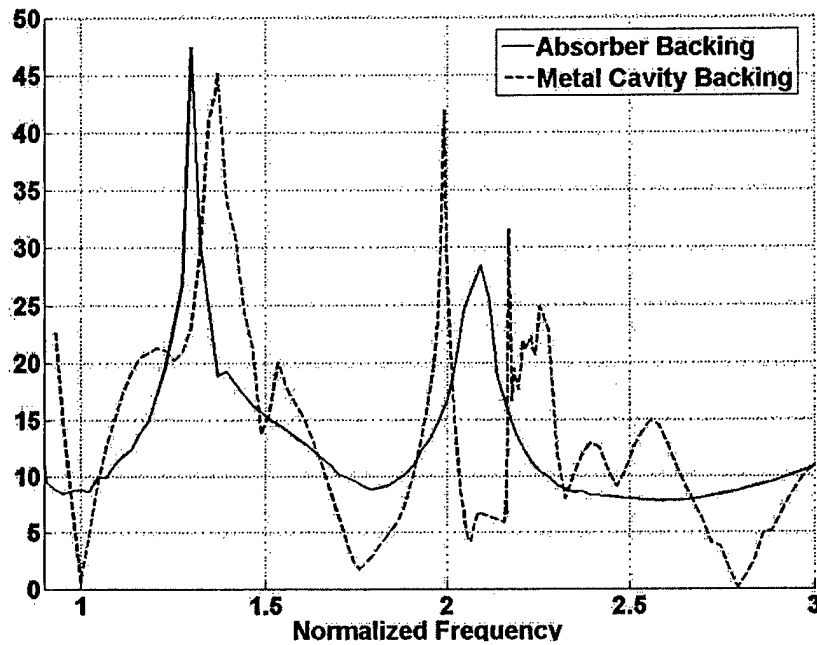
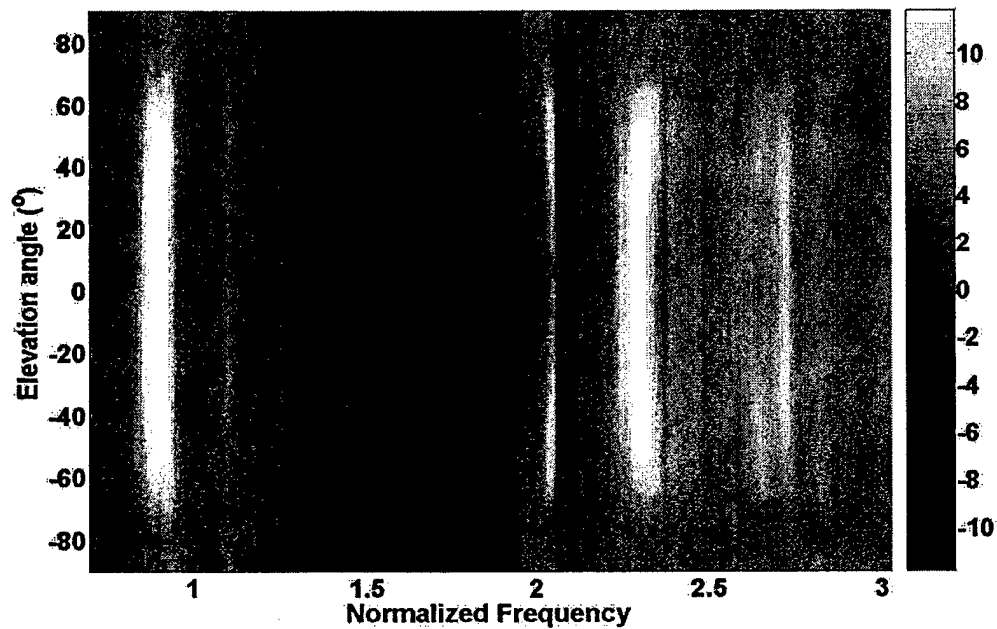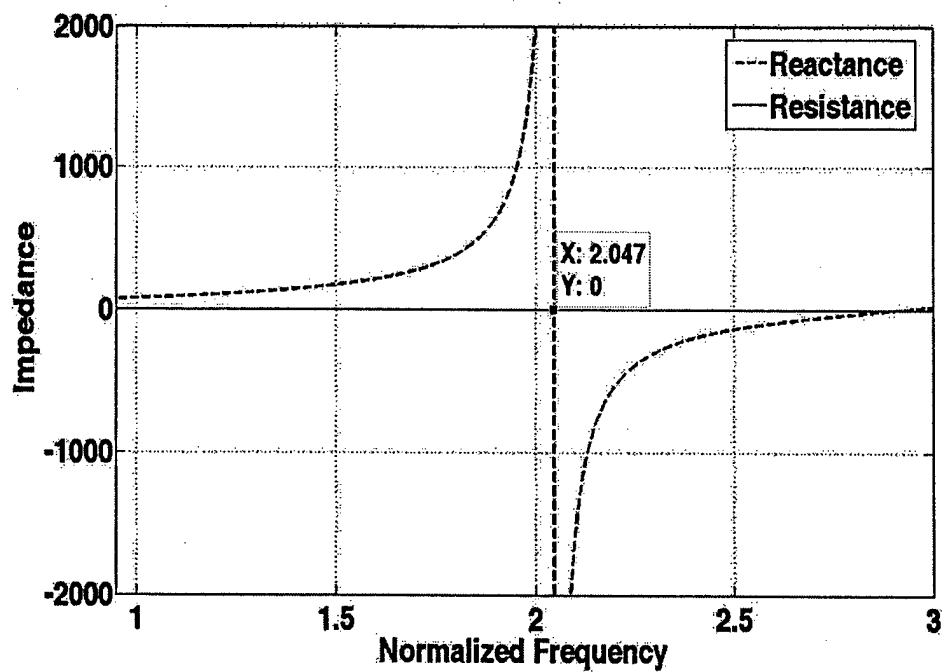Fig. 18 - Comparison of axial ratio between two-arm antenna with an absorptive cavity and a metal cavity backing.

Fig. 19 – Measured polarization signature of the two-arm slot sinuous antenna. Cross polarization difference is plotted with RHCP as white and LHCP as black.

Fig. 20 - The location of the cavity resonance can be seen by treating the stepped cavity as two series coaxial transmission lines with different characteristic impedances.
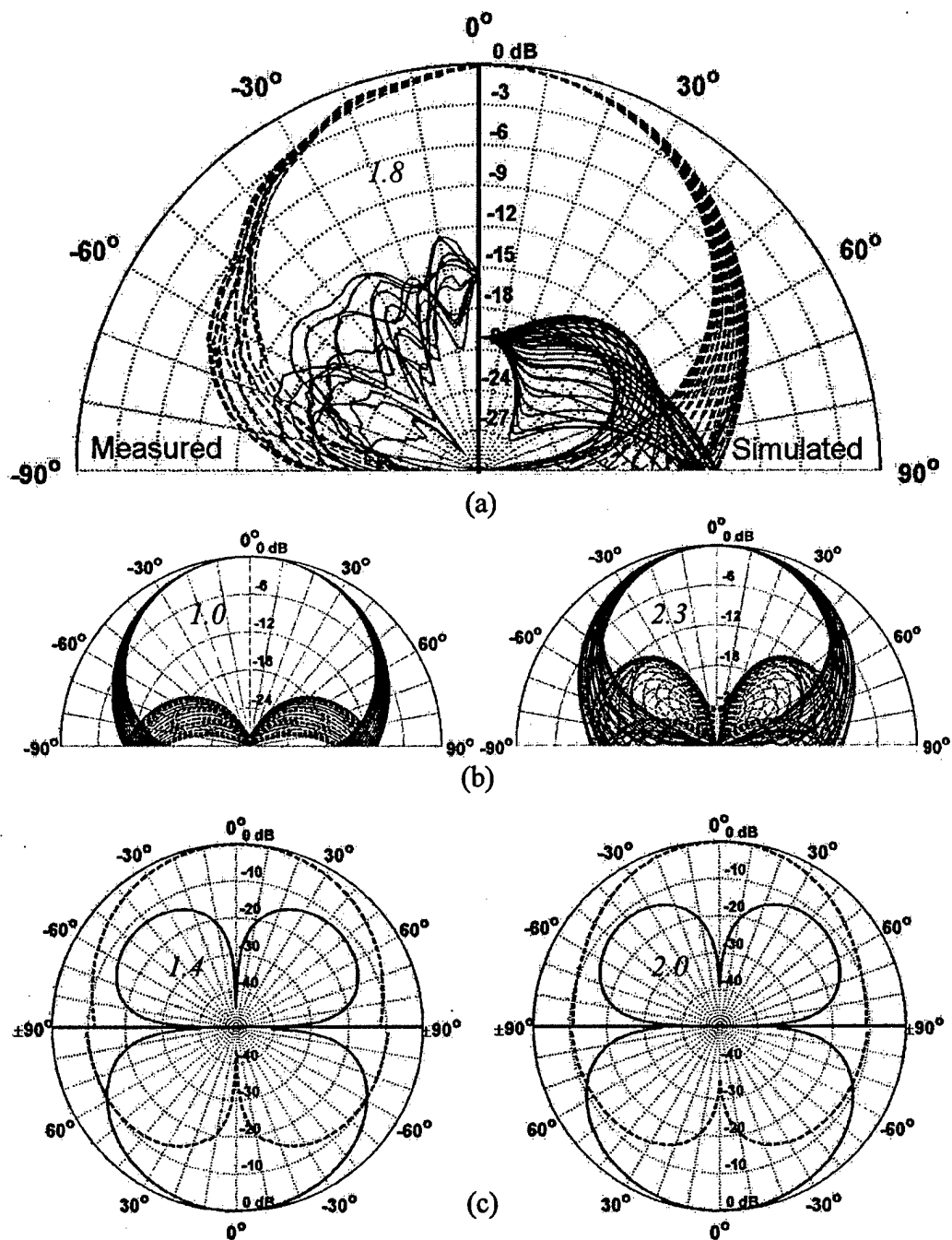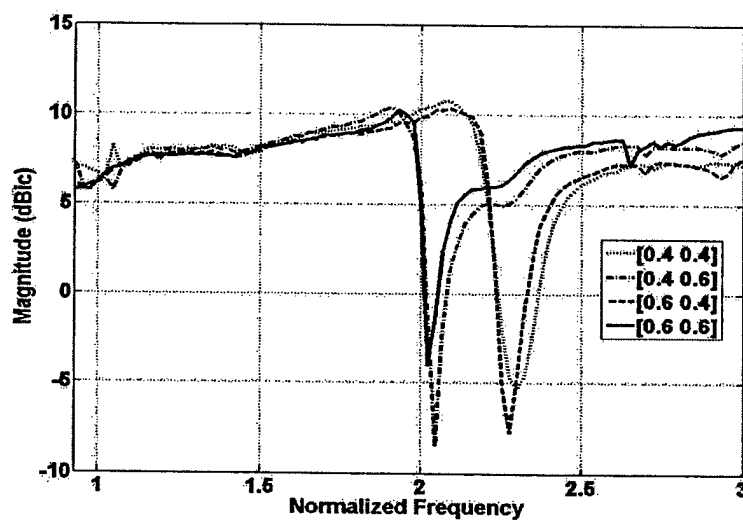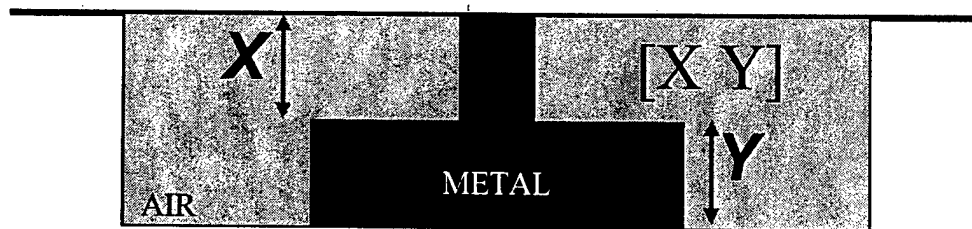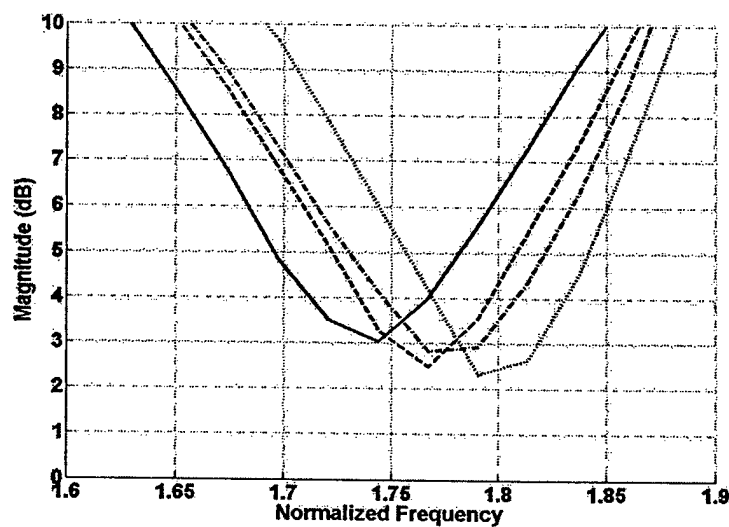
Fig. 21 - Far-field patterns of the two-arm slot sinuous antenna, (a) comparing numerical and measured results for the middle CP band, (b) numerical results from other CP bands, and (c) numerical results of the two linearly polarized bands for both E and H planes. For CP patterns, dashed lines denotes RHCP and solid, LHCP.

Fig. 22 - By changing the dimensions of the cavity for the two-arm antenna, the position of the cavity resonance gain null (a) can be moved as well as individual locations of the resonance bands of low axial ratio (b) can be fine-tuned.

432

Pages 433-453
Circulary Polarized Patch Array Operating in the 1.6GHz Iridium Band
Luis Artemio Sanchez Lopez
Paper not included no clearance submitted.

Low Q Electrically Small Linear and Elliptical Polarized Spherical Dipole Antennas

Steven R. Best
AFRL/SNHA
80 Scott Drive
Hanscom AFB, MA 01731
steven.best@hanscom.af.mil

Abstract: Electrically small antennas are generally presumed to exhibit high impedance mismatch (high VSWR), low efficiency, high quality factor (*Q*); and therefore narrow operating bandwidth. For an electric or magnetic dipole antenna there is a fundamental lower bound for the quality factor which is determined as a function of the antenna's occupied spherical volume. In this work, the quality factor of a resonant, electrically small electric dipole is minimized by allowing the antenna geometry to utilize the occupied spherical volume to the greatest extent possible. A self-resonant, electrically small electric dipole antenna is presented that exhibits an impedance near 50 Ohms, an efficiency in excess of 95% and a quality factor that is within 1.5 times the fundamental lower bound at a *ka* value less than 0.27. Through an arrangement of the antenna's wire configuration, the electrically small dipole's polarization is converted from linear to elliptical (with an axial ratio of 3 dB), resulting in a further reduction in the quality factor. The elliptically polarized, electrically small antenna exhibits an impedance near 50 Ohms, an efficiency in excess of 95% and it has an omnidirectional, figure-eight radiation pattern.

1. BACKGROUND

In their early work on electrically small antennas, Wheeler and Chu equated the small electric dipole to a lossy capacitor of a given effective height and effective cylindrical area. The input or feed point radiation resistance of the small dipole antenna is proportional to the square of its effective length [$\propto (l/\lambda)^2$] while its quality factor is inversely proportional to its effective volume [1] – [3]. For small dipole antennas of the same effective length, an increase in the effective cylindrical area decreases the antenna's quality factor [4]. In this work, a dipole is considered to be electrically small when $ka \leq 0.5$, where k is $2\pi/\lambda$ and a is the radius of an imaginary sphere circumscribing the maximum dimension of the dipole [5].

The quality factor of a tuned antenna is defined by the ratio of reactive energy to accepted power (power loss within the antenna plus radiated power):

$$Q(\omega_0) = \frac{\omega_0 W(\omega_0)}{P(\omega_0)} \tag{1}$$

where ω_0 is the tuned radian frequency. The tuned antenna's quality factor can also be determined directly from the antenna's untuned feed point impedance properties [6]

$$Q(\omega_0) = \frac{\omega_0}{2R(\omega_0)} \sqrt{R'(\omega_0)^2 + \left(X'(\omega_0) + \frac{|X(\omega_0)|}{\omega_0} \right)^2} \qquad (2)$$

where $R(\omega)$ and $X(\omega)$ are the frequency dependent feed point resistance and reactance, respectively, and $R'(\omega)$ and $X'(\omega)$ are their frequency derivatives. The antenna's quality factor and effective volume are related by [2]

$$r = \frac{\lambda}{2\pi} \left(\frac{9}{2Q} \right)^{\frac{1}{3}} \qquad (3)$$

where r is the radius of a sphere defining the effective volume of the antenna. The lower bound on the quality factor of an electric or magnetic dipole antenna is given by [7]

$$Q_{lb} = \eta \left(\frac{1}{(ka)^3} + \frac{1}{ka} \right) \qquad (4)$$

where η is the frequency dependent radiation efficiency of the antenna.

The work presented here is an extension of previous work in which an electrically small folded spherical helix monopole antenna was described [8]. A 4-arm folded spherical helix monopole configuration is simply·converted to a dipole configuration that exhibits a matched input impedance (relative to a characteristic impedance of 50 Ohms), high efficiency and vertical linear polarization for $ka \cong 0.27$. The wire geometry of the linearly polarized folded spherical helix dipole is then rearranged such that elliptical polarization, with 3 dB axial ratio, is achieved. As a result of being elliptically polarized, there is a corresponding reduction in quality factor.

2. THE LINEAR POLARIZED FOLDED SPHERICAL HELIX

The 1-turn, 4-arm folded spherical helix (FSH) monopole from [8] is depicted in Figure 1. This antenna has a height of approximately 6 cm and a wire diameter of 2.6 mm. The arm length in the 1-turn configuration is approximately 31 cm. There is a single feed point at the base of one of the individual arms. The remaining three arms are connected to ground. The simulated and measured impedance of this antenna is depicted in Figure 2. The simulations were performed using the NEC4 engine of EZNEC Pro [9]. The agreement between simulation and measurement over this wide range of frequencies provides sufficient confidence in NEC's capability in modeling these antenna configurations. The 4-arm FSH monopole exhibits a first series resonant frequency (where $X'(\omega) > 0$) at approximately 300 MHz with a resonant resistance of 43.1 Ohms. The quality factor of the FSH monopole is approximately 32, which is within 1.5 times the lower bound on Q for $ka \cong 0.38$.
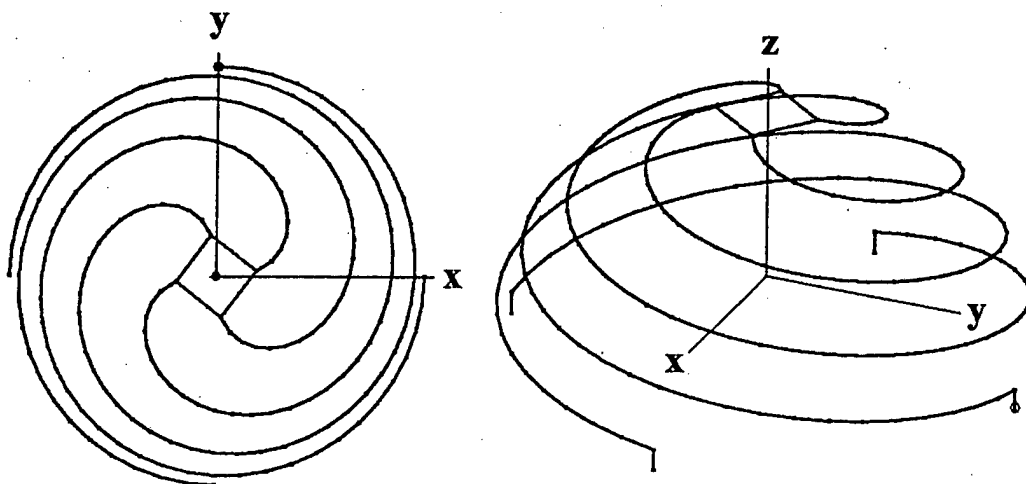
Figure 1. Depiction of the electrically small 1-turn, 4-arm, folded spherical helix monopole. The antenna height is 5.77 cm and the wire diameter is 2.6 mm. The antenna exhibits a first series resonance at 300.3 MHz with a resonant resistance of 43.1 Ohms.
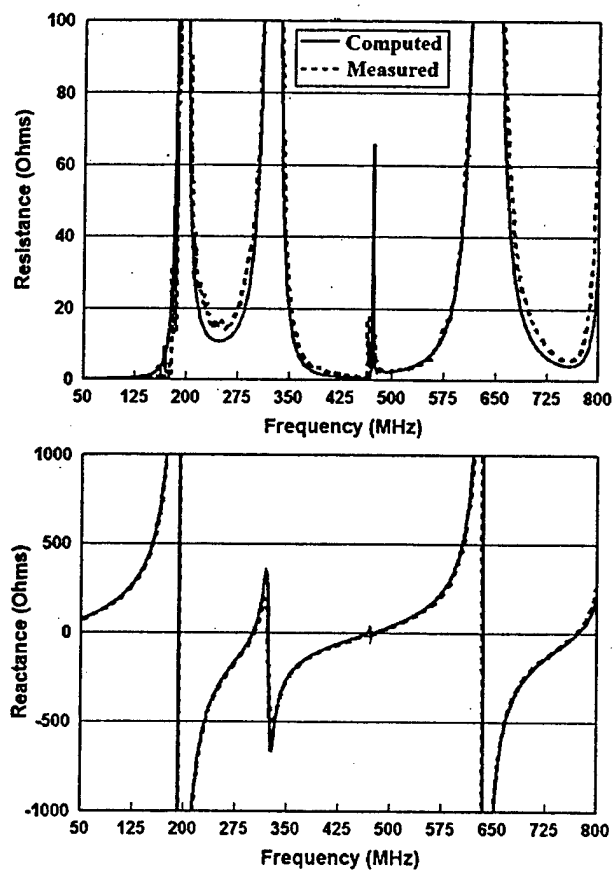

Figure 2. Simulated and measured impedance of the 1-turn, 4-arm, folded spherical helix monopole antenna depicted in Figure 1.

456

Converting the 4-arm FSH monopole into a dipole configuration is simply a matter of replacing the ground plane with a mirror image of wire below the antenna feed point as illustrated in the FSH dipole configuration of Figure 3. When the ground plane is replaced with mirror image wires, the resonant frequency of the antenna remains effectively unchanged but there is the expected 2 times increase in resonant resistance from 43.1 Ohms to 86.2 Ohms, which is not as well matched to a characteristic impedance of 50 Ohms. Since the resonant resistance of the antenna is directly proportional to the square of its overall length, it follows that the overall length of the antenna can be reduced to decrease the resonant resistance to 50 Ohms. At the same time as the overall length of the antenna is decreased, the individual arm lengths must be adjusted so that the resonant frequency of 300 MHz is maintained. In this case, the overall length of the FSH dipole is reduced from approximately 12 cm to 8.36 cm. The wire length in each individual arm is increased by approximately 2.6 cm. This antenna has a single feed point in one of the vertical arms at the center point in the antenna's geometry.
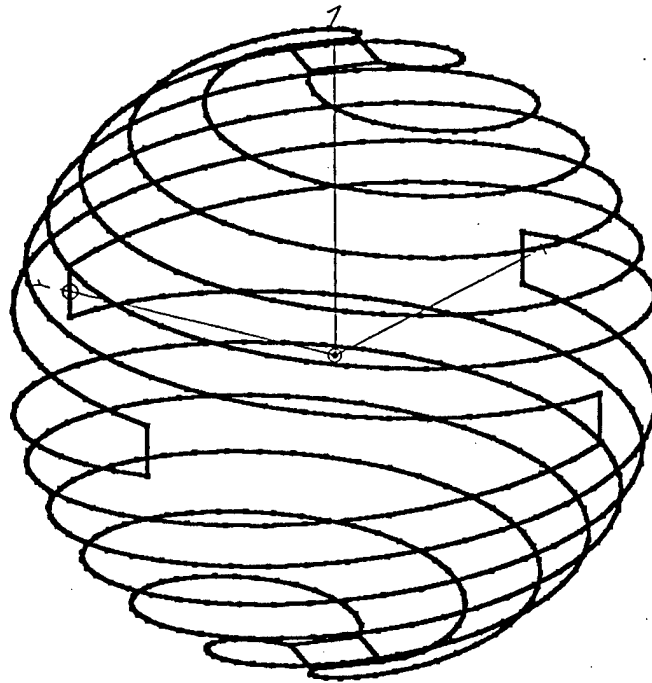

Figure 3. Depiction of the electrically small 4-arm spherical helix dipole antenna. The antenna has an overall length of 8.36 cm and is resonant at 299.9 MHz with a resonant resistance of 47.5 Ohms.

The FSH dipole antenna is self-resonant at 299.9 MHz with a resonant resistance of approximately 47.5 Ohms. The antenna's quality factor is 87.3. This increase in Q is expected with the decrease in occupied volume. The antenna has an efficiency of approximately 97.4%. Using Eq. (4), the lower bound on Q is determined to be approximately 57.3. The quality factor of the 4-arm FSH dipole is within 1.52 times the lower bound on Q for an electric dipole at $ka \approx 0.263$.

The antennas depicted in Figures 1 and 3 are equivalent to electric monopoles or dipoles because they exhibit a single resonance within their bandwidth consistent with a series RLC circuit and they exhibit a vertically polarized, omnidirectional radiation pattern consistent with that of a straight-wire monopole or dipole antenna. The horizontal polarized component of radiation (directivity) is significantly diminished because the horizontal components of current within the wire geometry effectively cancel. The radiation pattern of the 4-arm folded spherical dipole is depicted in Figure 4. The gain of the antenna including the affects of copper loss is 1.9 dBi.
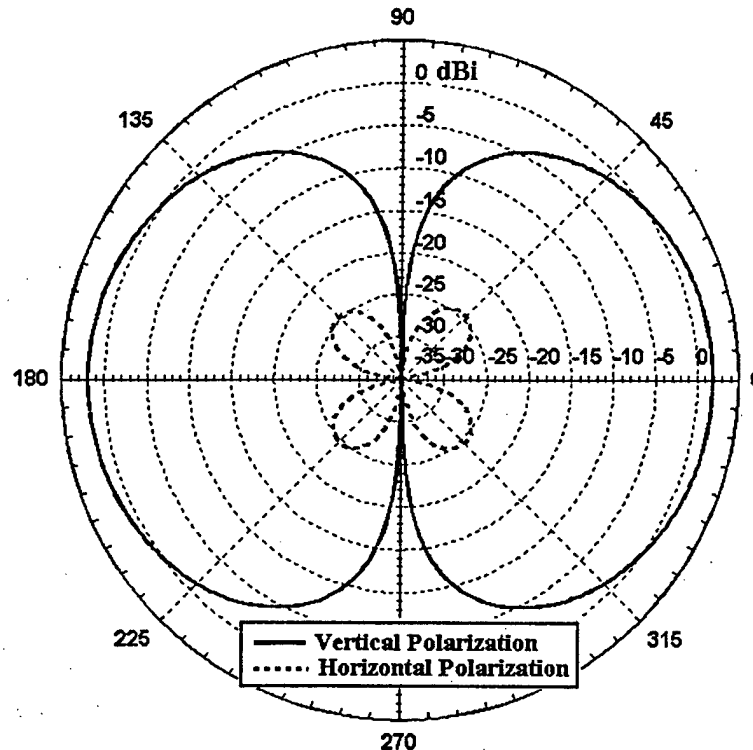

Figure 4. Radiation pattern of the 4-arm folded spherical helix dipole at 299.9 MHz. The antenna exhibits an omnidirectional, linearly polarized radiation pattern consistent with that of an electric dipole. The antenna has a gain of 1.9 dBi.

3. THE ELLIPICALLY POLARIZED FOLDED SPHERICAL HELIX

The 4-arm folded spherical helix dipole depicted in Figure 3 exhibits linear, vertical polarization because the horizontal component of current within the upper and lower dipole arms effectively cancel, diminishing the horizontal polarized radiation, as was depicted in Figure 4. With a rearrangement of wire within the lower dipole arms relative to the upper dipole arms, the horizontal component of current can be made to add constructively, re-enforcing the radiation of linear, horizontal polarization. Circular polarization is achieved when the linear vertical and horizontal polarizations are equal in amplitude and 90 degrees out-of-phase.

A rearrangement of wire that re-enforces the radiation of horizontal polarization is depicted in Figure 5. Additionally, the horizontal polarization is 90 degrees out-of-phase with the vertical

458

polarization at all angles, resulting in elliptical polarization. The level of horizontal polarized radiation is approximately 3 dB less than the vertical polarized radiation, resulting in an axial ratio of 3 dB. The radiation pattern of this antenna is depicted in Figure 6. The antenna is resonant at a frequency of 301.3 MHz with a resonant resistance of 61.5 Ohms, which is slightly higher than that of the linear polarized configuration. However, the VSWR with respect to 50 Ohms is less than 1.5:1. The efficiency of the antenna is 98.7%. It has a calculated "circular" polarized gain of approximately 1.7 dBic.
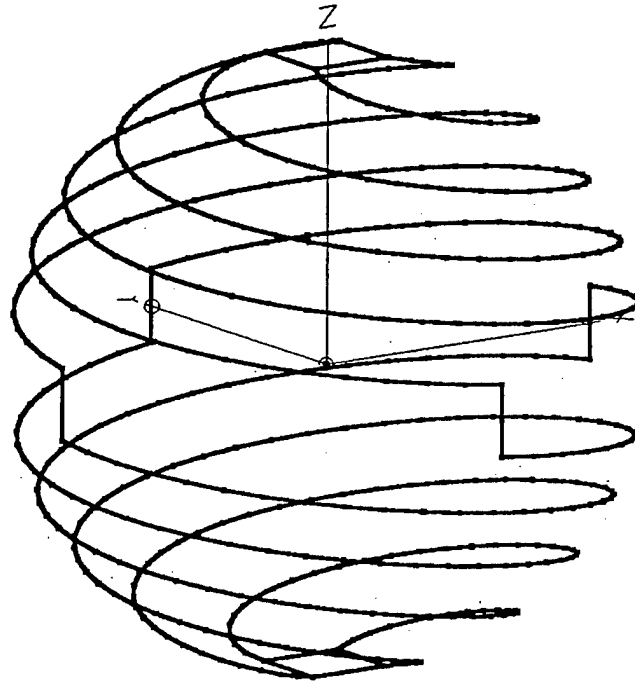

Figure 5. Depiction of the elliptically polarized, electrically small, 4-arm folded spherical helix antenna. The antenna has an overall length of 8.36 cm and is resonant at 301.3 MHz with a resistance of 61.5 Ohms.

The lower bound on the quality factor for a circular polarized antenna is less than that of a linear polarized antenna and is expressed as [7]

$$Q_{lbcp} = \eta \frac{1}{2}\left(\frac{1}{(ka)^3} + \frac{2}{ka} \right)$$

(5)

The quality factor of the elliptically polarized antenna configuration of Figure 5 would be approximately ½ of the quality factor of the linear polarized antenna configuration depicted in Figure 3 if its axial ratio were 0 dB, where the vertical and horizontal components each contain ½ the radiated power. With an axial ratio greater than 0 dB, the reduction in quality factor would be between ½ and 1 as a direct function of the ratio of power contained in the vertical and horizontal polarized components. The circular polarized antenna of Figure 5 has an axial ratio of 3 dB and the vertical polarized component of radiation contains 2/3 of the total radiated power.

459

With this ratio of power distribution between the vertical and horizontal polarization components it is expected that the quality factor of the circular polarized antenna would be reduced by approximately 2/3 (66.67%). Using Equation (2), the quality factor of the circular polarized antenna of Figure 5 is found to be 61.7, a 70.7% reduction. The lower bound on the quality factor for the elliptically polarized antenna calculated using Equation (5) is approximately 31. The quality factor of the elliptically polarized antenna is approximately 2 times the lower bound for a circular polarized antenna at $ka \approx 0.263$.
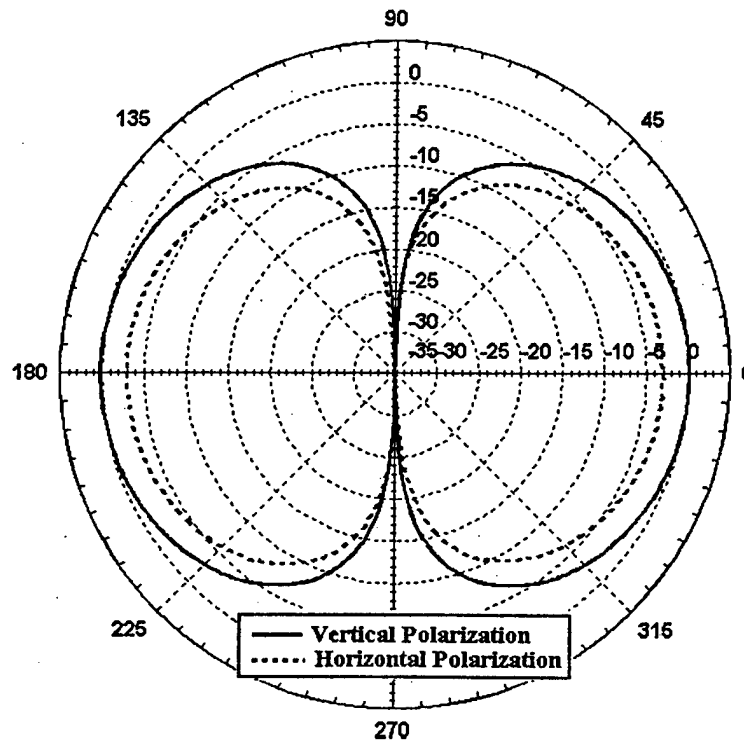

Figure 6. Radiation pattern of the circular polarized 4-arm folded spherical helix dipole at 301.3 MHz. The antenna exhibits an omnidirectional, elliptically polarized radiation pattern with a axial ratio of 3 dB. The antenna has a gain of 1.7 dBic.

4. DISCUSSION

An electrically small dipole antenna can be made to achieve self-resonance through an increase in total wire length while maintaining a fixed height and a fixed occupied volume. As the overall length of the dipole decreases relative to the resonant wavelength, the resonant resistance decreases in proportion to the decrease in $(l/\lambda)^2$. Multiple folded arms are used in the configurations presented here to match the antennas to a 50 Ohm characteristic impedance. To reduce the quality factor, the multiple folded arm configurations are also configured to take advantage of and occupy the full spherical volume for a fixed value of ka.

The 4-arm folded linear polarized spherical dipole presented exhibits self resonance at 300 MHz, occupying a volume where $ka \approx 0.263$. It has a resonant resistance of 47.5 Ohms, an efficiency

460

of 97.4% and a Q of 87.3, which is within 1.5 times the theoretical lower bound on Q for an electric dipole. Through an arrangement of wire geometry, the horizontal currents within the antenna are configured to add constructively resulting in a significant increase in horizontally polarized radiation. This electrically small antenna is circularly polarized with an axial ratio of 3 dB. It exhibits resonance near 300 MHz having a resistance of 61.5 Ohms, an efficiency in excess of 98% and a quality factor within 2 times the lower bound on quality factor for a circularly polarized antenna at a $ka \approx 0.262$.

5. REFERENCES

[1] L. J. Chu, "Physical Limitations of Omni-Directional Antennas," *Journal of Applied Physics*, Vol. 10, pp. 1163-1175, Dec. 1948.

[2] H. A. Wheeler, "Fundamental Relations in the Design of a VLF Transmitting Antenna," *IRE Trans Antennas Propagat.*, Vol. 6, pp. 120-122, Jan. 1958.

[3] R. B. Adler, L. J. Chu, and R. M. Fano, "Electromagnetic Energy Transmission and Radiation," John Wiley & Sons, New York, 1960.

[4] S. R. Best, "A Discussion on the Properties of Electrically Small Self-Resonant Wire Antennas," Accepted for Publication, *IEEE Antennas and Propagation Magazine*.

[5] S. R. Best, "On the Performance Properties of the Koch Fractal and Other Bent Wire Monopoles," *IEEE Trans. Antennas Propagat.*, Vol. 51, No. 6, pp. 1292-1300, June 2003.

[6] A. D. Yaghjian and S. R. Best, "Impedance, Bandwidth and Q of Antennas," *IEEE APS Symposium*, Vol. 1., pp. 501-504, Columbus, OH, June 2003.

[7] J. S. McLean, "A Re-Examination of the Fundamental Limits on the Radiation Q of Electrically Small Antennas," *IEEE Trans. Antennas Propagat.*, Vol. 44, pp. 672-676, May 1996.

[8] S. R. Best, "The Radiation Properties of Electrically Small Folded Spherical Helix Antennas," *IEEE Trans. Antennas Propagat.*, Vol. 52, No. 4, pp. 953-960, April 2004.

[9] R. Lewallen, EZNEC/4 Antenna Modeling Software, available online: http://www.eznec.com

[10] S. R. Best, "A Discussion on the Quality Factor of Impedance Matched Electrically Small Wire Antennas," Accepted for publication, *IEEE Trans. Antennas Propagat.*

Small Broadband Disk Loaded Folded Monopole Antennas

Steven R. Best
AFRL/SNHA
80 Scott Drive
Hanscom AFB, MA 01731
steven.best@hanscom.af.mil

Abstract: This paper presents an interim status of ongoing work in the development of an efficient, broadband, small disk loaded folded monopole. The objective of this work is to develop a small monopole antenna having a height less than 1/10 of the wavelength at the lowest operating frequency and a 2:1 VSWR bandwidth in excess of a 3:1 frequency range. A simple, single feed point design is presented for a disk loaded folded monopole that has a height of approximately 1/12 of the wavelength at the lowest operating frequency and a 2:1 VSWR bandwidth covering a 2.9:1 frequency range. The design is accomplished without the benefits of dielectric or resistive loading so that the antenna maintains high radiation efficiency over its operating band. A discussion of other techniques used to design small disk loaded folded monopoles is also presented.

1. BACKGROUND

Recently, there has been increased interest in the development of wideband and ultra-wideband dipole and monopole antennas. Specifically, there has been significant focus on developing antennas that operate in the 3.1 to 10.6 GHz frequency range (a 3.42:1 frequency bandwidth) as this spectrum has been allocated by the FCC as part of what has been designated Ultra Wideband (UWB). Although achieving a wide impedance bandwidth is many times the primary design consideration, other performance characteristics such as polarization purity and radiation pattern shape over the entire operating band are significant and must be considered. In UWB systems, which use pulse encoding schemes, transmitted and received pulse fidelity is perhaps the most important consideration. This requires the antenna designer to consider the antenna's Time Delay Impulse Response and the uniformity of the antenna's gain, radiation pattern, and phase center displacement as a function of frequency.

The work presented here is aimed at the development of a small, broadband disk loaded folded monopole antenna. The range of frequency coverage is not specifically concerned with the UWB band and the antenna's pulse fidelity is not considered. The UWB band is notable in that it has increased commercial focus on the development of wideband antennas. This section provides a brief background discussion on several techniques used in the design of small and broadband monopole antennas.

1.1 Broadband Planar Monopole Antennas

The development of many broadband monopole antennas is based on a number of well known design techniques. One of these is the use of planar elements derived from a number of geometric configurations, such as the bicone or bow-tie [1], square or rectangle [2] – [3], circle [4] and "volcano" or inverted cone shapes [5] – [6], as illustrated in Figure 1. While having different geometric shape, the design principles associated with these antennas are essentially the same. For a fixed height and width, each of these basic shapes can be used to design an antenna offering similar bandwidth performance. 2:1 VSWR bandwidths in excess of 5:1 or even 10:1 are common with a number of planar monopole configurations. Near the lowest range of their operating band, these planar, broadband monopole antennas generally exhibit omnidirectional azimuth coverage with reasonable, single lobe elevation coverage. Near the upper range of their operating band they may exhibit pattern degradation since the antenna occupies a larger volume with respect to the shorter operating wavelengths.

As an example of a simple planar monopole design, consider the tapered, planar monopole antenna depicted in Figure 2, which a combination of tapered rectangle and inverted cone shapes. This antenna exhibits a VSWR less than 2:1, with respect to a 50 Ohm characteristic impedance, from 1.88 GHz to a frequency in excess of 10 GHz. Simulated (Microwave Studio) and measured VSWR for this antenna are presented in Figure 3. At the lowest end of the operating band, the planar monopole antenna has a height of approximately 0.23λ, which is typical of many planar monopole antenna configurations. While a 2:1 VSWR is typically used to define the operating bandwidth of many antenna designs, a large number of commercial communications systems, IEEE Standard 802.11 for example, require the system antenna to exhibit a VSWR less than 1.5:1 over its operating band.

1.2 Disk Loaded Folded Monopole Antennas

Two common design techniques used in the development of small and broadband monopole antennas include the use of a capacitive top-hat or "disk" and the use of a single or multiple shunt connection to ground. The capacitive top-hat [7] increases the capacitance to ground, reducing the cylindrical monopole's feed point capacitive reactance, thereby reducing its resonant frequency. Alternately, the overall height of the cylindrical monopole can be reduced while maintaining a fixed resonant frequency. While simple disk or top-hat loaded monopoles offer lower resonant frequency or reduced height, there is a direct trade-off in a corresponding reduction of the resonant radiation resistance. However, small capacitive top-hat configurations offer higher radiation resistance relative to other design approaches that may be used to decrease antenna height such as inductive loading (increased wire length as an example). The use of single or multiple shunt connections to ground is derived from the basic principles of folded monopole and folded dipole antennas [8]. Single or multiple connections to ground significantly increase the radiation resistance of small antennas, which typically have resistances much less than 50 Ohms.

In many instances, both of these design techniques are incorporated into the design of small and broadband monopoles as illustrated by the disk loaded folded monopole configuration depicted

in Figure 4 [9]. While this antenna was studied in 1956, the author of [9] (E. W. Seeley) references publications dating back to 1946 that describe the properties of disk loaded folded monopoles [10] – [12]. (*Note: the author did not have access to these references but decided to include them via Seeley's paper as they establish a significant timeline in the development of disk loaded folded monopoles.*)

The disk loaded folded monopole antenna depicted in Figure 4 exhibits minimal VSWR at a frequency where its overall height is approximately 0.095λ. The 2:1 VSWR bandwidth is approximately 14%. As the height of the disk loaded monopole decreases relative to the operating wavelength, there is an inherent decrease in the achievable operating bandwidth. This trade-off in height versus operating bandwidth is the significant design challenge associated with these antennas.

A notable design in the discussion of small broadband antennas is the multi-element monopole antenna designed by Georg Goubau [13] – [14]. The Goubau antenna, depicted in Figure 5, has a height of 4.3 cm and a disk diameter of 12.3 cm. It has a 2:1 VSWR bandwidth covering a frequency range of approximately 470 – 890 MHz (1.9:1 bandwidth). The Goubau antenna has a height of approximately 0.067λ at its lowest operating frequency.

Friedman [15] described a double-tuned disk loaded monopole comprised of a conductive biconical center post and two structural side posts located under the disk as illustrated in Figure 6. This antenna has a height of 6.48 cm and a disk diameter of 18.44 cm. This antenna exhibits a 2:1 VSWR bandwidth covering a frequency range of 327 – 610 MHz (1.9:1 bandwidth). The Friedman antenna has a height of approximately 0.071λ at its lowest operating frequency.

2. DISK LOADED FOLDED ANTENNA DESIGN

The first antenna considered is a simple disk loaded planar monopole depicted in Figure 7. The maximum antenna height was chosen to be 6.8 cm and the maximum allowable disk diameter was chosen to be 18 cm. In the configuration of Figure 7 a disk diameter of 16 cm was used. The width of the planar monopole section is 5 cm and the bottom spacing above the ground plane is 4 mm. The planar monopole section is spaced 1 cm from the edge of the top disk. With this configuration, a resonant frequency of 276 MHz is achieved with a resonant radiation resistance 6.3 Ohms. The results presented in this section were simulations obtained using Microwave Studio.

The next step in the design process is to increase the radiation resistance of the antenna from 6.3 Ohms to a value closer to 50 Ohms. This is accomplished by introducing a shunt or folded connection ground as illustrated in the configuration shown in Figure 8. In this case, the shunt connection is another rectangular section 5 cm in width. It is spaced 1 cm from the edge of the top disk. This configuration exhibits a first resonant frequency of 472 MHz with a resonant resistance of 48 Ohms. Without optimizing the placement or width of the shunt connection to ground, the antenna exhibits a 2:1 VSWR bandwidth covering 411 – 595 MHz, a 44.7% bandwidth. (*Note: If a simple, thin, straight-wire folded monopole configuration were considered, where the monopole and the folded connection to ground were very closely spaced,*

the radiation resistance would have increased by a factor of approximately 4 and the resonant frequency would have been relatively unchanged.)

Considering the impedance of the antenna, as shown in Figure 8, it is evident that a better impedance match to 50 Ohms can be accomplished if a matching network comprised of a parallel capacitor and a series inductor were used placed at the antenna feed point. Rather than using lumped circuit elements, this matching network topology can be implemented with the antenna geometry as shown in Figure 9. An increase in parallel capacitance is accomplished by increasing the width of the planar monopole near the ground plane. The series inductance is accomplished by extending or increasing the height of the point of connection between the feed line center conductor and the planar monopole. This is implemented by cutting the two vertical slots in the planar monopole section near the center conductor, as illustrated in Figure 9. The improved impedance match is evident in the Smith chart shown in Figure 9. With this configuration, the antenna exhibits a 2:1 VSWR bandwidth covering a frequency range of 394 – 1085 MHz, a 2.75:1 bandwidth.

The next step in the design effort is to improve the impedance match at both the upper and lower ends of the frequency bands, thereby increasing the antenna's 2:1 VSWR bandwidth. It is very important to note that improving the impedance match at the low end of the band is considered to be the primary objective. At the low end of the operating band, the antenna is small and the radiation patterns are typical of those exhibited by a straight-wire monopole. At the upper end of the band, the antenna dimensions start to become a significant proportion of the operating wavelength. As this occurs, the radiation patterns of the antenna degrade quickly. At very high frequencies there may be considerable lobing and nulling in both the azimuth and zenith radiation patterns.

In the next antenna configuration considered, the top disk diameter is increased to 18 cm to improve the impedance match at the low end of the operating band. Additionally, two cut-outs are introduced into the top disk to improve the impedance match in the mid to upper end of the operating band. The two cut-outs in the top disk introduce additional resonances near the upper end of the band. A depiction of this configuration is illustrated in Figure 10. A Smith Chart and VSWR curve for this configuration are presented in Figure 11. This antenna exhibits a 2:1 VSWR covering a frequency range of 374 – 1093 MHz, a 2.9:1 bandwidth. This antenna has a height of 0.085λ at its lowest operating frequency.

Another version of this type of antenna was designed with dimensions exactly matching those of the Goubau antenna, having a height of 4.3 cm and a top disk diameter of 12.3 cm. This antenna and the corresponding VSWR curve are presented in Figure 12. This antenna has a 2:1 VSWR bandwidth covering 554.5 – 1400 MHz, a 2.5:1 bandwidth. This antenna has a height of 0.08λ at its lowest operating frequency.

A performance comparison of the disk loaded folded monopoles presented here and the Goubau and Friedman antennas is presented in Table 1.

Antenna	Height (cm) and (λ) at Lowest Operating Frequency	Top Disk Diameter (cm)	2:1 VSWR Frequency Coverage (MHz)	2:1 VSWR Frequency Bandwidth
Goubau [14]	4.3 cm; .067λ	12.3	470 - 890	1.9
Friedman [15]	6.48 cm; .071λ	18.42	327 - 610	1.9
Antenna –Figure 9	6.8 cm; .09λ	16	394 – 1085	2.75
Antenna – Figure 10	6.8 cm; .085λ	18	374 – 1093	2.92
Antenna – Figure 12	4.3 cm; .08λ	12.3	554 - 1400	2.9

3. DISCUSSION

Progress in the development of a simple disk loaded folded monopole has been presented. The performance properties presented were simulated results obtained using Microwave Studio. Future work includes simulating the Goubau antenna using Microwave Studio and fabricating several of the designs presented here so that their performance can be measured. Further work is to be directed at improving the impedance match of these antennas at the low end of their operating band.

4. REFERENCES

[1] C. A. Balanis, *Antenna Theory: Analysis and Design*, John Wiley and Sons, New York, Chapt. 9, pp. 441 – 448, 1997.

[2] M. J. Ammann and Z. N. Chen, "Wideband Monopole Antennas for Multiband Wireless Systems," *IEEE Antennas and Propagation Magazine*, Vol. 45, No. 2, pp. 146 – 150, April 2003.

[3] Z. N. Chen, M. Y. W. Chia and M. J. Ammann, "Optimization and Comparison of Broadband Monopoles," *IEE Proceeding on Microwaves, Antennas and Propagation*, Vol. 150, No. 6, pp. 429 – 435, December 2003.

[4] Z. N. Chen, M. J. Ammann, M. Y. W. Chia and T. S. P. Lee, "Circular Annular Planar Monopoles with EM Coupling," *IEE Proceeding on Microwaves, Antennas and Propagation*, Vol. 150, No. 4, pp. 269 – 273, August 2003

[5] J. D. Kraus, *Antennas*, McGraw-Hill Book Company, New York, Chapt. 2, pp. 61 – 64, 1988.

[6] S-Y. Suh, W. L. Stutzman and W. A. Davis, "A New Ultrawideband Printed Monopole Antenna: The Planar Inverted Cone Antenna(PICA)," *IEEE Transactions on Antennas and Propagation*, Vol. 52, No. 5, pp. 1361 – 1365, May 2004.

[7] R. A. Burberry, *VHF and UHF Antennas*, IEE (Peter Peregrinus Ltd.), London, pp. 30-34, 1992.

[8] R. C. Johnson and H. Jasik (Editors), Antenna Engineering Handbook, McGraw-Hill Book Company, New York, Chapter 4 (Chen To Tai), pp. 4.13-4.18, 1984.

[9] E. W. Seeley, "An Experimental Study of the Disk Loaded Folded Monopole," *IRE Transactions on Antennas and Propagation*, pp 27 – 28, January 1956.

[10] R. C. Raymond and W. Webb, "Radiation Resistance of Loaded Monopoles," *Journal of Applied Physics*, Vol. 20, pp. 328-330, April 1949.

[11] R. Guertler, "Impedance Transformation in Folded Dipoles," *Proceedings of the IRE*, Vol. 38, pp. 1042-1047, September 1950.

[12] E. G. Hill, "VHF Antennas for Trains," *Electronics*, Vol. 19, pp. 134-136, November 1946.

[13] G. Goubau, "Multi-Element Monopole Antenna," *Proceedings of the ECOM-ARO Workshop on Electrically Small Antennas*, Fort Monmouth, NJ, pp. 63-67, October 1976.

[14] G. Goubau, N. N. Puri and F. Schwering, "Diakoptic Theory for Multielement Antennas," IEEE Transactions on Antennas and Propagation, Vol. 30, No. 1, pp. 15-26, January 1982.

[15] C. H. Friedman, "Wide-Band Matching of a Small Disk-Loaded Monopole," *IEEE Transactions on Antennas and Propagation*, Vol. 33, No. 10, pp. 1142-1148, October 1985.

Planar Bow-Tie Monopole

Planar Tapered Square Monopole

Planar Circular Monopole

Planar Inverted Cone Monopole
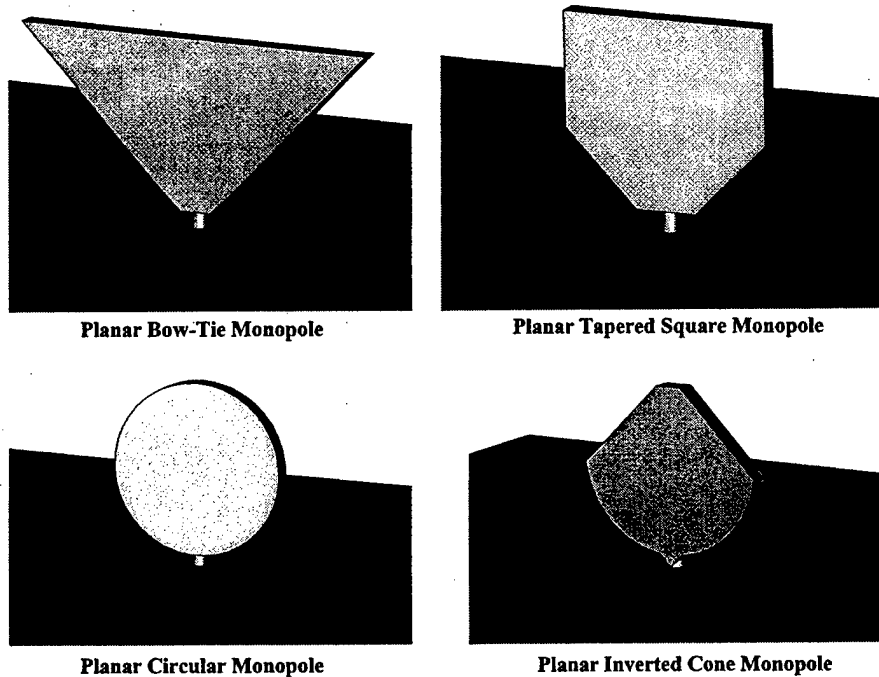
Figure 1. Depictions of typical geometries used in the design of broadband, planar monopole antennas. These geometries include the bow-tie, square or rectangle, circle and the inverted cone. For a fixed height and width, these basic geometries can be used to design antennas that offer similar bandwidth performance. 2:1 VSWR bandwidths in excess of 5:1 or 10:1 are possible with these configurations.

3.6 cm

2 cm
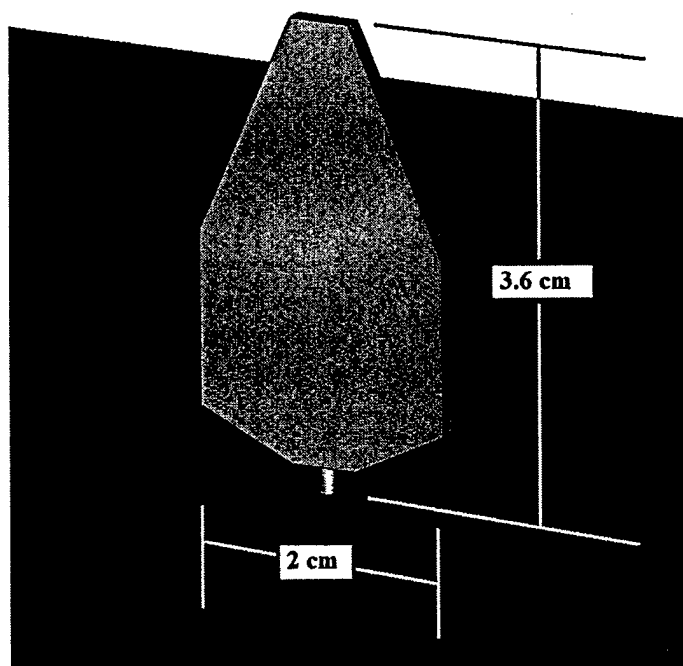
Figure 2. Depiction of a simple planar monopole antenna having a height of 3.6 cm and a width of 2 cm. This planar monopole antenna has a 2:1 VSWR bandwidth in excess of 7.5:1.
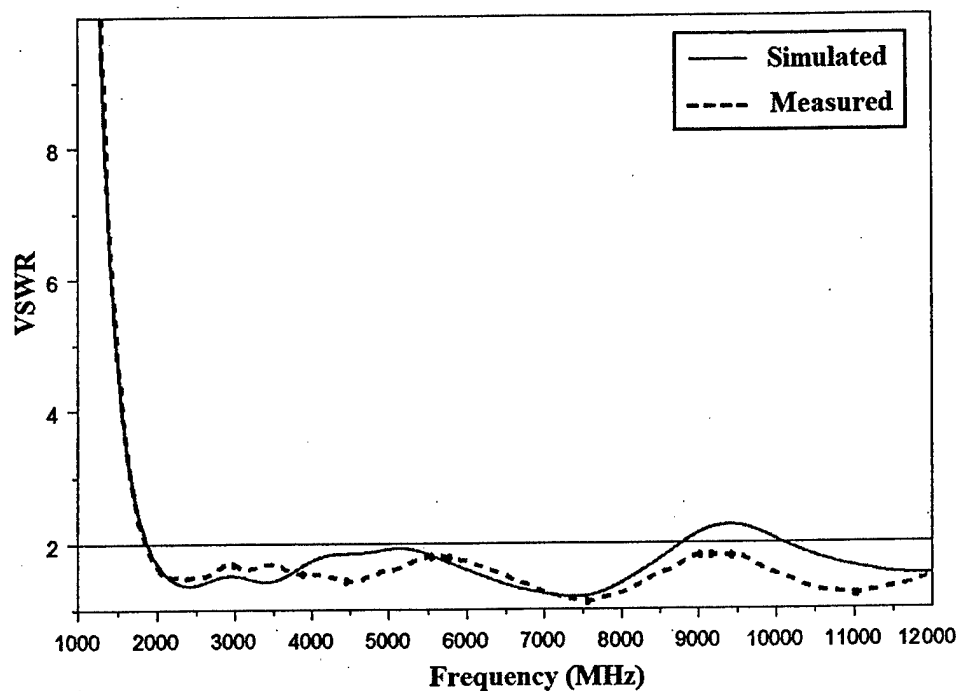
Figure 3. Simulated (Microwave Studio) and measured VSWR for the planar monopole antenna depicted in Figure 2.
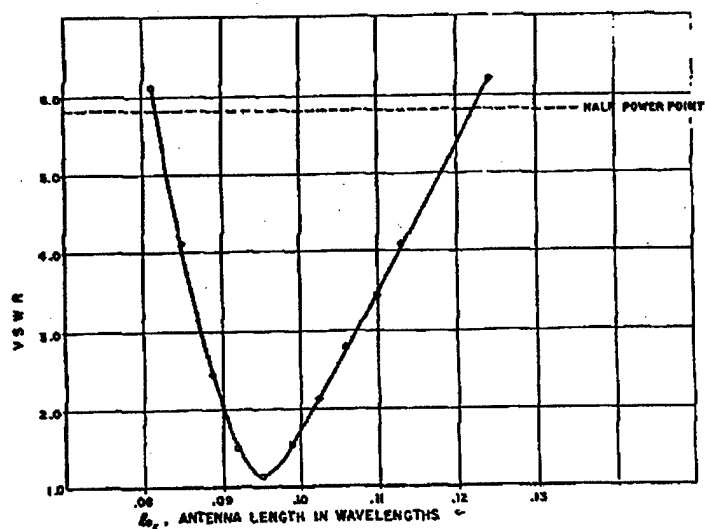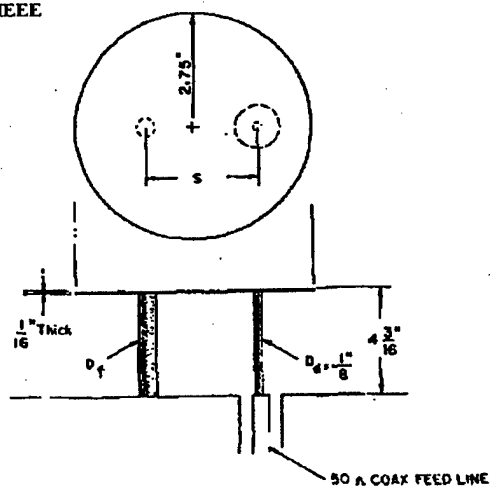
Figure 4. The disk loaded folded monopole antenna studied by Seeley in 1956 [9]. The VSWR for the antenna when $D_f/D_d = 1$ and $s = 2.5$ inches is also presented. The antenna exhibits minimum VSWR at a frequency where its overall height is approximately 0.095λ. The 2:1 VSWR bandwidth is approximately 14%.

469
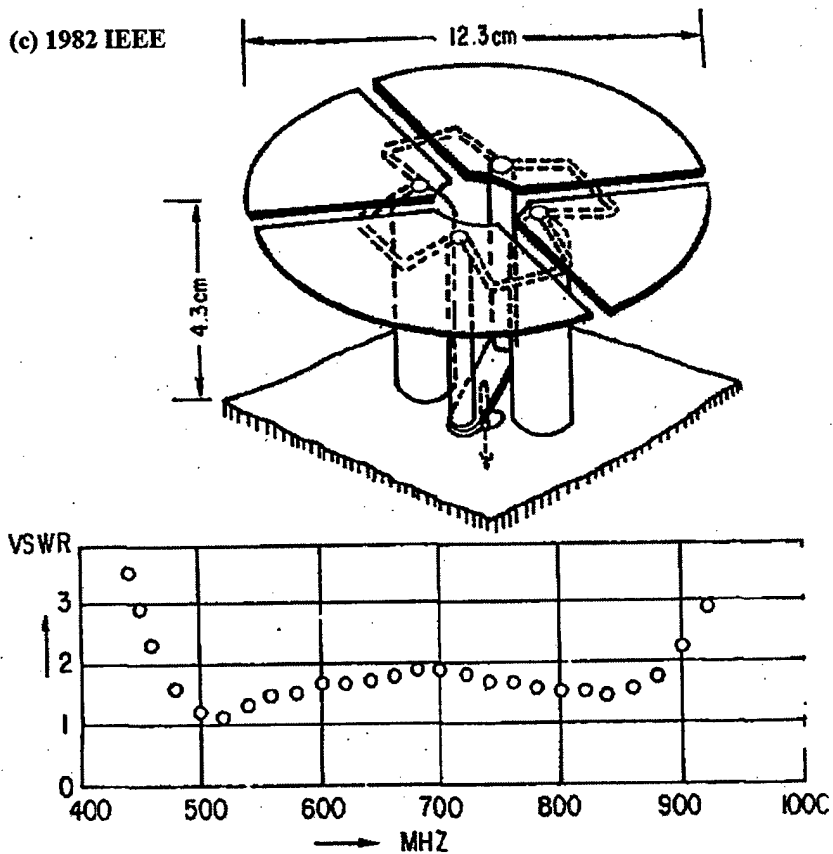
Figure 5. Depiction and measured VSWR of the Goubau multi-element monopole antenna [14]. The Goubau antenna exhibits a 2:1 VSWR bandwidth of approximately 1.9:1. The antenna has a height of 0.067λ at its lowest operating frequency.
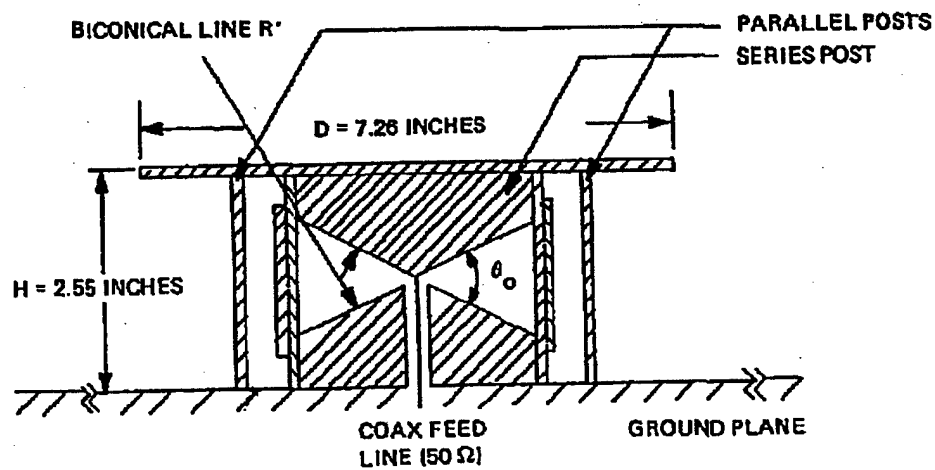
Figure 6. Depiction of Friedman's double-tuned disk loaded folded monopole antenna exhibiting a 2:1 VSWR bandwidth of approximately 1.9:1. The antenna has a height of 0.071λ at its lowest operating frequency [15].

470
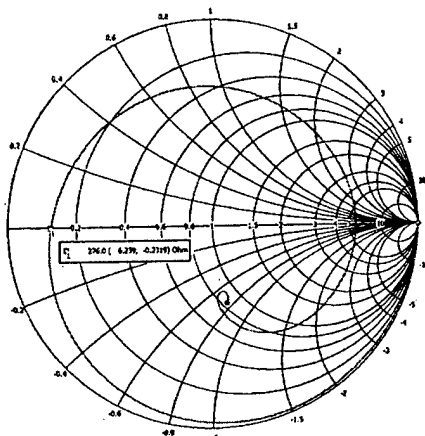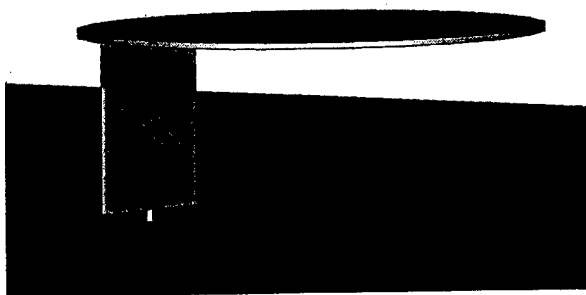
Figure 7. Disk loaded planar monopole resonant at 276 MHz with a resistance of 6.3 Ohms.
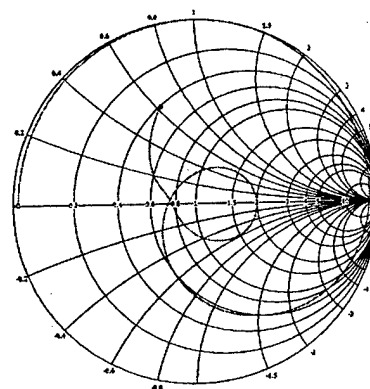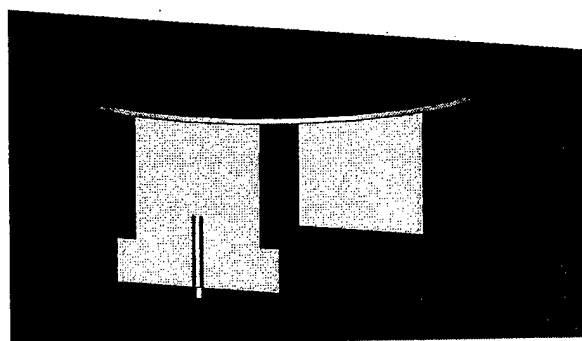
Figure 9. Disk loaded folded monopole with a 2:1 VSWR bandwidth covering 394 – 1085 MHz.
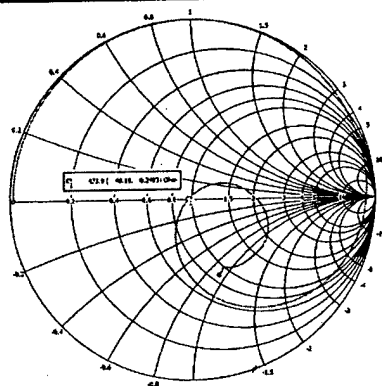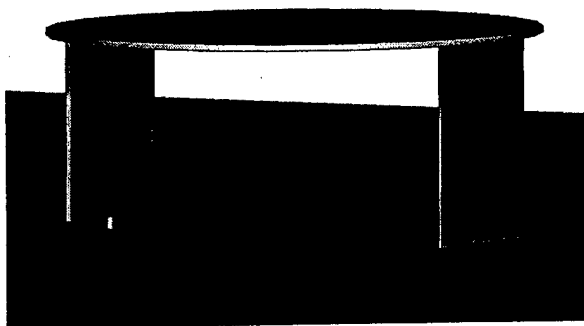
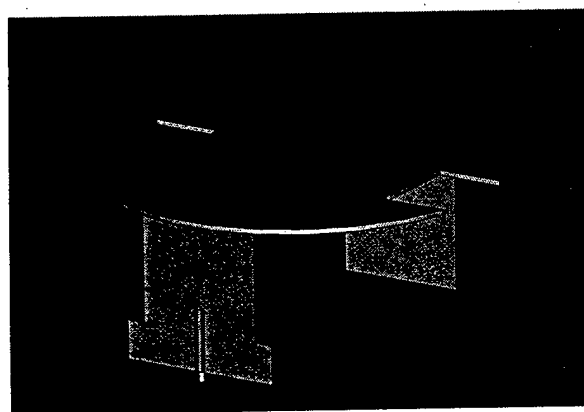Figure 8. Disk loaded folded planar monopole resonant at 473 MHz with a resistance of 48.2 Ohms.

Figure 10. Disk loaded folded monopole with increased top disk diameter and cut-outs introduced into the top disk. This antenna exhibits a 2:1 VSWR over a frequency range covering 374 – 1093 MHz, a 2.9:1 bandwidth. It has a height of 0.085λ at its lowest operating frequency.
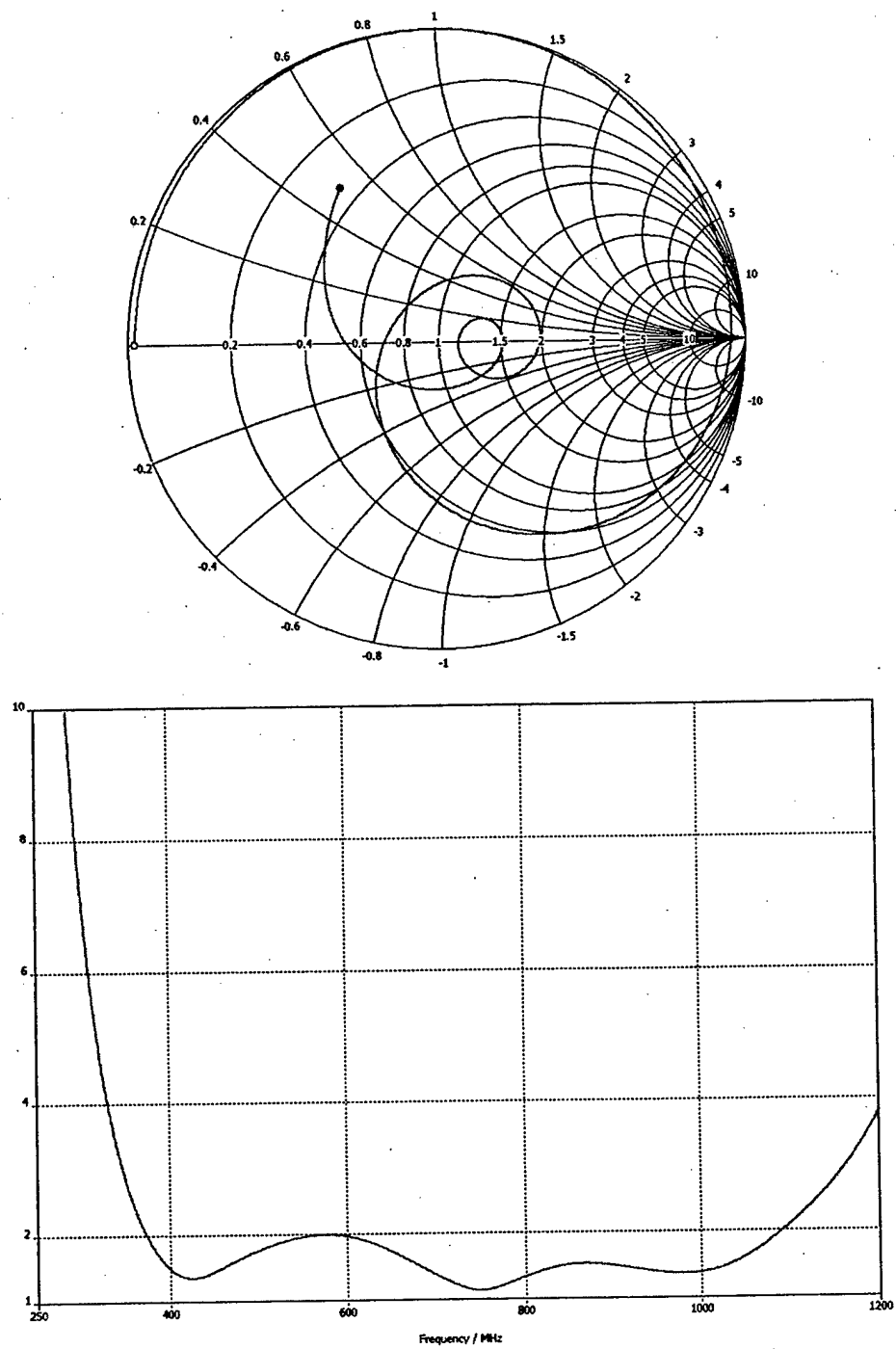
Figure 11. Smith chart and VSWR curve for the disk loaded folded monopole antenna depicted in Figure 10.
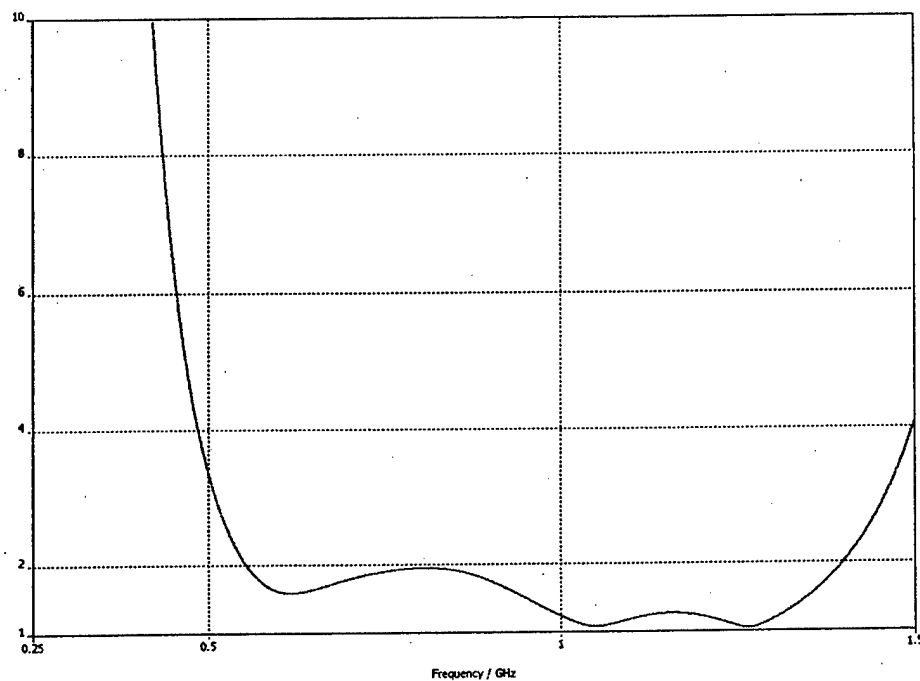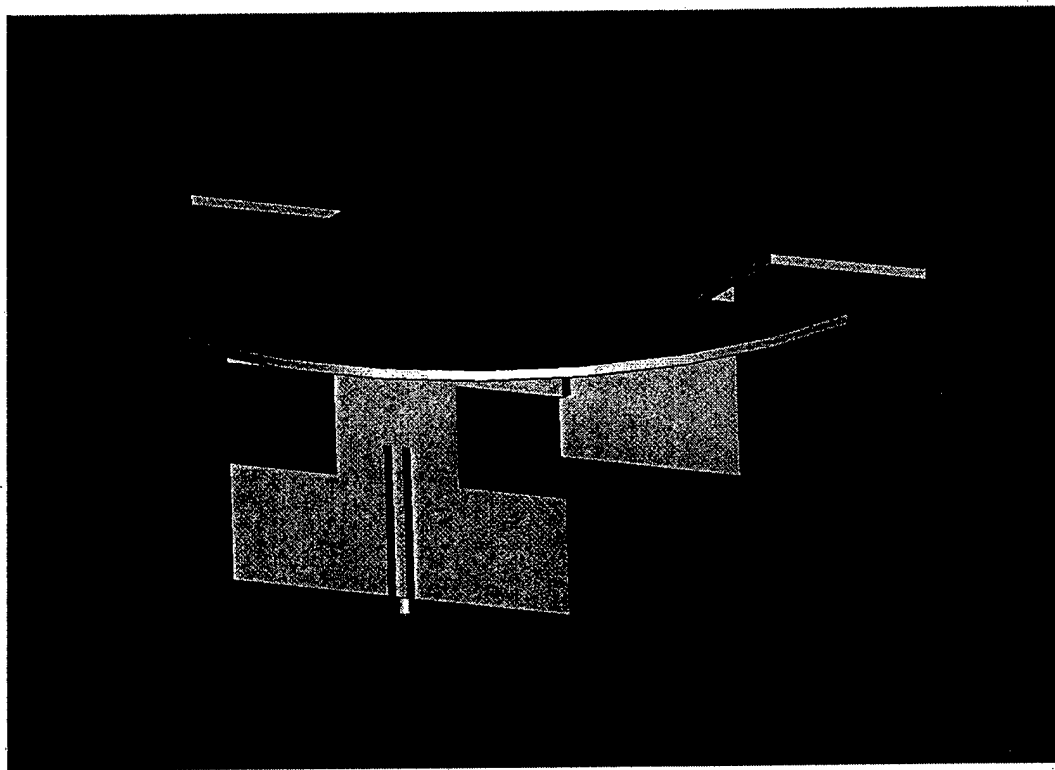
Figure 12. Depiction and VSWR curve of a disk loaded folded monopole antenna having dimensions matching those of the Goubau antenna [14]. This antenna exhibits a 2:1 VSWR bandwidth covering 554 – 1400 MHz, a 2.9:1 bandwidth. The antenna has a height of 0.08λ at its lowest operating frequency.